UNIVERSITÀ DEGLI STUDI DI MODENA E REGGIO EMILIA

DIPARTIMENTO DI SCIENZE CHIMICHE E GEOLOGICHE

Doctorate school in Multiscale Modelling, Computational Simulations and Characterization in Material and Life Sciences

XXVIII Cycle

Crystal chemistry and physical-chemical characterization of mineral fibres aimed at understanding their toxicity potential

Ph.D. Candidate: Simone Pollastri

Tutor: Prof. Alessandro F. Gualtieri

ACADEMIC YEAR 2014-2015

INDEX

1 – INTRODUCTION

In the following pages, a general introduction to the mineral fibres, their chemical-physical property and issues related to their toxicity, is given. Parts of this chapter are taken from Gualtieri *et al.* 2012 and from "ATSDR Case Studies in Environmental Medicine" (CSEM) Asbestos Toxicity. Course: WB 2344 (www.atsdr.cdc.gov).

1.1 Mineral fibres: an overview

The general term "mineral fibres" refers to a group of minerals ubiquitous on the Earth crust. Among them, the most relevant and certainly the most feared ones are asbestos minerals and fibrous zeolites such as erionite (Mossman *et al.* 1990; Baumann *et al.* 2013) which possess a dreadful reputation because they may provoke fatal lung diseases (mainly lung carcinoma and pleural/peritoneal mesothelioma) through inhalation.

The term 'asbestos' is a generic industrial-commercial term used to describe a group of hydrate silicate minerals that occur as bundles of flexible fibres, that can be separated into thin, durable threads (Benarie, 1986).

Asbestos minerals are further subdivided into two major groups: serpentine asbestos and amphibole asbestos; the fibrous-asbestiform variety of serpentine is called chrysotile and represent the most commonly used form of asbestos.

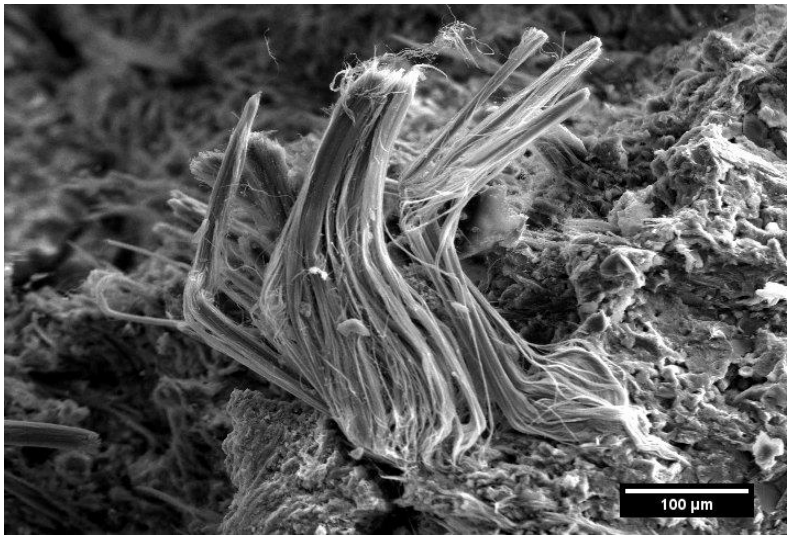

Fig. 1.1.1. SEM image of a bundle of chrysotile fibres.

Asbestos fibres are composed of smaller fibrillar components (usually called *fibril*s, Skinner *et al.*, 1988) clearly visible along a bundle of folded fibres (Fig. 1.1.1). This peculiar crystal habit is called fibrous-asbestiform.

The length of a single fibril may range from few microns up to decimetres, with a diameter in the order of tens nanometres, whereas the length of a fibre usually ranges from a few microns to decimetres, with a diameter usually smaller than 0.5 µm.

The family of amphiboles includes five minerals: actinolite, amosite, anthophyllite, crocidolite and tremolite. With respect to chrysotile, amphibole fibres are more brittle and exhibit a stiff, needle-like crystal habit (Fig. 1.1.2).

These six asbestos minerals exhibit outstanding properties that have been exploited in a countless number of mechanical and commercial applications, such as thermal insulation, building materials, fire- and bulletproof materials, textiles products, and many others.

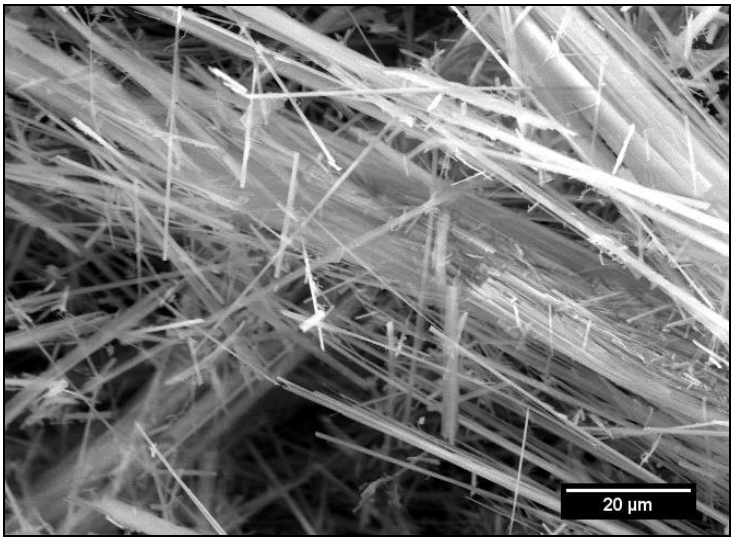

Fig. 1.1.2. SEM image of anthophyllite fibres.

The most important chemical-physical and technological properties of the three major commercial asbestos are reported in table 1.1.1:

Table 1.1.1
Physical–chemical and technological properties of the three commercial asbestos minerals (From Gualtieri, 2012).

Property	Chrysotile (white asbestos)	Amosite (brown asbestos)	Crocidolite (blue asbestos)
Acid resistance	Not resistant	Resistant	Resistant
Alkali resistance	Resistant	Resistant	Resistant
Decomposition point (°C)	450-700°C	950-1050 °C	950-1050 °C
Density (g/cm^3)	2.52-2.56	3.4-3.5	3.3-3.4
Flexibility[a]	Good	Fair	Good
Melting point (°C)	1500	1400	1200
Mohs hardness	2.5-3	3.5-4.5	3.5-4.5
Sound transmission coeff. (STC)[b]	70-90	60-70	60-70
Surface area (m^2/g)	10-20	5-15	5-15
Tensile strength (kg/cm^2)[a]	0.031	0.025	0.035
Thermal conductivity (W/m^{2}K)	0.1-0.2	0.2-0.4	0.2-0.4

[a] From Skinner *et al.* (1988); [b] STC is an integer number which rates how well a material attenuates airborne sound according to the ASTM International Classification E413 and E90 in the USA and the Sound Reduction Index (SRI) ISO standard outside the USA.

The fibrous zeolite erionite represents a special case, both from the chemical-mineralogical and socio-economical point of view. In fact, it does not show an asbestiform crystal habit as that of the asbestos minerals, but is composed of individual fibres of small size (Fig. 1.1.3).

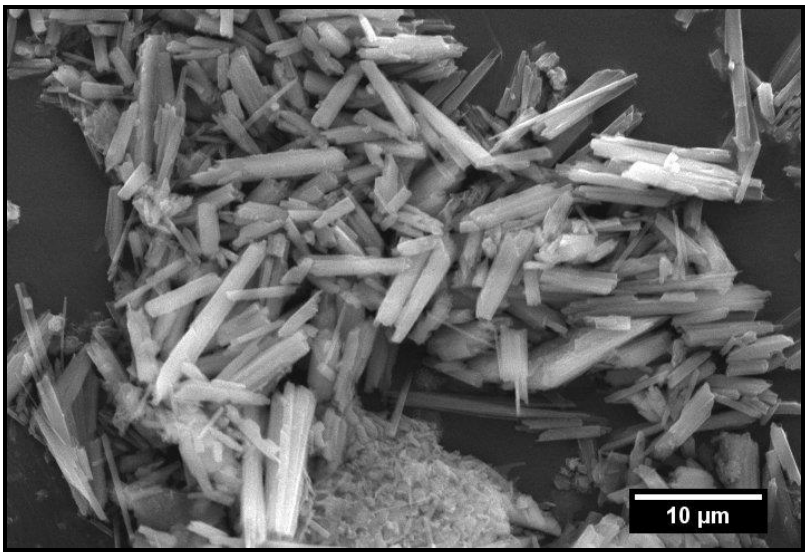

Fig. 1.1.3. SEM image of erionite fibres.

Its fame is primarily linked to the erionite-rich sedimentary stones used for building villages in Cappadocia (a region of central Anatolia in Turkey). There, mainly in the three villages of Karain, Tuzcöy and Sarihidir, exposure to erionite fibres occurs in the houses, annexes, and streets of the villages and could also be detected in air samples obtained from those places; this causes a long term hazard for the inhabitants (Emri *et al.* 2002). In those villages, an impressive rate of malignant mesothelioma (MM) causes 50% of deaths in men and women (Bariş *et al.* 1995; Roushdy-Hammady *et al.*, 2001). Recent studies indicate that the mutations of the enzyme BAP1 (a deubiquitylase that regulate key cellular pathways, including the cell cycle, cellular differentiation, cell death, gluconeogenesis and the DNA damage response, DDR) cause a novel cancer syndrome that, in conjunction with erionite exposure, seems to be an etiologic co-factor in the cause of malignant mesothelioma in genetically predisposed villagers (Roushdy-Hammady *et al.*, 2001; Carbone *et al.* 2013). Opposite to chrysotile and amphiboles, erionite has never been used for industrial applications.

Unfortunately, the fibrous crystal habit which confers excellent properties to all these minerals is also the casue of their toxicity potential. This concept especially applies to respirable fibres. In this regard, it's important to define the concept of regulated asbestos fibres, as this parameter determine whether an ACW (Asbestos Containing Waste) is hazardous, defined in the Occupational Health and Safety Act (Act 85, 1993) as the ability to release "0.5 regulated asbestos fibres per milliliter". A regulated asbestos fibre means: "A particle of asbestos with a length to diameter ratio greater than 3 to 1, a length greater than 5 µm and a diameter less than 3 µm", according to the Environment Conservation Act 73, (1989).

These fibres occur in different sizes in inhaled air: the largest one tend to deposit on the nasal mucosa or the oropharynx and are sneezed out or swallowed and never reach the lungs (NIOSH, 2011). Some of the smaller inhaled fibres are deposited on the surface of the larger airways where some of them are cleared by mucociliary transport and swallowing. Smaller fibres are deposited further down in the lung, especially in the bifurcations of the tracheobronchial tree, and some are deposited in the alveolar sacs (Broaddus, 2001).

There has been much scientific discussion about how fibre size affects the pathogenicity of asbestos. Some papers have shown cumulative fibre exposure to be an important risk factor for the development of asbestosis (Larson *et al.* 2010) but it should be remarked that asbestos fibres of all lengths cannot be excluded as contributors to asbestos-related diseases (Dodson *et al.* 2003).
Once deposited in the lungs, fibres are subject to several lung defenses. The most important means of removal of insoluble particles deposited in respiratory tract airways is by mucociliary clearance. This cleared material is usually swallowed and enters the gastrointestinal tract or is coughed out in sputum and eliminated from the body (NIOSH, 2011). When instead fibres are deposited in the alveoli, alveolar macrophages are involved. These specialized cells generally function to clear particles by enveloping them in a process called phagocytosis and then moving to the airways, where the particle-containing macrophages are transported out of the lungs via mucociliary clearance.
Nevertheless, in some cases, insoluble particles are not easily cleared from the alveoli by alveolar macrophages, because:

- Some particles are highly reactive and toxic to the macrophage cells, which die before they can clear the engulfed particles.
- Under "overload" conditions so many particles are inhaled that they overwhelm the ability of alveolar macrophages to clear them from the alveoli (Dodson and Hammar, 2011; Damjanov, 2012).
- Fibres that are >10-15 μm cannot be completely engulfed by a single phagocytic cell, prompting *frustrated phagocytosis* (Brown *et al.* 2007; Donaldson, 2012).

In addition to the above mechanisms, shorter fibres may travel from the alveoli to the lymphatic system of the lungs, or can migrate to pleural and peritoneal spaces, especially following patterns of lymphatic drainage (Broaddus 2001; Dodson *et al.* 2003).
In any case, many fibres are retained in lung tissues for many years and how rapidly the body's defenses can clear them depends partially on the type of asbestos. While all types of fibres are retained for years in the lungs (ATSDR, 2001), amphibole fibres are degraded more slowly than chrysotile fibres of the same dimensions (Hillerdal 1999; Bernstein *et al.* 2008) and this is one of the main reasons at the basis of the controversy to whether chrysotile asbestos is a potent carcinogen to humans or not (Kanarek, 2011; Qi *et al.* 2013).
Further details about the chrysotile issue are given in chapter 1.2 whereas in the following sections, a more detailed description of the aforementioned minerals is given.

1.1.1 Amphiboles

Amphiboles are one of the most complex group of rock-forming minerals, exhibiting large chemical variation and an incredible variety of parageneses (Hawthorne, 1983).
The forms and habits adopted by the amphibole minerals are also diverse, but commonly columnar, acicular, or fibrous. In this thesis, only the (hazardous) fibrous amphiboles will be considered; a more detailed description of the amphiboles group can be found in Hawthorne (1981, 1983) Skinner (1988) and Hawthorne *et al.* (2007).
Amphiboles crystallize in both igneous and metamorphic rocks; they have perfect prismatic cleavage that produces fine acicular fragments (Fig. 1.1.2) when the minerals are grounded or milled (Craighead and Gibbs, 2008).

The formation of amphibole asbestos is the result of single-crystal fibrillary growth through preferential extension along one crystallographic direction (Skinner, 1988). They typically occur in veins created when cracks form in rocks during earth movement (Skinner, 1988); in fact, it appears that fibres form in places where there is shearing (slip fibres) or rock dilatation (cross fibres) and it is not expected the formation of fibres in rocks that are not mechanically disturbed (Virta, 2003).
From the crystallographic point of view, amphiboles are double-chain silicates with a Si(Al):O ratio of 4:11 and the oxygen atoms of the chains coordinated not only to Si(Al) but to a variety of other cation sites, yielding the following simplified general formula (Veblen, 1981):

$$A_{0\text{-}1}B_2C_5T_8O_{22}(OH,F,Cl,O)_2$$

Where T are the tetrahedral sites within the silicate chain (Si^{4+}, Al^{3+}), C are fairly regular octahedral cation sites M(1), M(2) and M(3) (Mg^{2+}; Fe^{2+}, Mn^{2+}, Al^{3+}, Fe^{3+}, Ti^{3+}, Ti^{4+}), B are less regular octahedral or 8-fold coordinated cation sites M(4) (Na^{+}, Li^{+}, Ca^{2+}, Mn^{2+}, Fe^{2+}, Mg^{2+}), and A are irregular cation sites having coordination in the range 6 to 12 (Na^{+}, K^{+}).
The tetrahedral sites are indicate by T whereas octahedral sites are indicated by M; there are two distinct tetrahedra designated as T(1) and T(2) and three distinct types of octahedra designated as M(1), M(2) and M(3). The double chain of corner-sharing tetrahedra and the strip of octahedra are linked by the M(4) site, and below the hexagonal ring of tetrahedra there is the A site, at the center of a large cavity (Fig. 1.1.4).

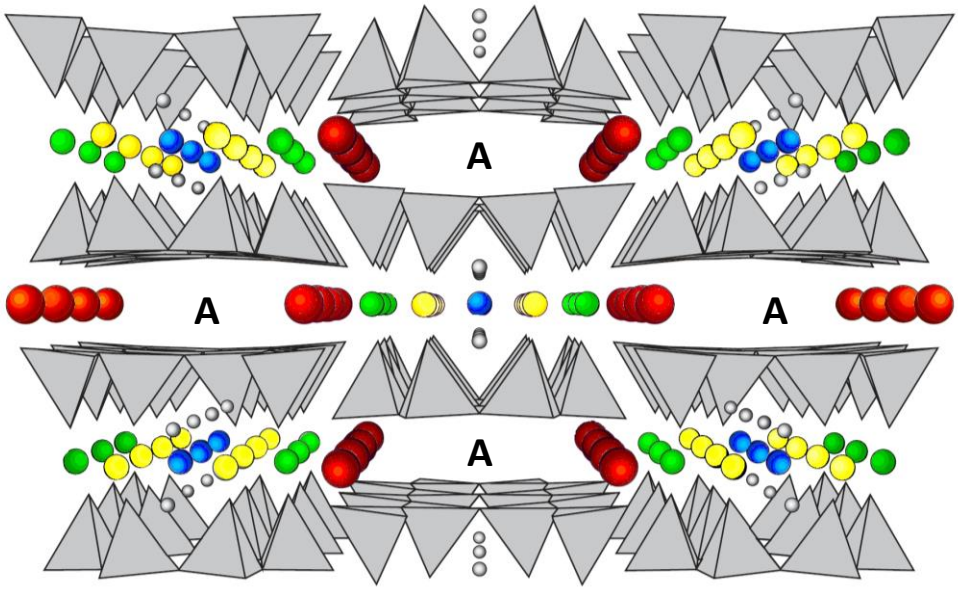

Fig. 1.1.4. Sketch of the structure unit of amphibole asbestos composed of one-dimensional double-chains (a–b crystallographic plane). Yellow=M(1), green=M(2), blue =M(3), red=M(4) and the A site.

Because of the presence of strong bonds, amphiboles normally crystallize along the crystallographic c direction (Ferraris, 2002). Hence, the fibrous crystal habit is due to the monodimensional character of their structural units (chains).
The group of fibrous amphiboles includes five species, listed in table 1.1.2:

Table 1.1.2
Chemical composition of the amphibole asbestos minerals together with their crystal symmetry.

Sample	Ideal chemical formula	Crystal System
fibrous actinolite (byssolite)	$Ca_2(Mg,Fe)_5Si_8O_{22}(OH)_2$	Monoclinic
amosite (fibrous variety of grunerite)	$(Fe^{2+},Mg)_7Si_8O_{22}(OH)_2$	Monoclinic
fibrous anthophyllite	$(Mg,Fe^{2+})_7Si_8O_{22}(OH)_2$	Orthorombic
crocidolite (fibrous variety of riebeckite)	$Na_2(Fe^{2+},Mg)_3Fe_2^{3+}Si_8O_{22}(OH)_2$	Monoclinic
fibrous tremolite	$Ca_2Mg_5Si_8O_{22}(OH)_2$	Monoclinic

1.1.2 Chrysotile

Chrysotile, the fibrous-asbestiform variety of serpentine, occurs most commonly in metamorphosed serpentinite deposits, the host rock containing cross-fibre veins (Wicks and O'Hanley, 1988). Chrysotile fibres are almost always contaminated with other minerals, and trace metals are particularly abundant.

Chrysotile (as well as lizardite and antigorite, all serpentine minerals) is a layer silicate composed of Si-centred tetrahedral (T) sheets in a pseudo-hexagonal network joined to Mg-centred octahedral (O) sheets in units with a 1:1 (T:O) ratio (Fig. 1.1.5a). The general chemical formula of serpentine minerals is $(Mg,Fe,Al)_3(Si,Al)_2O_5(OH)_4$.

The lateral dimension of an ideal magnesium occupied octahedral sheet (b = 9.43 Å) is larger than the lateral dimension of an ideal tetrahedral silicon-occupied sheet (b = 9.1 Å). This misfit between the sheets is significant and is solved in different ways in the three serpentine minerals structures (an example is given in Fig. 1.1.6).

In this thesis, only chrysotile will be considered; a full description of serpentine group minerals can be found in Giacobbe (2012).

As a result of the polarity of the TO unit and the misfit between the T and O sheet (Bailey, 1988), a differential strain occurs between the two sides of the layer.

The strain is released by rolling the TO layer around the fibril axis (Fig. 1.1.6), which is usually the crystallographic a axis (clinochrysotile and orthochrysotile) and more rarely the crystallographic b axis (parachrysotile).

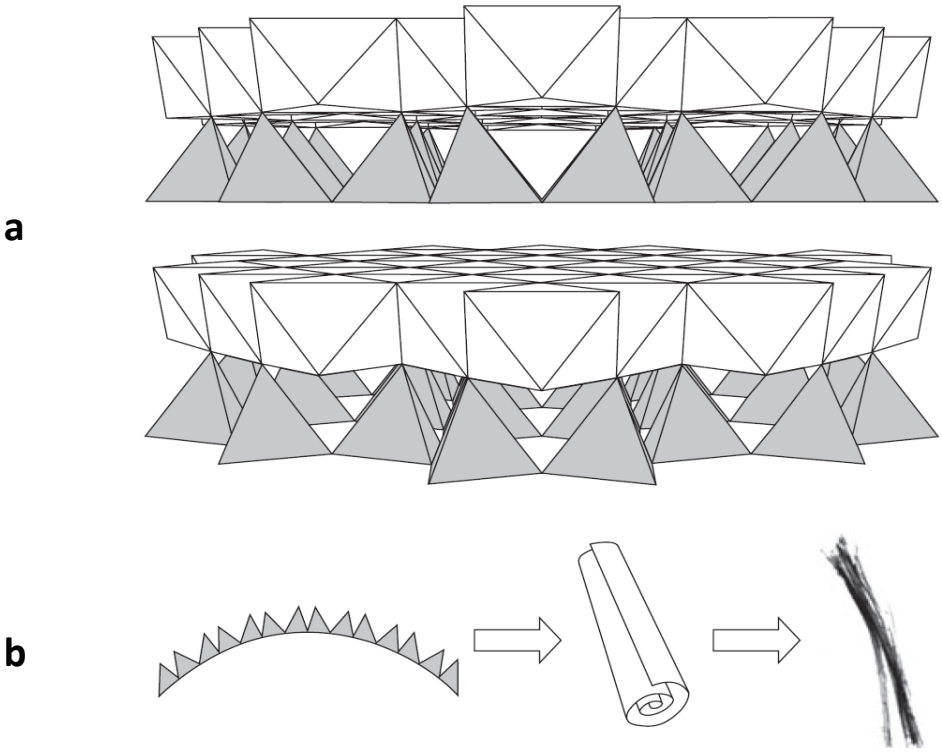

Fig. 1.1.5. a) Sketch of the structure unit of chrysotile asbestos with an Si-centred tetrahedral sheet joined to a Mg-centred octahedral sheet (b–c crystallographic plane); b) Bending of the layers in chrysotile at a molecular scale, resulting in a rolled carpet-like microstructure which is a fibril at the microscale (From Gualtieri 2012).

The fibrils are thus composed of concentrically or spirally curved layers, forming a tubular structure (Yada, 1971). By this mechanism, a layer silicate assumes a fibrous crystal habit (see Fig. 1.1.5b). Because the layers cannot energetically withstand too tight a curvature, the rolls possess hollow cores with a diameter of about 5–8 nm (Cressey *et al.*, 1994).

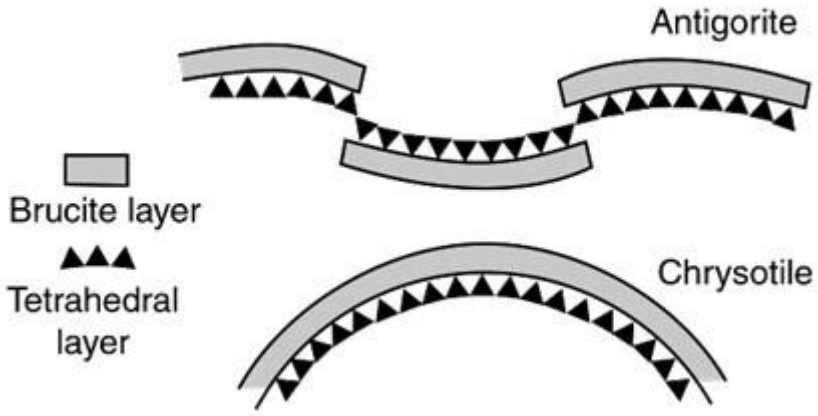

Fig. 1.1.6. Comparison between the structure of antigorite and that of chrysotile (www.cefns.nau.edu).

The earlier X-ray diffraction studies on chrysotile showed a remarkable distortion (curvature) of the unit cell with respect to the conventional crystal structures, so that a new theory specially formulated for cylindrical lattices was developed (Whittaker, 1956; Jagodzinski and Bagchi, 1953; Devouard and Baronnet, 1995).

1.1.3 Erionite

Erionite is a widespread natural zeolite-group mineral; its fibrous form has usually sedimentary origin and often occurs as altered product of volcanic tuffs (Virta, 2002; Ballirano *et al.* 2009).

From the structural point of view, it belongs to the ABC-6 family (Gottardi and Galli, 1985), and its framework consists of columns of cancrinite cages (Staples and Gard, 1959; Gard and Tait, 1972; Gualtieri *et al.*, 1998; Ballirano *et al.*, 2009) connected along the *z* direction by double six-membered rings of tetrahedra, forming hexagonal prisms (Staples and Gard 1959); the cancrinite cages are alternatively rotated by 60°. Adjacent columns are linked by single six-membered rings connecting cancrinite cages at the same level (Fig. 1.1.7), forming the larger cages distinctive of each topology: Erionite has large cages (erionite cages, or 23-hedra) with the larger openings formed by eight-membered rings (Smith and Bennett, 1981; Gualtieri *et al.* 1998; Ballirano *et al.* 2009).

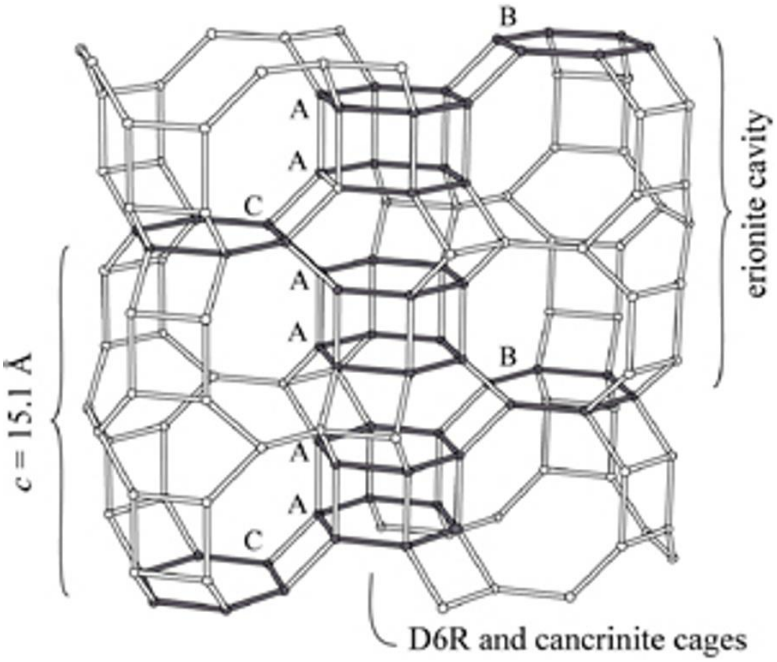

Fig. 1.1.7. Framework of erionite (From www.iza-online.org/natural/Datasheets/Erionite/erionite.htm).

The erionite framework can also be described by the stacking along the *z* direction of 6-rings following the AABAAC sequence. Intergrowth of erionite with offretite may occur, due to the close similarity between the two zeolites (Ballirano *et al.* 2009). In fact, offretite has an AABAAB sequence, and stacking faults corresponding to partial substitution of C with B six-membered rings have been observed (Schlenker *et al.* 1977).

Erionite is hexagonal, space group P6_3/mm*c* (Kawahara and Curien 1969) and has the following simplified general formula (Coombs *et al.* 1997):

$$K_2(Na,Ca_{0.5})_8[Al_{10}Si_{26}O_{72}]\cdot 30H_2O$$

A large chemical variability is typical of this mineral, and for this reason three different species are identified, according to the most abundant extra-framework cation: Na-erionite, K-erionite and Ca-erionite (Coombs *et al.* 1997; Passaglia *et al.* 1998; Gualtieri *et al.* 1998; Dogan and Dogan, 2008).

1.2 The “amphibole hypothesis”

In the last two decades, these mineral fibres have been the subject of intensive multidisciplinary investigations as the mechanisms by which they induce cyto- and genotoxic damage remain poorly understood. In general, the cause-effect relationship between exposure to the fibres and the onset of mesothelioma and other lung diseases remains ambiguous. The difficulties mainly arise from the fact that mineral fibres display great variability in their chemistry, molecular arrangement, size and diameter, surface activity (Pollastri *et al.*, 2014; paper 1, pag. 156), and ability to generate reactive oxygen species and biopersistence (Donaldson *et al.*, 2010; Pollastri *et al.*, 2014 and references therein) so that drawing a general conclusive model explaining their toxicity has been a pipe dream to date.

Because of the existence of a grey area in the scientific knowledge, although it was proven that these mineral fibres, if inhaled, may induce lethal lung diseases (Doll, 1955; Lemen *et al.,* 1980; Craighead *et al.,* 1982; Mossman *et al.,* 1996; Becklake *et al.,* 2007; Kamp, 2009) there is still considerable controversy in the scientific community to whether chrysotile asbestos is actually a (potent) carcinogen to humans (Kanarek, 2011; Qi *et al.,* 2013).

In general, the global scientific and political community is divided into two fronts: one side assumes that all above mineral fibres are indistinctly classified as potentially toxic substances; the other side instead promotes the *safe use* of chrysotile assuming that the potential toxicity of this fibre is much lower (or null) with respect to that of fibrous amphiboles and erionite.

This latter position relies primarily on the fact that chrysotile is much less biopersistent compared to amphiboles and erionite, and therefore it's almost impossible to observe chrysotile fibers in the pleural cavity in the long term (Bernstein, 2014).

At the moment, all amphibole asbestos minerals are banned worldwide whereas chrysotile is banned only in the countries where the line of the International Agency for Research on Cancer (IARC) of the World Health Organization and the National Toxicology Program has been fostered (Mossman and Churg, 1998; Hollan and Smith, 2001; Yano *et al.*, 2001; Roggli *et al.*, 2002; Pfau *et al.*, 2005; Yarborough, 2007). Erionite, a human carcinogen listed by the IARC as a Group 1 Carcinogen, surprisingly has not been banned to date (Dikensoy, 2008).

1.3 Aims of the thesis

The purpose of this thesis is the characterization of the major mineral fibres of social and economic-industrial importance (conducted, for the first time, in a systematic way) starting with a full mineralogical-structural and microstructural investigation combined with physical-chemical and biological tests, in order to explain the nature of the biological interaction mechanisms of chrysotile, amphiboles and erionite and compare them so to draw a convincing rank of toxicity of mineral fibres.

The final aim is to contribute to develop of a general conclusive model to assess the biological toxicity of mineral fibres and understanding the interaction mechanisms. This model would be very useful in consideration of the fact that there are many mineral fibres (like zeolites) not yet classified that might possess a toxicity potential. By applying the different chemical-physical properties of a not-classified fibre to the model, its potential degree of toxicity could be calculated and new cases of mass exposure as Biancavilla for fluoro-edenite (Comba *et al.* 2003) and Tuzcöy for erionite (Dumortier *et al.* 2001) could be avoided.

For the achievement of such objectives, since 2011 the research project "*Sviluppo di un modello generale di interazioni tra fibre minerali e cellule biologiche*", a part of the comprehensive granted long term Italian Research Project of National Interest (PRIN) entitled "*Interazione fra minerali e biosfera: conseguenze per l'ambiente* e *la salute umana*" is being in progress.

It should be remark that this topic has already been the subject of many studies, which, however, were always focused on a specific aspect of the problem and/or only on one of the mineral fibres considered, but never following a systematic and standardized approach; this strategy results in a very huge amount of spot data available in the literature which can be of support to our study.

As a first step, the mineralogical characteristics such as the presence of impurities, the surface reactivity, the crystal structure and the chemical environment of the iron within it will be studied. Then, reached a good level of physical-chemical characterization of the samples, investigations will be addressed on aspects of biological interaction; specifically, to the structural changes undergone by the fibres after being in contact with human cell cultures and to dissolution experiments in contact with simulated lung fluid solution (SLF) at acidic pH. A combination of several analytical techniques, both using conventional and non-conventional sources, will be applied to reach the objectives of the thesis.

2 – MATERIALS AND METHODS

2.1 Samples selection

The samples investigated in this thesis are eight mineral fibres, selected for their socio-economic and industrial importance; details of samples are given in Table 2.1.1:

Table 2.1.1
Nature and details of the investigated mineral fibres.

Sample	Provenance	Notes
Chrysotile	Quebec (Canada)[a]	UICC standard Chrysotile "B" Canadian NB #4173-111-1
Chrysotile	Balangero, Turin (Italy)	
Chrysotile	Val Malenco, Sondrio (Italy)	
Crocidolite	Koegas Mine, Northern Cape (South Africa)	UICC standard Crocidolite South African NB #4173-111-3
Amosite	Penge mine, Northern Province (South Africa)	UICC standard Amosite South African NB #4173-111-4
Fibrous tremolite	Val d'Ala, Turin (Italy)	
Fibrous anthophyllite	Paakkila mine, Paakkila (Finland)	UICC standard Anthophyllite Finnish NB #4173-111-5
Fibrous erionite	Jersey, Nevada (USA)	

[a]Mixture of fibre from the firms Bells, Carey, Cassair, Flintkote, Johns-Manville, Lake, Normandie and National, proportioned roughly to represent Canadian production of asbestos products at that time.

The chrysotile and amphibole samples have been selected because they are the mineral fibres that have been most widely used in human history (there is evidence that amphibole asbestos was used already in Stone Age, as long as 7000-10000 years ago) for an endless variety of applications (see Chapter 1), even if chrysotile is by far the predominant asbestos fibre ever used. Specifically, UICC Canadian chrysotile has been selected as standard reference; that of Balangero for the relevant implications that has been in Italian history (Silvestri *et al.* 2001; Mirabelli *et al.* 2008) and that of Val Malenco for the lack of data regarding its cancerogenicity. The UICC standard anthophyllite, crocidolite and amosite samples were selected as they occur in the most exploited and important mining areas worldwide. Fibrous tremolite has been selected both for its high toxicity potential (Pacella *et al.* 2008) and because it is not uncommon to find its fibres as contaminant in chrysotile, making it a determining variable in the already discussed chrysotile issue. Their large and widespread use results in a remarkable exposure of the population to these mineral fibres. Exposure continues today because a huge amount of asbestos containing materials are still present in the work and living environments, such as asbestos-cement (AC) slates.
Erionte was instead chosen both for its high toxicity potential (see Chapter 1), for its widespread occurrence throughout the world in sedimentary rocks and for its chemical-physical characteristics considerably different compared to that of the other mineral fibres.

Moreover, regarding chrysotile UICC, crocidolite UICC and erionite, these fibres were selected also because they are exactly the same used for a past *in vivo* testing performed in '80s by the Ramazzini Cancer Research Institute (Bentivoglio, Bologna, Italy) to assess their cancerogenicity (Maltoni and Minardi, 1989).

2.2 Samples preparation

The raw samples consist of actual clumps (UICC and Balangero) and macro-bundles (Val Malenco) of fibres regarding the three chrysotile samples whereas amphiboles and erionite appear as bulk or powders-like samples; for this reason, depending on the analysis to be performed and results to be achieved, different samples preparation techniques were used.

The main difficulties concern the chrysotile samples as these fibres are very flexible and resistant to abrasion, and therefore almost impossible to be powdered. It was necessary to obtain powder or at least short fibres samples for two main reasons: 1) Because of the need to perform analysis on two classes of length of the fibres, in order to check for any differences in toxic potential between short and long fibres, also in consideration of the dimensions of regulated fibres (see 1.1 section); 2) For the needs of some experimental techniques, such as XRPD, that must be carried out on powder homogeneous samples.

Furthermore, it should be remark that in any case it would be impossible to fill the capillary tubes for XRPD analysis (with a diameter ranging from 0.1 to 0.5 mm, because with larger diameters the absorption of X-rays would be too high), with raw chrysotile fibres.

2.2.1 Gravitational separation

In order to obtain two distinct size classes of fibres for each sample, gravitational separation in wet conditions were performed. After being coarsely crushed by hand in an agate mortar, samples have been diluted in a large quantity of distilled water to attempt wet gravitative separation using the Appiani levigator (Fig. 2.2.1) method (Jolicoeur *et al.* 1981). The procedure takes approximately 3 h per sample. The obtained material have been dried in heater at 60 °C until the complete evaporation of the water; then, the two classes were characterized by scanning electron microscope (SEM) analysis in order to verify the outcome of the separation procedure, to check for the chemical composition of the fibres using an energy dispersive X-Rays fluorescence spectrometer (EDS) and to estimate the average length of the fibres for each class (by analysing the SEM images using the ImageJ software, version 1.42q; Rasband, 2008). Analyses were conducted using a Philips XL-40/604 instrument equipped with EDS. For the observations, a tiny amount of sample was loaded on an aluminium stub and coated with a gold 10 nm thick film (further details are given in the paragraph 2.3.1).

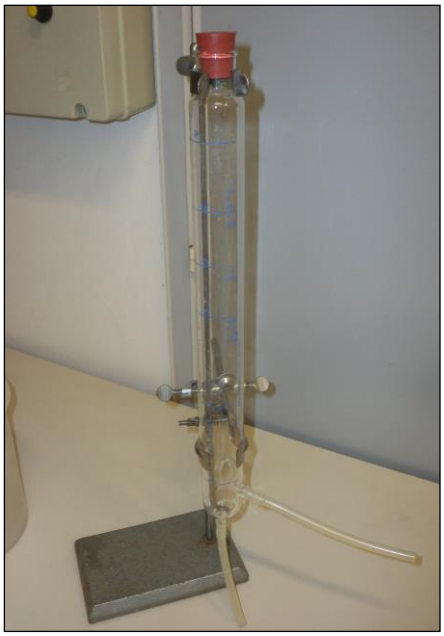

Fig. 2.2.1. The Appiani levigator.

2.2.2 Cryo-grinding

As already mentioned in paragraph 2.2, the need to perform XRPD experiments for structural analysis, has required the preparation of finely powdered samples. Whether this is relatively simple for amphiboles and erionite samples, it is considerably complicated for the chrysotile samples. In fact, conventional grinding techniques such as dry grinding in steel shatterbox (used in Viani *et al.* 2013) or wet grinding (both mechanical mill and manual in a mortar) have no effect on chrysotile fibres. For this reasons, we have opted for a cryo-milling in wet conditions, using a milling machine with jar and grinding balls in Cr-doped steel equipped with a vessel which injects liquid nitrogen directly on the jar while the machine is running (Fig. 2.2.2). This procedure allowed to obtain powderized chrysotile samples, perfectly suitable to be inserted in capillary tubes for synchrotron XRPD analysis.

Fig. 2.2.2. Cryo-milling machine in function. Liquid nitrogen descends from the vessel (1) through the tube on the right, to get in contact (externally) with the jar (2) containing the sample and the milling balls.

2.2.3 Preparation of Simulated Lung Fluids solutions

For selected experiments, Simulated Lung Fluids (S.L.F.) solutions have been prepared; specifically, for Zeta Potential (indicated by the Greek letter ζ) measurements, an organic Gamble's modified solution has been selected (Guldberg *et al.* 1998). Reagents used and their quantities are shown in Table 2.2.1a. With respect to the original formula, 250 ml of double-distilled water solution were used and no HCl was added. The pH of the obtained solution was monitored using a Criston Series 2000 instrument. A few drops of NaOH were also added to obtain a neutral pH. A starting solution having pH 7 was chosen to reproduce the extra-cellular environment. Subsequently, a part of the solution was adjusted to pH 4.5 using diluted HCl, to replicate the chemical environment present within phagolysosomes (intracytoplasmic vacuoles which are formed when a eukaryotic cell incorporates foreign material).

For dissolution experiments it was instead used another formula for the preparation of the so called Artificial Lysosomal Fluid (A.L.F.) solution (reported in Marques *et al.* 2011) whose composition is given in Table 2.2.1b.

During the preparation of both solutions, the components have been added in the order presented in Table 2.2.1 to avoid salt precipitation.

Table 2.2.1
S.L.F. liquid compositions starting from 250 ml of double-distilled water. 40% (15 ml) of formaldehyde was added to prevent growth of algae. a) Composition of the Gamble's solution; b) Composition of the A.L.F. solution.

a)

Reagent	Quantity used
$MgCl_2*6H_2O$	53.0 mg
NaCl	1.6 mg
Na_2HPO_4	37.0 mg
Na_2SO_4	20.0 mg
$CaCl_2*2H_2O$	64.0 mg
$NaHCO_3$	0.7 mg
Na_3 citrate$*2H_2O$	38.3 mg
NaOH	-
Citric acid	-
$C_2H_5NO_2$ (glycine)	29.5 mg
Na_3 tartrate$*2H_2O$	45.0 mg
Na lactate (60% w/w)	72.5 mg
Na pyruvate	43.0 mg

b)

Reagent	Quantity used
$MgCl_2*6H_2O$	26.7 mg
NaCl	802.0 mg
Na_2HPO_4	18.0 mg
Na_2SO_4	10.0 mg
$CaCl_2*2H_2O$	32.0 mg
$NaHCO_3$	-
Na_3 citrate$*2H_2O$	19.3 mg
NaOH	1500.0 mg
Citric acid	5200.0 mg
$C_2H_5NO_2$ (glycine)	14.8 mg
Na_3 tartrate$*2H_2O$	22.5 mg
Na lactate (60% w/w)	35.4 mg
Na pyruvate	21.5 mg

By comparing the two tables it should be remarked that, although many reagents are in common, use of citric acid and NaOH were used for the A.L.F. solution. This formulation allows to obtain a solution which possesses a suitable pH to the experiments of dissolution (namely that of the phagolysosome, around 4-4.50) without the need to adjust it with HCl.
We have chosen this new formulation since it is analogous to the organic fluid that inhaled particles come in contact with after phagocytosis by alveolar and interstitial macrophages in the lung (Marques *et al.* 2011). Therefore this fluid is similar to the environment of dissolution of the mineral fibres reaching the alveolar space.

2.2.4 *In vitro* toxicity tests

In order to explore the characteristics of the fibres after being in contact with cell cultures, representative samples of chrysotile UICC, crocidolite UICC, chrysotile Val Malenco and erionite have been selected and treated with cultured diploid human non-tumorigenic bronchial epithelial (Beas2B) and pleural transformed mesothelial (MeT5A) cells. Tests were conducted at the Department of Clinical and Molecular Sciences and Histology of the Marche Polytechnic University, under the supervision of Prof. Armanda Pugnaloni.

Both cell lines are widely used to assess the cytotoxicity *in vitro* of particles, nanoparticles and fibres. They also provide an *in vitro* model for the effects of asbestos fibres in lung and serous cavities (the mesothelium of pleura and peritoneum) which are key target tissues for asbestos-related disease (Wu et al., 2014; Li et al., 2012; Pugnaloni et al., 2007; Nygren et al., 2004; Liu et al., 2000; Pache et al., 1998).

MeT5A, human simian virus 40 (SV40)-immortalized pleural mesothelial cells, were grown at 37 °C in a humid atmosphere of 5% CO_2 in RPMI-1640 medium; Beas2B, SV40 large T antigen-immortalized (derived from normal human bronchial epithelium; ATCC® CRL9609™, Rockville, USA), were grown at 37 °C in DMEM High Glucose (4.5 g/l) medium with L-Glutamine. Both cell lines were supplemented with 10% fetal bovine serum (from Gibco, USA), 2mM l-glutamine, 100U/ml penicillin and 100U/ml streptomycin (Sigma-Aldrich, Milan, Italy).

Cells were passaged every 1–3 days by digestion with 0.25% trypsin (Sigma-Aldrich) containing 0.02% EDTA. Cells (70,000 Beas2B or 90,000 MeT5A) from log phase cultures were plated in T 25 flasks (area 25 cm^2) on the day prior to exposure. For the experiments, fibres have been weighed, suspended by vortexing in culture medium and added to the cultures at a concentration of 50 mg/ml; semi-confluent cultures of cells were exposed to for 24, 48, 72 and 96 h.

After exposure, samples were washed, firstly with culture medium and then with Phosphate-buffered saline (PBS). Cells were then trypsinized, re-suspended in medium, washed with PBS in vitreous vials and centrifuged. Later, to digest the biological components, materials have been rinsed in 13% sodium hypochlorite for at least 2 h at 50 °C until full transparency of the liquid was obtained.

Suspensions were finally filtered with a vacuum pump (Merck Millipore) on polycarbonate filters with pore diameter of 0.4 µm (Merck Millipore); filters were washed with warm distilled water to discard residual sodium hypochlorite crystals, deposited on glass and oven dried at 50 °C. In a second step, filters were sealed between two Kapton sheets for synchrotron investigation.

2.3 Conventional Methods

In this section the equipments, operating conditions and methodologies used for the characterization of samples using conventional methods, will be described. Parts of this chapter are taken from Murad and Cashion (2011), Giacobbe (2012), Gigli (2014), www.particle.dk and from www.rsc.org.

2.3.1 X-Ray Powder Diffraction (XRPD)

X-Ray Powder Diffraction (XRPD) patterns were collected for the determination of impurities (if present) and the refinement of the crystalline structure of the samples prior to synchrotron radiation experiments.

Measurements were conducted using a Bragg–Brentano PANalytical X'Pert Pro diffractometer, with a Θ–Θ geometry, Cu Kα radiation, 40 kV and 40 mA and an RTMS (Real Time Multiple Strip) detector.

When a large quantity of sample was available, a zero background sample holder made of glass was used, with the material placed with side loading mode. Instead, for small amounts of sample (i.e. all the resulting materials from the dissolution experiments), a zero background plate made of single crystal silicon, cut at special orientation, has been used; in this case, the material was dispersed on the sample holder with some drops of ethanol.

Data were collected in continuous mode, with 15 mm mask and 1/2° fixed divergence and antiscatter slits mounted in the incident beam pathway, 0.04 rad soller slits on both the incident and the diffracted beam pathway, and fixed 10 mm RTMS slit and a Ni filter in the diffracted beam pathway. An integrated step scan of the RTMS detector of 0.0167 °2Θ was used with a counting statistics of 75 s/step from 3 to 70 °2Θ.

Quantitative phase analysis (QPA) was performed using the Rietveld method (Rietveld, 1969). Refinements were accomplished with the GSAS package (Larson and Von Dreele, 1999) and its graphical interface EXPGUI (Toby, 2001). For the samples that could contain amorphous phase, pure α-alumina (corundum) NIST 676a has been added to the powders in a quantity of approximately 10 wt%, allowing the determination of both crystalline and amorphous content using the combined Rietveld–RIR method (Gualtieri, 2000).

For fibrous tremolite, the determination of the crystal structure has been performed using single crystal data, that have been collected using a Bruker Smart Breeze diffractometer (available at the department of Earth Sciences, University of Pisa) with an air-cooled CCD detector and graphite-monochromatized Mo *K*α radiation. Data were collected with a detector-to-crystal working distance of 50 mm, 50 kV and 40 mA, scan mode ω and ϕ, 0.5° amplitude rotation, 1188 frames collected with a 45 s exposure time for each frame, until 74 °2Θ. Data were refined using the software SHELXL (Sheldrick, 2015).

Through the Rietveld method, it is possible to perform the analysis of the measured profile trying to model and optimize simultaneously both the information related to the sample (type and relative abundance of crystalline phases, structural model, microstructural and textural parameters) and those related to the instrument used (wavelength, optical components, background instrumental, etc) (Rietveld, 1967 and 1969; Young, 1993; Bish and Post, 1989). This method is generally based on a nonlinear least squares minimization. It was introduced in the second half of the '60s by H. M. Rietveld and entered in the current terminology such as the Rietveld method.

To carry out a Rietveld refinement, diffraction pattern must have a numerical intensity value y_i, at each of several thousand equal increments (steps), i, in the pattern.

Typically step size range from 0.01 to 0.05 °2Θ for fixed wavelength X-ray data and the number of steps in powder diffraction is usually in the order of thousands. Important to note that, in all cases, the "best-fit" sought is the best least-squares fit to all of the thousands of y_i's simultaneously (Young, 1993). All the measured points of the experimental profile are used as observed parameters; the quantity minimized in the least-square refinement is the residual, S_y:

$$S_y = \sum_i w_i (y_i - y_{ci})^2 \qquad [2.3.1]$$

Where S_y is the residual function; Y_i the observed intensity for the *i*th step; Y_{ci} the calculated intensity for the *i*th step and w_i the weight of each individual observation according to Poisson statistics, and is equal to $1/y_i$ (Young, 1993).
The sum is extended to all the points of the diffraction pattern. For these reasons it can be used for qualitative analyses (phase identification) but also to obtain more detail information on the given phase (quantitative analysis, structural analysis, microstructural analysis, texture analysis)
The quantitative analysis of different crystalline phases present in a mixture is based, in general, on the principles that there is a proportionality between the measured diffraction intensities and the amount of the given crystalline phase in the mixture. The Rietveld method in QPA uses the refined scale factors over the whole powder pattern to obtain the phase quantitative information. Standardless method are based on assumption that the entire sample is crystalline and included in Rietveld model:

$$W_\alpha = S_\alpha (ZMV)_\alpha / \sum_j S_j (ZMV)_j \qquad [2.3.2]$$

Where W_α is the weight fraction of phase α, in an n component mixture; S the Rietveld scale factor and ZMV the mass and volume of unit cell.
Concerning structural analysis, the relative intensities of the peaks are determined by the type and position of the atoms within the unit cell, thermal displacement and occupancy factors. Indeed I_{hkl}, the intensity of each reflection, is proportional to the square of the structure factor F_{hkl} expressed by the summation extended to all the n atoms of the unit cell:

$$F_{hkl} = \Sigma_i X_i f_i \exp [2\pi i (hx_i + ky_i + lz_i)] \exp [- M_i] \qquad [2.3.3]$$

Where f_i is the scattering factor, which identifies the type of atom; *h, k, l* are the Miller indices; x_i, y_i and z_i are the position parameters of the i-th atom in the unit cell; M_i the parameter related to the thermal displacement factor and X_i the site occupancy factor.
A complete description of the theory at the base of the Rietveld method can be found in Young (1993) and in Dinnebier and Billinge (2008).

2.3.2 Electron Micro Probe Analysis (EMPA)

Electron Micro Probe Analysis (EMPA) for the quantitative chemical compositions of all samples was performed at the Department of Environmental and Territory Sciences and of Earth Sciences of the University of Milano-Bicocca (Italy). A JEOL 8200 Super Probe instrument with W hairpin type filament and minimum accelerating voltage of 30 kV, was used. Analyses were performed on accurately selected fibres (then they should be highly reliable) under the supervision of dott. Alessandro Cavallo.

2.3.3 Fourier Transformed Infrared (FTIR) and Raman Spectroscopy

FTIR and Raman data were collected at the Institute of Theoretical and Applied Mechanics of ASCR, Centrum of Excelence Telč, Batelovská, Telč (Czech Republic). FTIR analysis were performed using an Infrared Nicolet iN10 microscope with Nicolet iZ10 FT-IR module, with a 150x300 µm window.

Raman spectra were collected in the spectral range 1800 – 50 cm^{-1}, with a laser of 532 nm and a power of 10 mW, employing a DXR Raman spectrometer (Thermo Scientific) equipped with a 1024 x 256 CCD detector. The laser beam (diameter about 0.6 µm) was focused with a 100x objective (Numerical Aperture = 0.90). Several spectra were collected from different regions of each sample as matrices of points with steps of 1 µm. Both experimental techniques were performed under the supervision of dott. Petra Mácová.

2.3.4 Scanning Electron Microscopy (SEM)

Electron microscopy exploits the interactions that occur between an incident electron beam and the atoms in the sample (Fig. 2.3.1); a detailed description of the theory of the electron microscopy techniques is found in Wells (1974), Wenk (1976) and McLaren (1991).

The first necessary condition is obviously that the electrons hit the sample; those that pass through it constitute the so called direct beam and are used in transmission electron microscopy (TEM). When an electron hits a material, in general, two different kind of interactions can occur: elastic and inelastic.

In the elastic interaction, the energy is transferred from the electron to the sample, and thus the electron leaving the sample possess the same energy of the incident one; this is the case of backscattered electrons (BSE), which are “reflected” (backscattered) out of the specimen interaction volume. BSE are used mainly because their intensity is strongly related to the atomic number of the elements composing the sample; specifically, elements with an higher atomic number backscatter electrons more strongly and thus appear brighter in the image, allowing to detect information about the distribution of different elements.

Concerning the inelastic interactions, the energy is lost through the transfer of energy to the specimen and this can lead to the ejection of secondary electrons (SE) besides the production of visible light fluorescence (cathodoluminescence) and heat as a result of these interactions. Secondary electrons are further divided into slow and fast; slow SE result from the ejection of electron located in the valence or conduction band and need only the transfer of small amount of energy (< 50 eV) to be ejected in the vacuum.

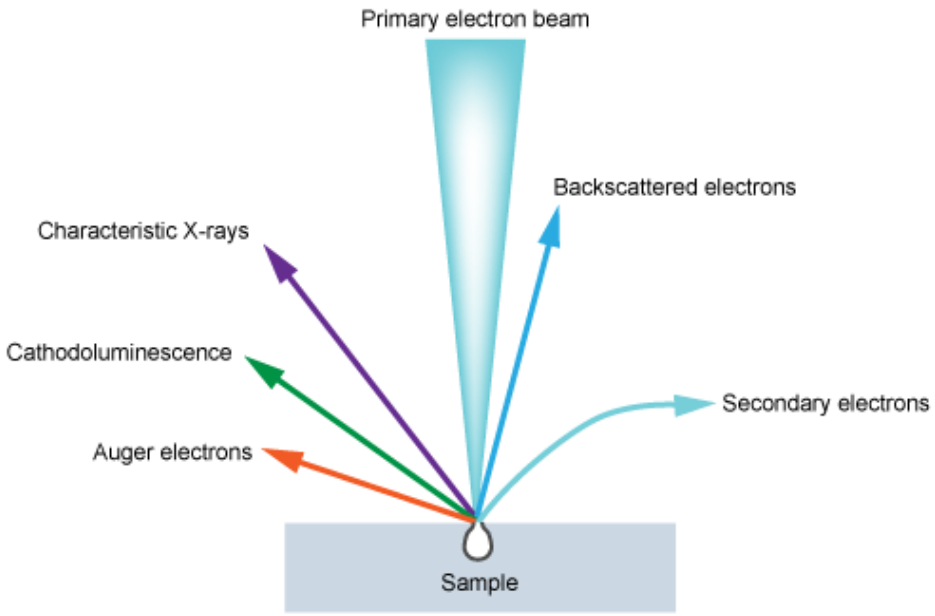

Fig. 2.3.1. Scheme of electron-matter interactions arising from the impact of an electron beam onto a sample (Image taken from www.ammrf.org.au).

Fast SE result from the inner shell of an atom, and thus less readily ejected; the process leads to an ionization of the atom and subsequently to the generation of characteristic X-rays and/or Auger electrons.
The electron microscopy technique was used mainly for estimating the average fibre length and diameter of each sample and to check the chemical composition of fibres and impurities eventually present (in Pollastri *et al.* 2014). Images were collected at CIGS (Centro Interdipartimentale Grandi Strumenti, University of Modena and Reggio Emlia) using a Philips XL40/604 and an ESEM Quanta-200 microscopes, both equipped with X-Ray fluorescence spectrometer which allows spot quantitative chemical analysis (EDS).
All specimens were mounted on Al stub and coated with gold (10 nm thick film).

2.3.5 Surface area measurements

The surface area of the samples has been measured using the Brunauer-Emmet-Teller theory (Brunauer et al. 1938), one of the most widely used method for the determination of the surface area of solids (the BET method). These authors showed that gas molecules are adsorbed layer by layer.
This technique allows to determine the specific surface area of powders by physical adsorption of gas (usually N_2) on the surface of a solid and by calculating the amount of adsorbate gas corresponding to a monomolecular layer on the surface.
Physical adsorption results from relatively weak forces (van der Waals forces) between the adsorbate gas molecules and the adsorbent surface area of the powder. The determination is usually carried out at the temperature of liquid nitrogen. The amount of gas adsorbed can be measured by a volumetric or continuous flow procedure.

The basis of the technique is the Brunauer-Emmett-Teller (BET) adsorption isotherm equation:

$$\frac{1}{\left[V_a\left(\frac{P_0}{P}-1\right)\right]}=\frac{C-1}{V_mC}\times\frac{P}{P_0}+\frac{1}{V_mC} \qquad [2.3.4]$$

Where P is the partial vapour pressure of adsorbate gas in equilibrium with the surface at the boiling point of the used gas (77.4 K for liquid nitrogen); P_0 is the saturated pressure of adsorbate gas; V_a is the volume of gas adsorbed at standard temperature and pressure (STP, 273.15 K and atmospheric pressure) in ml; V_m is the volume of gas adsorbed at STP to produce an apparent monolayer on the sample surface, in ml; C is a constant related to the enthalpy of adsorption of the adsorbate gas on the powdered sample.

A value of V_a is measured at each values of P/P_0; a minimum of 3 data points is required. Then the BET value (the left term in the equation 2.3.4) is plotted against P/P_0; this plot (shown in Fig. 2.3.2) should yield a straight line usually in the approximate relative pressure range 0.05-0.3. The data are considered acceptable if the correlation coefficient (r) of the linear regression is not less than 0.9975. Additional measurements may be carried out, especially when non-linearity is obtained at a P/P_0 value close to 0.3.

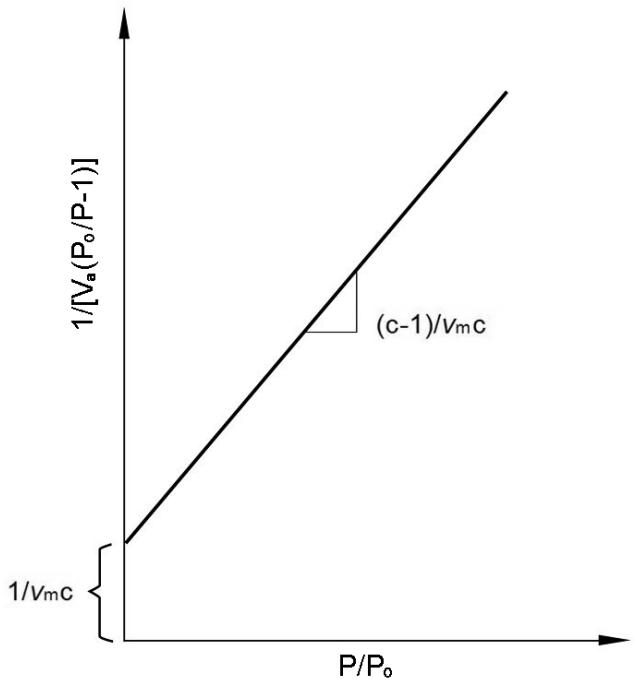

Fig. 2.3.2. Diagram of the P/P_0 ratio against the left term of the equation 2.3.4.

From the slope and intercept of the resulting liner plot (respectively equal to $(C-1)/V_mC$ and $1/V_mC$, evaluated by linear regression analysis) V_m is calculated as 1/(*slope+intercept*) while C is calculated as (*slope/intercept*)+1. Using the value of V_m so determined, the specific surface area, S, in $m^2 \cdot g^{-1}$, is calculated using the equation:

$$S=\frac{V_mN_Aa}{m\,\mathrm{x}\,22400} \qquad [2.3.5]$$

Where N_A is the Avogadro constant (6.022×10^{23} mol^{-1}); a is the effective cross-sectional area of one adsorbate molecule, in square metres (0.162 nm^2 for nitrogen and 0.195 nm^2 for krypton); m is the mass of the sample and 22400 is the volume occupied by 1 mole of the adsorbate gas at STP allowing for minor departures from the ideal.

Measurements were performed using a Gemini-V instrument (Micromeritics, supplied at the Department of Engineering “Enzo Ferrari”, University of Modena and Reggio Emilia) with nitrogen as probe gas. About 500mg of sample were mounted in the sample holder and conditioned at 50 °C prior to precise weight determination using an analytical balance.

2.3.6 Measurements of the ζ potential

Many of the important properties of colloidal systems are determined directly or indirectly by the electrical charge (or potential) on the particles. The potential distribution itself determines the interaction energy between the particles, and this is in many cases responsible for the stability of particles towards aggregation and for many aspects of the flow behaviour of the colloidal suspensions (Hunter, 1981).

ζ potential (or electrokinetic potential) is a physical property which is exhibited by any particle in suspension. Specifically, is the potential generated following the formation of an electrical double layer at the surface of a particle immersed in a liquid. The concept of electrical double layer was introduced for the first time in 1879 by Helmholtz, who suggested a metal/aqueous solution interface consisted of a layer of electrons at the surface of the electrode and a monolayer of ions in the electrolyte (Sparnaay, 1972).

Later, in the early 1900', Gouy, Chapman, and others (Namisnyk, 2003) developed a model according to which the double layer is not rigid, but diffuse, extending freely to a certain depth in the liquid. According to this model, the first layer of charges in the liquid phase, is not sufficient to compensate the number of charges adsorbed by the particle itself. As in the Helmholtz model, the charges of this first layer in the liquid phase are regularly arranged according to a constant value of surface charge density, but they are insufficient to compensate the electric potential raised by the presence of charges with opposite site on the surface of the particle. Consequently, the electric potential does not vanish at the distance of this layer, but at a greater distance. Hence, beyond this layer will occur the presence of negatively and positively charged ions , but with a preponderance of those useful to compensate the residual electric potential. This charge distribution is expected to be ordered according to shells or layers of increasingly rarefied charges, or disordered depending on the various proposed models. In any case, these models are still unable to correct deviations from the real behavior of the theoretical predictions of the Helmholtz model.

In 1924, Stern developed a model called “electrical double layer” or Gouy–Chapman–Stern model (Stern, 1924). According to it (Fig. 2.3.3), the double layer is composed of two coronas: the first one, called Stern layer (with a Stern potential), is fixed to a very short distance from the surface of the solid (the particle itself with a surface potential); the second one is widespread, penetrating to a certain extent in the liquid phase.

Within this diffused layer, there is a theoretical boundary where ions and particles form a stable entity (when the particle is moving, for example by gravity, the ions inside the boundary move with it, but all other ions beyond this limit do not travel with the particle) called surface of hydrodynamic cutting or sliding plane. The potential that exists at this boundary is known as ζ potential.

A high absolute (negative or positive) value of ζ potential gives greater stability to the colloidal systems, because electrostatic repulsions (which prevent the aggregation of dispersed particles) are originated; on the contrary, when the absolute value of the potential is low, coagulation and flocculation are favoured.

Generally, the line of separation between stable and unstable suspensions is taken from −30 mV to +30 mV whereas particles with ζ potential more positive than +30 mV or more negative than -30mV are normally considered stable.

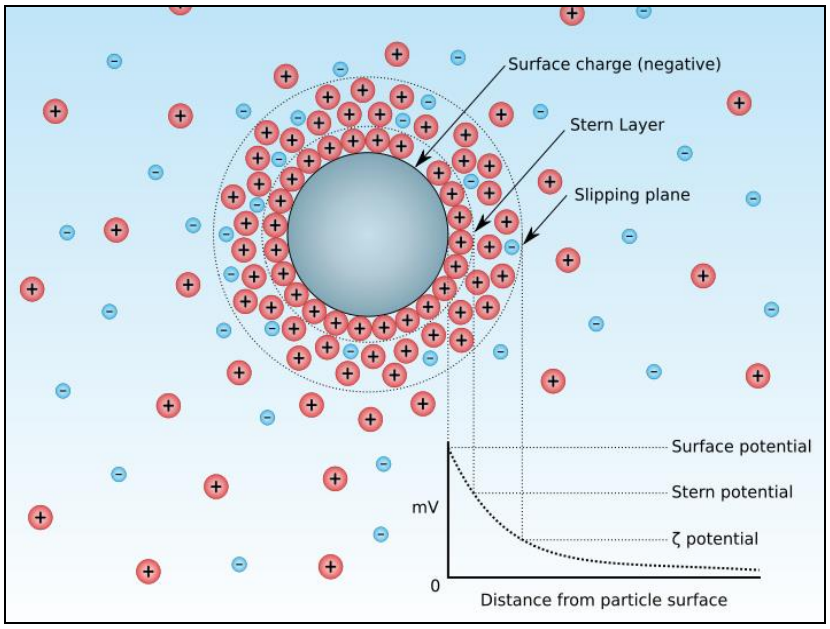

Fig.2.3.3. Diagram of the Gouy–Chapman–Stern model (From Wikipedia).

The most important factor that influences ζ potential is the pH. A ζ potential value without a pH is a virtually meaningless number.

If we imagine a suspended particle with a negative ζ potential: If alkalis are added to this suspension, the particles will tend to acquire a negative charge; if acid is then added to this suspension, a point at which the negative charge is neutralized will be reached and any further addition of acid can cause an accumulation of positive charge. Therefore a graph of ζ potential against pH will have a positive trend at low pH values, while it will be lower or negative at high pH values.

The point at which the curve passes through the zero value of ζ potential is called isoelectric point and represents the point at which normally the colloidal system is less stable.

It can be calculated using theoretical models, by measuring the electrophoretic mobility or can be determined from electrosmotic velocity (Smoluchowski, 1903):

$$\zeta = -\frac{v_{eo}\eta}{E\varepsilon_0\varepsilon} \qquad [2.3.6]$$

Where v_{eo} is the electrosmotic velocity, η is the viscosity of the medium, E is the applied electric field strength, ε_0 is the permittivity of vacuum, ε is the dielectric constant of the medium, assuming that ε and η have the same values in the double layer as in the bulk solution.

ζ potential of investigated sample has been determined using the instrument "Zetasizer Nano series" (Malvern, supplied at the Department of Engineering "Enzo Ferrari", University of Modena and Reggio Emilia) which can calculate the potential starting from the electrophoretic mobility and applying the Henry equation:

$$U_E = \frac{\mathbf{2}\varepsilon\zeta f(ka)}{\mathbf{3}\eta} \qquad [2.3.7]$$

Where ζ is the ζ potential, U_E is the electrophoretic mobility, ε is the dielectric constant, η the viscosity of the medium and *f(Ka)* is the Henry's Function (generally two values are used as approximations for the determination of *f(Ka)*: 1.5 or 1.0). The electrophoretic mobility is obtained by performing an experiment of electrophoresis on the sample and measuring the velocity of the particles via Laser Doppler velocimetry (LDV).
The ζ potential of the fibres belonging to the two size classes was determined both in distilled water and in organic Gamble's modified solution (Guldberg *et al.* 1998). For selected samples, measurements in the pH range 3 – 10 were conducted. The pH modifications in these cases were done using dilute HCl and NaOH (or KOH) solutions. Samples were added to the solute in a weight percentage of 0.1%; in addition to variations of the pH values, measurements were also conducted at different temperatures (25 °C and 37 °C, the latter being the physiological temperature of human body). Obviously, an instrumental standard error is associated to each measurement of ζ potential; for this reason, triplicate measurements were conducted for many samples to check for the reproducibility of the result.

2.3.7 ^{57}Fe Mössbauer spectroscopy

Mössbauer spectroscopy (MS) is an high resolution and accurate methodology based on the Mössbauer effect (discovered in 1957 by Rudolf Mössbauer), consisting in the recoil-free, resonant absorption and emission of gamma rays in solids. It is widely used in mineralogy, for the very precise quantitative determination of the valence state and coordination polyhedron of a chemical element. Despite it is limited to a relatively small number of isotopes, is commonly used for investigating ^{57}Fe, both in amorphous and crystalline phases. A complete discussion of the Mössbauer spectroscopy can be found in Greenwood and Gibb (1971) and in Murad and Cashion (2011).

2.3.7.1 Fundamentals of Mössbauer Spectroscopy

Nuclei in atoms undergo a variety of energy level transitions, often associated with the emission or absorption of gamma rays; these energy levels are influenced and can be changed or splitted by their surrounding environment, both electronic and magnetic. These changes can provide information about the local environment of an atom within a system and can be observed using resonance-fluorescence. There are, however, two major obstacles in obtaining this information: 1) The 'hyperfine' interactions between the nucleus and its environment are extremely small; 2) The recoil of the nucleus as the gamma-ray is emitted or absorbed prevents resonance. A free nucleus, during emission or absorption of a gamma rays, tend to recoil due to the conservation of momentum, just like a gun recoils when firing a bullet, with a recoil energy E_R (Fig. 2.3.4).

Fig.2.3.4. Recoil of free nuclei in emission or absorption of a gamma-ray (from www.rsc.org).

The emitted gamma ray possess E_R less energy with respect to the nuclear transition, but to be resonantly absorbed it must be E_R greater than the transition energy due to the recoil of the absorbing nucleus. To achieve resonance, the loss of the recoil energy must be overcome in some way. As the atoms will be moving due to random thermal motion, the gamma-ray energy has a spread of values E_D caused by the Doppler effect; this produces a gamma-ray energy profile as shown in Fig. 2.3.5.

To produce a resonant signal, the two energies need to overlap and this is shown in the red-shaded area. This area is shown exaggerated as in reality it is extremely small (a millionth or less of the gamma-rays are in this region) and impractical as a technique. What Mössbauer discovered is that when the atoms are within a solid matrix the effective mass of the nucleus is very much greater, namely the mass of the whole system, making E_R and E_D very small. If the gamma-ray energy is small enough, the recoil of the nucleus is too low to be transmitted as a phonon (vibration in the crystal lattice) and so the whole system recoils, making the recoil energy practically zero: a recoil-free event.

In this situation, if the emitting and absorbing nuclei are in a solid matrix, the emitted and absorbed gamma-ray is the same energy, so resonance can be achieved; if emitting and absorbing nuclei are in identical environments, the transition energies are identical and this produces a spectrum with a single absorption line.

As the environment of the nuclei in a system to be investigated will almost certainly be different to that of the source, the hyperfine interactions between the nucleus and its environment will change the energy of the nuclear transition.

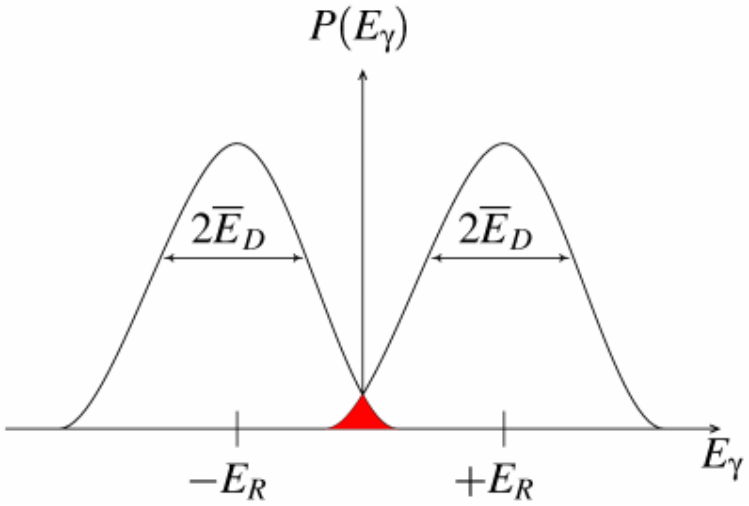

Fig. 2.3.5. Resonant overlap in free atoms. The overlap shown shaded is greatly exaggerated (from www.rsc.org).

To detect this we need to change the energy of the probing gamma-rays. As shown previously the energy changes caused by the hyperfine interactions to look at are very small, of the order of billionths of an electron volt; such minimal variations of the original gamma-ray are quite easy to achieve by the use of the Doppler effect. In the same way that when an ambulance's siren is raised in pitch when it's moving towards you and lowered when moving away from you, our gamma-ray source can be moved towards and away from the absorber. This is most often achieved by oscillating a radioactive source with a velocity of a few mm/s and recording the spectrum in discrete velocity steps. Fractions of mm/s compared to the speed of light ($3x10^{11}$mm/s) gives the minute energy shifts necessary to observe the hyperfine interactions. For convenience the energy scale of a Mössbauer spectrum is thus quoted in terms of the source velocity, as shown in Fig. 2.3.6.

With an oscillating source we can now modulate the energy of the gamma-ray in very small increments. Where the modulated gamma-ray energy matches precisely the energy of a nuclear transition in the absorber the gamma-rays are resonantly absorbed and we see a peak. As this is seen this in the transmitted gamma-rays, the sample must be sufficiently thin to allow the gamma-rays to pass through, since the relatively low energy gamma-rays can be easily attenuated. In Fig. 2.3.6 the absorption peak occurs at 0 mm/s, where source and absorber are identical.

The energy levels in the absorbing nuclei can be modified by their environment in three main ways: by the Isomer Shift, Quadrupole Splitting and Magnetic Splitting.

The isomer shift (δ) is a relative measure describing a shift in the resonance energy of a nucleus due to the transition of electrons within its *s* orbital. This leads to a monopole interaction, altering the nuclear energy levels. Hence, any difference in the s-electron environment between the source and the absorber produces a shift in the resonance energy of the transition. This cause the shift of the whole spectrum, positively or negatively, depending on the s-electron density, and sets the centroid of the spectrum (Fig. 2.3.6 a).

As the shift cannot be measured directly it is quoted relative to a known absorber; for example ^{57}Fe Mössbauer spectra will often be quoted relative to α-iron at room temperature.

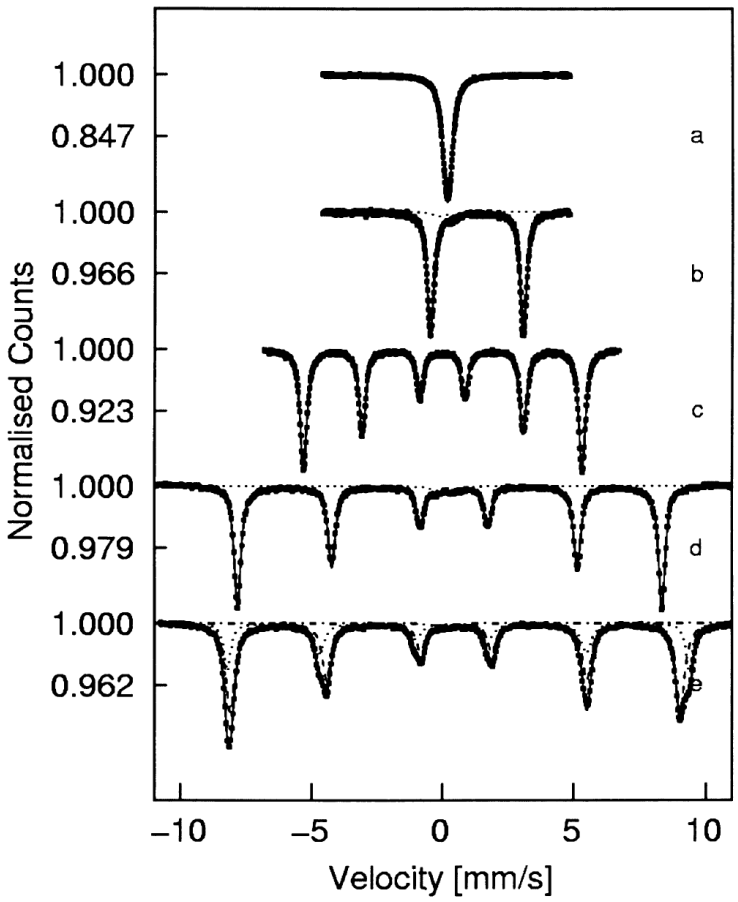

Fig. 2.3.6. Characteristic types of ^{57}Fe Mossbauer spectra. Legend: a) Simple spectrum showing an unsplit line with isomer shift; b) almandine, showing the characteristic large quadrupole splitting of high spin Fe^{2+} compounds; c) α-Fe showing a magnetically split sextet with no quadrupole splitting; d) hematite, showing a small quadrupole splitting accompanying magnetic splitting; d) Western Australian "zebra rock ", showing part of the hematite is above the Verwey transition and part is below, giving rise to two sextets with quadrupole splittings of the opposite signs (from Murad and Cashion, 2011).

Regarding the Quadrupole Splitting, it reflects the interaction between the nuclear energy levels and surrounding electric field gradient (EFG). It is due to the fact that nuclei in states with an angular momentum, I, greater than ½ posses a non-spherical charge distribution. This produces a nuclear quadrupole moment. In the presence of an asymmetrical electric field (produced by an asymmetric electronic charge distribution or ligand arrangement) this results in a splitting of the nuclear energy levels (Fig. 2.3.6 b).
Finally, magnetic splitting (hyperfine splitting) is a result of the interaction between the nucleus and any surrounding magnetic field. If the material is magnetically ordered, the nucleus usually sees the electrons as a static magnetic field. The effect of a magnetic field is to completely split each of the nuclear levels with a spin of I into their (2I+1) components. These splitting result in the original spectrum being split into a larger number of lines, depending on the I values of the ground and excited nuclear states (Fig. 2.3.6 c). Further details are provided in Murad and Cashion (2011).

2.3.7.2 Operating conditions adopted

The Mössbauer absorbers were prepared gently pouring powder samples together with powdered acrylic resin (Lucite) in a plastic holder 1 cm^2 diameter.
Given the different Fe content of the samples, a variable amount from 10 to 100 mg was used so that Fe total content of the absorber was between 1 and 5 wt%, within the limits for the thin absorber thickness (Long *et al.* 1983).
^{57}Fe-Mössbauer spectra were collected at room temperature, using a conventional spectrometer operating in constant acceleration mode with a ^{57}Co source of nominal strength of 25 mCi in rhodium matrix, and recorded with a multi-channel analyzer using 512 channels. The instrument is sited at the department of Earth Science of the University of Rome "La Sapienza" (responsible Prof. G. B. Andreozzi).
After velocity calibration using a high purity α-iron foil (25 mm thick), the raw data were folded to 256 channels. To have good statistics, about $5x10^6$ counts per channel were collected. The velocity range -10 to 10 mm/s was investigated to detect magnetic oxide impurities, in case they were present. The spectrum was fit using the Recoil 1.04 fitting program (Lagarec and Rancourt, 1998). Data analysis involved a curve-fitting procedure made by assuming a Lorentzian peak shape, and the statistical best fit was obtained by using the reduced χ^2 method, with uncertainties estimated on the basis of the covariance matrix.
In addition, fitting of Quadrupole Splitting Distribution was tried (as in the previously works of Gianfagna *et al.* 2007; Andreozzi *et al.* 2009) but did not improve the best fit obtained via Lorentzian curves. The experimental errors were estimated to be about 0.02 mm/s for centre shift (δ), quadrupole splitting (ΔE_Q) and line width (Γ), and about 0.5 Tesla for magnetic hyperfine field (H). The doublet and sextet areas were measured with an accuracy better than ±3 %.

2.3.8 X-ray Photoelectron Spectroscopy (XPS)

X-ray Photoelectron Spectroscopy (XPS) is a spectroscopic technique used to investigate the surfaces of materials. The sample is irradiated with a source of monochromatic X-rays; photons enter in the material and undergo various interactions, including photoelectric effect and Auger emission. In both cases, an electron is ejected from the material and by measuring its kinetic energy is possible to determine its binding energy, indicative of the chemical element concerned, according to the formula:

$$E_B = h\nu - K - \phi \qquad [2.3.8]$$

where E_B is the binding energy, hν the energy of the incident photons, K the kinetic energy of the electron and ϕ the spectrometer work function. In the case of a solid sample, this technique allows to analyse only the first atomic layers (a depth of few nm), since only the electrons excited close to the surface are able to get out from the sample without undergoing interactions (with consequent energy losses) and thus maintaining the transported information.
XPS analysis were performed on our samples for the study of the surface chemistry with specific attention to the surface iron content and its oxidation state. Data were collected at ENEA, Unità Tecnica Tecnologie dei Materiali, Laboratorio Tecnologia delle Superfici, research center of Casaccia, Rome (Italy). Measurements were performed under the supervision of dott. Theodoros Dikonimos Makris.

2.4 Non-conventional Methods: Synchrotron radiation

During the doctoral work, several experiments have been performed using non-conventional techniques. X-Ray Absorption Spectroscopy (XAS) experiments addressed to the study of the chemical environment of iron in our sample were conducted at the European Synchrotron Radiation Facility (ESRF, Grenoble, France) and at the Diamond Light Source (DLS, Oxford, United Kingdom). X-Ray Powder Diffraction experiments for the structural and mineralogical characterization were performed at ESRF, Swiss Light Source (SLS, Villigen, Switzerland) and Elettra (Trieste, Italy). Details about these experiments will be provided in 2.4.4 subsection, whereas in the following pages an introduction to the synchrotron radiation will be given. Parts of this chapter are taken from Mobilio *et al.* 2014; Newville 2014; Rossi 2014 and from www.iop.org.

2.4.1 Introduction and theory

Synchrotron radiation is produced when a charged particle of mass m (normally an electron or a positron) accelerated to relativistic velocity is being deflected in a magnetic field (Mottana 2014). In fact, when the speed of the charged particle increases to relativistic values $(v \approx c)$ the emitted radiation pattern is compressed into a narrow cone in the direction of motion, resulting into an emission tangential to the particle orbit. The vertical half-opening angle, ψ, is given by:

$$\psi \approx mc^2/E \approx \gamma^{-1} \qquad [2.4.1]$$

For electrons and positrons, in practical units, γ is equal to $1957E$(GeV), so synchrotron radiation is highly collimated. The deflection of the charged particle by a bending device generates an electromagnetic radiation (first observed at General Electric Research Laboratory in Schenectady, N.Y. (U.S.A.) on April 24, 1947; Elder *et al.* 1947) which is strongly polarized in the plane of the orbit of the electrons (for example horizontally if the acceleration facility leads its particles into a storage ring). This radiation possesses a large and continuous range of energies (it is white) and is very intense (several orders of magnitude greater than conventional X-ray tubes) so scientist can pick whatever wavelength they need for their experiments, as infrared light, ultraviolet or X-rays (soft or hard).

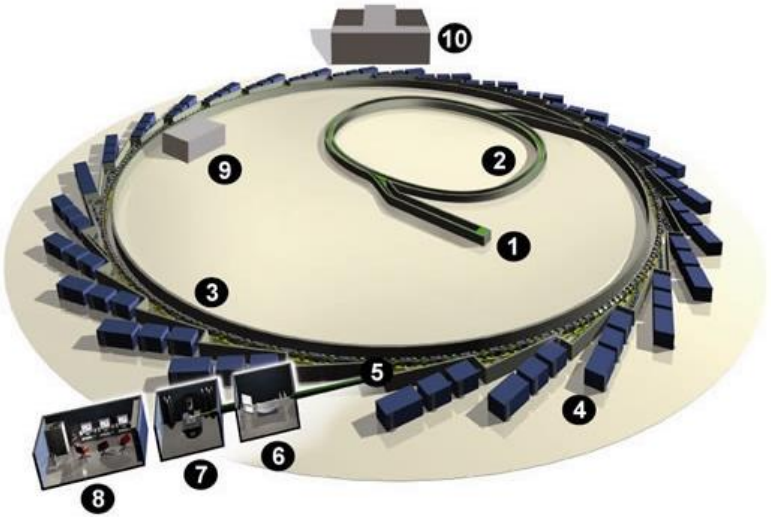

Fig. 2.4.1. Scheme of a synchrotron. Legend: 1) Linac; 2) Booster; 3) Storage ring; 4) Beamline; 5) Front end; 6) Optics hutch; 7) Experimental hutch; 8) Control cabin; 9) RF cavities. (From www.diamond.ac.uk).

Therefore, a synchrotron (Fig. 2.4.1) is a facility where charged particle are accelerated to extremely high energy (with magnets and radio frequency) and forced to change direction periodically (with bending device).
The original synchrotron facilities were used for high energy physics and the radiation was considered merely as a side product. The experiments which made use of the radiation were performed in a parasitic fashion.
However the interesting results which emerged led to the development of dedicated synchrotron radiation sources in the early '70s and the Synchrotron Radiation Source (SRS) of Daresbury can be considered the first dedicated storage ring for synchrotron radiation. The original emphasis was on the optimization of the life-time, the current and the energy of the beam. In the early '80s the emphasis switched to an optimization of the brilliance and also to the development of insertion devices to increase the intensity of high energy photons, as visible in Fig. 2.4.2.
The electrons are produced in an electronic gun (Linac) a device similar to the cathode ray tubes found in older televisions, by thermionic emission from an heated tungsten matrix cathode. The Linac accelerates the electron beam to an energy in the order of hundreds of MeV, over a distance of about 10 m; this involves a series of radiofrequency (RF) cavities operating at high frequency. Due to the nature of the acceleration, the beam must be separated into discrete packets, or "bunches", with a spacing consistent with the acceleration frequency of the Linac; this electron beam is then injected into the booster. The booster synchrotron represent a pre-accelerator where electrons are accelerated before being injected into the storage ring (at ESRF the energy reached is of 6 GeV). This device works only when the storage ring is refilled (for example, 2 times a day at ESRF) or continuously in the case of continuously refilled synchrotron, such as SLS.

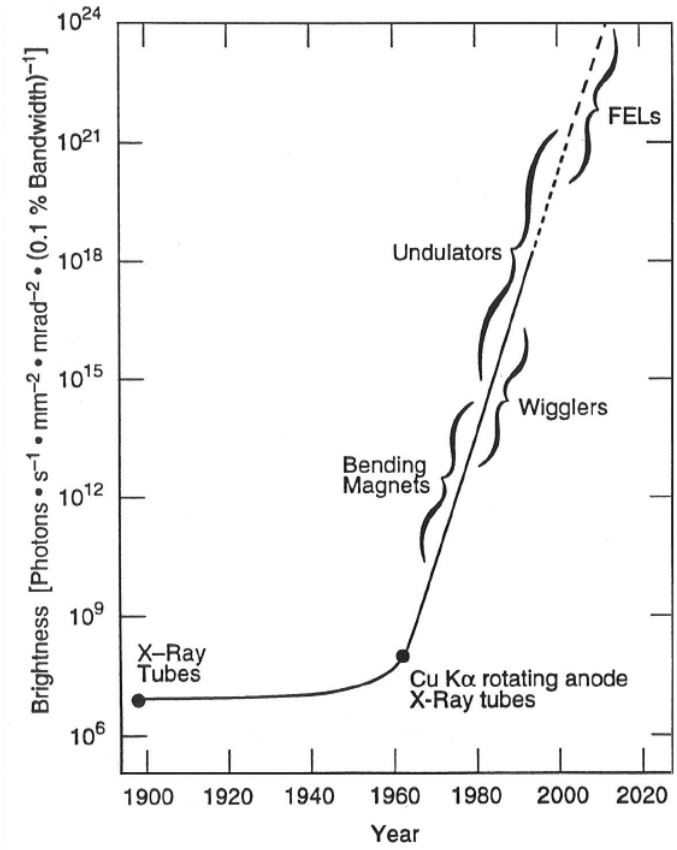

Fig. 2.4.2. Historical development of the brilliance of the available X-ray sources.

Then, accelerated electrons circulate for hours in the storage ring (a circumference tunnel maintained at very low pressure) at a velocity close to that of light, and as the electrons travel around the ring, they pass through different types of magnets. In general, they are subdivided into bending magnets (BM) and insertion devices (ID). The purpose of the bending magnets is to change the direction of the beam. They are placed at a number of locations on the ring to guide the beam along the reference path.
Ideally, each bending magnet would produces a uniform, vertical magnetic field through the beam pipe. The spectral distribution of the BM synchrotron radiation flux is a continuous function, that extends from the X-ray to the infrared region (Fig. 2.4.3).

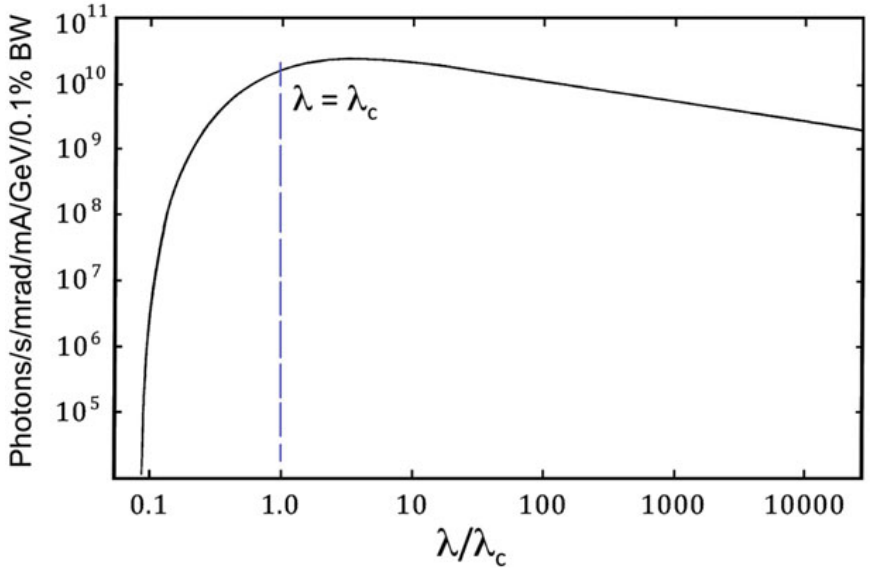

Fig. 2.4.3. Universal curve function of the spectral distribution of BM synchrotron radiation drawn as a function of λ_c/λ (from Mobilio *et al.* 2014).

This radiation is characterized by a critical wavelength, λ_c, determined by the magnetic field (B) in the magnets and the energy (E) of the electron stored:

$$\lambda_c = \frac{18.6}{E^2 B} \qquad [2.4.2]$$

The critical wavelength, λ_c, represented by the discontinuous line in Fig. 2.4.3, divides the spectrum into two parts of equal radiated power: 50% of the total power is radiated at wavelengths shorter than λ_c and 50% at wavelengths longer than λ_c.
Insertion devices are periodic magnetic structures installed in the straight sections of storage rings. Passing through such alternating magnetic field structures, electrons oscillate perpendicularly to the direction of their motion and therefore emit synchrotron radiation during each individual wiggle. The primary effects of the IDs are: (1) The shift of the critical energy to higher values due to the smaller bending radius with respect to the bending magnets; (2) the increase of the intensity of the radiation by a factor related to the number of wiggles induced by the many poles of the magnetic structure; (3) the relevant increase of the spectral brightness.

Insertion devices are of two kinds: wigglers and undulators. Inside both these devices the electron beam is periodically deflected but outside no deflection or displacement of the electron beam occurs (Fig. 2.4.4). A wiggler is a multipole magnet made up of a periodic series of magnets (N periods of length λ_u, the overall length being $L = N\lambda_u$), whose magnetic field forces the electrons to wiggle around the straight path.

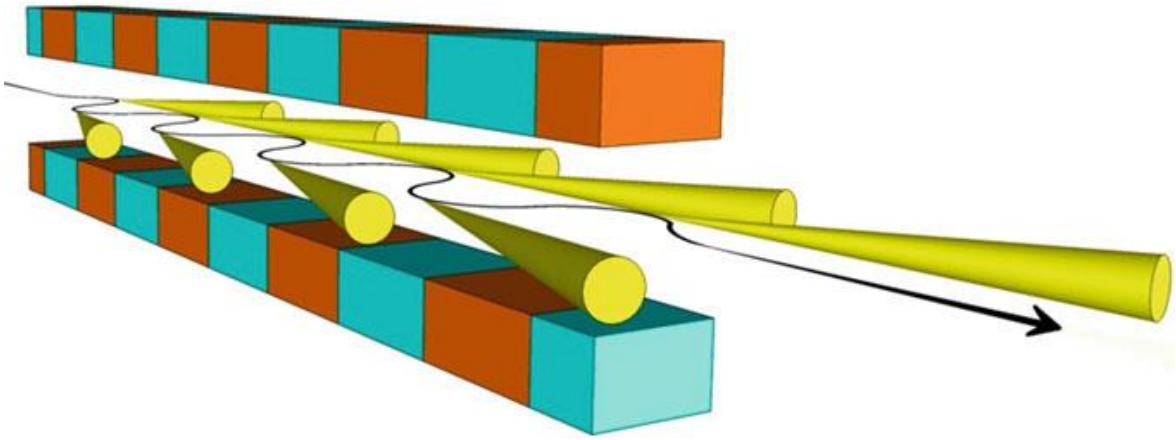

Fig. 2.4.4. Artistic view of the radiation beam emission from a multipole wiggler magnetic structure (from Mobilio *et al.* 2014).

The alternating magnetic field is normally applied in the vertical direction so the sinusoidal trajectory of the electron beam lies in the horizontal plane. Electrons follow in this way a curved trajectory with a smaller local radius of curvature with respect to the one of the dipole-bending magnet, because higher magnetic fields can be used in a wiggler with respect to a bending magnet. The use of higher magnetic fields increases the critical wavelength (see the relation 2.4.2) with respect to the values achievable with bending magnets and extends the spectral range of a storage ring towards higher energies.An undulator is very similar to a wiggler, but with the wiggling angle α smaller than, or close to, the photon natural emission angle γ^{-1} (formula 2.4.1).
For this thesis, beamlines using a bending magnet source were used for XAS experiments whereas both undulator and bending magnet based beamlines were used for XRD experiments (further detail in paragraph 2.4.3).
The applications of synchrotron light are virtually limitless, from condensed matter physics to structural biology, environmental science, cultural heritage and many others; for more detailed information about the synchrotron radiation are available in Mobilio *et al.* 2014.

2.4.2 X-ray absorption spectroscopy

Absorption spectroscopy is a term referring to a number of experimental techniques used to acquire information on the electronic, structural and magnetic properties of the matter. They are based on the study of the variations of the linear absorption coefficient as a function of the energy of the incident photons (parts of this chapter are taken from Rossi 2014).

In the particular case in which X-rays are used as radiation we are talking about XAS acronym of X-ray absorption spectroscopy. Generally the linear attenuation coefficient depends both on the scattering phenomena (elastic or inelastic), and on the photoelectric absorption. In the range of energies used to perform XAS (1-40 KeV) the component due to the absorption clearly dominates on that caused by diffusion; therefore, the attenuation coefficient can be approximated as the coefficient of photoelectric absorption. On large energy ranges, absorption coefficient varies according to a law as the one reported in equation 2.4.3, where *Z* is the atomic number of the target atom, *m* its mass, *d* the density of the sample and *E* the energy of the photon:

$$\mu \approx \frac{dZ^4}{mE^3} \qquad [2.4.3]$$

The typical trend of the coefficient is visible in Fig. 2.4.5 where it is shown the example of Pb. Observing the figure it is immediately possible to note the presence of some discontinuity in correspondence of particular energies. These are due to photoelectric absorption by the atomic electrons that possess only some discrete and quantized energy values.

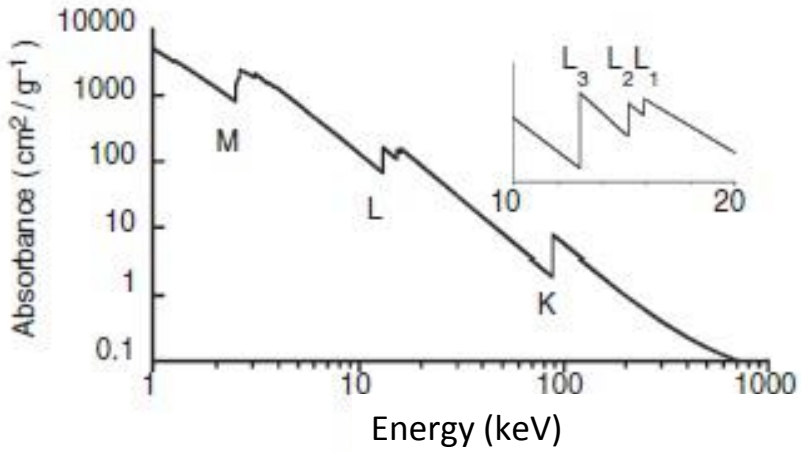

Fig. 2.4.5. Graph of the absorption coefficient of Pb in function of the energy of the photons of the beam.

When the energy of the beam is sufficient to extract or induce in transition these electrons, a large number of photons is absorbed by the sample, dramatically decreasing the number of transmitted particles. This consequently causes the appearance, in the vicinity of that particular value of energy, of a discontinuity in the absorption spectrum.

These apparently irregular structures were discovered already in 1913 by Louis de Broglie and by their energy distribution is possible to obtain that of the innermost electronic shells of the various elements of the periodic table.

The potentialities of XAS, however, does not stop here; in fact in 1920 Hugo Fricke became aware of the presence of sinusoidal oscillations of the absorption coefficient around the value assumed in the peak, namely of the presence of a fine structure, as shown in Fig. 2.4.6, where the trend of the absorption coefficient close to the K-edge of iron is showed.
This discovery immediately triggered the curiosity of many physicists, but for several years the origin of what today is called fine structure of the X-ray absorption spectroscopy (XAFS) has been the subject of debate, until in 1971 Stern, Sayers and Lytle (Sayers *et al.* 1971) evolved a quite simple theory linking the oscillations to the local structure of the sample. From that moment, a development of the theoretical models and experimental equipment to extract this information in a more precise and accurate way have started.

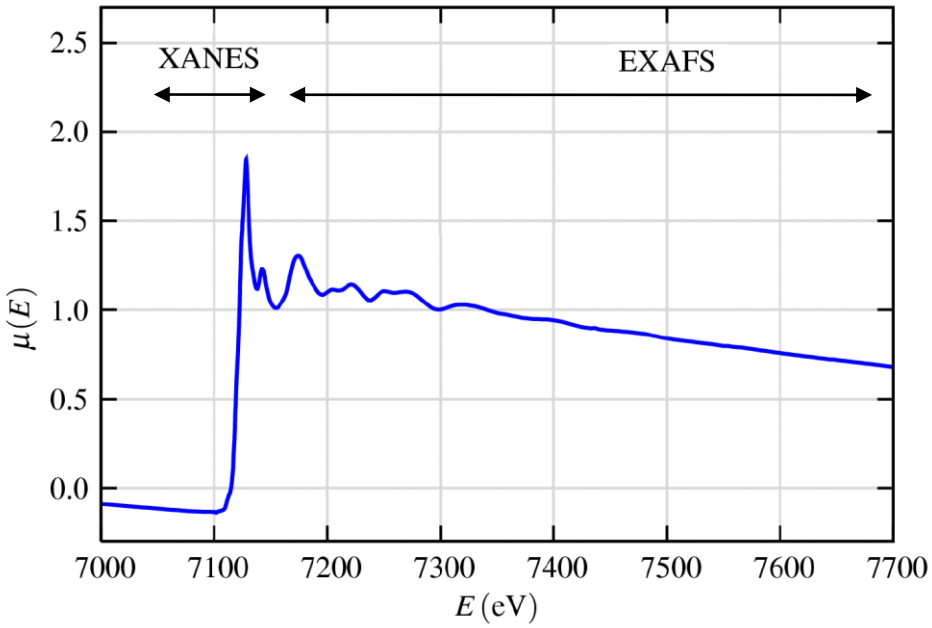

Fig. 2.4.6. Trend of the absorption coefficient *μ(E)* for FeO in the vicinity of the iron K-edge, with the XANES and EXAFS regions identified (From Newville 2014).

When a XAFS spectrum is analyzed, is possible to obtain different information depending on the considered range of energy; for this reason is convenient to divide the spectrum into three distinct regions (Fig. 2.4.6):

- Pre-edge region: Limited energy range to a few eV before the absorption edge. It's possible to detect the presence of weak discontinuities (pre-edge peaks) due to transition of core electrons to other bound states.

- XANES (X-ray Absorption Near Edge Structure): Is intended as the part of the spectrum which extends from 0 to 50 eV above the absorption edge; the combined study of XANES and pre-edge provides information on geometric and electronic local configuration. In other words it is particularly useful to obtain information on the state of chemical bond between different atoms of the sample and is strongly affected by the oxidation state of the absorber atom.

- EXAFS (Extended X-ray Absorption Fine Structure): Defines the region of the spectrum between 100 and 1000 eV beyond the absorption edge. From EXAFS analysis is possible to determine the geometric structure of the sample in the immediate vicinity of the absorber atom (around 10 Å).

2.4.2.1 XANES

Since XANES is a much larger signal than EXAFS, spectra can be collected even in sample containing lower concentrations of the target element and in less than perfect sample conditions. The interpretation of XANES is complicated by the fact that there is not a simple analytic or physical description of XANES. However, there is much chemical information from the XANES region, notably formal valence (very difficult to experimentally determine in a non-destructive way) and coordination environment.
Clearly, the edge position and shape is sensitive to formal valence state, ligand type, and coordination environment, then XANES can be used as a fingerprint to identify phases. An important and common application of XANES is to use the shift of the edge position to determine the valence state, as exemplified in Fig. 2.4.7.

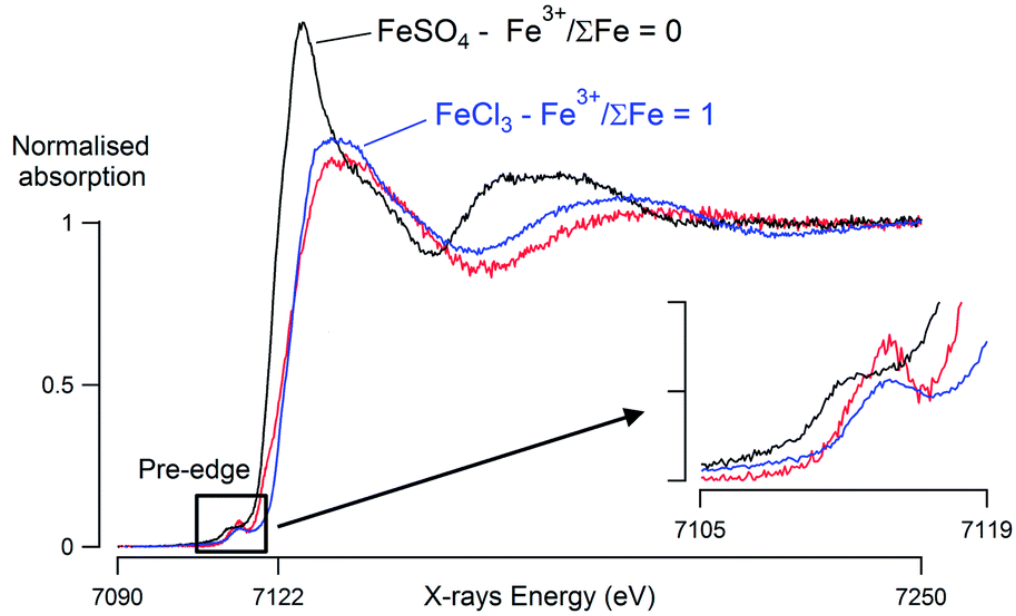

Fig. 2.4.7. Normalized XANES spectra of reference compounds $FeSO_4$ (Fe^{2+}), $FeCl_3$ (Fe^{3+}) and a glass sample, showing an evident shift of the absorption edge (From Ceglia *et al.* 2014).

For example, with good model spectra, Fe^{3+}/Fe^{2+} ratios can be determined with very good precision and reliability and similar ratios can be made for many other ions. The heights and positions of pre-edge peaks can also be reliably used to empirically determine oxidation states and coordination chemistry.
These approaches of assigning formal valence state based on edge features and as a fingerprinting technique make XANES somewhat easier to crudely interpret than EXAFS, even if a complete physical understanding of all spectral features is not available. For many systems, XANES analysis based on linear combinations of known spectra from "model compounds" is sufficient to tell ratios of valence states and/or phases.

2.4.2.2 EXAFS: The origin of the fine structure

The easier and more intuitive interpretation to describe the origin of the fine structure was provided already in the '70s by Stern, Lytle and Sayers. They considered a system composed of an atom that works as absorber within a structure that can be ordered or not in the long range. To simplify the dynamics of the process it is assumed that the photon interacts with only one electron core with a position coincident with the center of the atom it belongs to. This assumption is reasonable, since the electrons of low energy levels tend to be found with high probability in a position very close to the atomic nucleus.

Once excited, this electron can escape from the atomic cloud. The photoelectron once escaped can be spread from the atomic potential of neighboring atoms and come back to the starting atom. The excited state is therefore formed by a linear superposition of the wave outgoing and those retrodiffuse by neighboring atoms.

The various waves possess in general a phase difference which can lead to interference phenomena that modify the probability of finding the electron in the center of the atom.

These oscillations of probability are reflected on the absorption coefficient *(μE)*, giving origin to the fine structure of the absorption spectroscopy. The oscillation frequency depends on several parameters of the sample as the interatomic distance or the energy of the photoelectrons which modifies the wavelength. In Fig. 2.4.8, this phenomenon is represented in a schematic way.

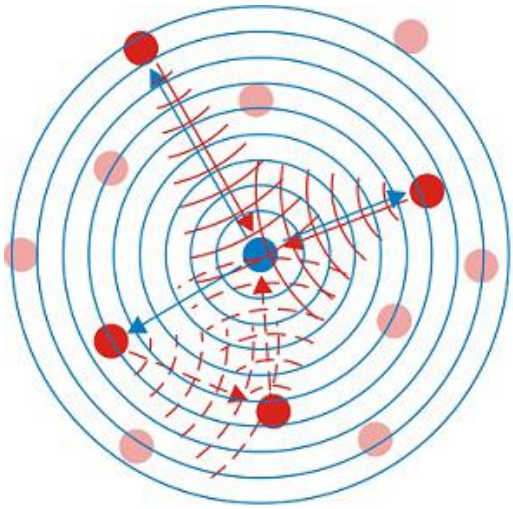

Fig. 2.4.8. Diagram of the mechanism that originates the fine structure.

The theoretical problem therefore lies in the search for appropriate atomic potentials to describe the system, but allowing at the same time the simulation of possible scattering paths completed by the photoelectron.

Once calculated these parameters, it is possible to simulate the interference generated by the overlap of the wave functions of electrons that go towards the atom or coming out from it and especially the phase shift between the waves which generates interference.

At the moment, there are several programs that can modulate EXAFS spectra with good accuracy, whereas XANES spectra remain quite problematic to predict, although significant progress has been made in recent years.

The main difficulty is due to the fact that at high energies (typical of EXAFS) is possible to consider relevant only the effects of single scattering with the surrounding atoms, instead in the XANES this simplification is not possible and is necessary to take into account the

multiple scattering phenomena. The main difference between XANES and EXAFS is then linked to the energy of photoelectron which determines the interaction with the surrounding environment.
In order to better analyze the fine structure, it is usual to subtract to the measured spectra those that would occur in the case where the outgoing photoelectron is not subject to any scattering phenomena (Fig. 2.4.9).

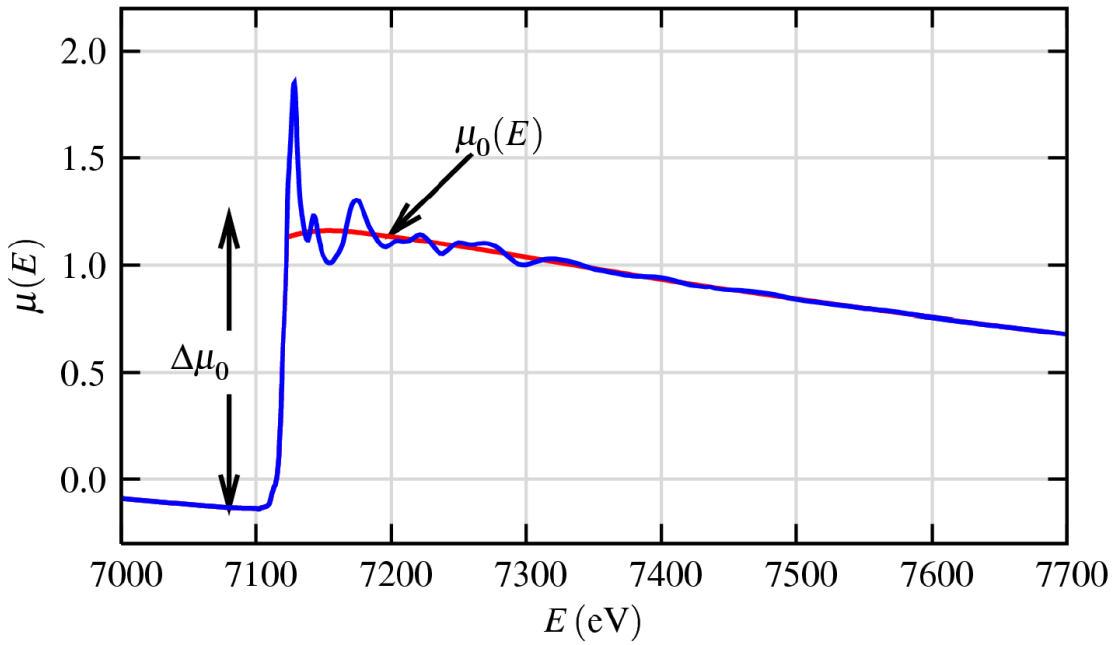

Fig. 2.4.9. XAFS $\mu(E)$ for FeO with smooth background function $\mu_0(E)$ and the edge-step $\Delta\mu_0(E_0)$ (From Newille 2014).

The XAFS spectrum is thus defined as the following quantity:

$$\chi(E) = \frac{\mu(E) - \mu_0(E)}{\Delta\mu_0} \qquad [2.4.4]$$

where $\mu(E)$ is the linear absorption coefficient; $\mu_0(E)$ the background function and $\Delta\mu_0$ the edge-step. It is divided by the magnitude of the jump in the vicinity of the energy edge $\Delta\mu_0$, in order to make the spectrum independently from this quantity. Each absorption edge is closely linked both to the type of element in the sample and to the energy level that is energized. Different chemical elements, in fact, present different energies for the various energy levels, then the distribution in energy of the absorption peaks, already in itself, provides important information regarding the composition of the sample.
The outgoing photoelectron behaves like a wave generated by a stone thrown in water, which can be reflected by some object in the vicinity causing the formation of an interference pattern.
The figure obtained is more or less complicated depending on the configuration of the surrounding atoms. The oscillations due to the interference tend to modulate the value of the matrix element and the magnitude of the modulation depends upon the energy transferred by the photons, which generates photoelectrons more or less energetic and thus fitted with a variable wavelength.

The fact that the photoelectrons produced have an energy fairly high means that their lifetime is relatively short and therefore that are able to explore only the configuration of the sample in the immediate vicinity of the absorber. This necessarily implies that the study of the fine structure can reveal only local configurational order information and in no case a possible long-range order. The general equation of EXAFS is the following (Vlaic and Olivi, 2004):

$$\chi(k) = \sum_R S_0^2 N_R \frac{|f(k)|}{kR^2} \times \sin(2kR + 2\delta_c + \Phi) e^{-\frac{2R}{\lambda(k)}} e^{-2\sigma^2 k^2} \qquad [2.4.5]$$

Where k is the wave vector modulus for the photoelectron; $f(k)$ is a scattering amplitude function of the atoms neighbouring the excited atom; N is the number of neighbouring atoms and R is the distance to the neighbouring atom. The exponential term $e^{-2R/\lambda(k}$ takes account of finite elastic mean free paths of photoelectrons $\lambda(k)$; S_0^2 is an average amplitude reduction factor and its value is the percent weight of the main excitation channel with respect to all possible excitation channels. $2\delta_c$ and Φ are phase functions that takes account of the varying potential field along which the photoelectron moves (the former given by the absorber, the latter given the scatterer). The quantity σ^2 represents the mean square fluctuation of the interatomic distances and increases with increasing temperature or with the degree of configurational disorder of the system; in analogy with the diffraction techniques, it is called the Debye Waller factor. Therefore the exponential term $e^{-2\sigma^2 k^2}$ produces a damping of the oscillations of the fine structure as a function of temperature, but also depending on the square of k, so with increasing energy of the photoelectron this term strongly reduces the oscillations; thus, it is of particular importance when analysis are accomplished in the EXAFS region farther from the edge.
To have a good fit between the measured data and the calculated EXAFS function is necessary to take account of multiple scattering, that is when the photoelectron is not backscattered only once by a single potential. In fact it may happen that it is diffused by different atomic potential or that interacts more than one time with the same potential.
For this reason, the absorption coefficient is expressed by the following series:

$$\mu(k) = \mu_0[1 + \chi_2(k) + \chi_3(k) + \chi_4(k) + \ldots] \qquad [2.4.6]$$

where the subscript of the χ function indicates the number of atom-atom paths made by the photoelectron to return to the starting point. For EXAFS this series is strongly convergent and often is sufficient to assume single scattering (i.e. to stop the calculation at second step) to obtain a good fit with the experimental data.
Considering the model represented by the formula [2.4.4] Sayers *et al.* (1971) realized that making the Fourier transform with respect to k of the $\chi(k)$ corresponds to a radial distribution function with peaks at the interatomic distances with the first neighboring atoms, confirming that the study of the fine structure is a powerful method of investigation to derive the local structure of samples.
A full discussion about EXAFS can be found in Rossi (2014).

2.4.3 Experimental section

As already mentioned, several experiments at synchrotron radiation facilities have been performed during the doctoral work. In this section, a brief description for each of them is given, together with the techniques used for the preparation of the samples and the adopted experimental conditions.

2.4.3.1 XRPD experiments at MS-X04SA - SLS

During this experiment (scheduled for the study of *in situ* setting reaction kinetics of magnesium-potassium phosphate cement, resulted in the published paper of Viani *et al.* 2016) high resolution XRPD patterns were collected for crocidolite, amosite and erionite samples. Data were collected at the MS-X04SA beamline at SLS (Villigen, Switzerland) under the beam time allocated for the experiment 20130049 (July 2013).
The beamline is powered by a short-period (14 mm) in-vacuum, cryogenically cooled, permanent-magnet undulator, (CPMU, U14). Powdered samples were inserted in quartz capillary tubes with a diameter of 0.3 mm and data were collected on rotating capillary tubes, employing a wavelength of 0.775 Å. The used diffractometer works in Debye-Scherrer geometry and is equipped with a unique solid-state silicon microstrip detector, called MYTHEN (Microstrip sYstem for Time-rEsolved experimeNts), an outstanding *in-house* PSI detector group development (Bernd Schmitt, group leader and Anna Bergamaschi, MYTHEN II development). A detailed description of the beamline from the undulator source to the end stations is available in Willmott *et al.* (2013).

2.4.3.2 XAS experiments at BM08 – ESRF

The objective of this experiment was the systematic structural investigation of iron in all the samples reported in table 2.1, through the combined use of both XANES and EXAFS analysis. Data were collected at the BM08 GILDA-CRG beamline at ESRF (Grenoble, France) under the beam time allocated for the experiment 08-01-954 (March 2014, resulted in the published paper Pollastri *et al.* 2015, paper 2, pag. 169).
Powdered samples were mixed with cellulose powder (except for chrysotile samples, for which boron nitride was used to increase homogenization of the mixture), pressed into pellets and sealed within two kapton foils (Fig. 2.4.10).

Fig. 2.4.10. Pellet of erionite sample sealed between kapton foils.

All the spectra were collected at room temperature and in transmission mode using two ion chambers filled with N_2 and Ar gases (500 mbar of N_2 for I_0 and 100 mbar of Ar for I_1 to have 10% and 80% of absorption at 7 kev, respectively), with the exception of erionite and tremolite, for which fluorescence collection was used because of the low Fe content.

A monochromator equipped with Si (311) crystals was used and operated in flat crystals mode; harmonics were rejected using two Pd-coated mirrors working at an incidence angle of 3.6 mrad.
For all the experiments, energy calibration was achieved using iron foil as reference with the position of the first inflection point taken at 7112.0 eV. A reference spectrum of Fe metal foil placed in a second experimental chamber after the sample was collected simultaneously with each sample scan in order to monitor and correct energy drifts due to possible monochromator instabilities.
The following reference compounds were used: almandine (Fe^{2+} [VIII]), hercynite (Fe^{2+} [IV]), siderite (Fe^{2+} [VI]), olivine (Fe^{2+} [VI]), biotite (Fe^{2+} [VI]), hematite (Fe^{3+}[VI]), goethite (Fe^{3+}[VI]), magnetite (Fe^{2+} [VI]) and Fe^{3+} [IV–VI]), iron phosphate (Fe^{3+} [IV]) (2 samples) and silicalite (Fe^{3+} [IV]). All spectra were collected with a variable step energy as a function of energy: finer step (0.2 eV), in the edge region and increasingly larger step (up to 4 eV) in the EXAFS region up to 8100 eV (16 A^{-1}).

Data analysis

The XANES spectra of samples and reference compounds were normalized with respect to the high-energy side of the curve using *Athena* (a software within the IFEFFIT package; Ravel and Newville, 2005). The contribution of the edge jump to the pre-edge was accounted for by subtracting the background (both manually and using a spline function) with the program *Origin 8.0*. The analysis of the pre-edge region was then performed by least-square fitting of pseudo-Voigt functions to the pre-edge spectral envelope, using the program *PeakFit 4.12*. Pseudo-Voigt functions were modelled assuming the same width for each pre-edge feature.
For all samples and reference compounds, the entire pre-edge analysis (from the background removal to the peak fit refinements) has been performed not less than three times, in order to evaluate the data reproducibility and get an estimation of the total pre-edge area and of the standard deviation of the centroid position. The average pre-edge information was derived by calculating its centroid (intensity-weighted average of the position of each component).
EXAFS spectra were analyzed using the IFEFFIT-1.2.9 package (Newville, 2001; Ravel and Newville, 2005). The edge position E_0 was determined using the maximum of the first order derivative of the absorption spectrum (or main inflection point, MIP). A minimum of two scans were executed and averaged for each sample. Normalization after the edge was performed using a cubic spline function for subtraction of background and low-frequency noise from the EXAFS oscillations. The $k^1\chi(k)$ EXAFS signals were Fourier transformed with an Hanning window in the range 2.00 – 11.50 $Å^{-1}$; fits were performed in the R-space in the range 0.90 – 2.15 Å.

2.4.3.3 XRPD experiments at MCX beamline - ELETTRA

The objective of this experiment was the collection of high-intensity high resolution XRPD patterns of cryo-milled chrysotile (following the procedures reported in the 2.2.2 section) and erionite fibers, to be used for the determination of their crystal-structure. Data were collected at the MCX beamline at ELETTRA (Trieste, Italy) under the beam time allocated for the experiment 20150053 (July 2015).
Powdered samples were inserted in quartz capillary tubes with a diameter of 0.5 mm. Data were collected with an analyzer crystal detector in Debye-Sherrer mode.

It was chosen to collect spectra with either resonant radiation at the absorption K-edge of Fe (≈7 keV, λ 1.7428 Å) and with wavelength off of the absorption edge (≈10 keV, λ 1.2408 Å) in order to investigate the crystal chemistry of iron within the fibres.
In fact, when is selected an energy of the beam in the vicinity of an absorption edge of one of the constituent chemical elements of the sample, anomalous dispersion phenomena occurs (the refraction index increases with increasing wavelength) causing Anomalous X-ray Scattering (AXRS) which vary the scattering factor of the element. Thus a particular element can be 'high-lighted' and through structural refinements is possible to better define whether the element is internal or external to the crystal lattice, and in which crystallographic site is located.

2.4.3.4 *In situ* µXANES, µXRD and XRF iron mapping at I18 - DLS

The objective of this experiment was to explore *in vitro* and *in situ* (through synchrotron XRF, µ-XRD and µ-XAS) the structural changes undergone by the fibres after being in contact with cell cultures. Data were collected at the I18 beamline (Mosselmans *et al.*, 2009) at DLS (Oxford, United Kingdom) under the beam time allocated for the experiment SP9574 (June 2014). The experiment has been conducted on the three more representative samples of crocidolite UICC, chrysotile UICC and erionite treated with cultured diploid human non-tumorigenic bronchial epithelial (Beas2B) and pleural transformed mesothelial (MeT5A) cells (details about *in vitro* toxicity tests are given in 2.2.4 subsection). The collected data resulted in the paper Pollastri *et al.* 2016 (submitted).
The beamline uses a cryogenically cooled Si(111) monochromator and the final beam focusing is performed with KB mirrors. All measurements were conducted at room temperature; beam size on the samples was 2x2 µm.
Each sample was positioned in a vertical plane at 80° to the incident beam, to reduce the effect of self-absorption on XANES spectra, with the fluorescence detector positioned horizontally at 90° to the X-ray beam. First, samples were observed in optical microscopy in order to identify suitable areas for µXRF mapping (based on the asbestos-like morphologies observed) as shown in Fig. 2.4.11; as a result, the scan dimensions of the examined areas differed from sample to sample.
A four-element Vortex ME4 Si drift detector with Xmap processing electronics from SII-Nanotechnology was used; the XRF maps were collected at 8 keV incident X-ray energy in rastering mode, with a variable collection time depending on the iron content and dimensions of the scanned area (between 0.06 and 0.29 s per pixel). Almost all maps had a pixel size of 2 µm in both directions. About twenty XRF maps were collected in total.
The study was focussed on Fe because, even if the distribution of other elements with excitation energy below 8 keV (Mn, Cr, V, Ti, Sc, Ca, K, Cl, S, P) was also recorded, the major elements of potential interest for the study (Si, Na, Al and Mg) could not be detected with the experimental operative range of the beamline (5-15 keV). On the basis of the obtained distributions of iron from the XRF maps, Fe K-edge µ-XANES and µ-XRD spectra from individual fibres and aggregates have been collected. XANES spectra were collected in fluorescence mode using the same detector used for XRF mapping.
At some points with high Fe concentrations, an aluminium foil (placed on the detector)was used as attenuator in order to avoid non-linear detector response. Energy calibration was achieved collecting iron foil as a reference in transmission mode prior to each series of collections, using an ion chamber positioned behind the samples.

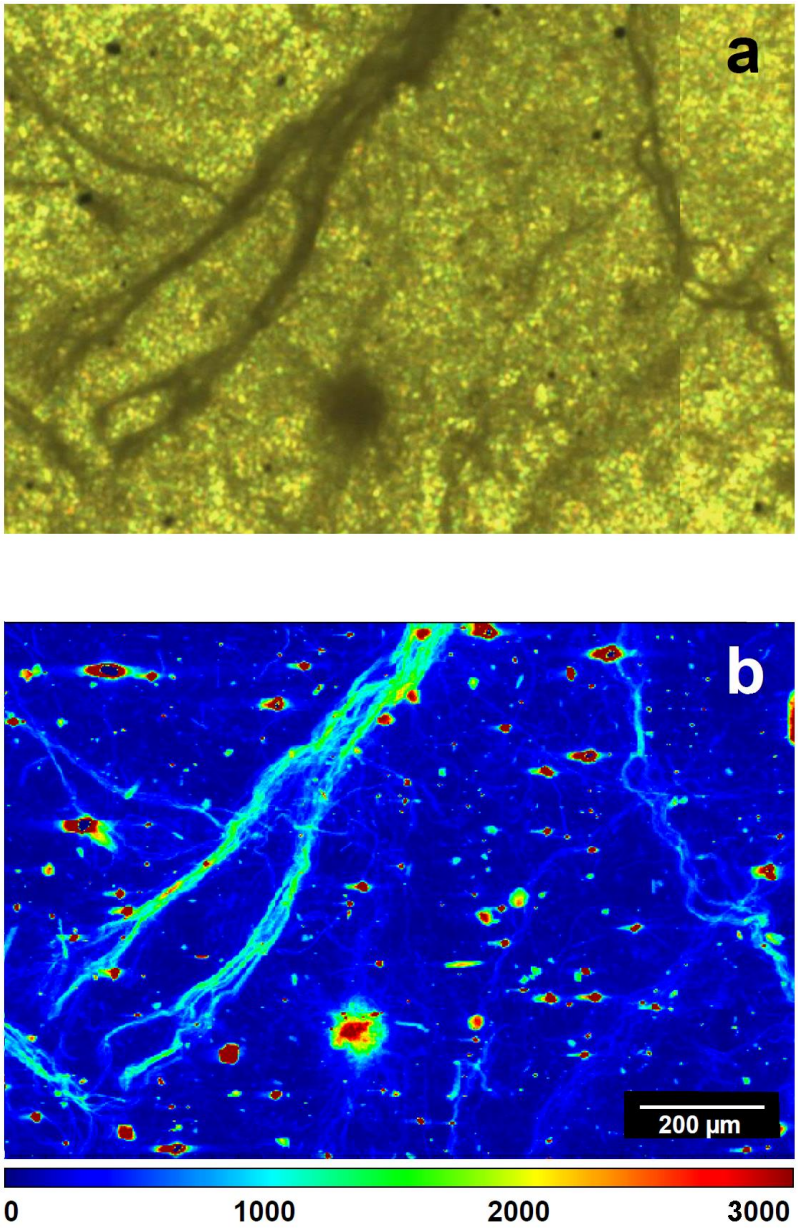

Fig. 2.4.11. (a) Visible light image of chrysotile after 96h *ct* in MeT5A; (b) The corresponding Fe XRF map showing the distribution of iron. The bar below XRF map represents the scale of iron intensities. Arrows indicate the points at which the XRD and/or XANES spectra were collected.

There was no detectable shift in the edge position of the reference foil during the measurements. µXRD data were collected using a Photonic Science SCMOS GEV camera with 4150 x 2083 pixels in transmission mode at an energy of 8 kev; calibration was performed by measuring a LaB6 standard at the sample position.
A collection time of 15 - 20 s was used for each measurement. The XRD data was saved in NEXUS file format.

Data analysis

Iron XRF maps were exported from the program *Dawn (Version 1.7,* Basham *et al.*, 2015) as tiff images using the *Processing* tool available in the program; for each map, a variable scale of intensity of iron concentration was selected to obtain the best image contrast. The differences in the intensity scales of iron are due to both the different time per step used and the different iron content of the investigated mineral fibres.

The collected Fe K-edge μ-XANES spectra were analysed following the same approach reported in the 2.4.4.1 section. Results obtained for each spectrum were averaged to obtain the pre-edge parameters representative of the relative sample. Iron foil was used for energy calibrations, with the position of the first inflection point taken at 7112.0 eV.
XRPD data were recorded in the form of 2D nxs-hdf files (Mosselmans *et al.*, 2009). The detector–sample distance and beam centre were determined on a collected spectrum of LaB6 standard, using the *Powder Calibration* tool in the program *Dawn*; spectra were calibrated and azimuthally integrated using the *Processing* tool available in the same program. Spectra from Dawn were exported as ascii 1D files so as to be opened with the program *X'Pert Highscore Plus* (PANalytical, version 2.0) used for the determination and removal of the background and, when necessary, for merging of multiple spectra. Spectra saved as raw files have been used for structural analysis using the Rietveld method (Rietveld, 1969) in order to evaluate possible structure changes due to the contact with cell cultures.
Given the poor quality of the raw data, only partial structure refinements, aimed at assessing ion exchange, were accomplished for crocidolite and erionite by refining the site population of inter-chain positions for crocidolite and population of the extra-framework K and Na atoms for erionite, respectively. Refinements were accomplished with the GSAS (Larson and Von Dreele, 1994) package and its graphical interface EXPGUI (Toby, 2001). For all collected spectra, peak profiles were modelled in order to study the peaks evolution through time in a semi-quantitative way; in particular, the theta independent Gaussian (Gw) term has been fixed whereas the Lorentzian Lx coefficient ($\propto 1/\cos\theta$, crystal size broadening, empirically correlated to the crystallite size) of the pseudo-Voigt function (Young and Wiles, 1982) was refined.

2.4.3.3 XRPD experiments at ID13 - ESRF

The objective of this experiment was the collection of XRPD patterns of fibers extracted from histological tissues of rats, in order to investigate their structural modifications. Data were collected at the ID13 beamline at ESRF (Grenoble, France) under the beam time allocated for the experiment LS/2296 (June 2015).
Fibers are within histological organs of rats, embedded in paraffin. These organs come from *in vivo* experiments conducted during a past long term project for the determination of the carcinogenicity of mineral fibres by the Ramazzini Cancer Research Institute (Bentivoglio, Bologna, Italy). For the *in vivo* tests on male and female Sprague–Dawley rats, single 25 mg injection of UICC chrysotile, UICC crocidolite and erionite in 1 ml of H_2O was delivered (Maltoni and Minardi, 1989). The detailed description of the experiments and of the experimental part are reported in Bursi *et al.* 2015 (paper 3, pag. 180).
For the synchrotron investigations, the entire organs were heated at 60-70 °C for 1 h, in order to dissolve and allow drainage of melting paraffin; then, organs have been immersed in xylene and placed in a sonic bath for 10 min. The obtained deparaffinized organs were digested using a modification of the sodium hypochlorite digestion technique described in Roggli and Brody (1984), according to the following steps:

- **Step 1**: About 0.5 g of the selected sample was weighed on an analytical balance and minced with the scalpel blade.

- **Step 2**: The specimen was transferred in a 100 ml polypropylene screw-top container completely filled with 14 % sodium hypochlorite solution.

- **Step 3**: The polypropylene container was placed on a laboratory roller mixer and the digestion process proceeds all over the night.

- **Step 4**: Digested suspension were filtered on two 25 mm diameter polycarbonate filters with 0,4 µm pore size (using a vacuum filtering apparatus) and a final wash was performed with absolute ethanol.

The material was scraped off by the filters, stuck on a kapton sheet and then sealed using another kapton sheet. Finally, the Kapton sheets were fixed with two small pieces of glass (Fig. 2.4.12) in order to give more stability and rigidity to the sample.

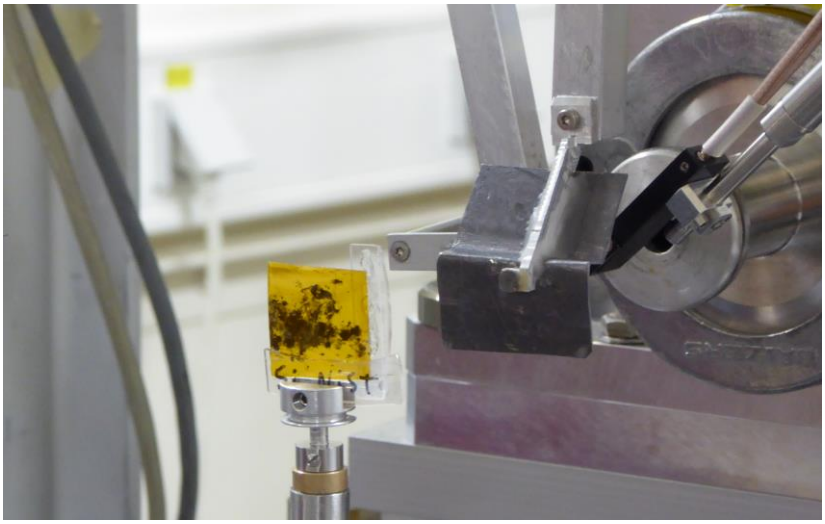

Fig. 2.4.12. Standard powder of Si NIST embedded between glass supported kapton sheets.

Data were collected with the DECTRIS EIGER 4M single photon counting 2D detector, that provides frames with 2070x2167 pixels (with a 75x75 μm^2 pixel size), employing a 2x3 µm beam size, with a wavelength of 0.9393 Å.
Since the signal obtained from a single frame was very weak, and in order to obtain a representative powder-like pattern for each sample, the totality of the frames collected at different locations of each sample were merged.
For each sample, two merged XRD patterns were produced: One making the total average of all the diffraction circles present in all collected frames (called “averaged”); the other, making the average of only the more intense diffraction circles present in every single frame (called “max-project”). The result is that the averaged demonstrate a very high resolution, but obviously they are suffering from the presence of diffraction bands due to the Kapton foils (and any other polluting phase present in the sample) whereas the max-project are more cleaned but possess a lower resolution.

3 RESULTS

3.1 Conventional methods

In this section, all the results obtained through conventional methods will be reported.

3.1.1 X-ray Powder Diffraction (XRPD)

As already stated in the 2.3.1 subsection, XRPD analyses were conducted for the qualitative determination of impurities eventually present, and for the preliminary refinements of the crystalline structure prior to synchrotron experiments. In Fig. 3.1.1 is reported an example of qualitative phase analysis on the erionite sample.

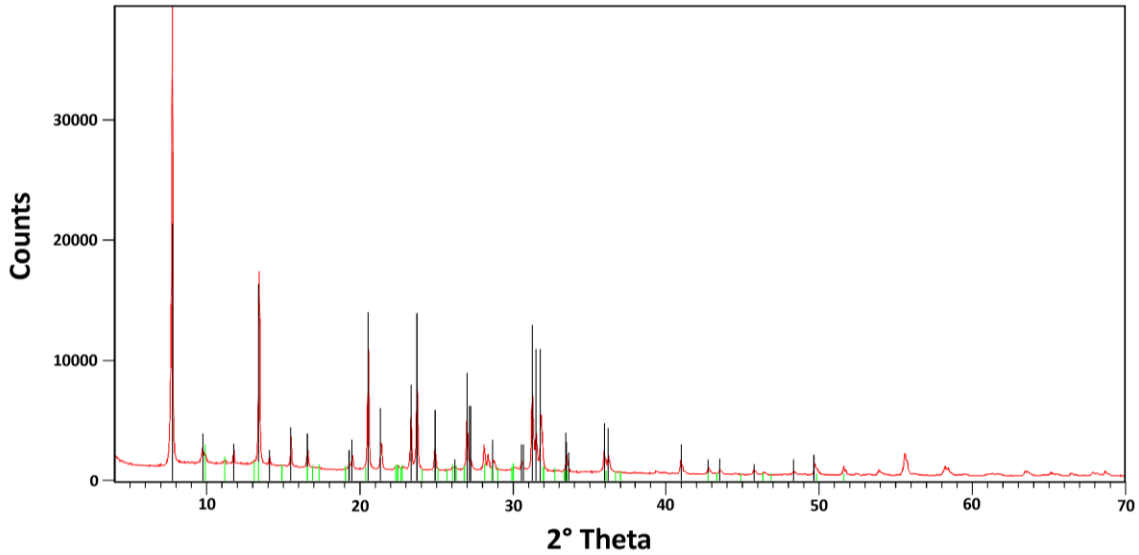

Fig. 3.1.1. Example of qualitative phase analysis. Red continuous line represent the XRPD pattern of erionite; vertical bars mark Bragg reflection positions corresponding to erionite (black) and clinoptilolite (green).

In table 3.1.1, the impurities detected through qualitative phase analysis are reported.

Table 3.1.1
Mineral impurities detected in the investigated mineral fibres.

Sample	Impurities
Amosite	calcite, hematite, quartz
Fibrous anthophyllite	biotite, clinochlore/vermiculite, talc
Crocidolite	hematite, magnetite, quartz, talc[1], lizardite[1]
Fibrous tremolite	antigorite, clinochlore, hematite, talc
Chrysotile UICC	brucite, calcite, clinochlore, dolomite, magnetite, microcline, pyroaurite, talc
Chrysotile Balangero	antigorite, balangeroite, calcite, clinochlore, diopside, dolomite, magnetite, microcline, plagioclase, talc
Chrysotile Val Malenco	calcite, forsterite, magnetite, quartz, lizardite/antigorite, clinochlore
Fibrous erionite	clinoptilolite

[1]Close to the detection limit.

Furthermore, as reported in 2.3.1 paragraph, structural refinements were carried out using XRPD data of anthophyllite (Fig. 3.1.2) and syngle crystal XRD data of tremolite. Results are reported in the following tables.

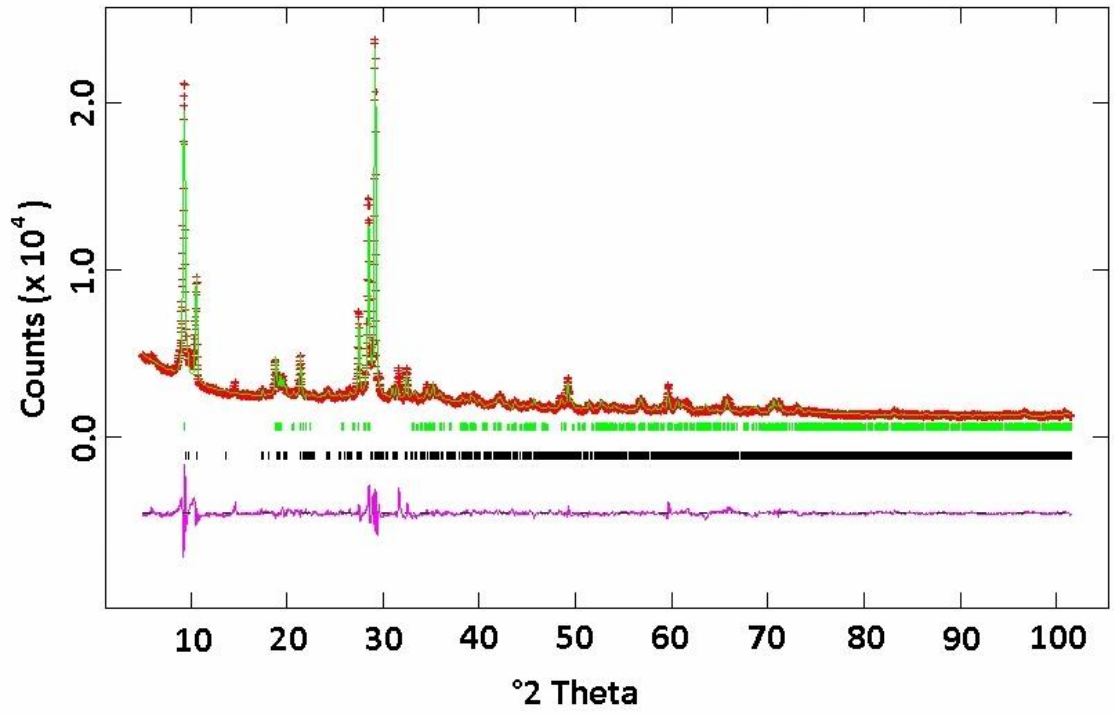

Fig. 3.1.2. Rietveld refinement of anthophyllite sample. Observed (crosses), calculated (continuous line), and difference (bottom line) curves are reported. Vertical bars marking Bragg reflection positions are also reported, and corresponding to talc (green) and anthophyllite (black).

Table 3.1.2
Unit cell parameters and agreement factors of the refinement for anthophyllite and tremolite.

	Anthophyllite		Tremolite	
a (Å)	18.5770(8)	R_{wp} 5.93 %	9.8475(3)	R_{int} 8.27 %
b (Å)	18.0353(22)	R_p 4.18 %	18.0628(5)	R_σ 10.87 %
c (Å)	5.27285(9)	χ^2 8.53	5.2800(1)	R1 14.69 %
β (°)	90		104.717(2)	wR2 13.38 %
sp. gr.	P*n*m*a*		*C*2/m	χ^2 1.059

Table 3.1.3
Final atomic coordinates, occupancies and atomic displacement parameters (Å^2) for anthophyllite.

site	*x*	*y*	*z*	occupancy	U_{iso}
M(1)	0.1333(13)	0.15014(83)	0.4081(61)	$Mg_{1.00}$	0.030(5)
M(2)	0.1233(13)	0.0771(12)	-0.1028(57)	$Mg_{1.00}$	0.047(6)
M(3)	0.1282(20)	¼	-0.1453(74)	$Mg_{1.00}$	0.026(5)
M(4)	0.12422(60)	-0.01148(82)	0.4155(42)	$Fe_{0.62}Mg_{0.38}$	0.004(7)
T(1)A	0.23048(88)	-0.16276(92)	-0.4547(65)	$Si_{1.00}$	0.022(4)
T(1)B	0.02164(91)	-0.1657(11)	0.2911(58)	$Si_{1.00}$	0.030(8)
T(2)A	0.22418(99)	-0.0861(15)	0.0832(71)	$Si_{1.00}$	0.047(5)
T(2)B	0.0198(10)	-0.0892(14)	-0.2461(62)	$Si_{1.00}$	0.015(5)
O(1)A	0.18220(89)	0.1664(15)	0.0512(60)	$O_{1.00}$	0.006(6)
O(1)B	0.06546(90)	0.1632(16)	-0.2768(64)	$O_{1.00}$	0.005(9)
O(2)A	0.1911(10)	0.0672(12)	-0.4167(55)	$O_{1.00}$	0.028(4)
O(2)B	0.0657(11)	0.0735(14)	0.2359(53)	$O_{1.00}$	0.024(4)
OH(3)A	0.1817(20)	¼	-0.4855(76)	$O_{1.00}$	0.005(5)
OH(3)B	0.1309(31)	¼	0.2398(75)	$O_{1.00}$	0.037(7)
O(4)A	0.1750(22)	-0.0128(19)	0.0678(58)	$O_{1.00}$	0.042(6)
O(4)B	0.0684(20)	-0.0154(15)	-0.2465(54)	$O_{1.00}$	0.006(8)
O(5)A	0.1945(21)	-0.1004(17)	0.3659(76)	$O_{1.00}$	0.007(4)
O(5)B	0.0378(22)	-0.1303(32)	0.0174(76)	$O_{1.00}$	0.014(5)
O(6)A	0.2103(21)	-0.1289(35)	-0.1809(78)	$O_{1.00}$	0.023(5)
O(6)B	0.0538(22)	-0.1024(18)	-0.5239(72)	$O_{1.00}$	0.032(5)
O(7)A	0.2129(32)	¾	0.521(20)	$O_{1.00}$	0.032(7)
O(7)B	0.0450(28)	¾	0.230(17)	$O_{1.00}$	0.021(9)

Table 3.1.4
Selected distances (in Å) for M and T sites in anthophyllite.

M(1)	- O1A	2.110(11)	M(2)	- O1A	2.108(11)	M(4)	- O2A	2.083(11)
	- O1B	2.099(11)		- O1B	2.100(11)		- O2B	2.105(11)
	- O2A	2.059(11)		- O2A	2.086(11)		- O4A	2.062(12)
	- O2B	2.079(11)		- O2B	2.084(11)		- O4B	2.063(12)
	- OH3A	2.089(11)		- O4A	2.090(11)		- O5A	2.085(11)
	- OH3B	2.008(11)		- O4B	2.100(11)		- O6B	2.122(11)
	average	2.074		average	2.095		average	2.087
M(3)	- O1A x2	2.085(8)	T(1)A	- O1A	1.624(6)	T(2)A	- O2A	1.611(6)
	- O1B x2	2.072(8)		- O5A	1.614(6)		- O4A	1.609(6)
	- OH3A	2.050(12)		- O6A	1.612(6)		- O5A	1.610(6)
	-OH3B	2.031(12)		- O7A	1.612(6)		- O6A	1.612(6)
	average	2.066		average	1.615		average	1.610
			T(1)B	- O1B	1.620(6)	T(2)B	- O2B	1.614(6)
				- O5B	1.607(6)		- O4B	1.608(6)
				- O6B	1.617(6)		- O5B	1.610(6)
				- O7B	1.613(6)		- O6B	1.613(6)
				average	1.614		average	1.611

Table 3.1.5
Final atomic coordinates, occupancies and atomic displacement parameters (Å^2) for tremolite.

site	*x*	*y*	*z*	occupancy	U_{eq}
M(1)	0	0.08769(10)	½	$Mg_{0.48}Fe_{0.02}$	0.00631(34)
M(2)	0	0.17676(9)	0	$Mg_{0.48}Fe_{0.02}$	0.00539(34)
M(3)	0	0	0	$Mg_{0.24}Fe_{0.01}$	0.00474(46)
M(4)	0	0.27782(6)	½	$Ca_{0.48}Na_{0.02}$	0.00871(23)
T(1)	0.28007(12)	0.08404(6)	0.29669(21)	$Si_{1.00}$	0.00511(21)
T(2)	0.28829(12)	0.17104(6)	0.80434(21)	$Si_{1.00}$	0.00523(21)
O(1)	0.11147(28)	0.08618(15)	0.21735(52)	$O_{1.00}$	0.00634(50)
O(2)	0.11899(29)	0.17135(15)	0.72372(52)	$O_{1.00}$	0.00705(51)
O(3)	0.11134(44)	0	0.71689(77)	$O_{0.5}$	0.00899(76)
O(4)	0.36561(31)	0.24765(15)	0.79302(55)	$O_{1.00}$	0.00819(53)
O(5)	0.34627(30)	0.13410(15)	0.09878(53)	$O_{1.00}$	0.00719(49)
O(6)	0.34344(31)	0.11853(15)	0.58834(55)	$O_{1.00}$	0.00832(51)
O(7)	0.33622(42)	0	0.29214(80)	$O_{0.5}$	0.00910(75)

Table 3.1.6
Selected distances (in Å) for M and T sites in tremolite.

M(1)	- O1 x2	2.0652(27)	M(2)	- O4 x2	2.0187(31)	M(3)	- O1 x4	2.0749(27)
	- O2 x2	2.0853(30)		- O2 x2	2.0926(27)		- O3 x2	2.0662(40)
	- O3 x2	2.0940(30)		- O1 x2	2.1352(30)			
	average	2.0815		average	2.0822		average	2.063
M(4)	- O4 x2	2.3232(29)	T(1)	- O1	1.6063(29)	T(2)	- O4	1.5878(30)
	- O2 x2	2.4008(29)		- O7	1.6179(17)		- O2	1.6125(30)
	- O6 x2	2.5426(29)		- O6	1.6311(30)		- O5	1.6544(29)
	- O5 x2	2.7715(29)		- O5	1.6372(29)		- O6	1.6764(29)
	average	2.5095		average	1.6231		average	1.6328

Important to note that the obtained structure of anthophyllite and tremolite are very similar to that reported in Walitzi *et al.* 1989 (anthophyllite from Ochsenkogel, Gleinalpe, Austria) and in Pacella *et al.* 2008 (tremolite from Val d'Ala, exactly the same sample investigated in this work). Moreover, the cationic sites occupancies are in line with the chemical composition of samples from EMPA analysis (Table 3.1.7 in the following page).

3.1.2 Electron Micro Probe Analysis (EMPA)

In Table 3.1.7, chemical composition obtained from EMPA analysis is reported.

Table 3.1.7
Chemical composition of samples from EMPA analysis. The Fe^{3+} concentration was independently calculated using the stoichiometric criteria of the Droop method (Droop, 1987). Reported chemical compositions are mean values of several analysis carried out on various fibres.

Oxides	Amosite	Anthop.	Crocid.	Trem.	Chrys. UICC	Chrys. Bal.	Chrys. Mal.	Erionite
SiO_2	49.8 (2)	57.3 (4)	51.7 (3)	57.8 (1)	42.5 (3)	40.6 (5)	42.5 (2)	59.5 (2)
TiO_2	0.04 (2)	0.02 (2)	0.03 (3)	0.02 (2)	0.01 (2)	0.01 (2)	0.06 (5)	0.13 (3)
Al_2O_3	0.04 (2)	0.11 (5)	0.12 (4)	0.11 (7)	0.2 (1)	2.4 (6)	0.20 (8)	14.2 (2)
Cr_2O_3	0.01 (1)	0.04 (3)	0.01 (1)	0.02 (2)	0.05 (4)	0.2 (3)	0.08 (8)	0.004 (7)
MnO	0.42 (6)	0.4 (1)	0.04 (2)	0.15 (5)	0.05 (4)	0.06 (4)	0.06 (4)	0.01 (1)
MgO	6.23 (9)	28.5 (2)	2.3 (4)	22.8 (2)	41.9 (2)	39.8 (6)	41.6 (2)	0.15 (2)
CaO	0.09 (1)	0.27 (7)	0.22 (7)	12.9 (1)	0.01 (1)	0.02 (2)	0.09 (6)	0.30 (5)
Na_2O	0.03 (2)	0.02 (1)	6.7 (2)	0.23 (6)	0.013 (9)	0.012 (9)	0.02 (1)	5.9 (2)
K_2O	0.02 (1)	0.02 (1)	0.05 (4)	0.05 (2)	0.004 (5)	0.003 (7)	0.05 (9)	3.6 (1)
NiO	0.02 (4)	0.04 (4)	0.01 (2)	0.08 (5)	0.06 (4)	0.05 (7)	0.2 (1)	-
Fe_2O_3	0.9 (4)	2.1 (9)	18 (1)	0.8 (4)	0.2 (2)	0.4 (3)	0.00 (2)	0.8 (3)
FeO	40.2 (4)	8.0 (7)	18 (1)	1.9 (4)	1.4 (3)	2.5 (5)	1.4 (1)	-
Total	97.7	96.8	97.7	96.7	86.4	86.1	86.3	84.6

By using the chemical compositions together with data from thermogravimetric (TG) analysis for the determination of the water content (details in Bloise *et al.* 2015) chemical formula of samples were calculated, and are presented in Table 3.1.8.

Table 3.1.8
Chemical formula of samples determined using electron microprobe and thermogravimetric data.

Sample	Crystallochemical formula
Amosite	$(Ca_{0.02}Na_{0.01})(Fe^{2+}_{5.36}Mg_{1.48}Fe^{3+}_{0.11}Mn_{0.06})_{7.01}(Si_{7.93}Al_{0.01})_{7.94}O_{21.94}(OH)_{2.06}$
Anthophyllite	$Ca_{0.04}(Mg_{5.81}Fe^{2+}_{0.92}Fe^{3+}_{0.21}Mn_{0.04})_{6.98}(Si_{7.83}Al_{0.02})_{7.85}\ O_{21.63}(OH)_{2.37}$
Crocidolite	$(Na_{1.96}Ca_{0.03}K_{0.01})_2(Fe^{2+}_{2.34}Fe^{3+}_{2.05}Mg_{0.52})_{4.91}(Si_{7.84}Al_{0.02})_{7.86}O_{21.36}(OH)_{2.64}$
Tremolite	$(Ca_{1.91}Na_{0.06}K_{0.01})_{1.98}(Mg_{4.71}Fe^{2+}_{0.22}Fe^{3+}_{0.08}Mn_{0.02})_{5.03}(Si_{8.01}Al_{0.02})_{8.03}O_{22.14}(OH)_{1.86}$
Chrysotile UICC[1]	$(Mg_{5.93}Fe^{2+}_{0.04}Al_{0.02}Fe^{3+}_{0.08})_{6.07}Si_{4.03}O_{10}(OH)_{7.66}$
Chrysotile Balangero[1]	$(Mg_{5.81}Fe^{2+}_{0.15}Al_{0.27}Fe^{3+}_{0.09}Cr_{0.01})_{6.33}Si_{3.97}O_{10}(OH)_{7.11}$
Chrysotile Val Malenco[1]	$(Mg_{5.85}Fe^{2+}_{0.06}Al_{0.02}\ Fe^{3+}_{0.05}Ni_{0.01})_{5.99}Si_{4.01}O_{10}(OH)_{7.86}$
Erionite[2]	$(Na_{5.35}K_{2.19}Ca_{0.15}Mg_{0.11}Ti_{0.05})_{7.85}\ (Si_{28.01}Al_{7.90})_{35.91}O_{72} \cdot 28.13H_2O$

[1]The Fe^{2+}/Fe^{3+} ratio is referred to the accurate result obtained from XAS and ^{57}Fe Mossbauer analysis. [2]Iron not present in the formula as it seems to be outside the crystalline structure, following the results from XAS, ^{57}Fe Mossbauer and TEM investigation (more details in the pertinent chapter and in Pollastri *et al.* 2015).

3.1.3 Fourier Transformed Infrared Spectroscopy (FTIR)

In the following Figures, the collected FTIR spectra for each sample are reported.

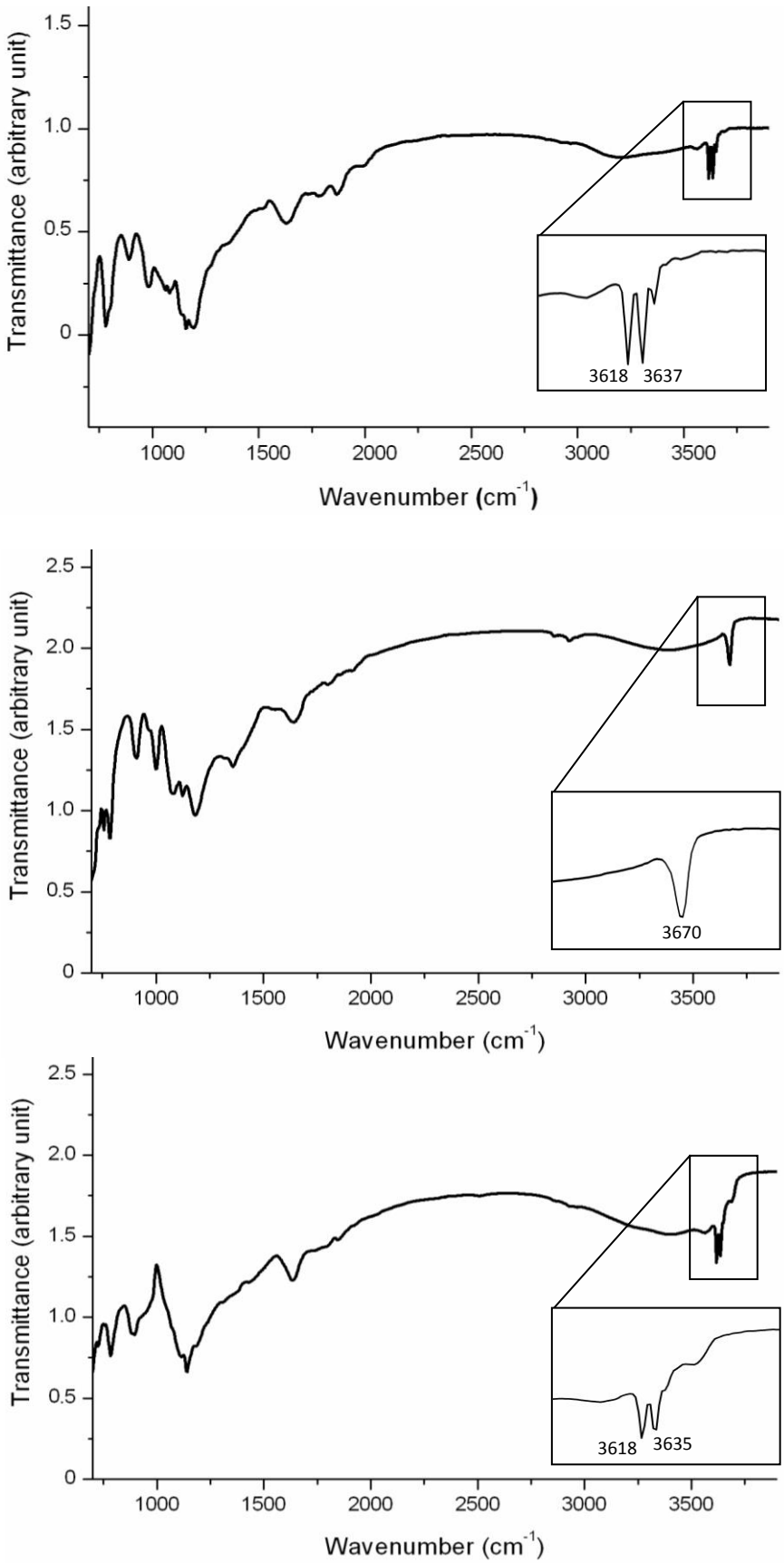

Fig. 3.1.3. From the top: amosite, anthophyllite and crocidolite

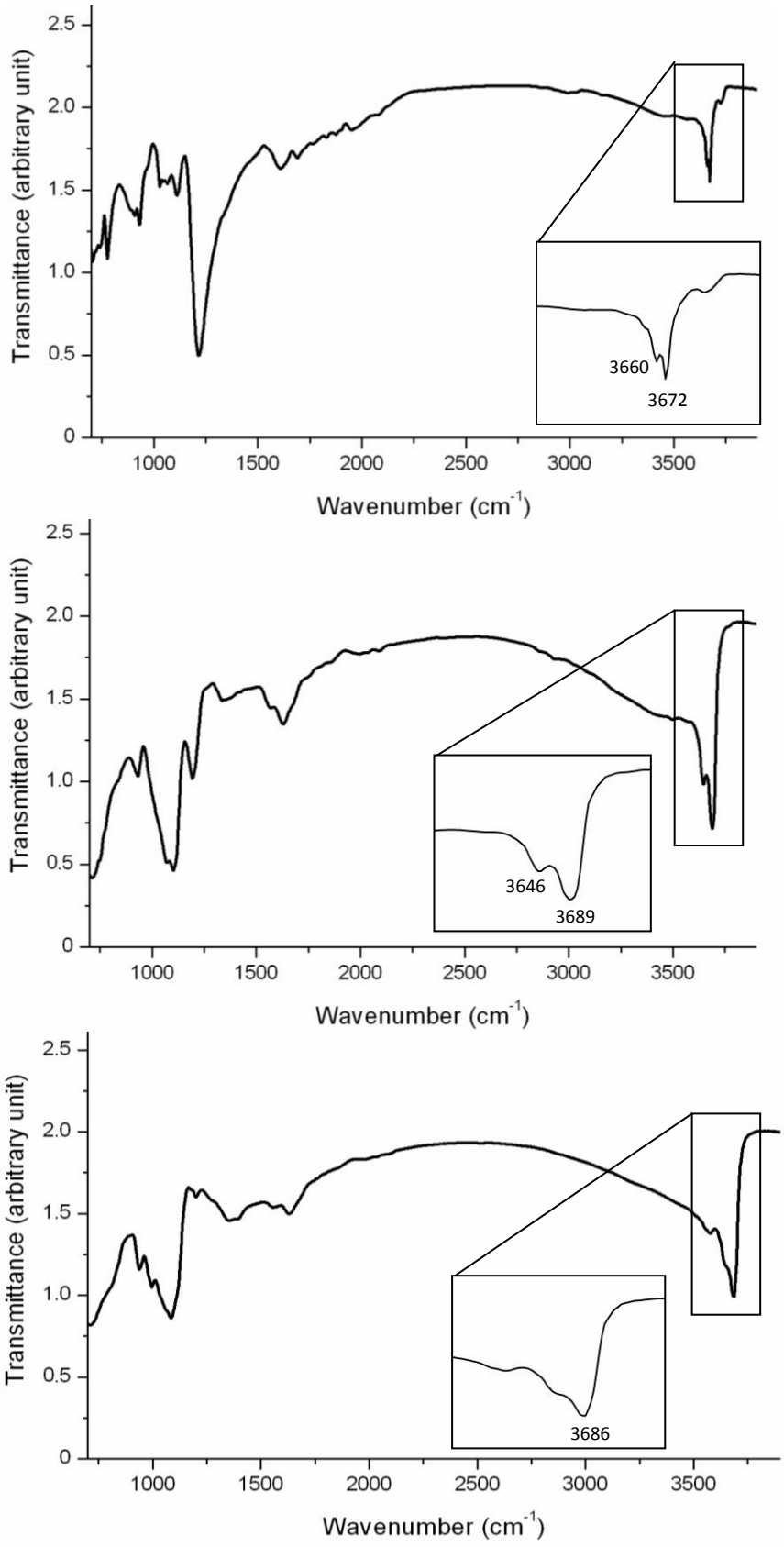

Fig. 3.1.4. From the top: tremolite, chrysotile UICC and chrysotile Balangero

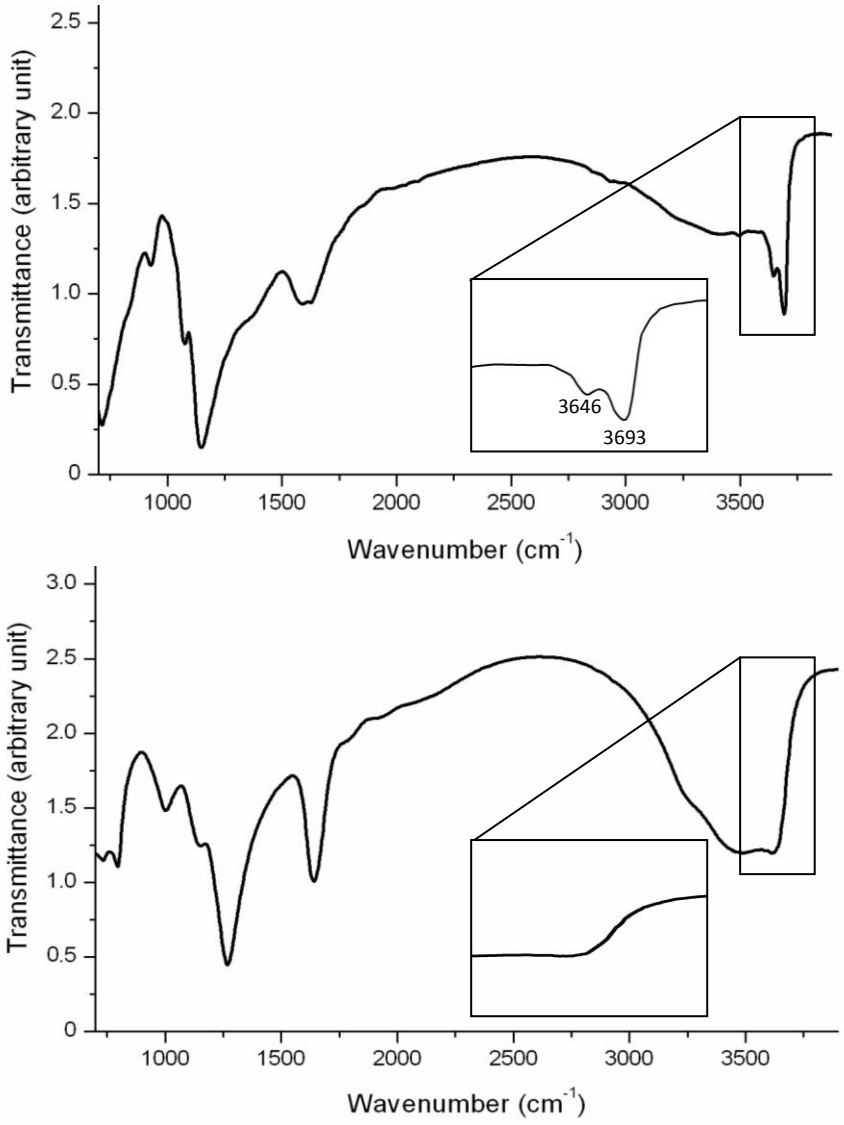

Fig. 3.1.5. From the top: chrysotile Val Malenco and erionite.

In all the collected FTIR spectra, the characteristic absorption bands of asbestos minerals due to OH- and Si-O stretching vibration (Farmer, 1974; Stănescu-Dumitru, 2008) at about 3600 and 1000-1100 cm^{-1}, respectively, are clearly visible and are in agreement with literature data (Pacella *et al.* 2008; Stănescu-Dumitru, 2008).

3.1.4 Raman Spectroscopy

Raman spectra were collected only on representative samples crocidolite, chrysotile UICC and erionite and are visible in Fig. 3.1.6.

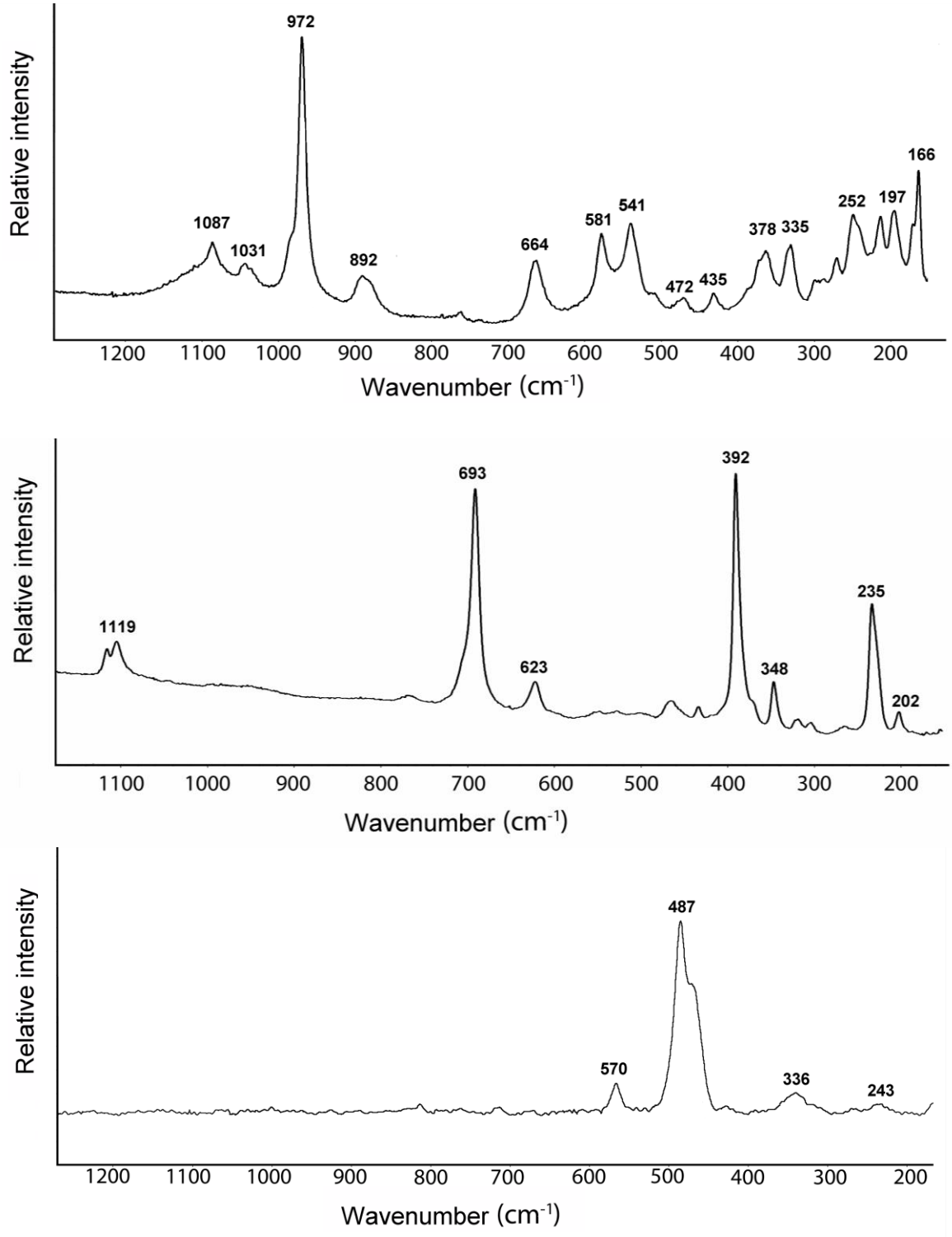

Fig. 3.1.6. Raman spectra collected on representative samples; from the top: Crocidolite, chrysotile UICC and erionite. The characteristic bands of asbestos minerals are clearly visible in all collected spectra and are in agreement with literature data (Bard *et al*., 1997; Croce *et al.,* 2013).

3.1.5 Scanning Electron Microscopy (SEM)

In this section a gallery of representative SEM images for each of the investigated (raw) samples is reported.

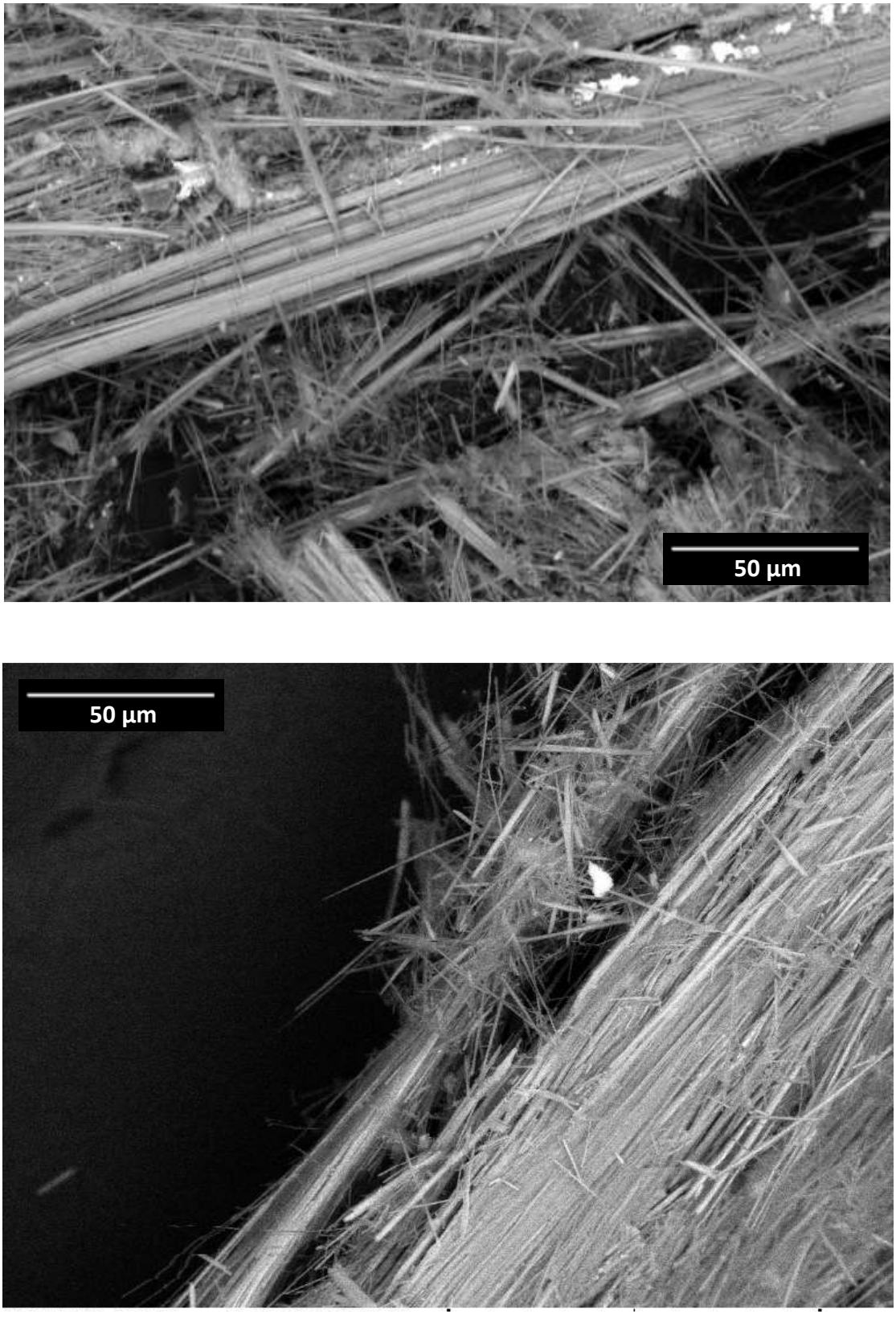

Fig. 3.1.7. High-resolution SEM images of amosite (top) and anthophyllite (bottom).

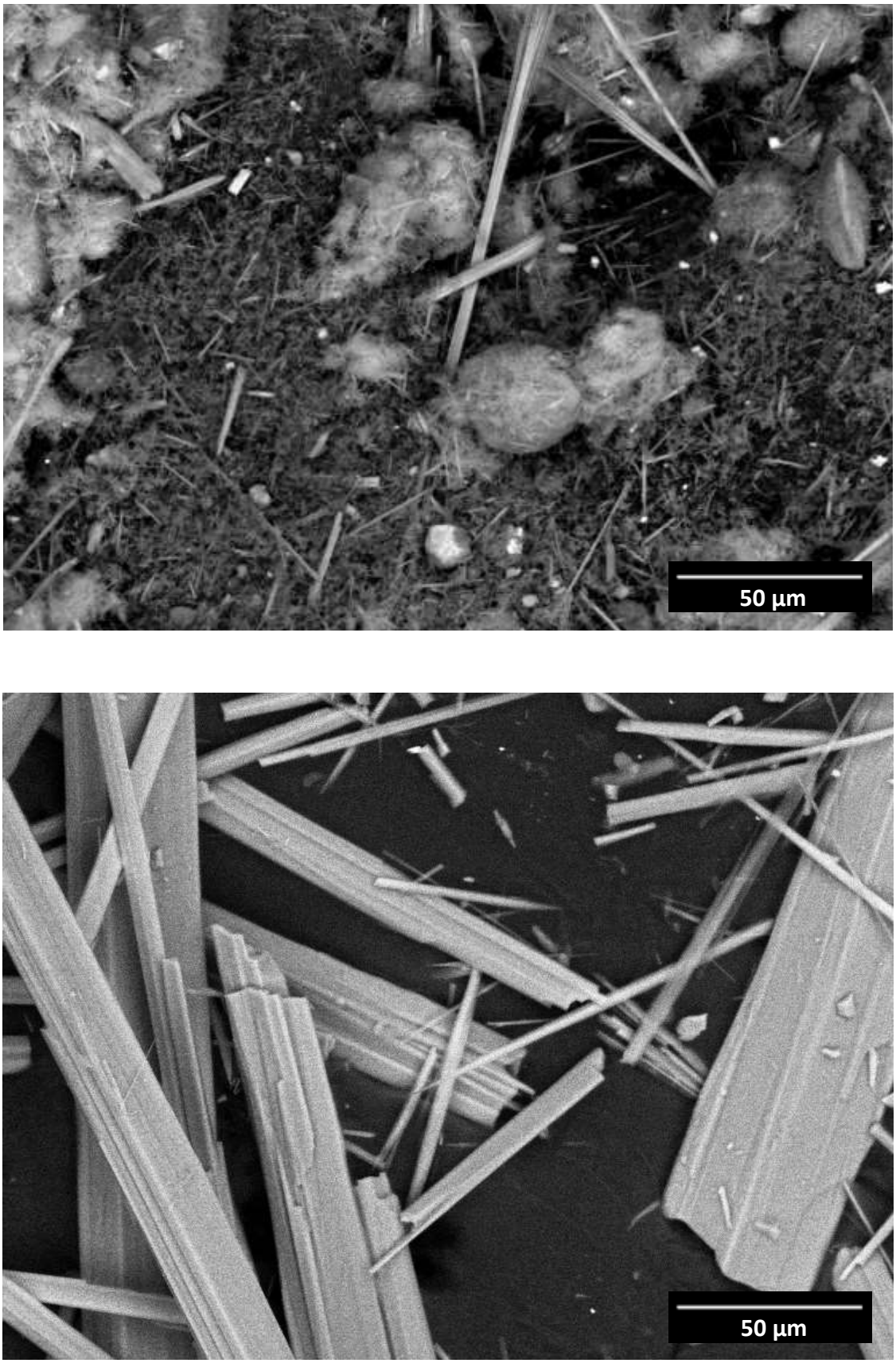

Fig. 3.1.8. High-resolution SEM images of crocidolite (top) and tremolite (bottom).

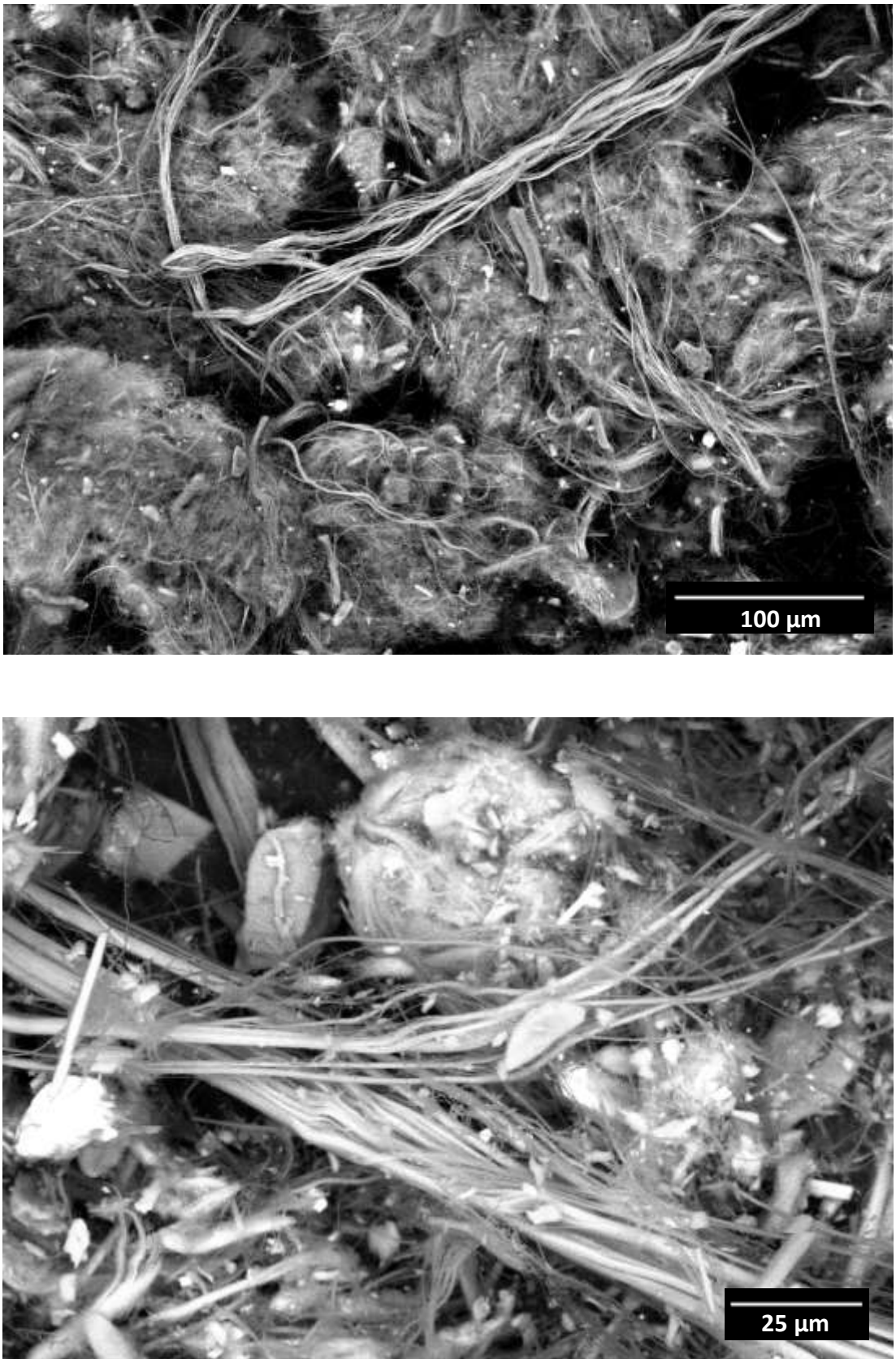

Fig. 3.1.9. High-resolution SEM images of chrysotile UICC (top) and chrysotile Balangero (bottom).

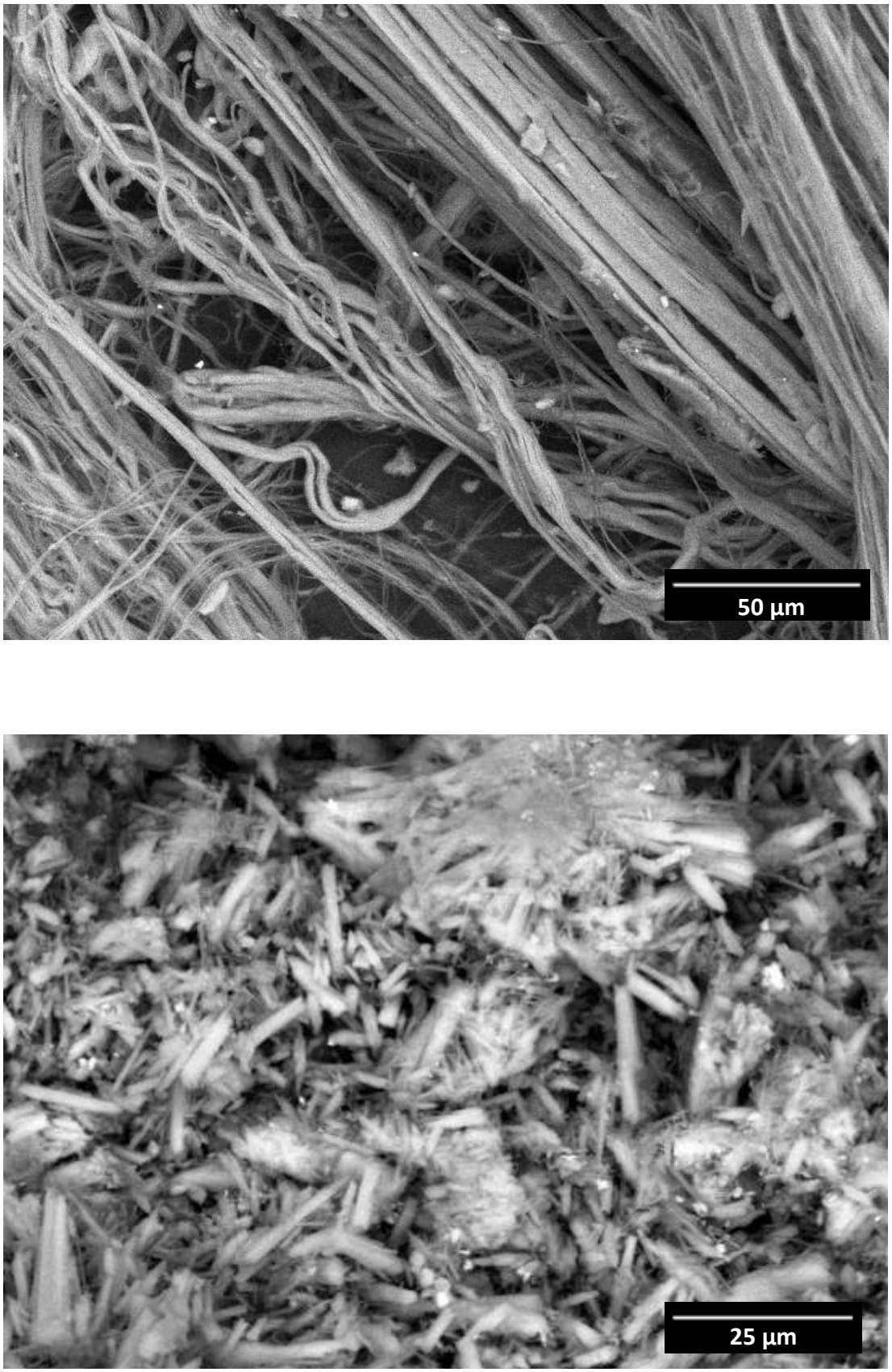

Fig. 3.1.10. High-resolution SEM images of chrysotile Val Malenco (top) and erionite (bottom).

Following the gravitational separation experiments described in the pertinent paragraph, in this section, SEM images for each of the 2 size classes obtained are reported.

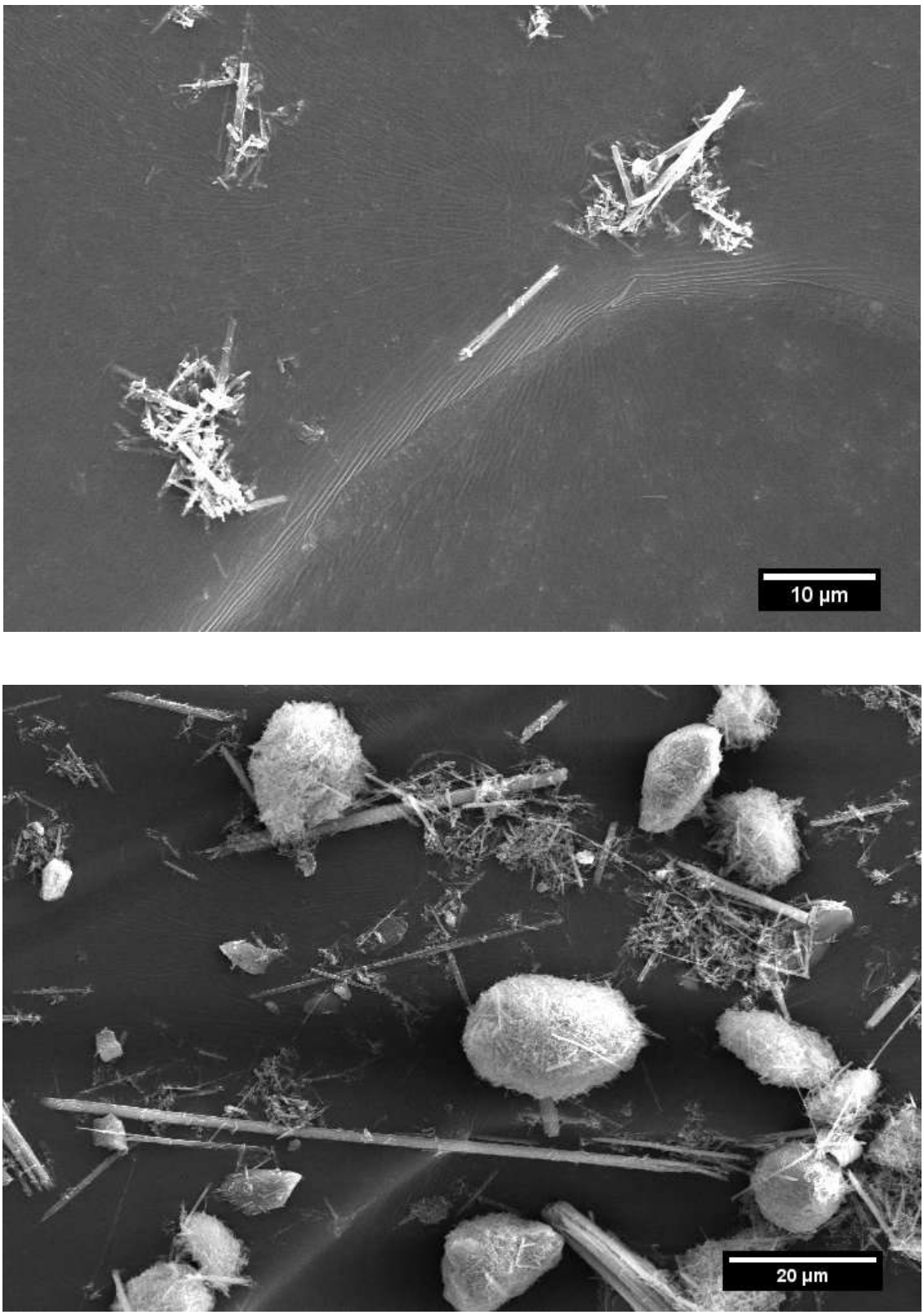

Fig. 3.1.11. High-resolution SEM images of short fibres (top) and long fibres (bottom) samples of crocidolite**.**

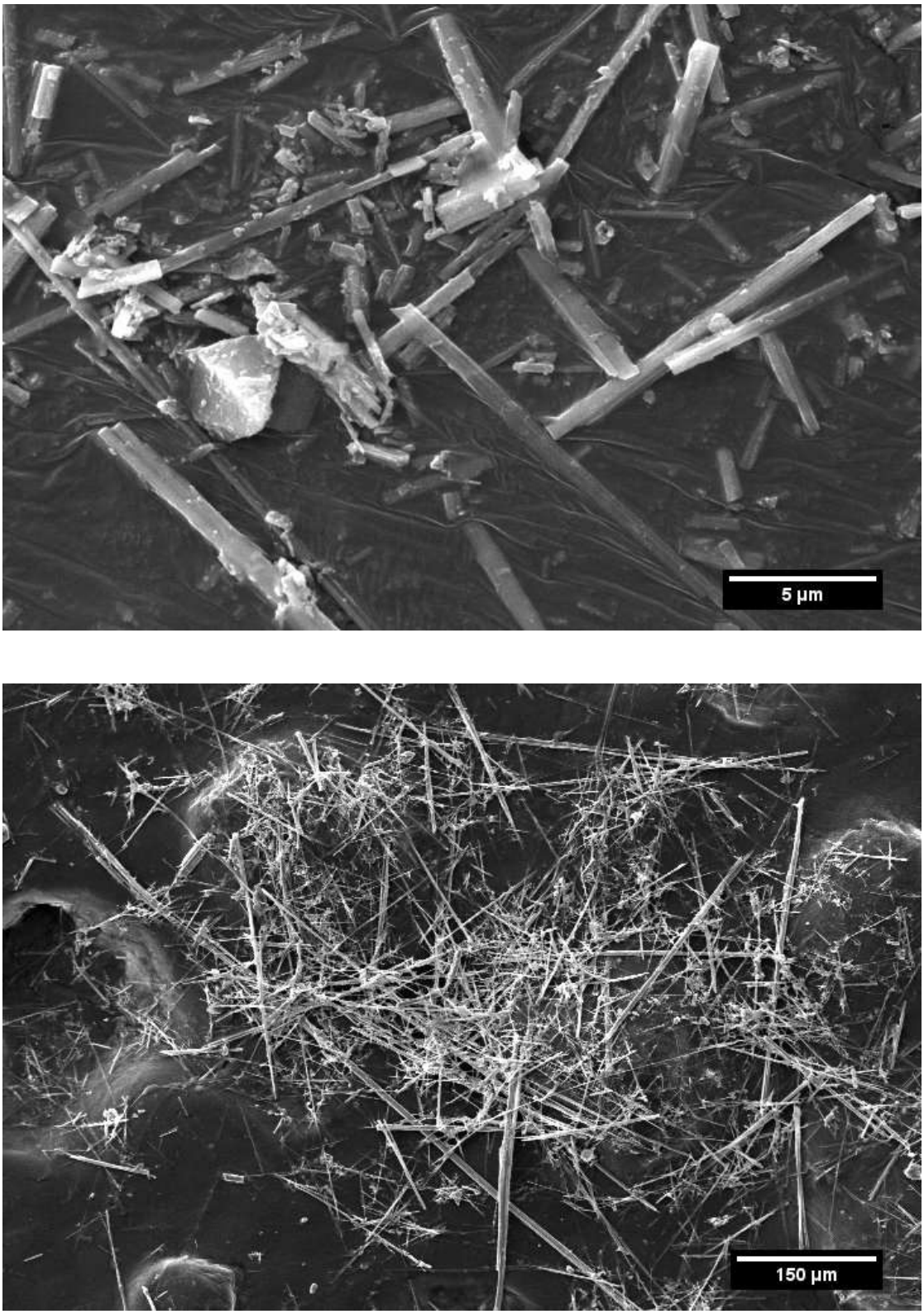

Fig. 3.1.12. High-resolution SEM images of short fibres (top) and long fibres (bottom) samples of amosite**.**

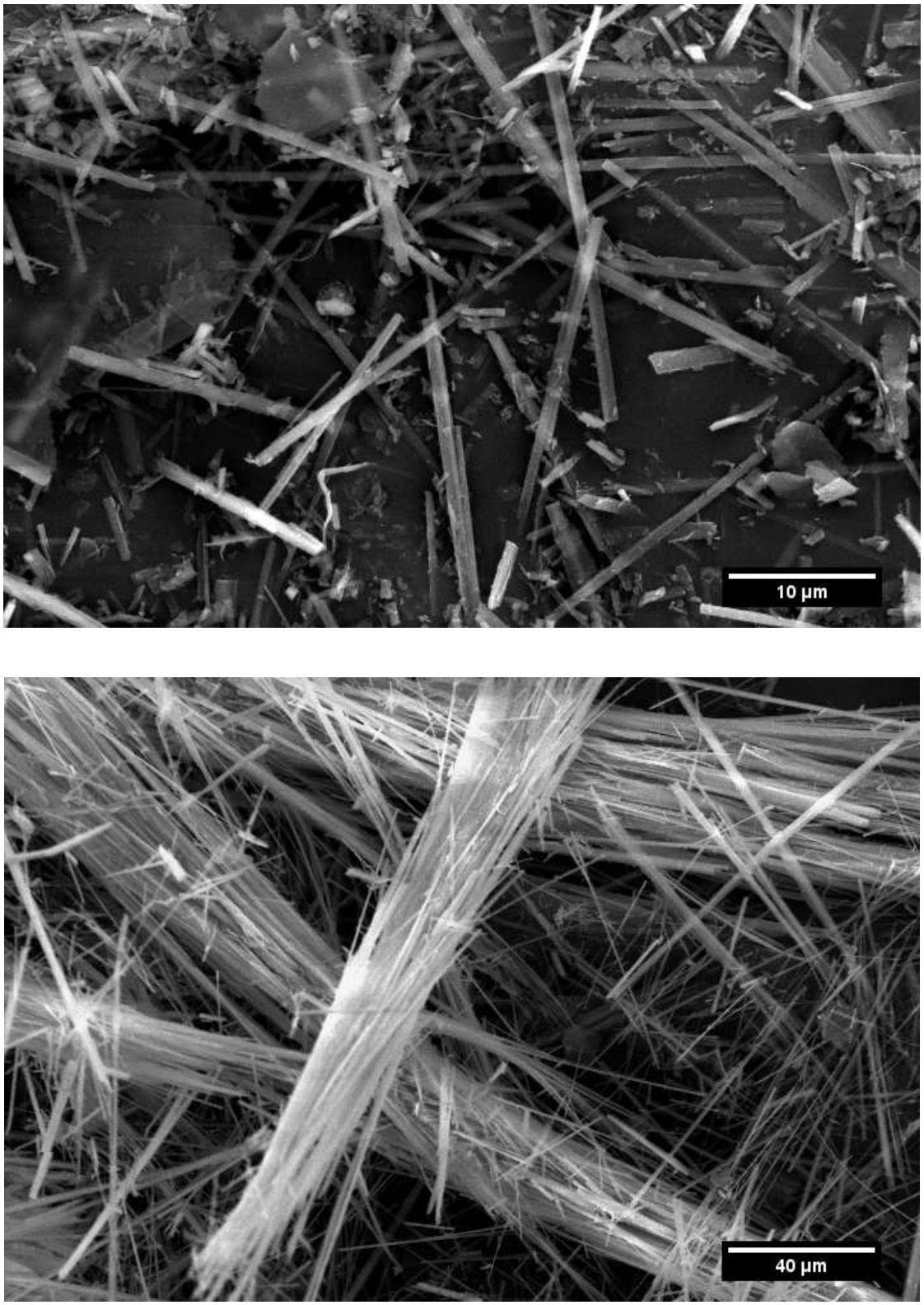

Fig. 3.1.13. High-resolution SEM images of short fibres (top) and long fibres (bottom) samples of anthophyllite.

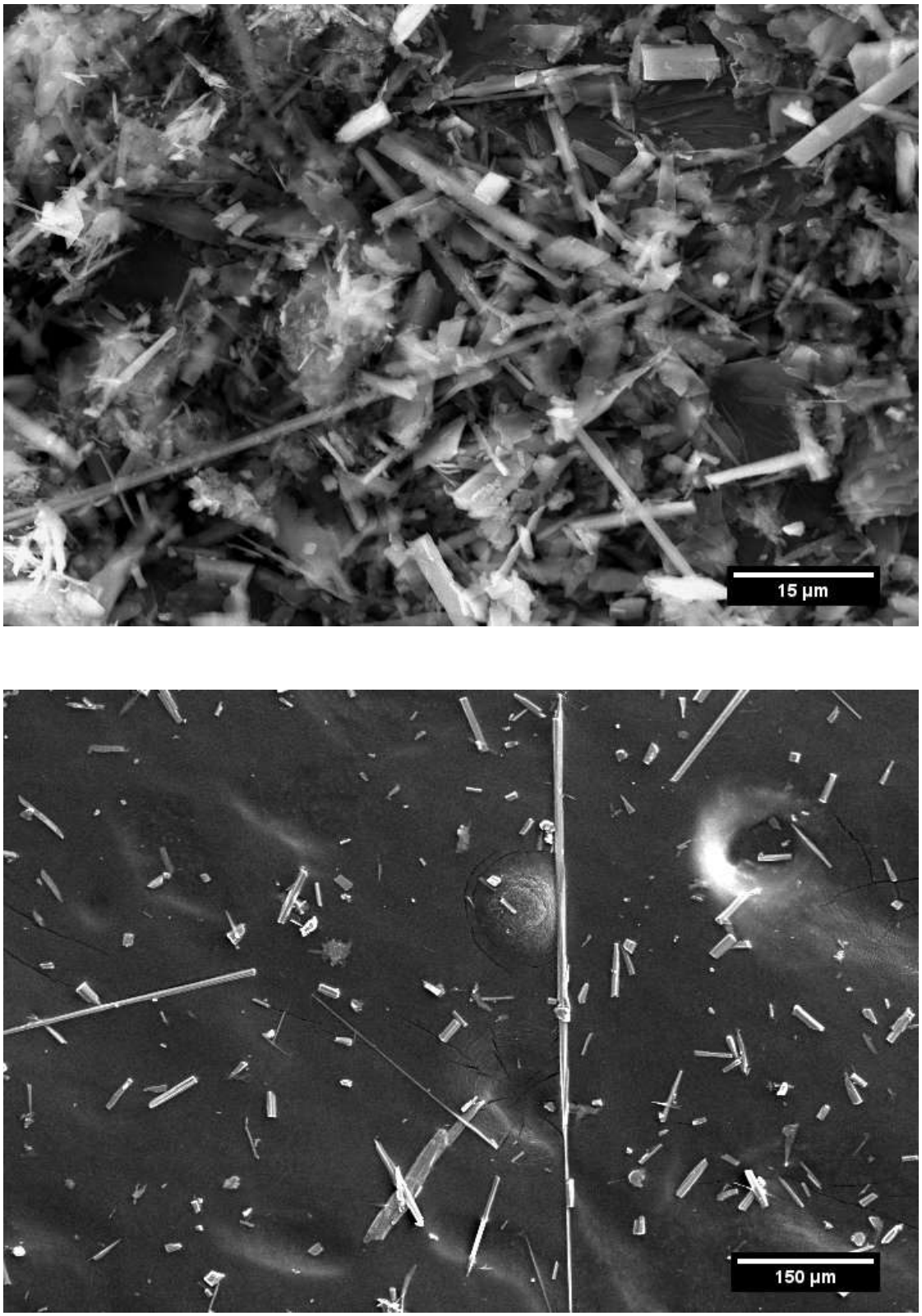

Fig. 3.1.14. High-resolution SEM images of short fibres (top) and long fibres (bottom) samples of tremolite.

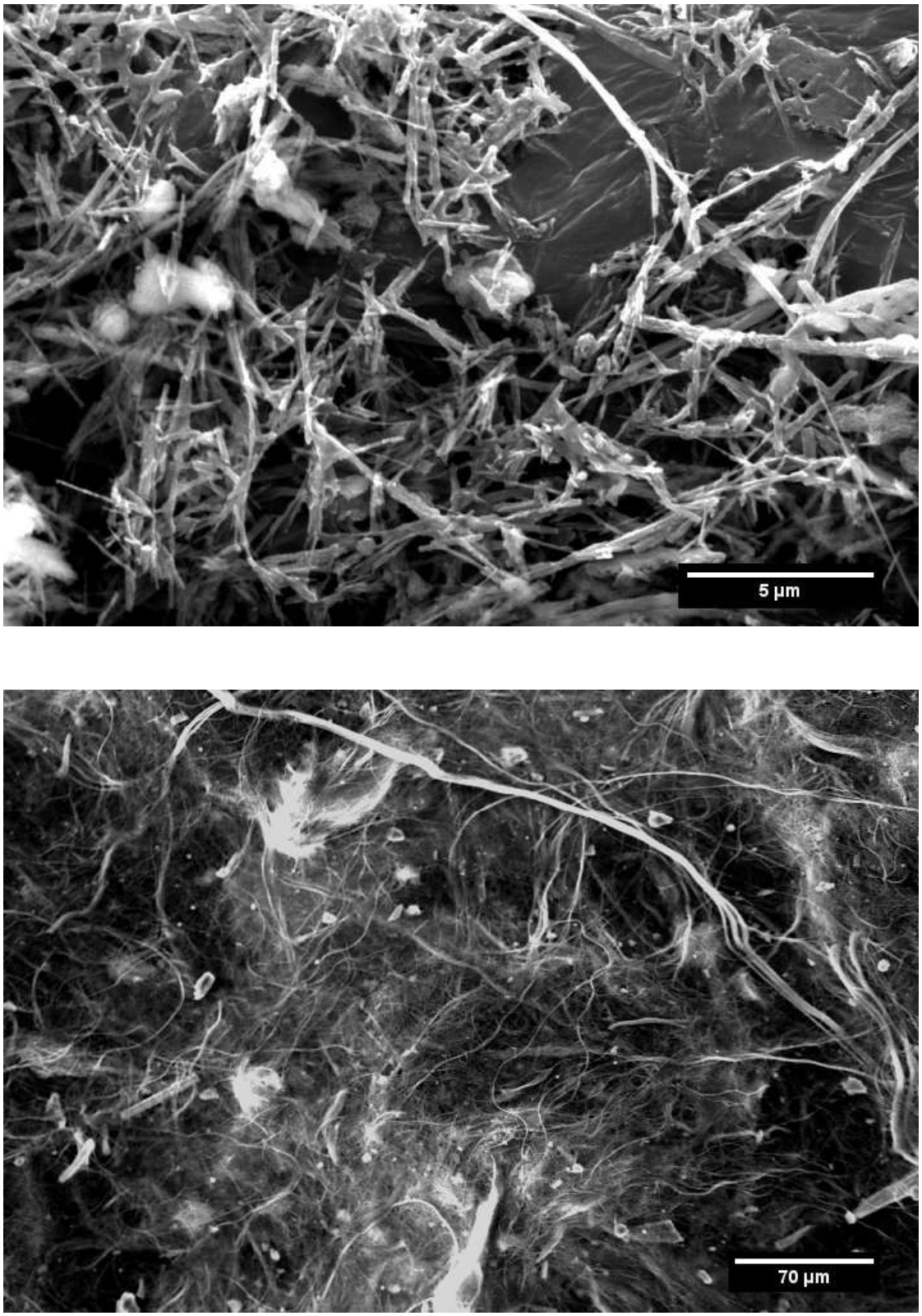

Fig. 3.1.15. High-resolution SEM images of short fibres (top) and long fibres (bottom) of chrysotile UICC.

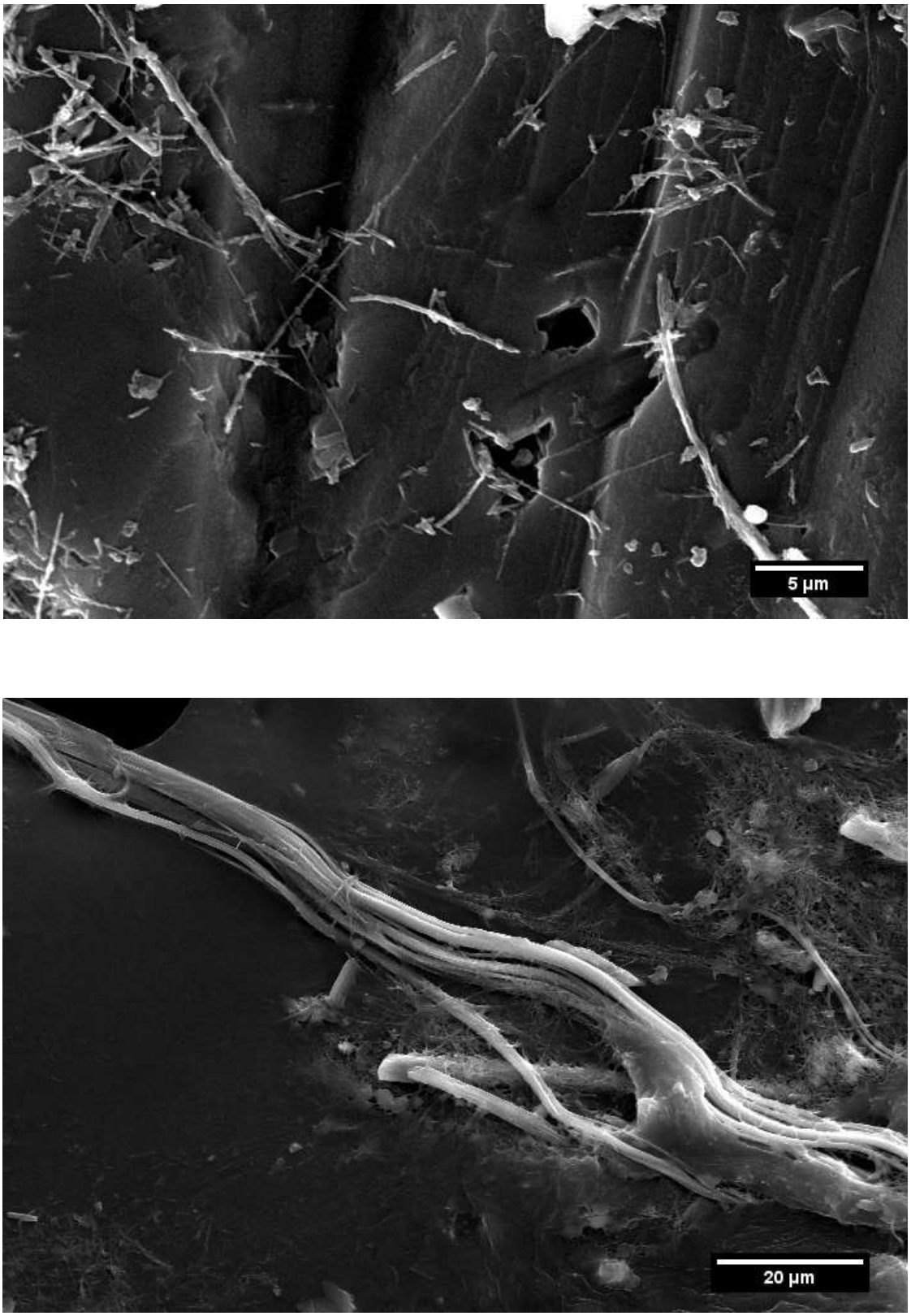

Fig. 3.1.16. High-resolution SEM images of short fibres (top) and long fibres (bottom) samples of chrysotile Balangero.

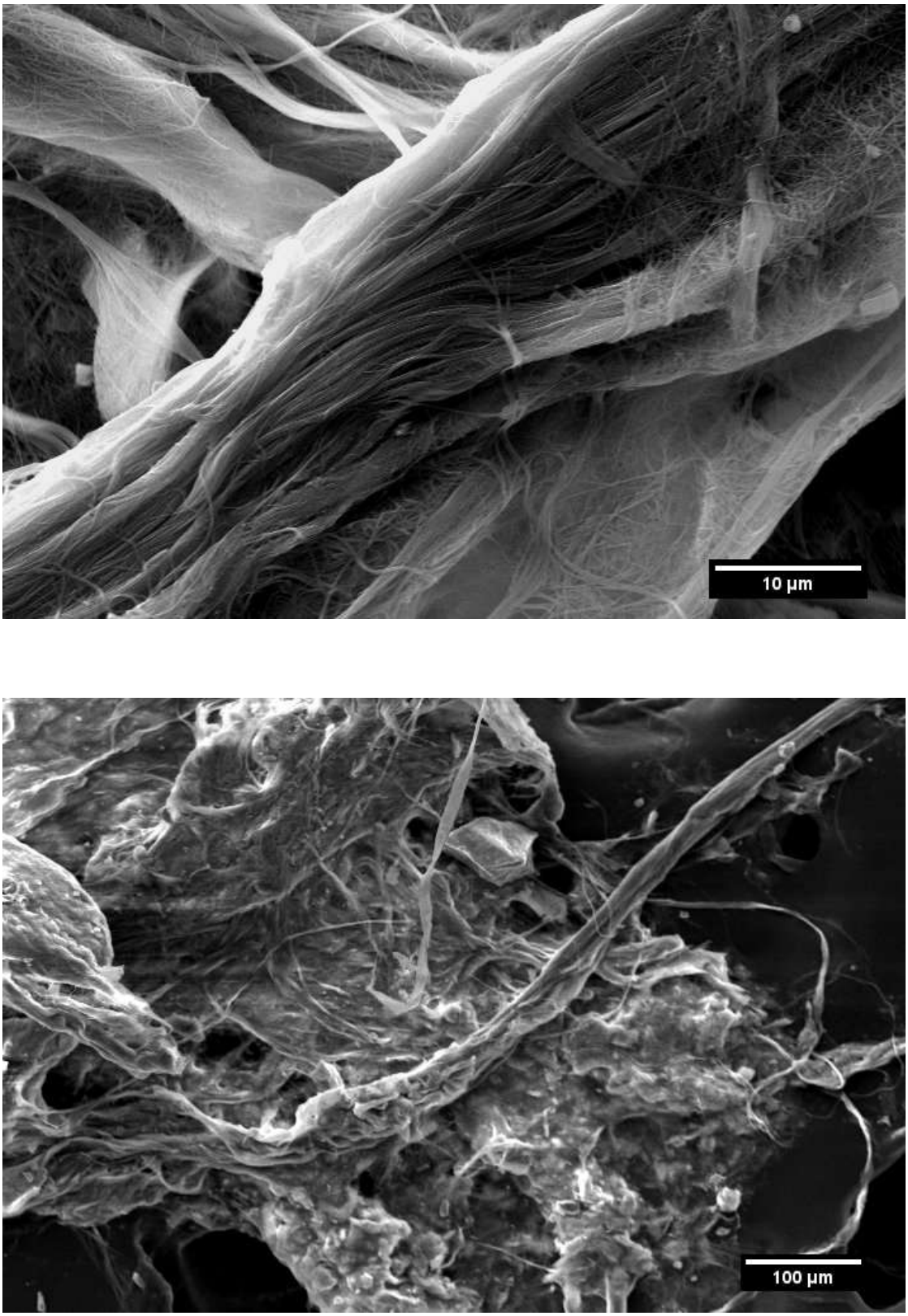

Fig. 3.1.17. High-resolution SEM images of short fibres (top) and long fibres (bottom) samples of chrysotile Val Malenco.

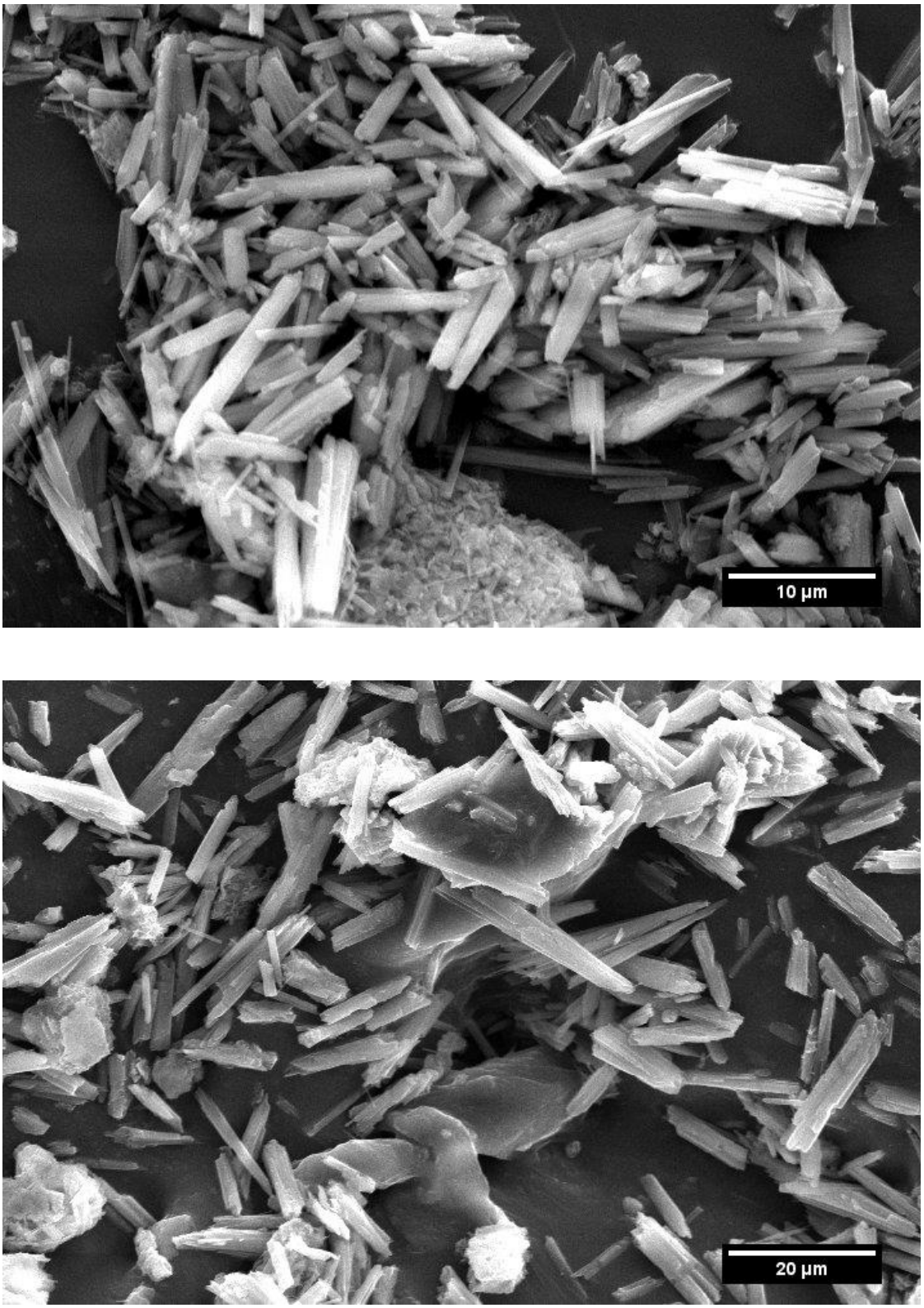

Fig. 3.1.18. High-resolution SEM images of short fibres (top) and long fibres (bottom) samples of erionite.

Through the collected SEM images, it was possible to perform the statistical analysis aimed at the determination of the average fibre size of each sample. The result of this analysis is reported in Table 3.1.9 and plotted in diagram of Fig. 3.1.19.

Table 3.1.9
Average length (in µm) of investigated fibres.

Sample	Short fibres sample	Long fibres sample
Amosite	7 (2)	125 (9)
Anthophyllite	17 (2)	95 (9)
Crocidolite	6 (1)	30 (3)
Tremolite	11 (1)	78 (1)
Chrysotile UICC	5 (2)	99 (5)
Chrysotile Balangero	6 (1)	65 (3)
Chrysotile Val Malenco	10 (5)	160 (9)
Erionite	9 (1)	16 (1)

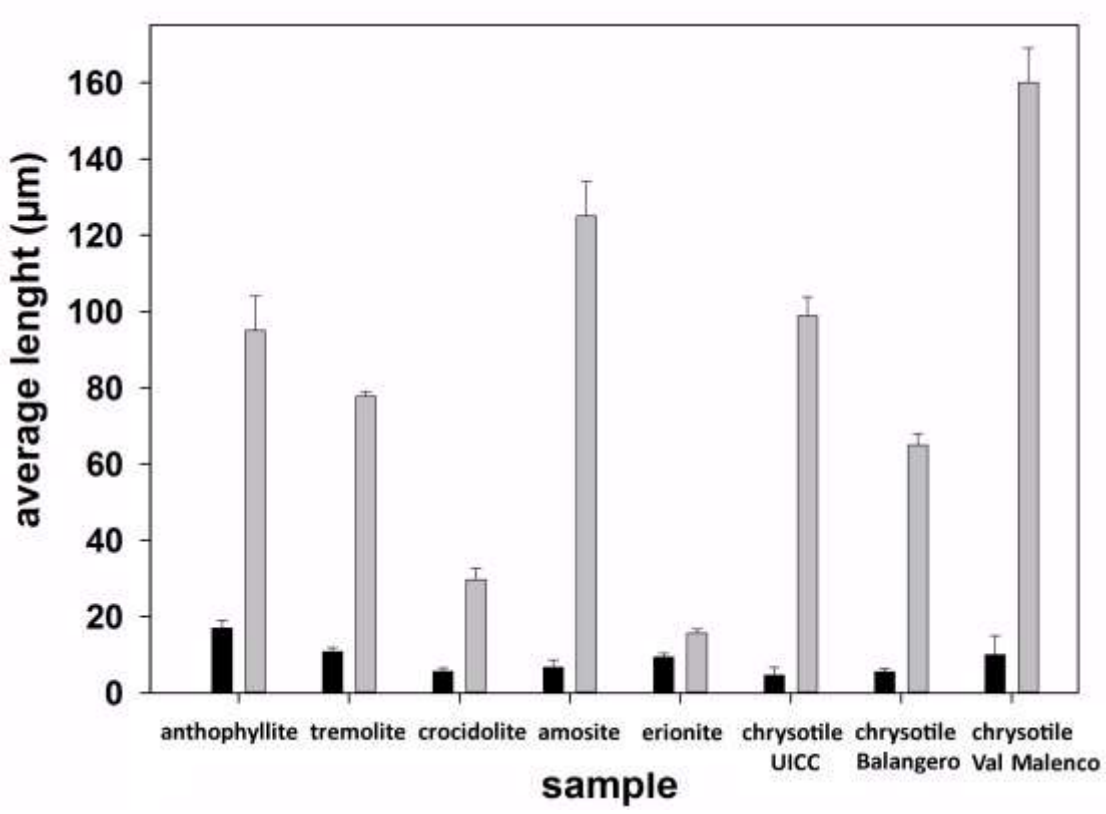

Fig. 3.1.19. Average length of fibres from the two size classes obtained with gravitational separations. Legend: dark columns, short fibres; gray columns, long fibres.

3.6 Surface area

The surface area of samples from BET analysis is reported in Table 3.1.10.

Table 3.1.10
Surface area (m^2/g) of investigated samples.

Sample	Short fibres sample	Long fibres sample
Amosite	9.5 (3)	3.9 (1)
Anthophyllite	14.4 (5)	4.4 (2)
Crocidolite	16.1 (6)	11.5 (4)
Tremolite	9.2 (3)	0.66 (2)
Chrysotile UICC	42 (1)	29 (1)
Chrysotile Balangero	43 (2)	24.8 (9)
Chrysotile Val Malenco	68 (9)[1]	45 (2)
Erionite	28 (1)	12.7 (5)

[1]Calculated from geometrical measurements.

3.7 Zeta Potential

In the following tables are reported all the value of the ζ potential collected on samples, in different chemical-physical conditions (temperature, solute, pH). All ζ potentials are expressed in mV.

Table 3.1.11

ζ potentials of mineral fibres in suspension in Gamble's solution (concentration 0.1 wt%) at 37 °C.

pH (±0.2)		3.0	3.5	4.0	4.5	5.0	5.5	6.0	6.5	7.0	7.5	8.0	8.5	9.0	9.5	10.0
amosite	L[a]	-	-	-	-13 (3)	-	-23 (8)	-	-	-24 (5)	-	-	-	-	-	-
	S[a]	-16 (4)	-	-19 (4)	-21 (4)	-20 (5)	-	-	-21 (4)	-21 (4)	-25 (3)	-21 (5)	-14 (5)	-15 (6)	-	-18 (5)
anthophyllite	L	-	-	-6 (8)	-5 (3)	-	-	-	-	-15 (3)	-	-	-	-	-	-
	S	-	-	-	-15 (6)	-	-	-	-	-17 (4)	-	-	-	-	-	-
crocidolite	L	-	-20 (4)	-	-23 (5)	-	-	-22 (4)	-	-20 (6)	-	-	-	-	-	-
	S	-21 (4)	-23 (4)	-28 (4)	-21 (4)	-29 (5)	-28 (4)	-	-	-24 (4)	-31 (4)	-21 (4)	-30 (3)	-17 (5)		-19 (4)
tremolite	L	-	-	-	-15 (5)	-	-17 (4)	-	-	-17 (5)	-	-	-	-	-	-
	S	-	-	-	-17 (4)	-	-19 (5)	-	-	-20 (5)	-	-	-	-	-	-
chrysotile UICC	L	+4 (2)	-	-4 (3)	-8 (3)	-	-	-8 (3)	-	-8 (3)	-	-13 (2)	-	-	-	-18 (5)
	S	-9 (6)	-12 (3)	-16 (3)	-14 (5)	-20 (2)	-19 (4)	-	-18 (2)	-16 (5)	-22 (4)	-20 (5)	-	-	-20 (3)	-20 (4)
chrysotile Balangero	L	+1 (5)	-12 (5)	-18 (5)	-23 (4)	-19 (5)	-25 (4)	-	-16 (2)	-19 (2)	-17 (4)	-17 (2)	-	-15 (2)	-	-16 (3)
	S	-	-	-	-27 (3)	-	-13 (9)	-	-	-27 (3)	-	-	-	-	-	-
chrysotile Val Malenco	L	-	-	-	-26 (4)	-	-21 (6)	-	-	-27 (7)	-	-	-	-	-	-
	S	-	-	-	-27 (2)	-	-27 (3)	-	-	-23 (2)	-	-	-	-	-	-
erionite	L	-	-	-	-25 (4)	-	-	-23 (5)	-	-20 (6)	-	-	-	-	-	-
	S	-16 (6)	-23 (5)	-20 (5)	-26 (6)	-27 (5)	-27 (6)	-31 (6)	-28 (6)	-29 (6)	-26 (5)	-25 (5)	-	-18 (6)	-14 (4)	-16 (4)

[a] L = long; S = short.

Table 3.1.12
ζ potentials of mineral fibres in suspension in double distilled water (concentration 0.1 wt%): (a) 37 °C; (b) 25 °C.

a)

pH (±0.2)		3.0	4.0	5.0	6.0	6.5	7.0	7.5	8.0	8.5	9.0	10.0	10.5
amosite	Short	-1 (4)	-19 (3)	-21 (4)	-20 (3)	-	-	-30 (9)	-33 (8)	-33 (7)	-	-26 (9)	-
anthophyllite	Short	-4 (6)	-30 (9)	-35 (6)	-25 (5)	-	-	-23 (3)	-	-36 (9)	-51 (9)	-36 (4)	-27 (5)
crocidolite	Short	-16 (3)	-31 (5)	-34 (5)	-38 (6)	-34 (4)	-36 (5)	-37 (4)	-39 (7)	-37 (4)	-37 (5)	-39 (5)	-42 (5)
tremolite	Short	-5 (6)	-18 (7)	-15 (7)	-16 (9)	-24 (7)	-17 (7)	-	-22 (8)	-	-	-32 (7)	-
chrysotile UICC	Long	-	+26 (2)	+19 (2)	+10 (3)	-	+12 (2)	-	+8 (3)	-	+4 (2)	-7 (4)	-
chrysotile UICC	Short	-	-	+49 (5)	-	+32 (3)	-	-	-	-	+30 (3)	+19 (3)	-
chrysotile Bal.	Short	+29 (3)	-	+17 (2)	+11 (3)	+3 (6)	-	-2 (3)	-	-4 (9)	+14 (4)	-	+11 (4)
chrysotile Mal.	Long	-3 (4)	-14 (6)	-19 (5)	-16 (9)	-32 (3)	-	-18 (9)	-	+1 (6)	-4 (8)	-	-
chrysotile Mal.	Short	-10 (3)	-13 (2)	-25 (4)	-27 (4)	-23 (3)	-	-29 (6)	-	-	-28 (5)	-23 (8)	-
erionite	Short	-21 (4)	-25 (5)	-26 (5)	-31 (5)	-	-33 (6)	-34 (7)	-35 (7)	-	-35 (8)	-37 (5)	-

b)

pH (±0.2)		3.0	4.0	4.5	5.0	6.0	6.5	7.0	8.0	9.0	10.0	10.5	-
crocidolite	Short	-16 (4)	-26 (4)	-32 (4)	-36 (4)	-	-38 (5)	-40 (5)	-43 (7)	-43 (6)	-45 (6)	-48 (6)	-
chrysotile UICC	Long	-	+29 (3)	-	+28 (3)	+17 (3)	-	+10 (3)	+7 (4)	+8 (5)	-10 (4)	-	-
erionite	Short	-26 (6)	-34 (6)	-	-38 (7)	-40 (7)	-	-40 (7)	-42 (7)	-41 (6)	-47 (7)	-48 (6)	-

Table 3.1.13
ζ potentials of selected mineral fibres in suspension in double distilled water (d.d.) and in S.L.F. solutions (concentration 0.1 wt%) at 37 °C, with the addition of cations in the form of salts. The table also shows the conductivity of the suspension, which is directly proportional to the amount of ions present in solution; as can be seen, with increasing conductivity, in general, an increase in the value of ζ potential is observed.

pH (±0.5)	Liquid and salt used	Conductivity (±5)	3.0	4.5	5.0	7.0	7.5	9.5
crocidolite	d.d.	0	-	-22 (5)	-28 (5)	-34 (5)	-	-
	d.d. + NaCl	35	-	-12[a]	-	-16	-	-
	d.d. + KCl	30	-	-8	-	-16	-	-
	d.d. + $CaCl_2*2H_2O$	35	-	+1	-	-2	-	-
	SLF	20	-14	-18	-	-24	-	-
	SLF + $CaCl_2*2H_2O$	30	-4	-11	-	-9	-	-
	SLF + $CaCl_2*2H_2O$	45	-2	-5	-	-3	-	-
	SLF + $CaCl_2*2H_2O$	85	-	-	-	+2	-	-
chrysotile	d.d.	0	-	+49 (5)	-	+32 (3)	-	+30 (3)
UICC	d.d. + NaCl	80	-	+77	-	+48	-	+21
	d.d. + KCl	25	-	-	-	+38	-	+38
	d.d. + KCl	50	+62	+77	-	+60	-	-
	d.d. + $CaCl_2*2H_2O$	16	-	+47	-	+45	-	-
	d.d. + $CaCl_2*2H_2O$	35	+81	+76	-	+67	-	-
	SLF	15	+15	-16.5	-	-28	-	-
	SLF + $CaCl_2*2H_2O$	32	+21	+18	-	+14	-	-
	SLF + $CaCl_2*2H_2O$	55	+43	+33	-	+48	-	-
erionite	d.d.	0	-20 (6)	-	-	-35 (7)	-36 (8)	-
	d.d. + NaCl	10	-	-27	-	-30	-	-38 (7)
	d.d. + KCl	15	-	-18	-	-24	-	-
	SLF + $CaCl_2*2H_2O$	10	-9	-	-	-	-	-
	SLF + $CaCl_2*2H_2O$	25	-6	+9	-	+2	-	+4
	SLF	20	-22	-23	-	-26	-	-
	SLF + $CaCl_2*2H_2O$	25	-14	-17	-	-18	-	-
	SLF + $CaCl_2*2H_2O$	40	-9	-12	-	-11	-	-

[a]For many of these data the standard deviation is not reported because, above a certain threshold of conductivity, the instrument used is not capable of providing it.

Table 3.1.14
ζ potentials of the investigated mineral fibres in contact with the Gamble's solution (concentration 0.1 wt%) at 25 °C.

pH (±0.2)		4.0	4.5	5.0
anthophyllite	Long	-	-15 (5)	-
	Short	-	-20 (4)	-
crocidolite	Long	-	-	-
	Short	-	-26 (5)	-
chrysotile UICC	Long	-8 (4)	-	-
	Short	-	-	-
erionite	Long	-	-	-
	Short	-	-33 (5)	-36 (9)

For representative samples crocidolite, chrysotile UICC and erionite, ζ potential values in water at 25 and 37°C and in Gamble's solution at 37°C were plotted in the following Figures.

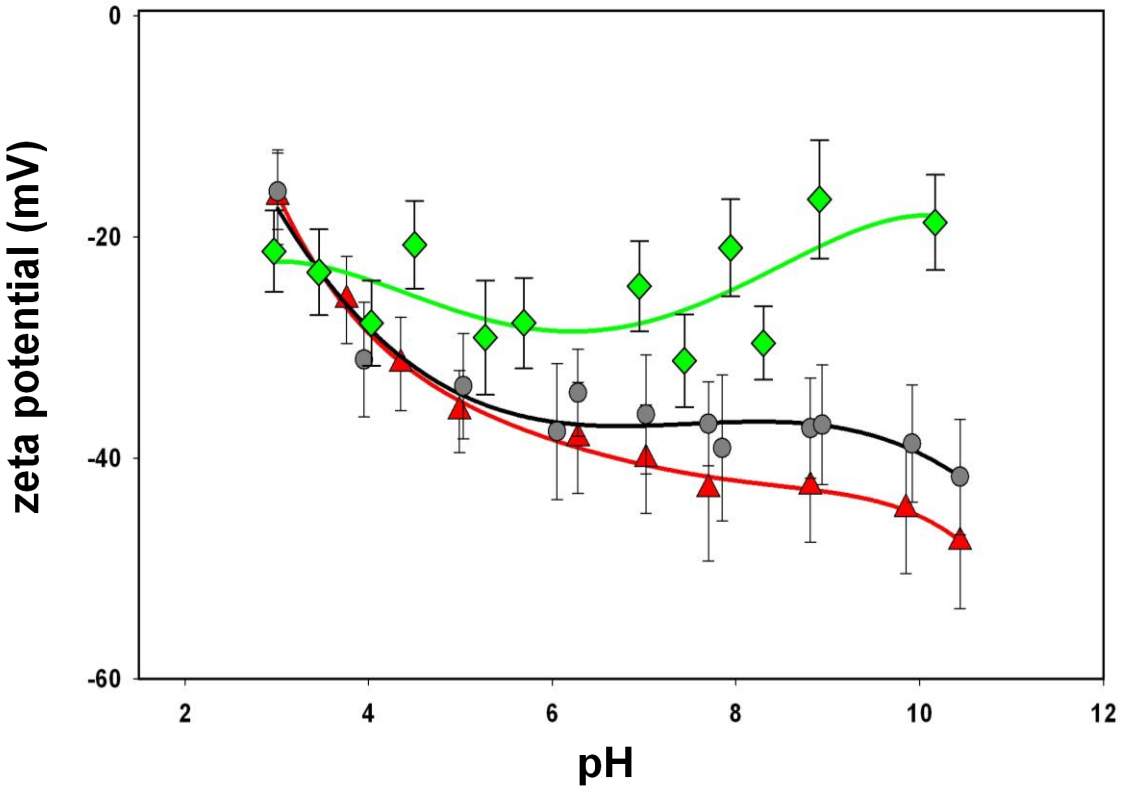

Fig. 3.1.20. Variations of the ζ potential values as a function of pH in different chemical–physical conditions on crocidolite. Legend: (●) 37 °C double distilled water; (▲) 25 °C double distilled water; (♦) 37 °C Gamble's solution.

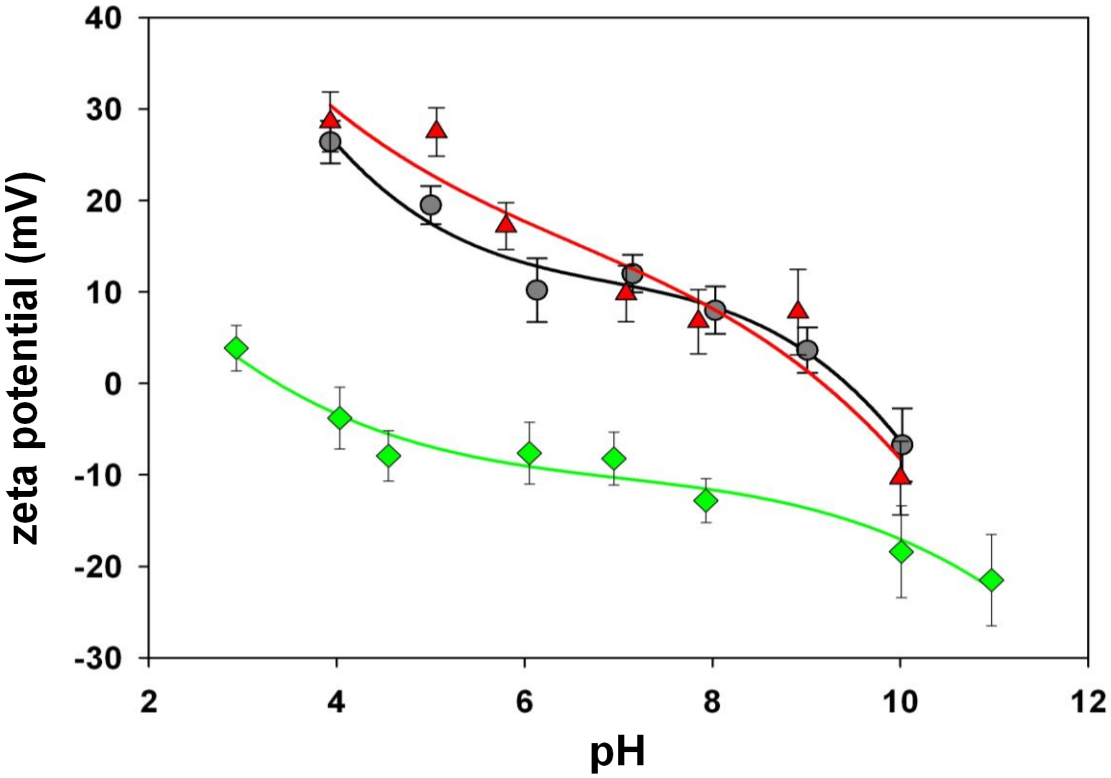

Fig. 3.1.21. Variations of the ζ potential values as a function of pH in different chemical–physical conditions on chrysotile UICC. Legend: (●) 37 °C double distilled water; (▲) 25 °C double distilled water; (♦) 37 °C Gamble's solution.

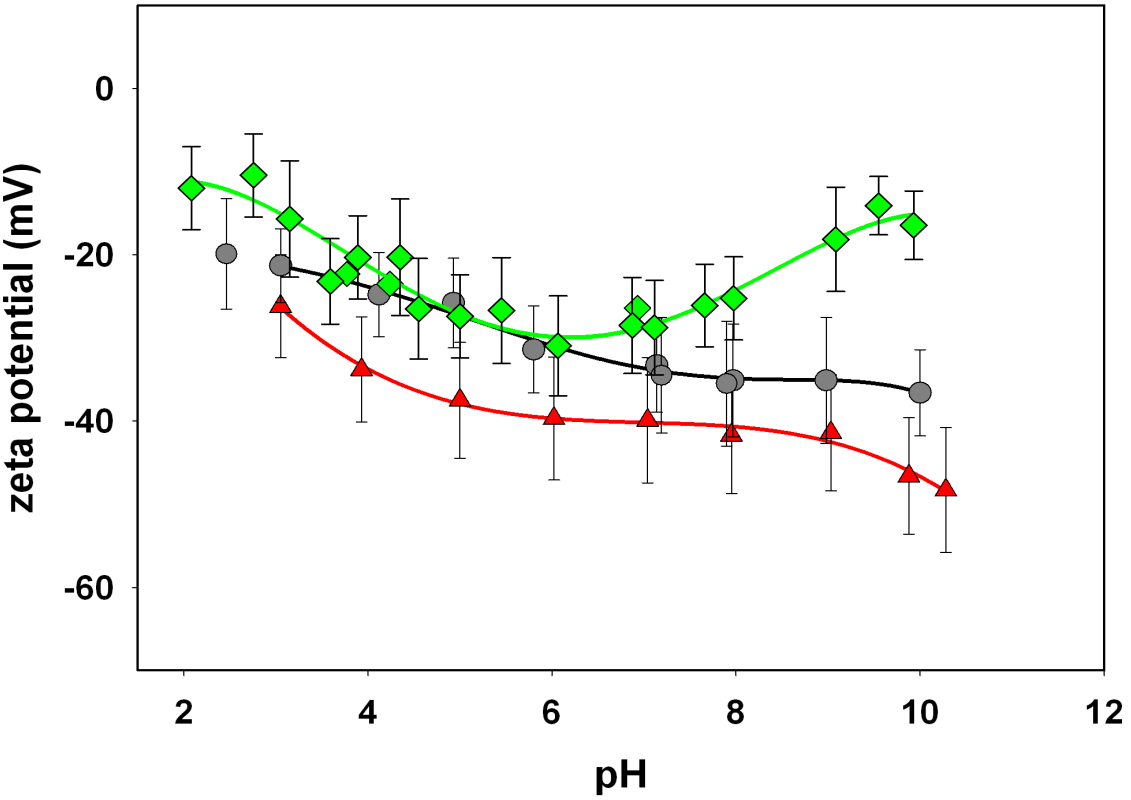

Fig. 3.1.22. Variations of the ζ potential values as a function of pH in different chemical–physical conditions on erionite. Legend: (●) 37 °C double distilled water; (▲) 25 °C double distilled water; (♦) 37 °C Gamble's solution.

3.1.8 ^{57}Fe Mössbauer

^{57}Fe Mössbauer spectra were collected on representative sample amosite for checking the data reproducibility with respect to literature data, and on chrysotile Balangero, Val Malenco and erionite samples, since no literature data are available for these fibres.

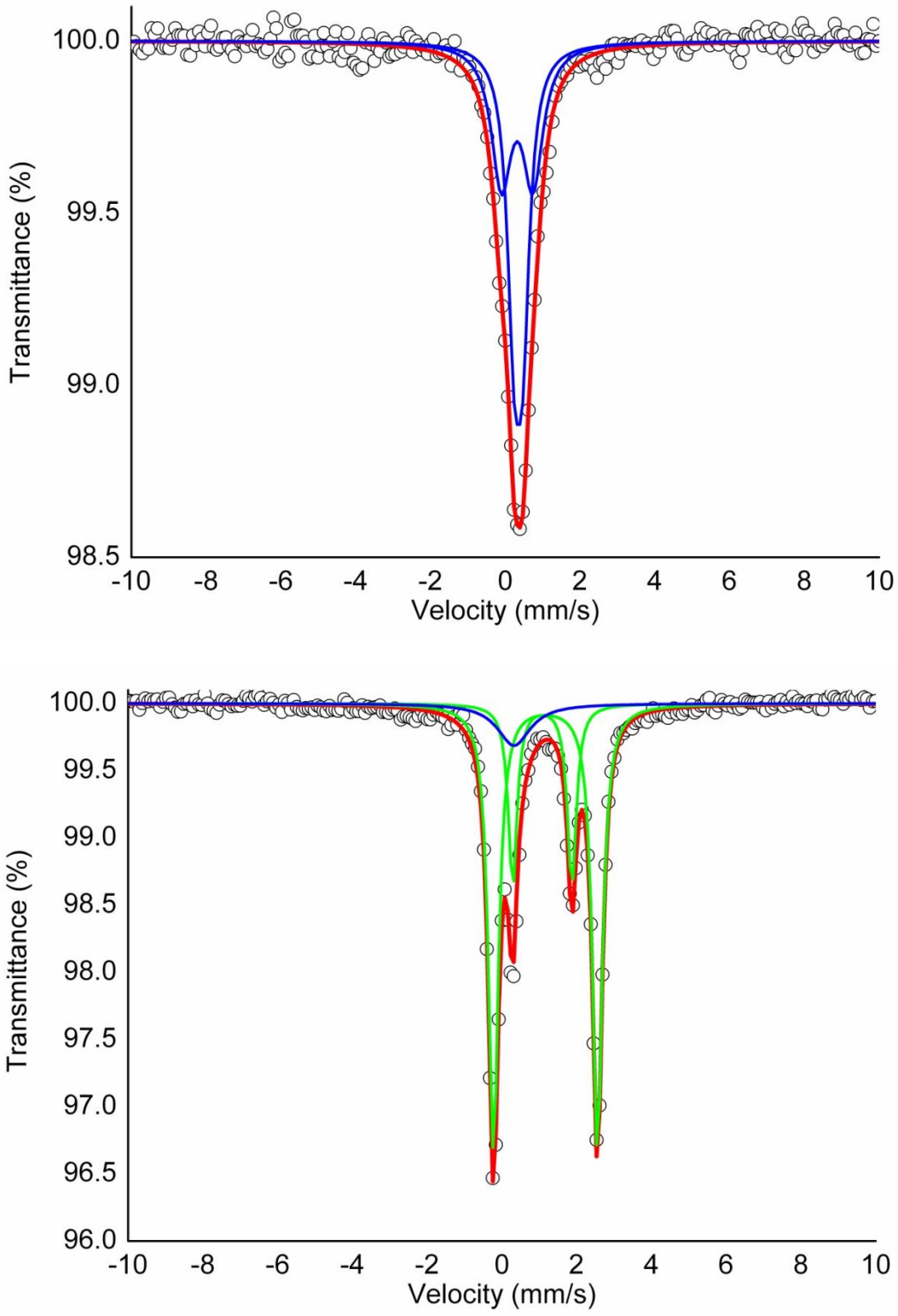

Fig. 3.1.23. ^{57}Fe Mössbauer spectra of erionite (top) and amosite (bottom). Open circles= experimental spectrum; red thick line= calculated spectrum; green thin line = Fe^{2+} paramagnetic subspectra; blue thin line= Fe^{3+} paramagnetic subspectra.

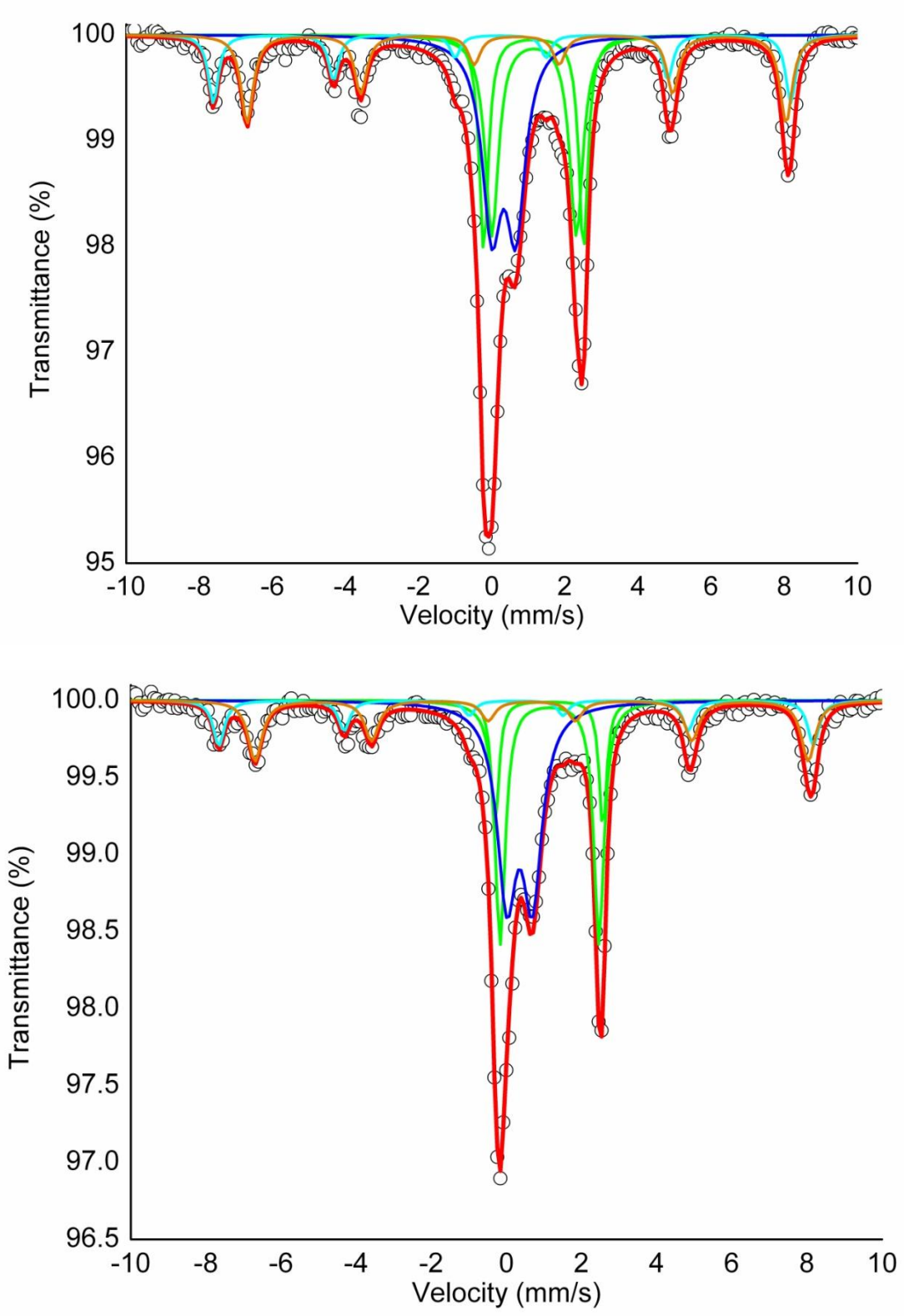

Fig. 3.1.24. ^{57}Fe Mössbauer spectra of chrysotile Blangero (top) and chrysotile Val Malenco (bottom). Open circles= experimental spectrum; red thick line= calculated spectrum; green thin line = Fe^{2+} paramagnetic subspectra; blue thin line= Fe^{3+} paramagnetic subspectra; orange thin line = $Fe^{2.5+}$ magnetic subspectra; cyan thin line = Fe^{3+} magnetic subspectra.

The fit of the spectra allowed to obtain hyperfine parameters (details about the adopted procedure are given in 2.3.8 subchapter) reported in table 3.1.15.

Table 3.1.15

Room temperature ^{57}Fe Mössbauer hyperfine parameters for the investigated samples.

Sample	X^2	Fe^{2+}				Fe^{3+}					Fe^{3+}_{raw} (% Fe_{tot})	Fe^{3+}_{corr} (% Fe_{tot})
		δ (δ_0) (mm/s)	ΔE_Q (Δ_0) (mm/s)	Γ (σ_Δ) (mm/s)	Area (%)	δ (δ_0) (mm/s)	ΔE_Q (Δ_0) (mm/s)	Γ (σ_Δ) (mm/s)	(H) Tesla	Area (%)		
Amosite	1.12	1.16	2.79	0.32	64	0.30	0.00	0.82		9	9	8
		1.08	1.57	0.32	26							
Chrysotile	0.97	1.14	2.73	0.30	17	0.33	0.66	0.64		30	51	43
Balangero		1.16	2.32	0.44	23	*0.26*			*49*	*12*		
						0.68			*46*	*18*		
Chrysotile	0.88	1.13	2.88	0.24	10	0.35	0.69	0.62		37	56	47
Val Malenco		1.15	2.63	0.33	26	*0.26*			*49*	*10*		
						0.67			*46*	*17*		
Erionite	0.49					0.35	0.24	0.44		55	100	100
						0.32	0.85	0.64		45		

Center shift (δ) measured with respect to α-iron. Lorentzian site analysis: uncertainties were estimated at about ± 0.02 mm/s for both δ, quadrupole splitting (ΔEQ) and line width (Γ), ± 0.5 Tesla for magnetic field (H), and no less than ± 3 % for absorption area (expressed as % of Fe_{tot}). In *italics*: parameters assigned to Fe^{3+} and $Fe^{2.5+}$ of accessory magnetite in chrysotile. Fe^{3+}_{raw}: area of absorption peaks assigned to Fe^{3+}; Fe^{3+}_{corr}: obtained from raw value by applying the correction factor of Dyar *et al.* (1993) for amphiboles and chrysotiles, and that of De Grave and Van Alboom (1991) for magnetite; this parameter is referred to the total amount of Fe^{3+} in the sample (including possible impurities). Symbols according to Rancourt and Ping (1991).

3.1.9 X-ray Photoelectron Spectroscopy (XPS)

In the following Figures, the spectra for all samples are shown, with indication of the spectral lines of the elements detected in each sample.

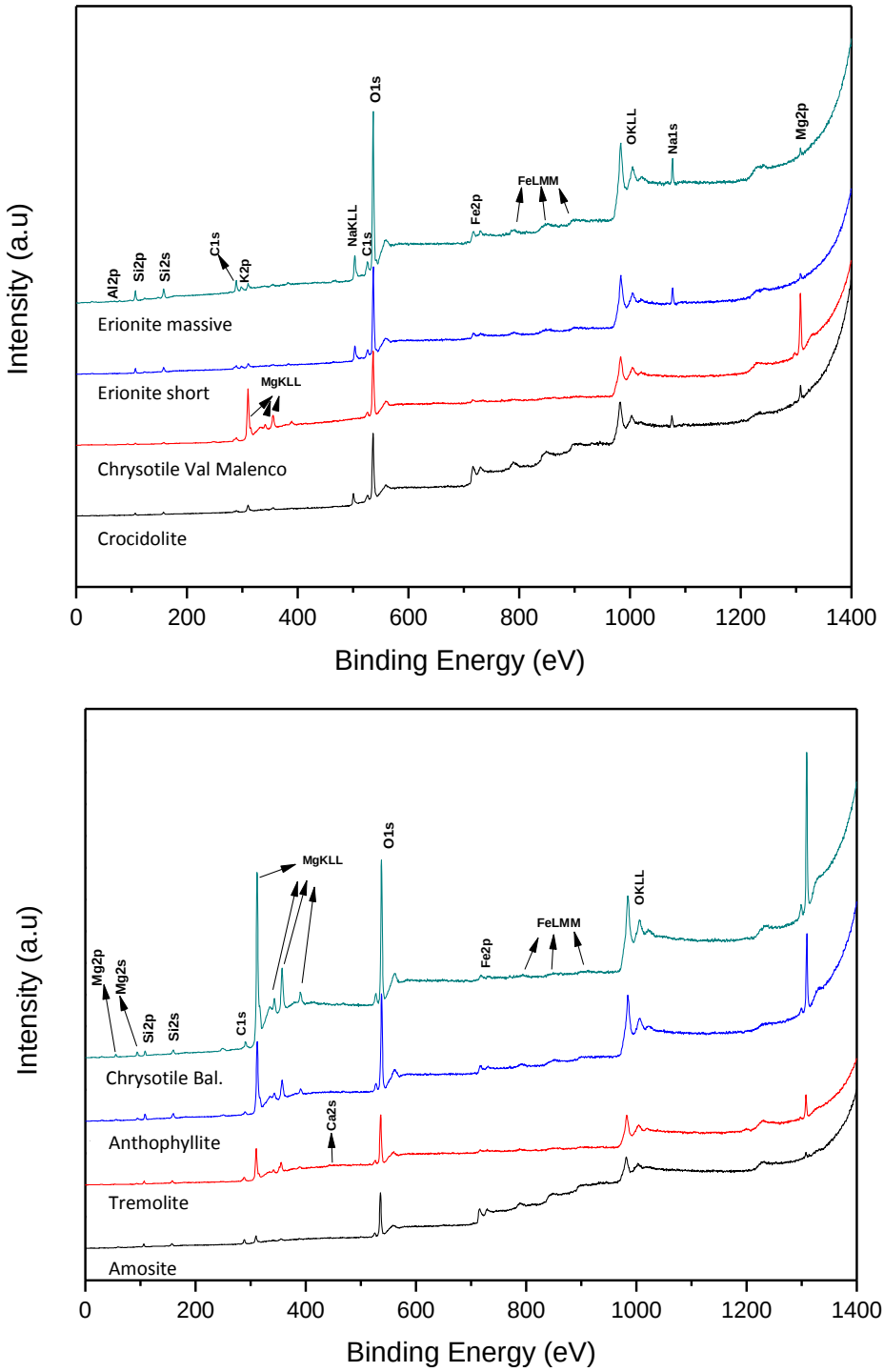

Fig. 3.1.25. XPS spectra collected on samples. In the case of erionite, analysis have been performed both on massive and short fibres sample, in order to check for differences with respect to the fibre size.

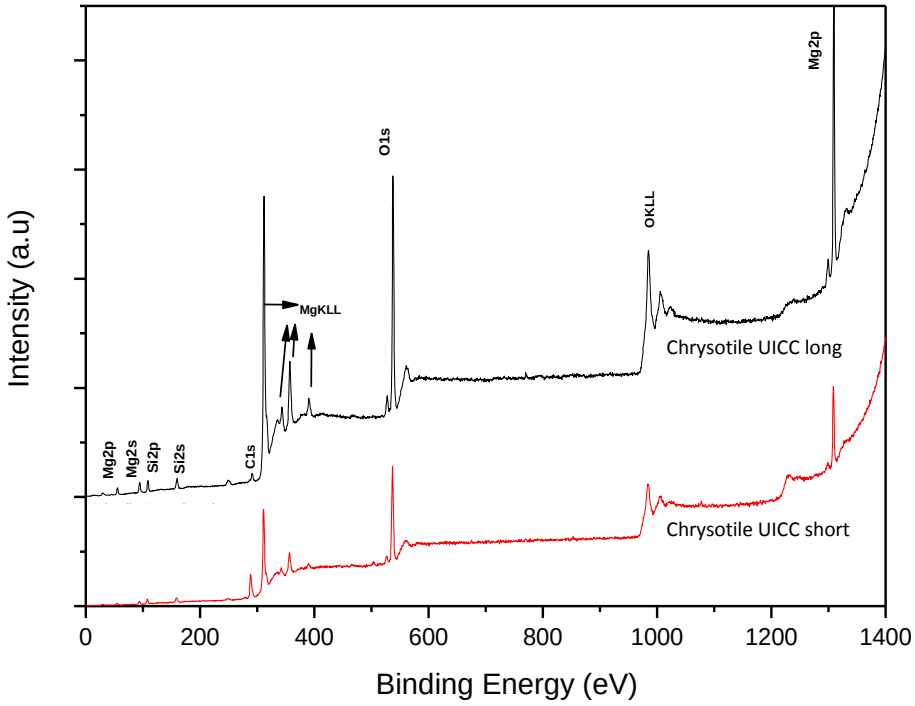

Fig. 3.1.26. XPS spectra collected on chrysotile UICC. Also in this case, analysis have been performed both on long and short fibres sample to check for differences.

Table 3.1.16
Atomic percentages of the elements calculated on the peaks: Fe2p; O1s; C1s; Mg1s; Na1s; Si2p; K2p; Al2p and Ca2s.

Sample	Fe	O	Mg	Na	Si	K	Al	Ca
amosite	8,3	80,7	2,7	-	8,3	-	-	-
antofillite	1,7	71,5	20,0	-	6,9	-	-	-
crocidolite	7,6	76,7	6,1	4,4	5,2	-	-	-
tremolite	1,8	78,2	9,7	-	8,1	-	-	2,2
crisotilo UICC lungo	-	64,5	29,8	-	5,8	-	-	-
crisotilo UICC corto*	-	72,7	20,1	-	7,2	-	-	-
crisotilo Balangero	1,0	68,7	26,9	-	3,5	-	-	-
crisotilo Val Malenco	1,2	69,7	25,8	-	3,3	-	-	-
erionite corta	2,1	77,4	2,3	6,5	9,1	1,2	1,3	-
erionite solida	2,4	74,4	2,3	6,6	9,6	2,5	2,3	-

*The powder for this sample was not sufficient to cover the entire area of the adhesive support.

Furthermore, in order to identify the percentages of different oxidation states of iron, the peak deconvolution of the spectrum Fe $2p_{3/2}$ has been made (following the same approach used in Fantauzzi *et al.* 2010). The peak fit has identified Fe^{2+}, Fe^{3+} and FeOOH. There was also another peak, with low intensity, attributed to the shake-up of Fe^{2+} (Fig. 3.1.27). This procedure has been applied only on crocidolite, amosite and erionite (massive) samples, since on the other samples the signal/noise ratio on the peak of Fe was so great to not allow the deconvolution.

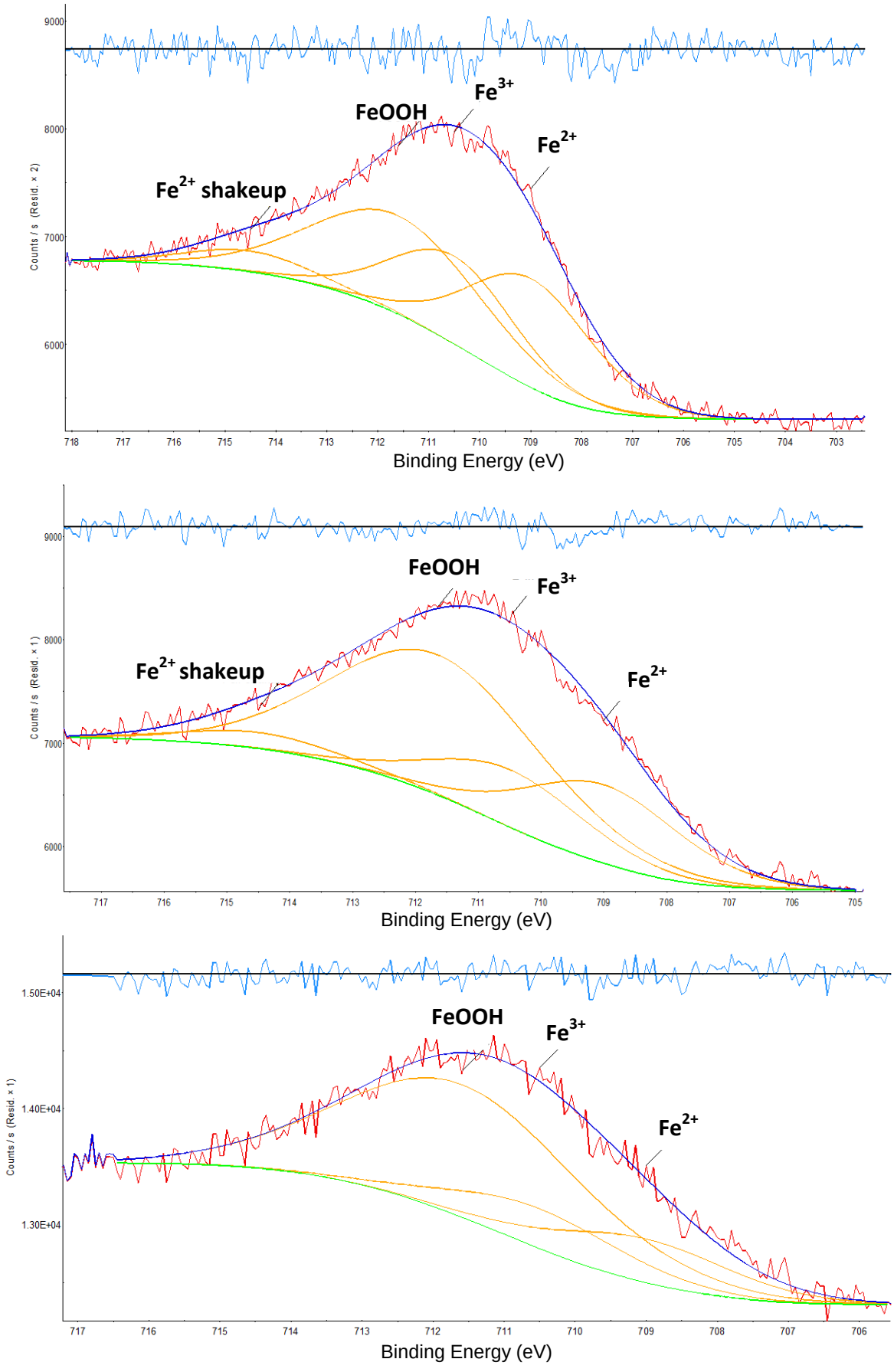

Fig. 3.1.27. Fe $2p_{3/2}$ spectra curve fit for: Amosite (top); crocidolite (middle); erionite (bottom).

The results of the peak fitting has allowed the calculation of the percentages of Fe^{2+}, Fe^{3+} and FeOOH with respect to the total Fe in the three samples (Table 3.1.17).

Table 3.1.17
Percentage ratios of Fe^{2+}, Fe^{3+} and FeOOH compared to the total iron present in samples.

Sample	Fe^{2+}/Fe_{tot}	Fe^{3+}/Fe_{tot}	$FeOOH/Fe_{tot}$
Amosite	33	26	41
Crocidolite	24	17	59
Erionite (massive)	16	15	69

3.2 Non-Conventional methods

In this section, all the obtained results through non-conventional methods will be described.

3.2.1 XRPD experiments at MS-Powder beamline – SLS

The conducted experiment allowed to obtain high-resolution and high-intensity XRPD pattern, reported in Figs. 3.2.1 and 3.2.2.

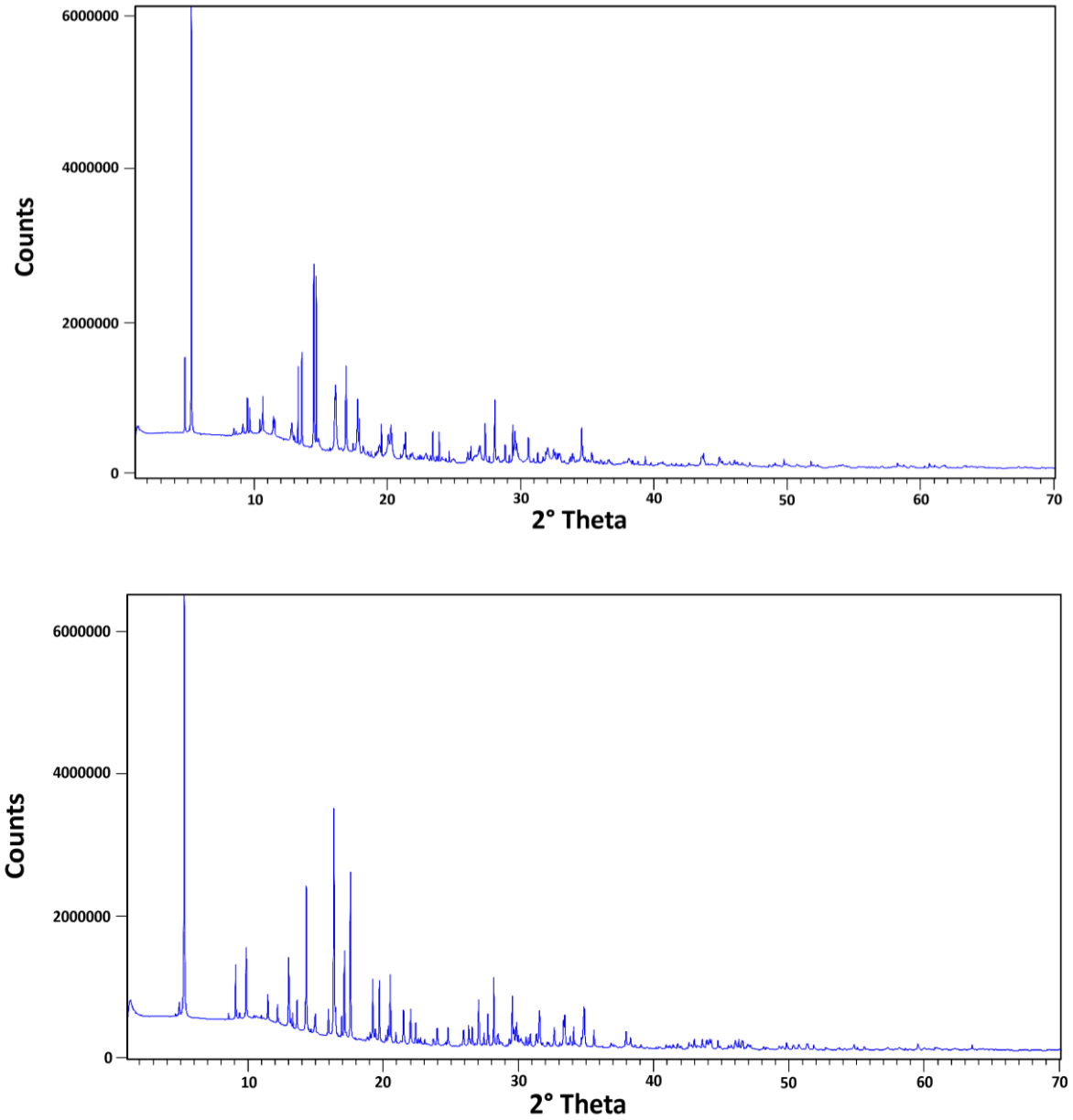

Fig. 3.2.1. XRPD pattern of amosite (top) and crocidolite (bottom).

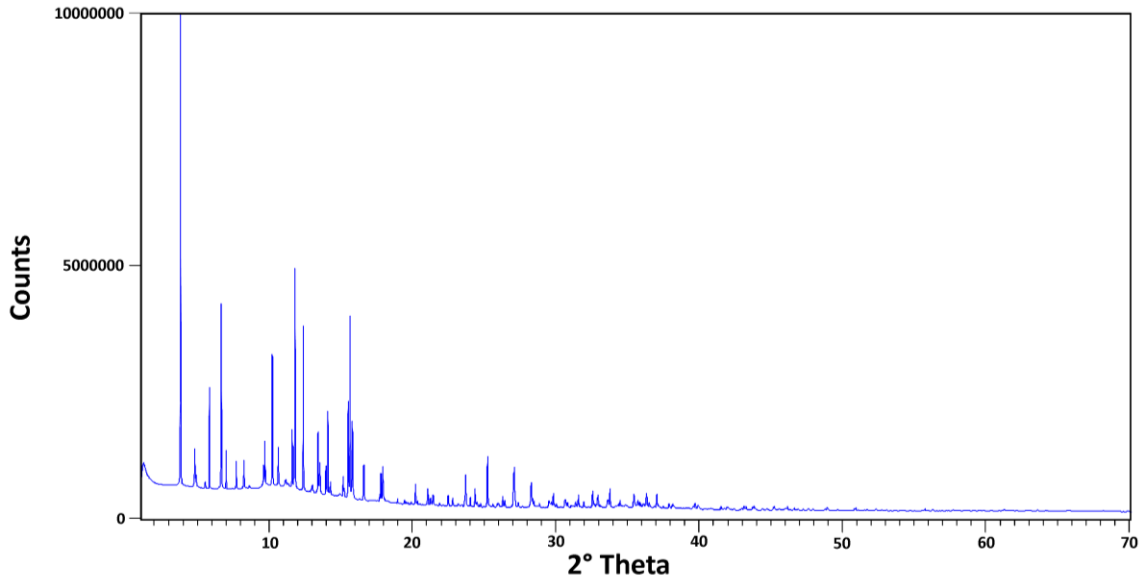

Fig. 3.2.2. XRPD pattern of erionite.

On this data, structural refinements have been performed (Fig. 3.2.3, 3.2.4), allowing to obtain unit cell parameters, thermal parameters, spatial group, and anion-cation distances, listed in the following Tables.

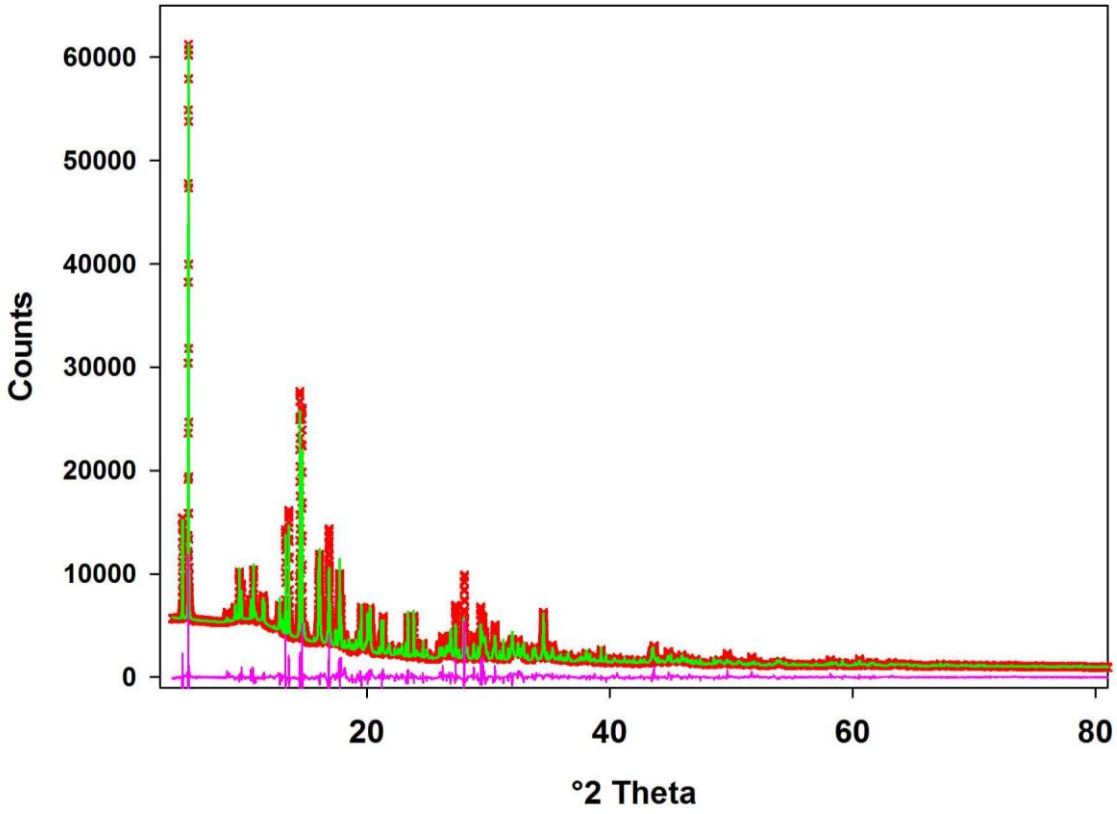

Fig. 3.2.3 Rietveld refinement of amosite sample, made with Topas. Observed (crosses), calculated (continuous line), and difference (bottom line) curves are reported.

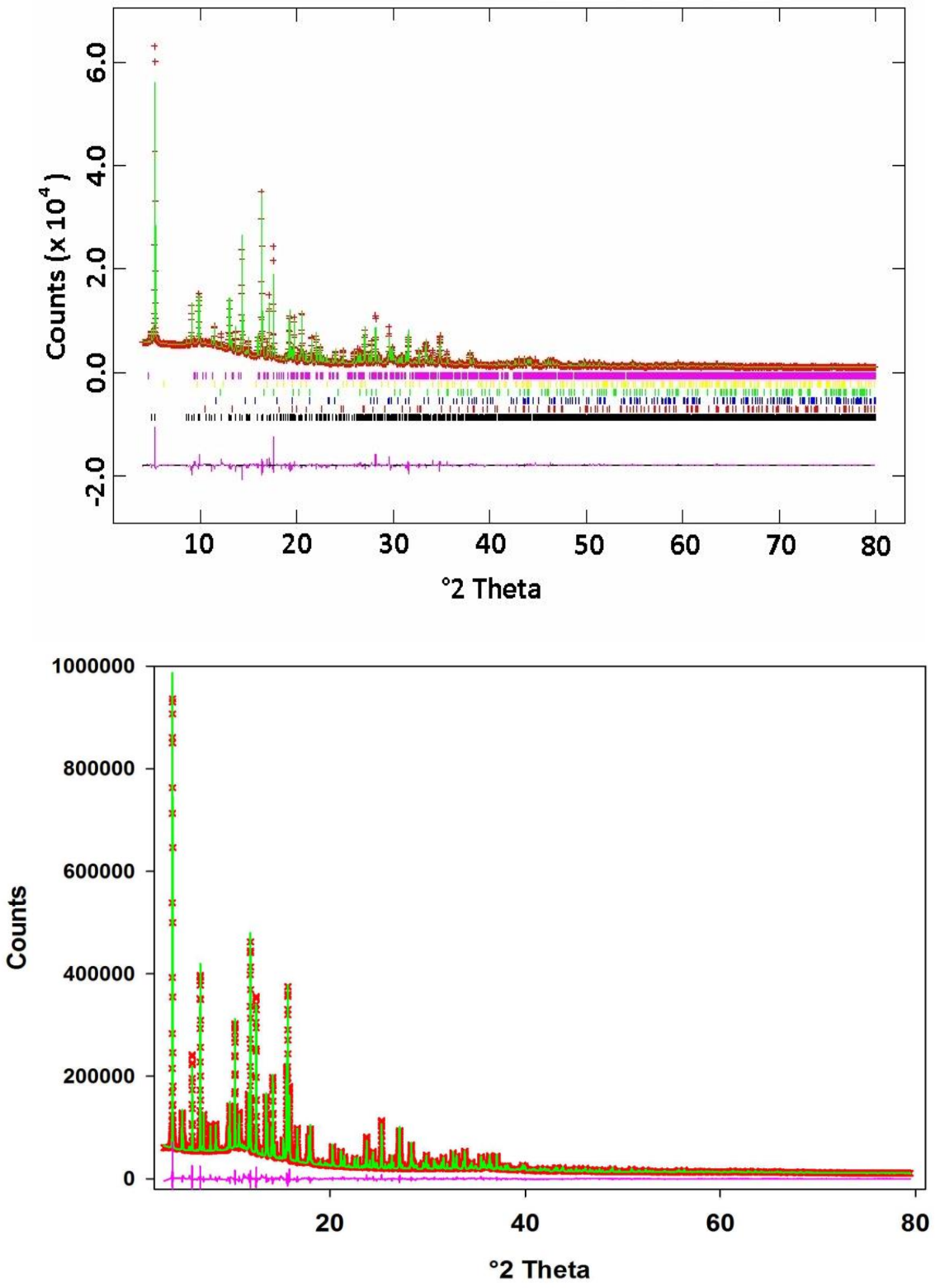

Fig. 3.2.4 Rietveld refinement of crocidolite (top, made with GSAS) and erionite (bottom, made with Topas). Observed (crosses), calculated (continuous line), and difference (bottom line) curves are reported. For the crocidolite sample, vertical bars marking Bragg reflection positions are also reported, and corresponding to crocidolite, quartz, calcite, hematite and lizardite (from top to bottom).

Table 3.2.1
Unit cell parameters and agreement factors of the refinement for amosite, crocidolite and erionite.

	Amosite		Crocidolite		Erionite	
a (Å)	9.553(1)	R_{wp} 6.694 %	9.73238(7)	R_{wp} 5.25 %	13.21981(4)	R_{wp} 1.462 %
b (Å)	18.346(1)	R_p 4.133 %	18.0414(1)	R_p 3.61 %	-	R_p 1.135 %
c (Å)	5.336(1)	χ^2 3.147	5.32794(4)	χ^2 6.716	15.06271(6)	χ^2 1.88
β (°)	101.820(2)		103.515(1)		-	
sp. gr.	*C*2/m		*C*2/m		P6_3/mm*c*	

Table 3.2.2
Final atomic coordinates, occupancies and atomic displacement parameters (Å^2) for amosite.

site	*x*	*y*	*z*	occupancy	U_{iso}
M(1)	0	0.0873(2)	½	$Fe_{0.8}Mg_{0.2}$	0.0068(10)
M(2)	0	0.1791(2)	0	$Fe_{0.75}Mg_{0.25}$	0.0068(11)
M(3)	0	0	0	$Fe_{0.8}Mg_{0.2}$	0.0068(15)
M(4)	0	0.2524(2)	½	$Fe_{0.8}Mg_{0.2}$	0.0068(10)
T(1)	0.2806(5)	0.0819 (2)	0.2645(10)	$Si_{1.00}$	0.0085(11)
T(2)	0.3066(6)	0.1677(2)	0.7748(12)	$Si_{1.00}$	0.0109(13)
O(1)	0.1102(10)	0.0802(5)	0.2173(22)	$O_{1.00}$	0.0084(28)
O(2)	0.1232(10)	0.1725(4)	0.6997(22)	$O_{1.00}$	0.0084(30)
O(3)	0.1389(14)	0	0.7155(33)	$O_{1.00}$	0.0109(42)
O(4)	0.4072(9)	0.2450(4)	0.7962(25)	$O_{1.00}$	0.0109(33)
O(5)	0.3421(14)	0.1334(5)	0.0737(2)	$O_{1.00}$	0.0109(30)
O(6)	0.3373(13)	0.1241(5)	0.5307(18)	$O_{1.00}$	0.0084(29)
O(7)	0.3416(13)	0	0.2673(30)	$O_{1.00}$	0.0109(40)

Table 3.2.3
Selected distances (in Å) for M and T sites in amosite.

M(1)	- O1 x2	2.013(12)	M(2)	- O4 x2	1.873(9)	M(3)	- O1 x4	2.030(10)
	- O2 x2	2.109(9)		- O2 x2	2.177(12)		- O3 x2	2.211(18)
	- O3 x2	2.242(10)		- O1 x2	2.290(11)			
	average	2.121		average	2.193		average	2.090
M(4)	- O4 x2	1.965(13)	T(1)	- O5	1.587(13)	T(2)	- O6	1.606(12)
	- O2 x2	2.038(9)		- O1	1.596(11)		- O5	1.684(13)
	- O6 x2	2.772(10)		- O7	1.623(9)		- O4	1.704(9)
	average	2.258		- O6	1.611(11)		- O2	1.717(11)
				average	1.604		average	1.677

The obtained structure of amosite is similar to the only available structure of grunerite present in literature (Finger, 1969) and in perfect agreement with the chemical data from EPMA analysis (Table 3.1.7).

Table 3.2.4
Final atomic coordinates, occupancies and atomic displacement parameters (Å^2) for crocidolite.

site	*x*	*y*	*z*	occupancy	U_{iso}[1]
Am	-0.086(1)	½	-0.221(4)	$Na_{0.18}$	0.01967
M(1)	0	0.0921(5)	½	$Fe_{0.60}Mg_{0.25}$	0.01109
M(2)	0	0.18108(9)	0	$Fe_{1.00}$	0.01109
M(3)	0	0	0	$Fe_{1.00}$	0.01109
M(4)	0	0.2744(3)	½	$Na_{0.83}$	0.01967
T(1)	0.2814(2)	0.0866(1)	0.2922(4)	$Si_{1.00}$	0.02245
T(2)	0.2849(3)	0.1719(1)	0.7966(5)	$Si_{1.00}$	0. 02245
O(1)	0.1126(4)	0.0935(3)	0.2244(8)	$O_{1.00}$	0.01695
O(2)	0.1144(4)	0.1670(2)	0.7237(8)	$O_{1.00}$	0.01695
O(3)	0.1112(6)	0	0.681(1)	$O_{1.00}$	0.01695
O(4)	0.3607(5)	0.2490(2)	0.7900(8)	$O_{1.00}$	0.01695
O(5)	0.3464(5)	0.1322(2)	0.0770(7)	$O_{1.00}$	0.01695
O(6)	0.3326(5)	0.1243(3)	0.5760(7)	$O_{1.00}$	0.01695
O(7)	0.3191(6)	0	0.297(1)	$O_{1.00}$	0.01695

[1]Fixed to the values reported in Gualtieri *et al.* (2013).

Table 3.2.5
Selected distances (in Å) for M and T sites in crocidolite.

M(1)	- O1 x2	2.026(4)	M(2)	- O4 x2	1.992(4)	M(3)	- O1 x4	2.205(4)
	- O2 x2	1.976(4)		- O2 x2	2.058(4)		- O3 x2	2.217(7)
	- O3 x2	2.093(4)		- O1 x2	2.125(4)			
	average	2.031		average	2.058		average	2.209
M(4)	- O4 x2	2.320(5)	T(1)	- O5	1.6522(33)	T(2)	- O6	1.6095(32)
	- O2 x2	2.407(5)		- O1	1.6036(34)		- O5	1.638(4)
	- O6 x2	2.544(5)		- O7	1.6033(22)		- O4	1.5780(34)
	- O5 x2	2.930(5)		- O6	1.6269(33)		- O2	1.6164(35)
	average	2.550		average	1.622		average	1.610

The only available structure in literature is that of fluoro-riebeckite of Hawthorne (1978), that is quite similar to our structure, with the exception of the coordinates of the Am site. Also in this case, cationic sites occupancies are in agreement with the chemical data from EPMA analysis (Table 3.1.7).

Table 3.2.6
Final atomic coordinates, occupancies and atomic displacement parameters (Å^2) for erionite.

site	*x*	*y*	*z*	occupancy	U_{iso}
T1	0.99364(7)	0.22974 (6)	0.10581(6)	$Si_{0.81}Al_{0.19}$	0.01140(25)
T2	0.08850(2)	0.41671(4)	¼	$Si_{0.70Al0.30}$	0.01051(51)
O1	0.03422(19)	0.35966(15)	0.14993(12)	$O_{1.00}$	0.0229(10)
O2	0.10064(14)	2*x*	0.11973(26)	$O_{1.00}$	0.0274(17)
O3	0.12601(14)	2*x*	0.64899(16)	$O_{1.00}$	0.0274(14)
O4	0.26631(24)	0	0	$O_{1.00}$	0.0272(11)
O5	0.23310(23)	2*x*	¼	$O_{1.00}$	0.0224(19)
O6	0.08366(43)	$\overline{x}$	¼	$O_{1.00}$	0.0229(19)
K	0	0	¼	$O_{1.00}$	0.0379(11)
Na1	⅓	⅔	0.108(14)	$Na_{0.33(1)}$	0.0851(81)
Na2	⅓	⅔	0.888(14)	$Na_{0.32(1)}$	0.0906(77)
Na4	½	0	0	$Na_{0.26(1)}$	0.0957(75)
NaW1	0.28267(76)	2*x*	0.0855(13)	$Na_{0.19(1)}$	0.1094(90)
W2	0.24996(27)	2*x*	0.69974(46)	$O_{0.68(1)}$	0.1092(30)
W2b	0.26885(67)	2*x*	0.5319(12)	$O_{0.30(1)}$	0.1101(79)
W3	0.43326(46)	2*x*	0.83401(60)	$O_{0.51(1)}$	0.1106(55)
W3b	0.44668(82)	2*x*	0.9317(10)	$O_{0.37(1)}$	0.1106(80)
W3c	0.43370(47)	2*x*	0.01067(70)	$O_{0.57(1)}$	0.1093(42)

Table 3.2.7
Selected distances (in Å) for M and T sites in erionite (Non occurring distances are in *italics*).

K1	- O2 x6	3.0266(35)	Na4	- *W3c x2*	*1.527(11)*	T1	- O3	1.6236(13)
				- *W3b x2*	*1.596(17)*		- O2	1.6489(14)
Na1	- W2b x6	2.572(25)		- W3 x2	2.930(9)		- O4	1.6554(12)
				- O4 x2	3.089(3)		- O1	1.6607(21)
Na2	- *W2b x3*	*1.902(21)*		- O1 x4	3.096(2)		average	1.6471
	- W2 x3	2.327(14)						
	- W3 x3	2.431(13)	NaW1	- *Na1*	*1.208(19)*	T2	- O1 x2	1.6776(18)
	- W3b x3	2.676(19)		- *W2b*	*1.796(26)*		- O5	1.6827(23)
	- W3c x3	2.944(17)		- *NaW1 x2*	*2.009(30)*		- O6	1.6870(21)
				- W3c x2	2.287(14)		average	1.6812
				- O5	2.725(19)			
				- W2b x2	2.892(23)			
				- *Na2*	*3.185(14)*			
				- O1 x2	3.193(14)			

With respect to the literature data, the obtained structure of our erionite sample is similar to that of Ca-erionite reported in Gualtieri *et al.* (1998).

The obtained cell parameters of erionite have been also compared with those of other erionite samples (of different origin) from the literature; results are listed in Table 3.2.8 and plotted in Fig. 3.2.5.

Table 3.2.8
Unit cell parameters of erionite samples from literature.

a (Å)	c (Å)	Cell volume (Å^3)	Reference
13.220	15.062	2280	This work
13.310	15.070	2312	Passaglia *et al.* (1998)
13.320	15.186	2333	Passaglia *et al.* (1998)
13.333	15.091	2323	Passaglia *et al.* (1998)
13.339	15.112	2328	Passaglia *et al.* (1998)
13.289	15.079	2306	Passaglia *et al.* (1998)
13.336	15.084	2323	Passaglia *et al.* (1998)
13.338	15.126	2330	Passaglia *et al.* (1998)
13.321	15.194	2334	Passaglia *et al.* (1998)
13.330	15.174	2335	Passaglia *et al.* (1998)
13.344	15.128	2332	Passaglia *et al.* (1998)
13.331	15.220	2342	Passaglia *et al.* (1998)
13.264	15.067	2295	Passaglia *et al.* (1998)
13.304	15.078	2311	Passaglia *et al.* (1998)
13.345	15.124	2332	Passaglia *et al.* (1998)
13.316	15.095	2317	Passaglia *et al.* (1998)
13.277	15.124	2308	Passaglia *et al.* (1998)
13.340	15.110	2328	Passaglia *et al.* (1998)
13.311	15.067	2311	Passaglia *et al.* (1998)
13.227	15.075	2284	Passaglia *et al.* (1998)
13.338	15.100	2326	Passaglia *et al.* (1998)
13.290	15.132	2314	Passaglia *et al.* (1998)
13.312	15.162	2326	Passaglia *et al.* (1998)
13.233	15.055	2283	Passaglia *et al.* (1998)
13.289	15.079	2306	Gualtieri *et al.* (1998)
13.339	15.112	2329	Gualtieri *et al.* (1998)
13.264	15.067	2296	Gualtieri *et al.* (1998)
13.304	15.078	2311	Gualtieri *et al.* (1998)
13.311	15.095	2316	Alberti *et al.* (1997)
13.228	15.069	2284	Ballirano *et al.* (2009)
13.150	15.020	2249	Kawahara and Curien (1969)
13.252	14.810	2252	Schlenker *et al.* (1977)
13.270	15.050	2295	Gard and Tait (1973)

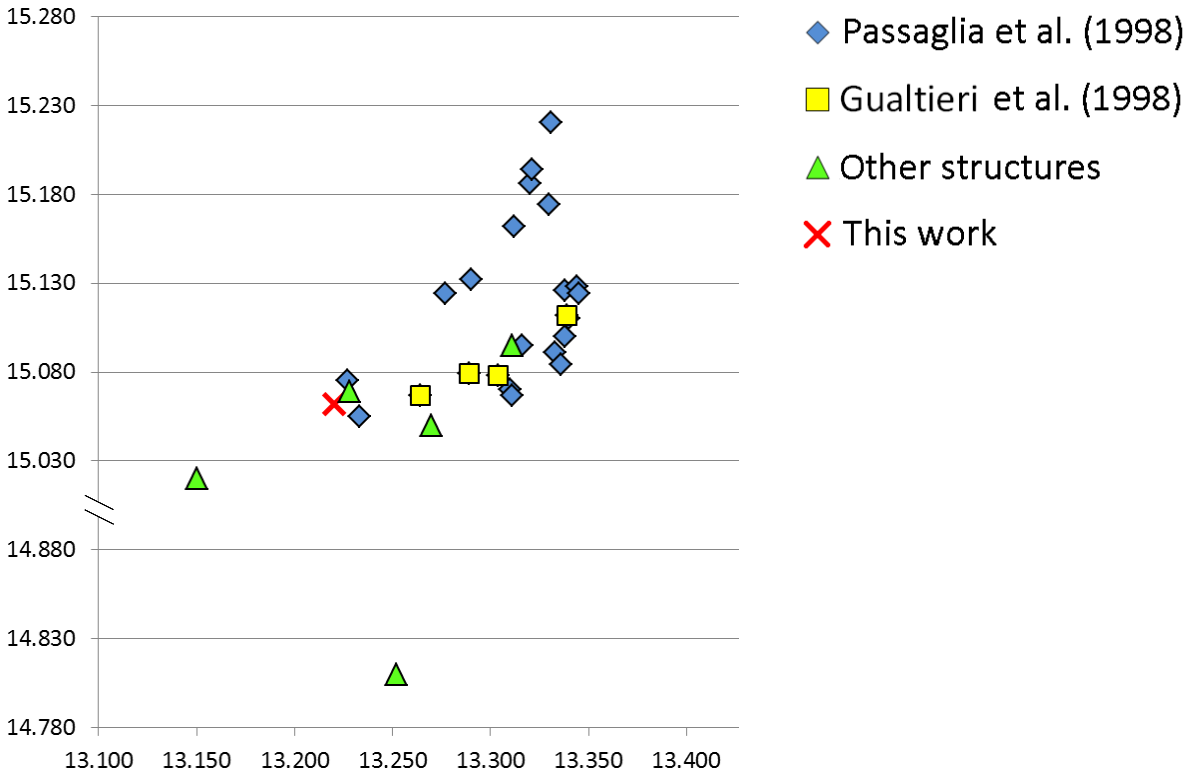

Fig. 3.2.5 Unit cell parameters of erionite samples listed in table 3.2.8; green triangles refer to the last 5 samples at the bottom of table 3.2.8.

3.2.2 XAS experiments at BM08 – ESRF

The conducted experiment allowed to obtain high-resolution XAS spectra at the Fe K-edge, reported in Fig. 3.2.6.

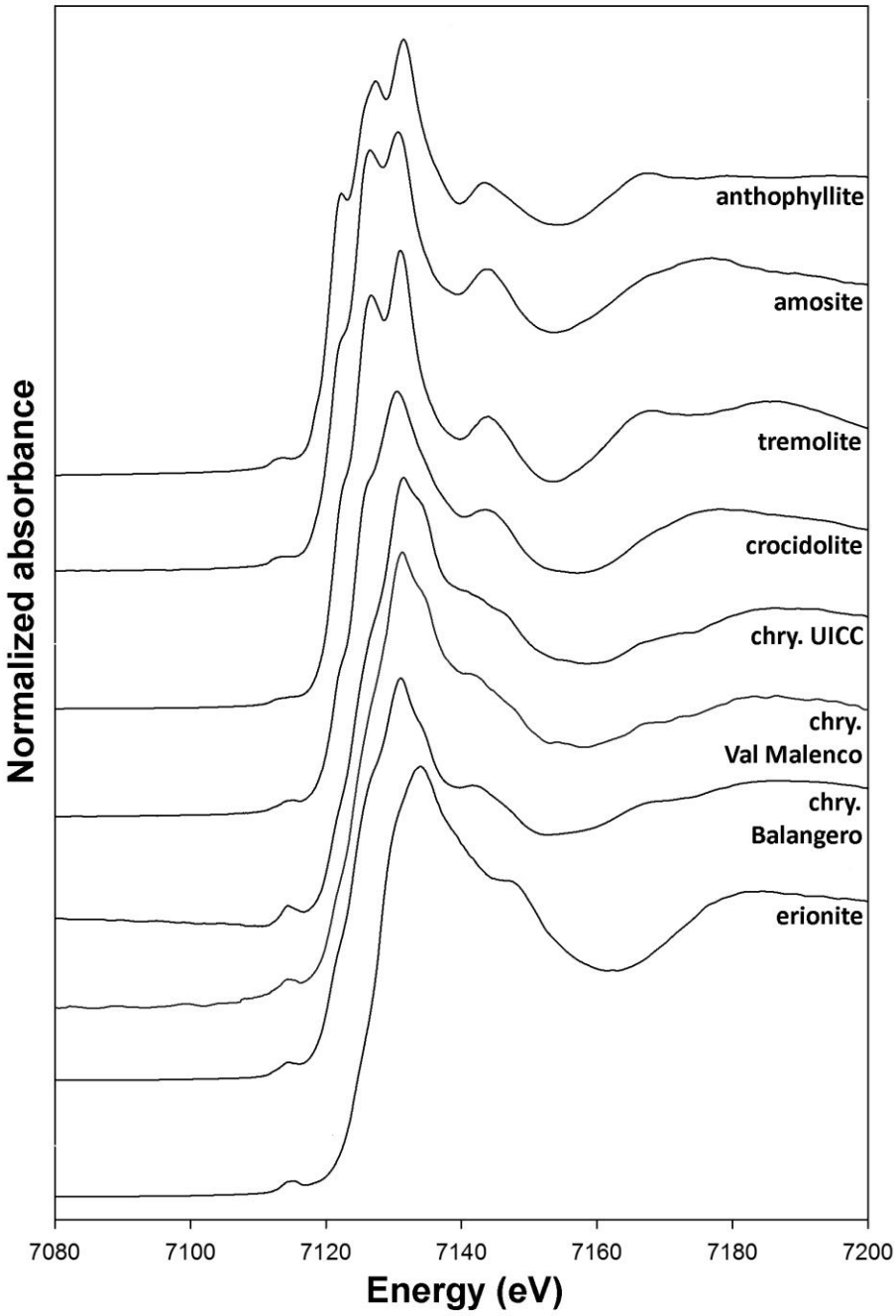

Fig. 3.2.6. Fe K-edge XANES spectra of investigated samples.

Regarding the XANES analysis (following the procedure described in paragraph 2.4.4.1), the deconvolution of the pre-edge peaks has been carried out, and the results are shown in Fig. 3.2.7 and listed in Table 3.2.9.

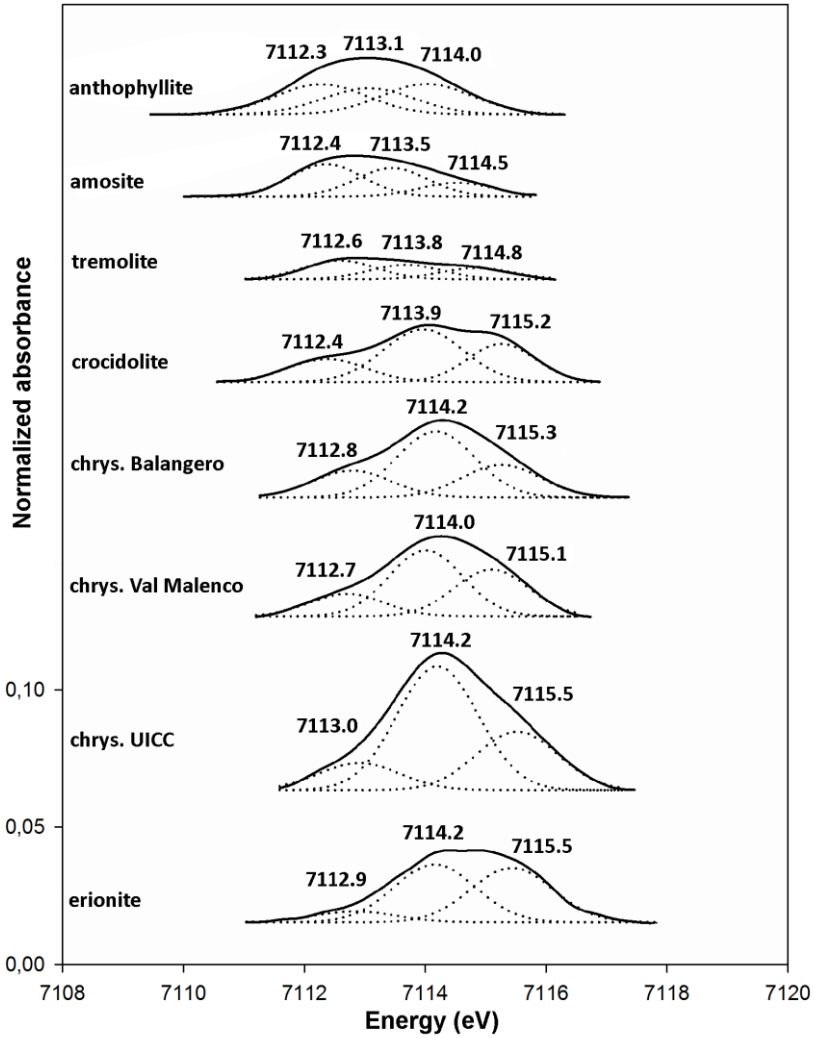

Fig. 3.2.7. Fit of the pre-edge peaks of investigated samples.

Table 3.2.9
XANES pre-edge parameters of investigated samples

Sample	Component position (eV)	Component area	Total area	r^2	Centroid position (eV)
Anthophyllite	7112,44	0.026	0.054 (5)	0.9997	7113.13 (3)
	7113,77	0.028			
Amosite	7112,57	0,025	0.045 (5)	0.9997	7113.17 (4)
	7113,92	0,018			
	7115,50	0,002			
Tremolite	7112,44	0.008	0.032 (8)	0.9996	7113.56 (9)
	7113,48	0.016			
	7114,87	0.008			
Crocidolite	7112,38	0.011	0.055 (7)	0.9997	7114,05 (5)
	7113,96	0.026			
	7115,26	0.017			
Chrysotile Balangero	7112,69	0.016	0.074 (7)	0.9993	7114,04 (9)
	7114,32	0.055			
	7115,61	0.004			
Chrysotile Val Malenco	7112,50	0,009	0.072 (5)	0.9993	7114,13 (5)
	7114,21	0,055			
	7115,46	0,008			
Chrysotile UICC	7112,75	0,011	0.129 (8)	0.9998	7114.42 (5)
	7114,17	0,081			
	7115,52	0,037			
Erionite	7112,35	0,001	0.076 (2)	0.9994	7114.65 (3)
	7114,31	0,051			
	7115,51	0,024			

Regarding the EXAFS analysis (following the procedure described in paragraph 2.4.4.1), after data reduction, fit in the range 0.90 – 2.15 Å (first coordination shell of iron) have been performed, and the results are shown in Fig. 3.2.8 and 3.2.9 and listed in Table 3.2.10.

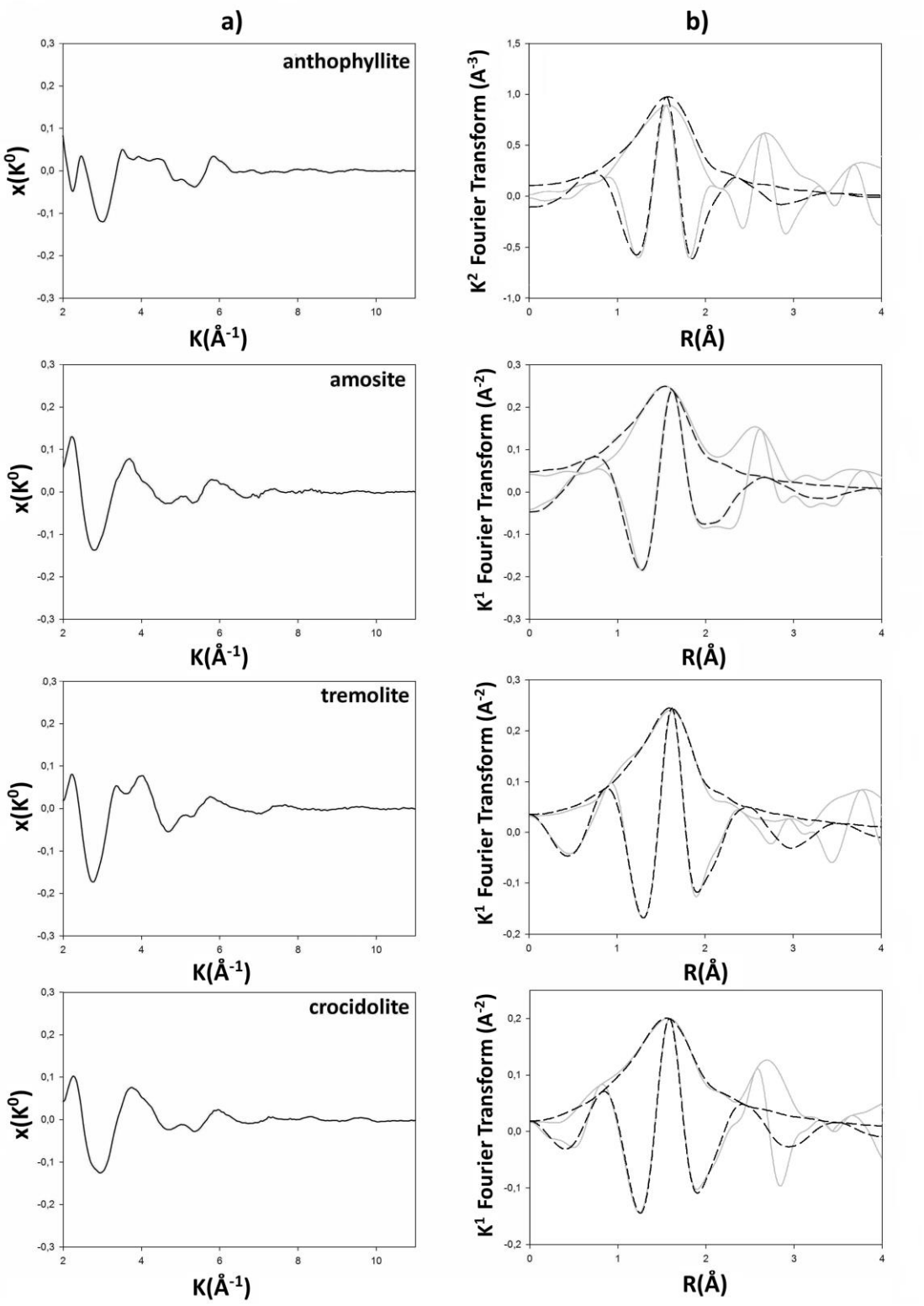

Fig. 3.2.8. Results of the fit of the EXAFS spectra: (a) χ(k0) experimental data; (b) k1,2 Fourier transformed experimental (gray solid line) and fitted (black medium dash) data of amphiboles samples, both supplied with the real part.

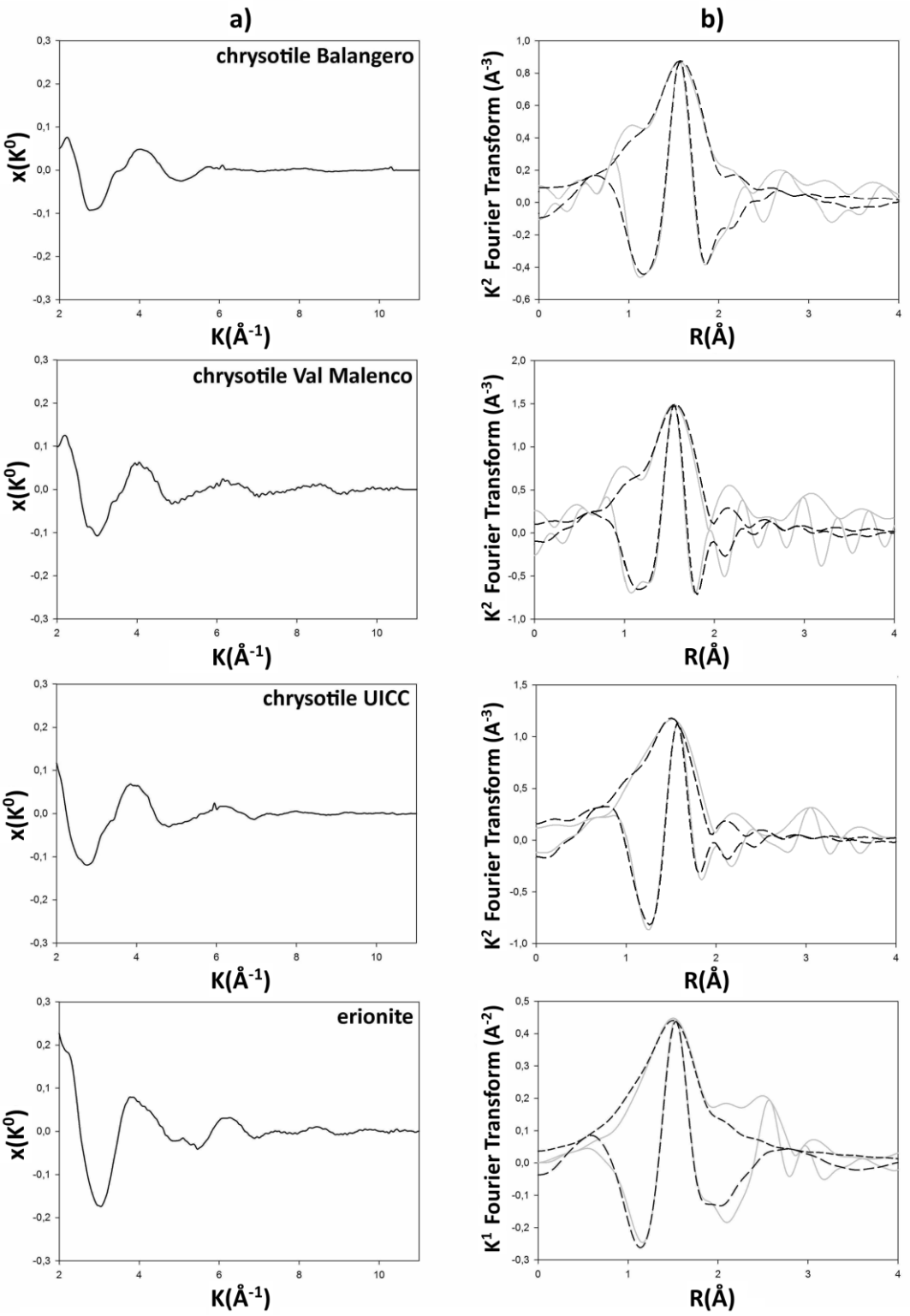

Fig. 3.2.9. Results of the fit of the EXAFS spectra: (a) χ(k0) experimental data; (b) k1,2 Fourier transformed experimental (gray solid line) and fitted (black medium dash) data of chrysotiles and erionite samples, both supplied with the real part.

Table 3.2.10
Crystallographic data and structural parameters as obtained from the *R*-space fit by using the theoretical references.

Shells	%	Ref.[a]	N	*R*(Å)	S_0^2	R-factor	σ^2(Å^2)	ΔE_0(eV)
anthophyllite					0.73[b]	0.054	0.012 (5)	7 (3)
Fe – O_1			3	2.07 (3)				
Fe – O_2			3	2.08 (3)				
amosite					0.73[b]	0.017	0.011 (2)	1 (3)
Fe – O_1			6	2.083 (4)				
tremolite					0.73[b]	0.004	0.007 (0)	2 (1)
Fe – O_1			6	2.093 (4)				
crocidolite					0.73[b]	0.004	0.011 (1)	2 (2)
Fe – O_1			6	2.059 (8)				
chry. Balangero					0.73[b]	0.013	0.011 (3)	3 (1)
Site1 - Fe – O_1	0.2[c]		4	1.770 (5)				
Site2 - Fe – O_1	0.8[c]		6	2.054 (4)				
chry. Val Malenco					0.73[b]	0.034	0.003 (4)	3 (3)
Site1 - Fe – O_1	0.2[c]		4	1.81 (3)				
Site2 - Fe – O_1	0.8[c]		6	2.033 (3)				
chry. UICC					0.73[b]	0.012	0.003 (3)	3 (2)
Site1 - Fe – O_1	0.3[c]		4	1.86 (2)				
Site2 - Fe – O_1	0.7[c]		6	2.028 (6)				
erionite					0.74 (9)	0.005	0.006 (3)	5 (1)
Fe – O_1			6	2.011 (8)				

[a]References are not reported because structural models have been modified from the original (number of oxygens, number of coordination spheres).
[b]Kept fixed throughout the refinement because of the low values assumed when left free; this value was determined based on results from the refinements of the standards.
[c]Kept fixed in the refinement to the values from the Fe^{57} Mössbauer analysis.

3.2.3 XRPD experiments at MCX beamline – ELETTRA

The conducted experiment allowed to obtain high-resolution XRPD pattern, both at 7 and 10 keV for each of the investigated samples (chrysotiles and erionite). In Fig. 3.2.10 is reported the example of the two pattern collected on chrysotile UICC.

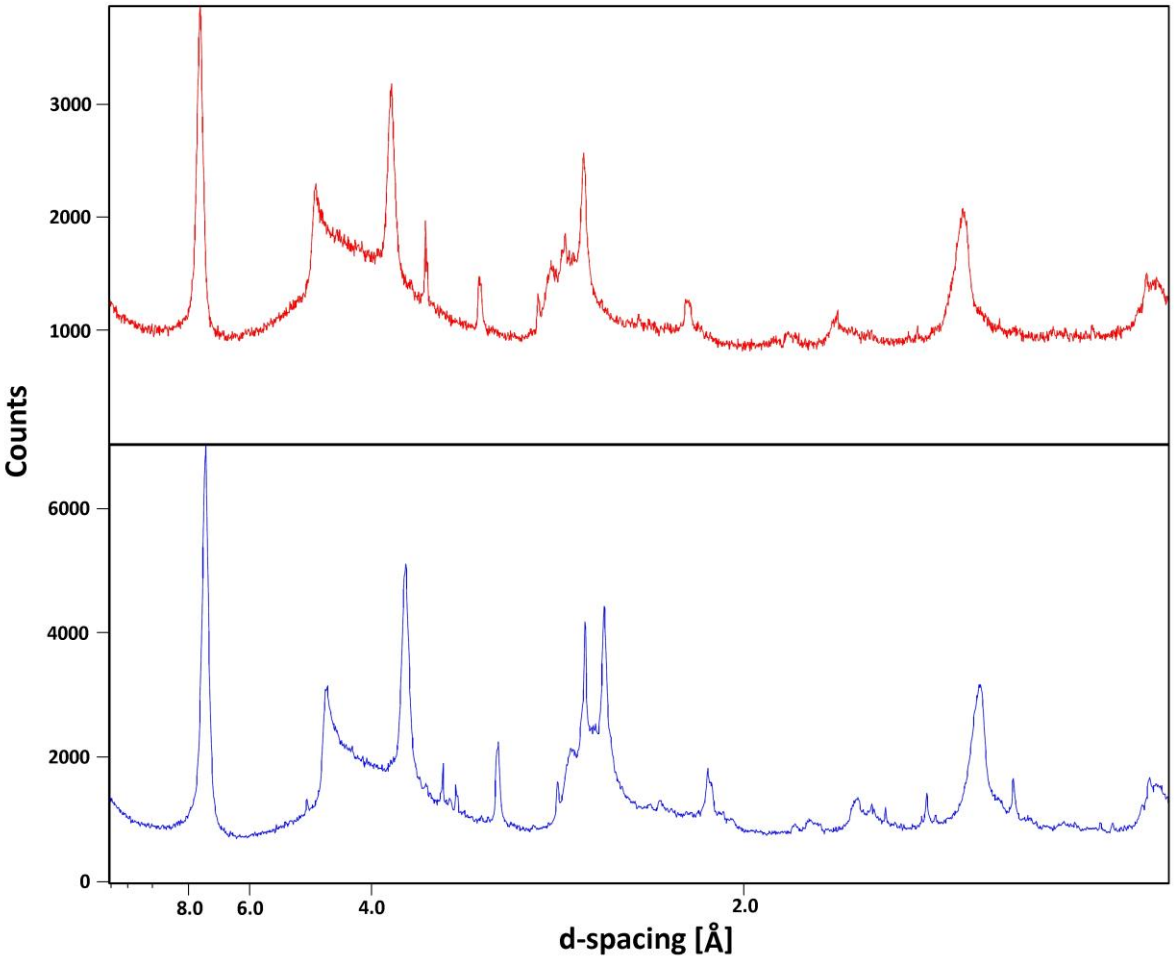

Fig. 3.2.10. XRPD pattern of chrysotile UICC collected at 7 keV (top) and at 10 Kev (bottom).

On this data, structural refinements have been performed (in Figs. 3.2.11, 3.2.12) allowing to obtain unit cell parameters, thermal parameters, spatial group and anion-cation distances. These data are listed in the following Tables (3.2.11 – 3.2.17); for the refinements, the structural model of Falini *et al*. 2004 was used. These results are the product of the combined refinement of data at 7 and 10 keV.

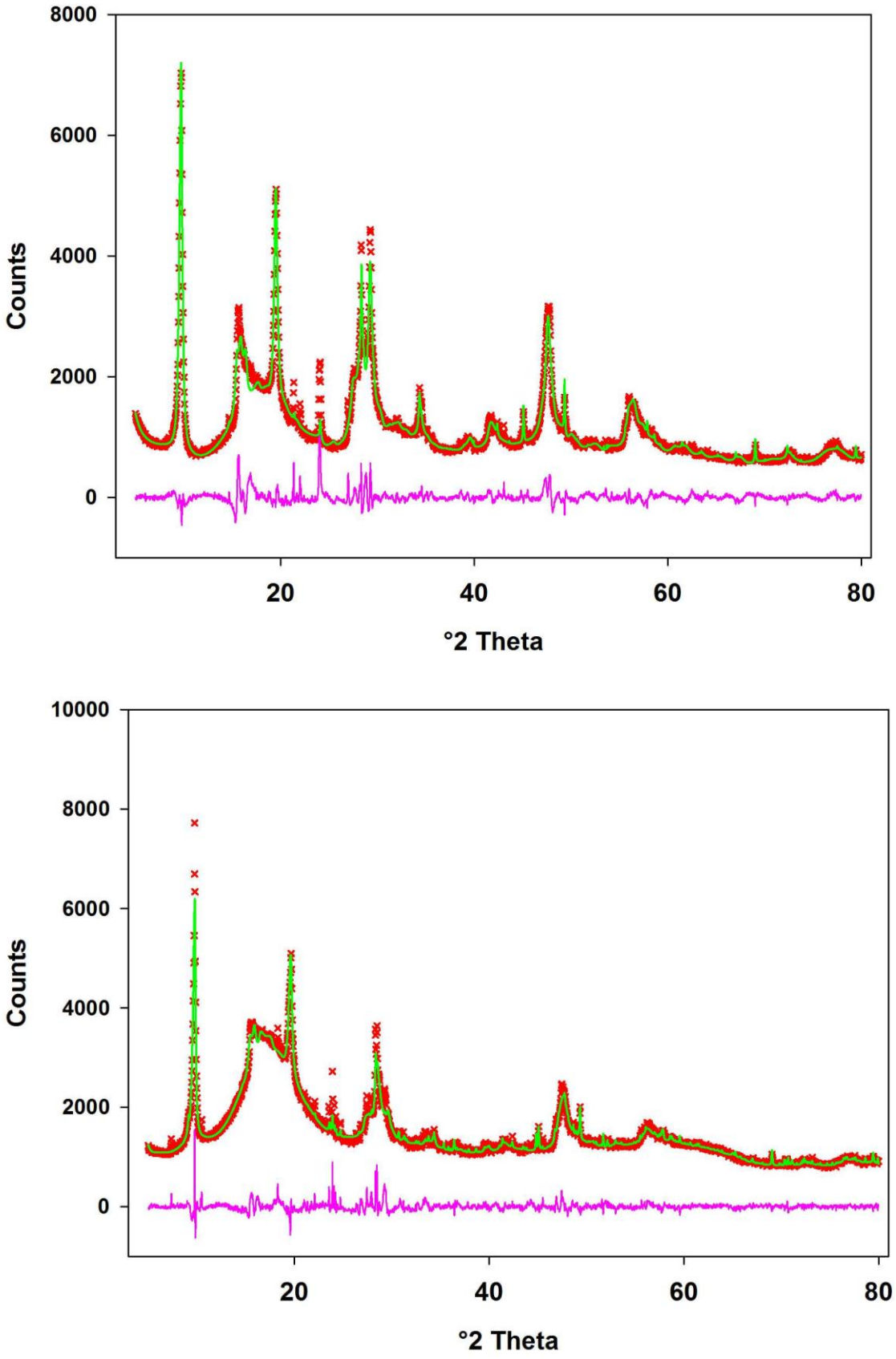

Fig. 3.2.11 Rietveld refinements (made with Topas) of data collected at 10keV of chrysotile UICC (top) and chrysotile Balangero (bottom). Observed (crosses), calculated (continuous line), and difference (bottom line) curves are reported.

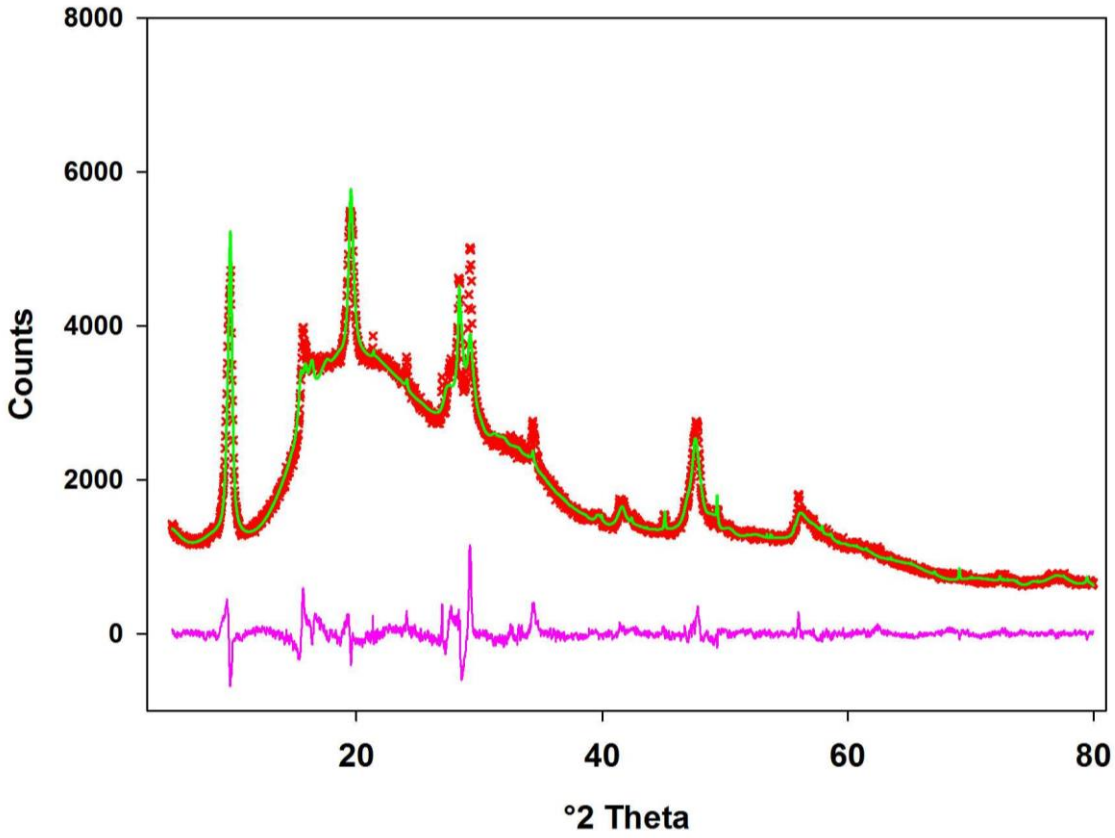

Fig. 3.2.12 Rietveld refinement (made with Topas) of data collected at 10keV of chrysotile Val Malenco. Observed (crosses), calculated (continuous line), and difference (bottom line) curves are reported.

Table 3.2.11
Unit cell parameters and agreement factors of the refinement for chrysotile UICC, Balangero and Val Malenco.

	UICC		Balangero		Val Malenco	
a (Å)	5.354 (3)	R_{wp} 5.805 %	5.394 (3)	R_{wp} 3.880 %	5.348 (3)	R_{wp} 4.220 %
b (Å)	9.155 (6)	R_p 3.994 %	9.204 (5)	R_p 2.722 %	9.23 (1)	R_p 2.946 %
c (Å)	14.735 (5)	χ^2 2.001	14.553 (3)	χ^2 1.766	14.717 (7)	χ^2 2.107
β (°)	93.60 (4)		94.10 (8)		93.96 (6)	
sp. gr.	*Cc*		*Cc*		*Cc*	

Table 3.2.12
Final atomic coordinates, occupancies and atomic displacement parameters (Å^2) for chrysotile UICC.

site	*x*	*y*	*z*	occupancy	U_{iso}
M(1)	0.9237(16)	0.13699(83)	0.24947(64)	$Mg_{0.96}Fe_{0.04}$	0.0038(37)
M(2)	0.4100(20)	0.29534(99)	0.24564(75)	$Mg_{0.96}Fe_{0.04}$	0.0038(37)
M(3)	0.8992(15)	0.45047(77)	0.21374(57)	$Mg_{0.96}Fe_{0.04}$	0.0038(37)
T(1)	0.0433(10)	0.30156(58)	0.04850(35)	$Si_{1.00}$	0.0063(36)
T(2)	0.52246(96)	0.47400(58)	0.04615(35)	$Si_{1.00}$	0.0063(36)
O(1)	0.0406(17)	0.13852(87)	0.00278(48)	$O_{1.00}$	0.0076(36)
O(2)	0.25835(85)	0.40178(86)	0.00294(48)	$O_{1.00}$	0.0076(36)
O(3)	0.77057(91)	0.37946(99)	0.02314(55)	$O_{1.00}$	0.0076(36)
O(4)	0.0999(14)	0.27988(82)	0.15867(37)	$O_{1.00}$	0.0076(36)
O(5)	0.5105(13)	0.47545(88)	0.15796(33)	$O_{1.00}$	0.0076(36)
OH(1)	0.7586(23)	0.3127(15)	0.3155(12)	$OH_{1.00}$	0.0076(36)
OH(2)	0.2857(18)	0.1062(14)	0.30993(63)	$OH_{1.00}$	0.0076(36)
OH(3)	0.5725(22)	0.1241(16)	0.17598(59)	$OH_{1.00}$	0.0076(36)
OH(4)	0.2260(22)	0.4564(15)	0.29770(85)	$OH_{1.00}$	0.0076(36)

Table 3.2.13
Selected distances (in Å) for octahedral (M) and tetrahedral (T) sites in chrysotile UICC.

M(1)	- O5	2.074(11)	M(2)	- OH4	1.957(17)	M(3)	- OH3	1.940(16)
	- OH2	2.101(13)		- O4	2.038(12)		- OH4	2.079(14)
	- OH1	2.104(17)		- OH1	2.081(17)		- O4	2.088(11)
	- OH4	2.110(16)		- OH3	2.093(17)		- OH2	2.126(14)
	- OH3	2.114(14)		- OH2	2.102(15)		- OH1	2.133(18)
	- O4	2.133(11)		- O5	2.183(12)		- O5	2.201(11)
	average	2.106		average	2.076		average	2.0945
			T(1)	- O1	1.6375(94)	T(2)	- O3	1.6386(85)
				- O4	1.6453(74)		- O1	1.6416(95)
				- O3	1.6468(80)		- O2	1.6520(75)
				- O2	1.6479(83)		- O5	1.6534(72)
				average	1.6444		average	1.6464

Table 3.2.14
Final atomic coordinates, occupancies and atomic displacement parameters (Å^2) for chrysotile Balangero.

site	*x*	*y*	*z*	occupancy	U_{iso}
M(1)	0.9156(16)	0.14156(84)	0.24723(65)	$Mg_{0.96}Fe_{0.04}$	0.0138(42)
M(2)	0.4234(15)	0.30777(92)	0.24954(64)	$Mg_{0.96}Fe_{0.04}$	0.0138(42)
M(3)	0.8895(14)	0.45246(74)	0.21113(57)	$Mg_{0.96}Fe_{0.04}$	0.0138(42)
T(1)	0.0470(11)	0.27915(57)	0.04666(35)	$Si_{1.00}$	0.0189(57)
T(2)	0.52933(99)	0.45194(57)	0.04630(35)	$Si_{1.00}$	0.0189(57)
O(1)	0.0174(25)	0.11419(72)	0.00009(51)	$O_{1.00}$	0.0214(48)
O(2)	0.2894(12)	0.3555(12)	0.00366(45)	$O_{1.00}$	0.0214(48)
O(3)	0.7863(13)	0.3680(14)	0.02203(57)	$O_{1.00}$	0.0214(48)
O(4)	0.1025(12)	0.27568(79)	0.15933(43)	$O_{1.00}$	0.0214(48)
O(5)	0.5062(14)	0.4718(10)	0.15749(39)	$O_{1.00}$	0.0214(48)
OH(1)	0.7705(24)	0.3192(15)	0.3228(12)	$OH_{1.00}$	0.0214(48)
OH(2)	0.2753(18)	0.1150(13)	0.30328(68)	$OH_{1.00}$	0.0214(48)
OH(3)	0.5727(18)	0.1406(13)	0.17099(61)	$OH_{1.00}$	0.0214(48)
OH(4)	0.2099(22)	0.4752(14)	0.30110(85)	$OH_{1.00}$	0.0214(48)

Table 3.2.15
Selected distances (in Å) for octahedral (M) and tetrahedral (T) sites in chrysotile Balangero.

M(1)	- OH2	2.065(13)	M(2)	- O5	2.088(12)	M(3)	- OH3	2.098(14)
	- OH4	2.077(15)		- OH1	2.090(16)		- OH4	2.103(14)
	- OH3	2.088(13)		- OH4	2.095(15)		- OH2	2.129(14)
	- O4	2.088(11)		- OH3	2.110(14)		- O4	2.159(10)
	- O5	2.116(12)		- O4	2.117(11)		- O5	2.164(10)
	- OH1	2.149(18)		- OH2	2.118(15)		- OH1	2.169(18)
	average	2.097		average	2.103		average	2.137
			T(1)	- O3	1.644(11)	T(2)	- O1	1.6372(85)
				- O4	1.6460(79)		- O5	1.6420(77)
				- O2	1.6470(96)		- O3	1.647(10)
				- O1	1.6657(86)		- O2	1.6529(94)
				average	1.651		average	1.645

Table 3.2.16
Final atomic coordinates, occupancies and atomic displacement parameters (Å^2) for chrysotile Val Malenco.

site	*x*	*y*	*z*	occupancy	U_{iso}
M(1)	0.9167(20)	0.1390(11)	0.24702(83)	$Mg_{0.96}Fe_{0.04}$	0.0048(56)
M(2)	0.3919(25)	0.3039(12)	0.24975(91)	$Mg_{0.96}Fe_{0.04}$	0.0048(56)
M(3)	0.8849(19)	0.45094(96)	0.20887(74)	$Mg_{0.96}Fe_{0.04}$	0.0048(56)
T(1)	0.0356(14)	0.28513(72)	0.04490(44)	$Si_{1.00}$	0.0074(74)
T(2)	0.5193(12)	0.46132(71)	0.04441(44)	$Si_{1.00}$	0.0074(74)
O(1)	-0.0190(33)	0.1236(12)	0.00004(69)	$O_{1.00}$	0.0081(56)
O(2)	0.2865(13)	0.3557(12)	0.00383(57)	$O_{1.00}$	0.0081(56)
O(3)	0.7876(14)	0.3877(14)	0.02121(92)	$O_{1.00}$	0.0081(56)
O(4)	0.0869(17)	0.27528(98)	0.15641(58)	$O_{1.00}$	0.0081(56)
O(5)	0.4948(17)	0.4715(14)	0.15565(51)	$O_{1.00}$	0.0081(56)
OH(1)	0.7524(29)	0.3151(19)	0.3102(17)	$OH_{1.00}$	0.0081(56)
OH(2)	0.2818(27)	0.1064(17)	0.30423(82)	$OH_{1.00}$	0.0081(56)
OH(3)	0.5666(22)	0.1412(15)	0.17260(74)	$OH_{1.00}$	0.0081(56)
OH(4)	0.1969(28)	0.4756(15)	0.2996(10)	$OH_{1.00}$	0.0081(56)

Table 3.2.17
Selected distances (in Å) for octahedral (M) and tetrahedral (T) sites in chrysotile Val Malenco.

M(1)	- O4	2.087(15)	M(2)	- OH4	2.061(19)	M(3)	- OH4	2.076(18)
	- OH4	2.094(18)		- OH1	2.069(21)		- OH3	2.094(16)
	- OH2	2.094(17)		- O4	2.075(15)		- OH2	2.108(17)
	- OH1	2.096(22)		- OH2	2.093(19)		- OH1	2.108(24)
	- OH3	2.103(15)		- OH3	2.137(18)		- O4	2.124(13)
	- O5	2.110(16)		- O5	2.173(17)		- O5	2.185(13)
	average	2.0973		average	2.101		average	2.116
			T(1)	- O2	1.644(11)	T(2)	- O2	1.642(12)
				- O3	1.647(12)		- O3	1.645(11)
				- O4	1.648(11)		- O5	1.654(10)
				- O1	1.649(13)		- O2	1.660(11)
				average	1.647		average	1.650

The obtained structures of chrysotile samples are very similar to each other and quite similar to the only available structure of chrysotile present in literature (Falini *et al.*, 2004). The cationic sites occupancies are in general agreement with the chemical compositions from EMPA analysis (Table 3.1.7). It should be remarked that these data are an approximation, since the distortion of the unit cell due to the cylindrical lattice is not considered (stacking disorder, Leoni *et al.* 2004). The peak anisotropic broadening was empirically corrected here by using spherical harmonics at 8 terms and convolution according to the function exp_conv_const = (sh1-1) Tan (Th); in addition, soft constrains were imposed on Mg-O, Si-O and O-O distances, with weight according to the function of Topas penalties_weighting_K1 5 (low weight).

3.2.4 *In situ* µXANES, µXRD and XRF at I18 - DLS

As a first step of the experiment, µXRF maps were collected for all samples treated with MeT5A cell culture, and on selected samples treated with Beas2B cell culture. The resulting maps are shown in Figures 3.2.13 and 3.2.14.

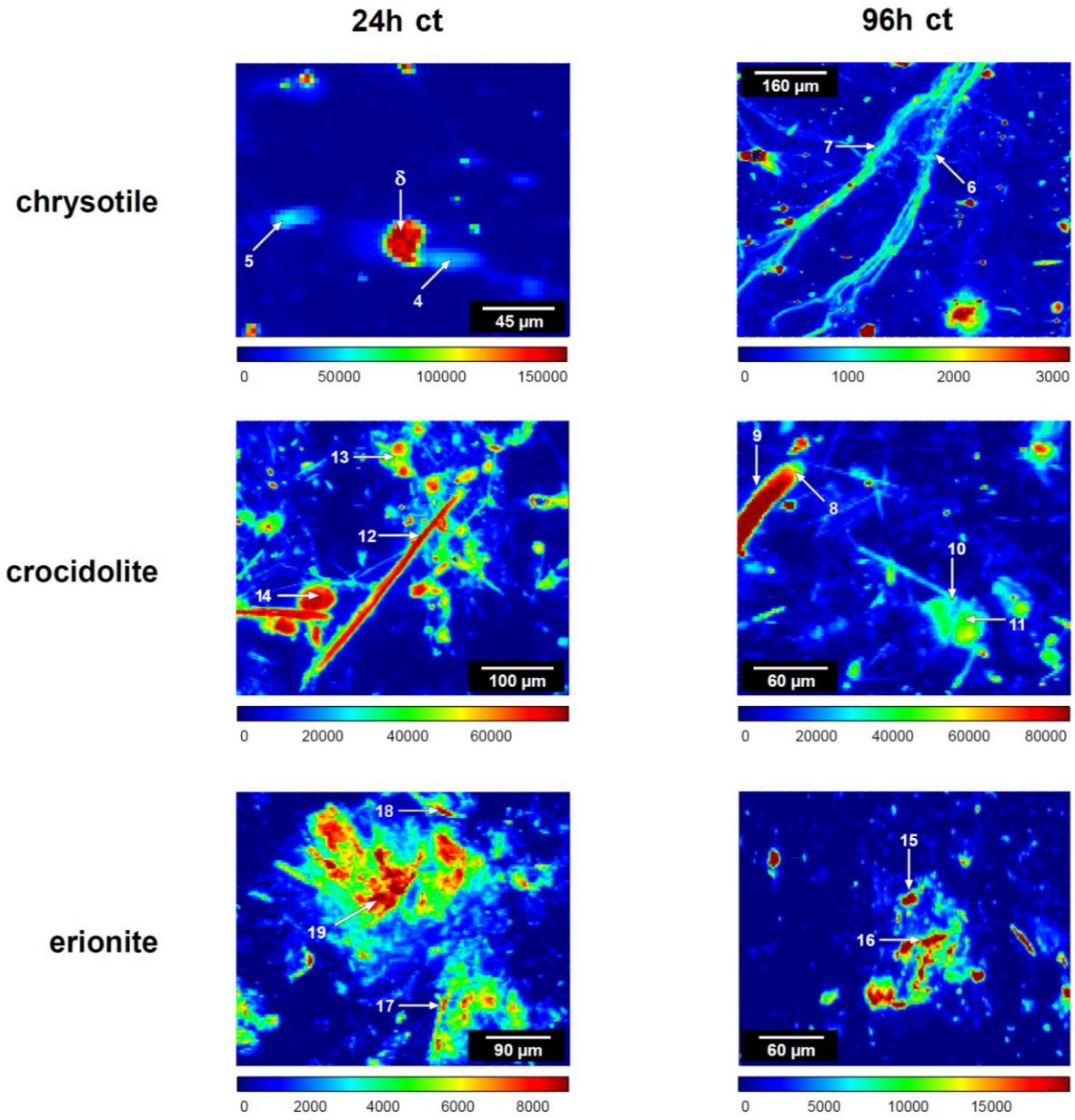

Fig. 3.2.13. µXRF maps of samples after 24 and 96h ct with Met5A cell culture. Arrows indicate the points at which XRD and/or XANES spectra were collected. Maps have variable dimensions (and consequently different scale) depending on the identified objects in the visible light.

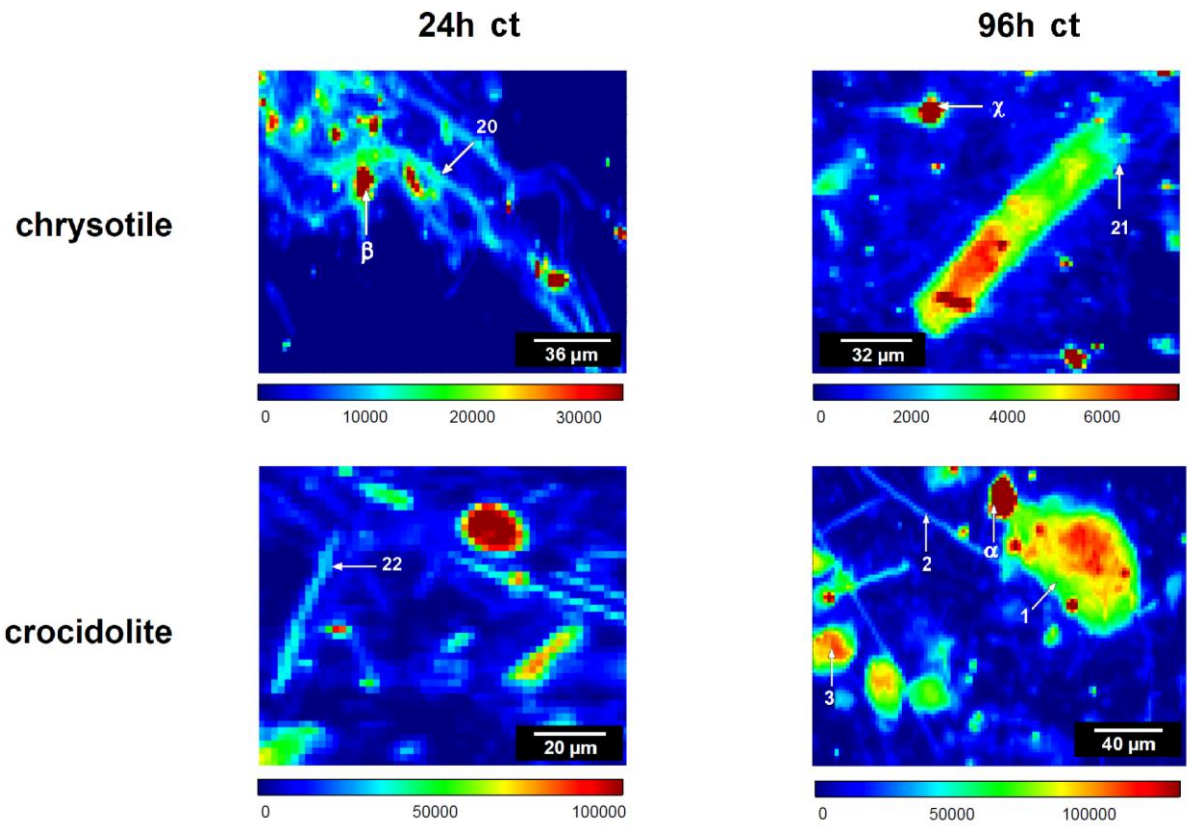

Fig. 3.2.14. µXRF maps of samples after 24 and 96h ct with Beas2B cell culture. Arrows indicate the points at which XRD and/or XANES spectra were collected. Maps have variable dimensions (and consequently different scale) depending on the identified objects in the visible light.

Orienting on the basis of the distribution of iron from the XRF maps, µXRD patterns and Fe K-edge µXANES spectra from individual fibres and aggregates were collected. The results are showed in the figures below.

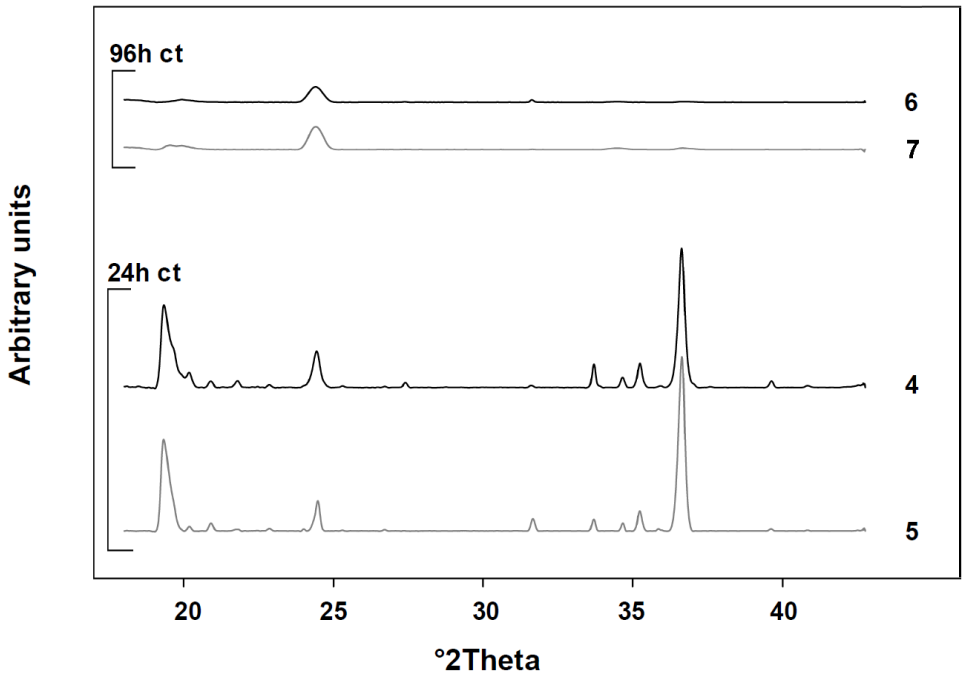

Fig. 3.2.15. Representative XRD spectra of chrysotile after 24 and 96h ct in Met5A; numbers on the side indicate the point at which data collection was taken, as shown in Fig. 3.2.13.

In some spectra of the chrysotile and crocidolite samples, the contribution from magnetite-maghemite particles is visible, with the main reflection (label m in the graphs) at about 35.4 °2θ. It should be remarked that such peak partially overlap with minor peaks which belong to both chrysotile and crocidolite; this contribution is particularly evident in spectra 1, 14 and 20.

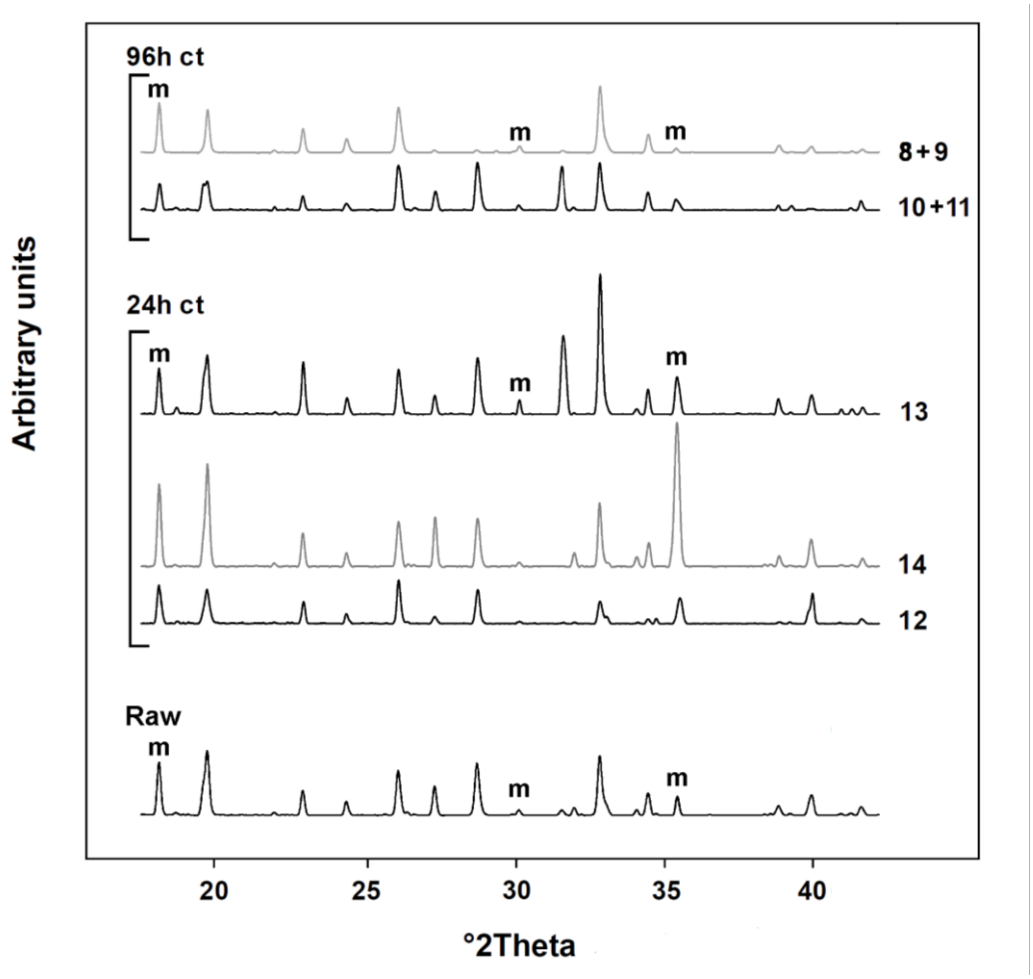

Fig. 3.2.16. XRD spectra of crocidolite after 24 and 96h ct in Met5A; numbers on the side indicate the point at which data collection was taken, as shown in Fig. 3.2.13. (the "+" sign indicates that the two spectra have been summed; m = magnetite reflections).

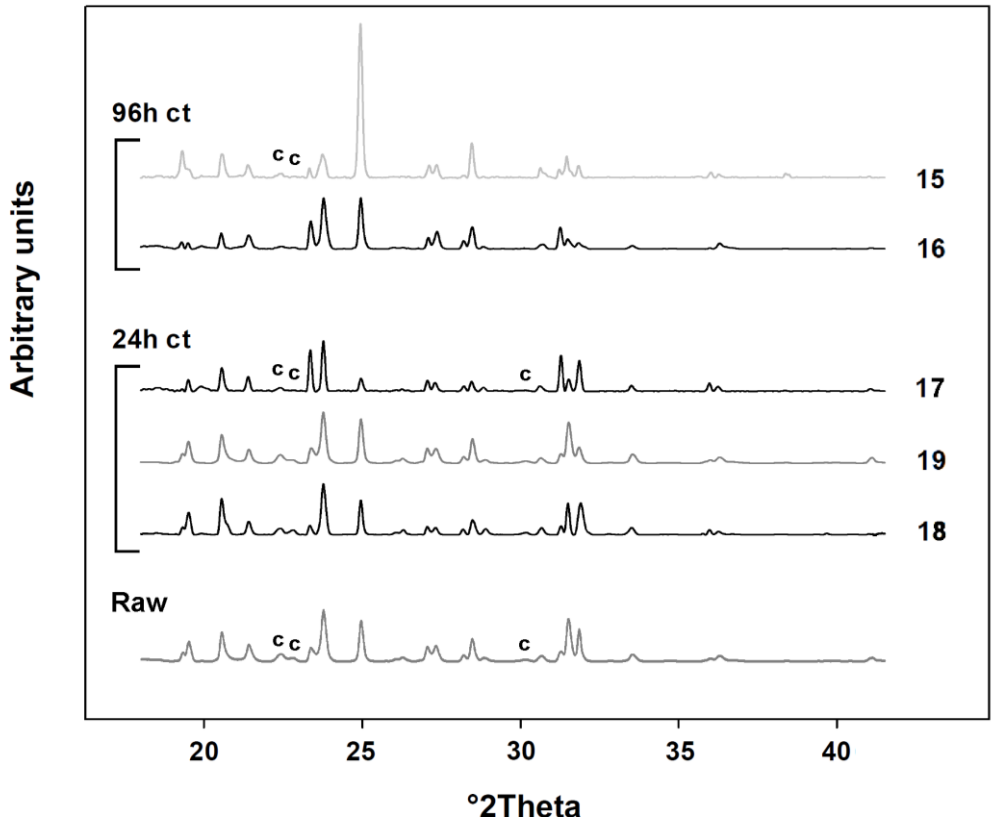

Fig. 3.2.17. XRD spectra of erionite after 24 and 96h ct in Met5A; numbers on the side indicate the point at which data collection was taken, as shown in Fig. 3.2.13. (c = clinoptilolite reflections).

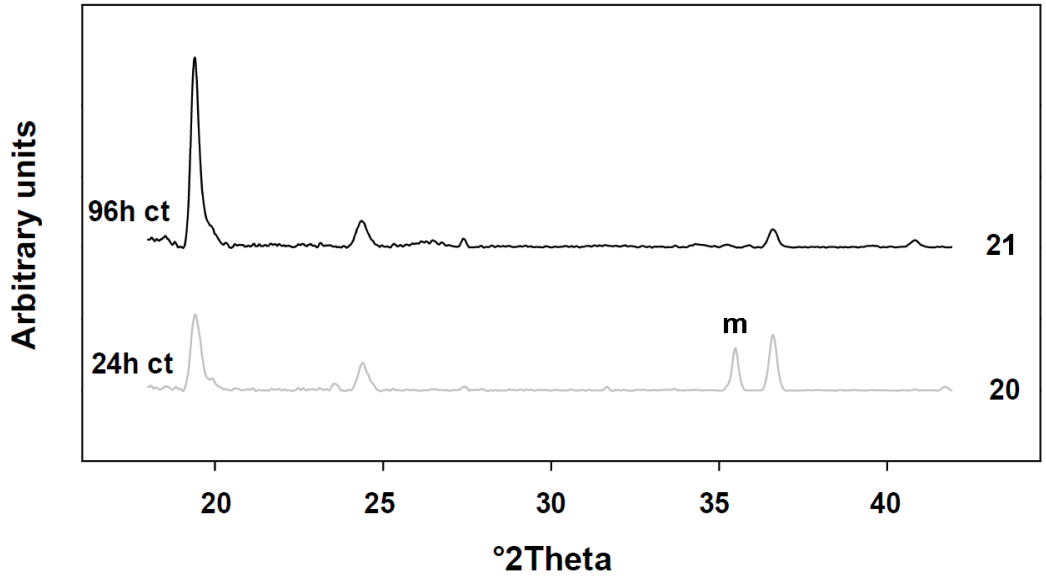

Fig. 3.2.18. Representative XRD spectra of chrysotile after 24 and 96h ct in Beas2B; numbers on the side indicate the point at which it was made the collection, as shown in Fig. 3.2.14 (m = magnetite reflections).

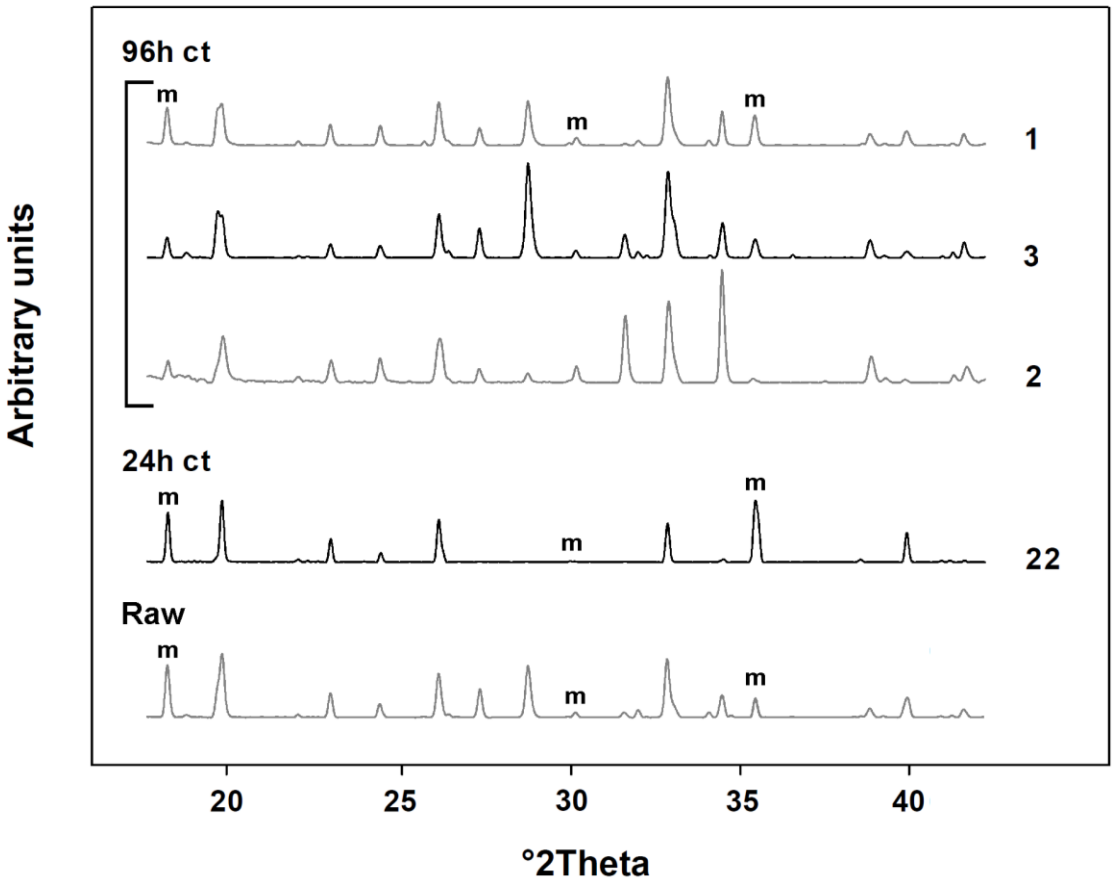

Fig. 3.2.19. Representative XRD spectra of crocidolite after 24 and 96h ct in Beas2B; numbers on the side indicate the point at which it was made the collection, as shown in Fig. 3.2.14 (m = magnetite reflections). Spectra of erionite sample not reported due to their poor quality.

Results obtained from the modelling of the peak profiles are reported in Table 3.2.18; for chrysotile sample, from 24 to 96h *ct* in both cell cultures, the Lx value remarkably increases whereas it slightly increases for erionite and crocidolite samples.

Table 3.2.18

Medium values for Lx profile parameter of samples after 24 and 96h *ct* in cell culture Beas2B and MeT5A.

Sample	Cell culture type	24h *ct*	96h *ct*
Chrysotile UICC	MeT5A	25(6)	51(8)
	BeaS2B	44(8)	68(10)
Crocidolite UICC	MeT5A	10(1)	12(2)
	BeaS2B	6(2)	12(2)
Erionite	MeT5A	6(1)	8(3)
	BeaS2B	-	-

In addition, partial structural refinements were tentatively performed for crocidolite and erionite to get information on possible ion exchange during the dissolution process. Unfortunately, it was not possible to define a clear trend of cation mobilization with *ct* time. Notwithstanding, results for crocidolite sample (listed in Table 3.2.xa) indicate that after 96h *ct* in both cell cultures, Na and Mg in Am and M1 position, respectively, tend to decrease their site population whereas Fe^{2+} in M1 and M3 slightly decreases. Although the results require further confirmation, in erionite, after 96h *ct*, cationic site occupancy indicate Na ion exchange with partial migration (see Table 3.2.19).

Table 3.2.19
Medium values for cationic site occupancies in crocidolite (top) and erionite (bottom).

Treatment	Cell parameters (Å)[a]	Ag. Fct. (%)	Analized Spectra	Am site		M(4) site		M(1) site		M(2) site		M(3) site	
				atom	occ. [a]	atom	occ. [a]	atom	occ. [a]	atom	occ. [a]	atom	occ. [a]
Untreated	a=9.7324(1) b= 18.0414(1) c= 5.32800(3) β=103.5(1)	R_{wp}= 5.38 R_p= 3.65	[b]	Na	0.18(2)	Na	0.83(2)	Mg Fe^{2+}	0.27(3) 0.52(2)	Fe^{3+}	1.00	Fe^{2+}	1.00
96h in MeT5A	a= 9.720 (3) b= 18.078 (6) c= 5.311 (5) β= 103.7 (1)	R_{wp}= 1.65 R_p= 0.91	9;10;11	Na	0.0	Na	0.8(1)	Mg Fe^{2+}	0.0 0.2(1)	Fe^{3+}	0.98(2)	Fe^{2+}	0.64(7)
96h in Beas2B	a= 9.724 (3) b= 18.077 (4) c= 5.318 (2) β= 103.6 (1)	R_{wp}= 2.23 R_p= 1.31	1;2;3	Na	0.0	Na	0.70(7)	Mg Fe^{2+}	0.0 0.55(6)	Fe^{3+}	0.9(1)	Fe^{2+}	0.75(9)

Treatment	Cell parameters (Å)[a]	Ag. Fct. (%)	Analized Spectra	e1 site		e2 site	
				atom	occ.[a]	atom	occ.[a]
Untreated	a=b= 13.227(1) c= 15.071(2)	R_{wp}= 10.28 R_p= 7.69	[b]	Na	0.55(5)	Na	0.22(4)
24h in MeT5A	a=b= 13.180(1) c= 15.020(2)	R_{wp}= 7.95 R_p= 3.98	17;18;19	Na	0.62(5)	Na	0.56(5)
96h in MeT5A	a=b= 13.23(1) c= 15.07(1)	Rwp= 7.70 Rp= 2.66	15;16	Na	0.0	Na	0.88(5)

[a]Results are mean values; [b]Spectra collected on few mg of untreated fibres embedded between two kapton foils.

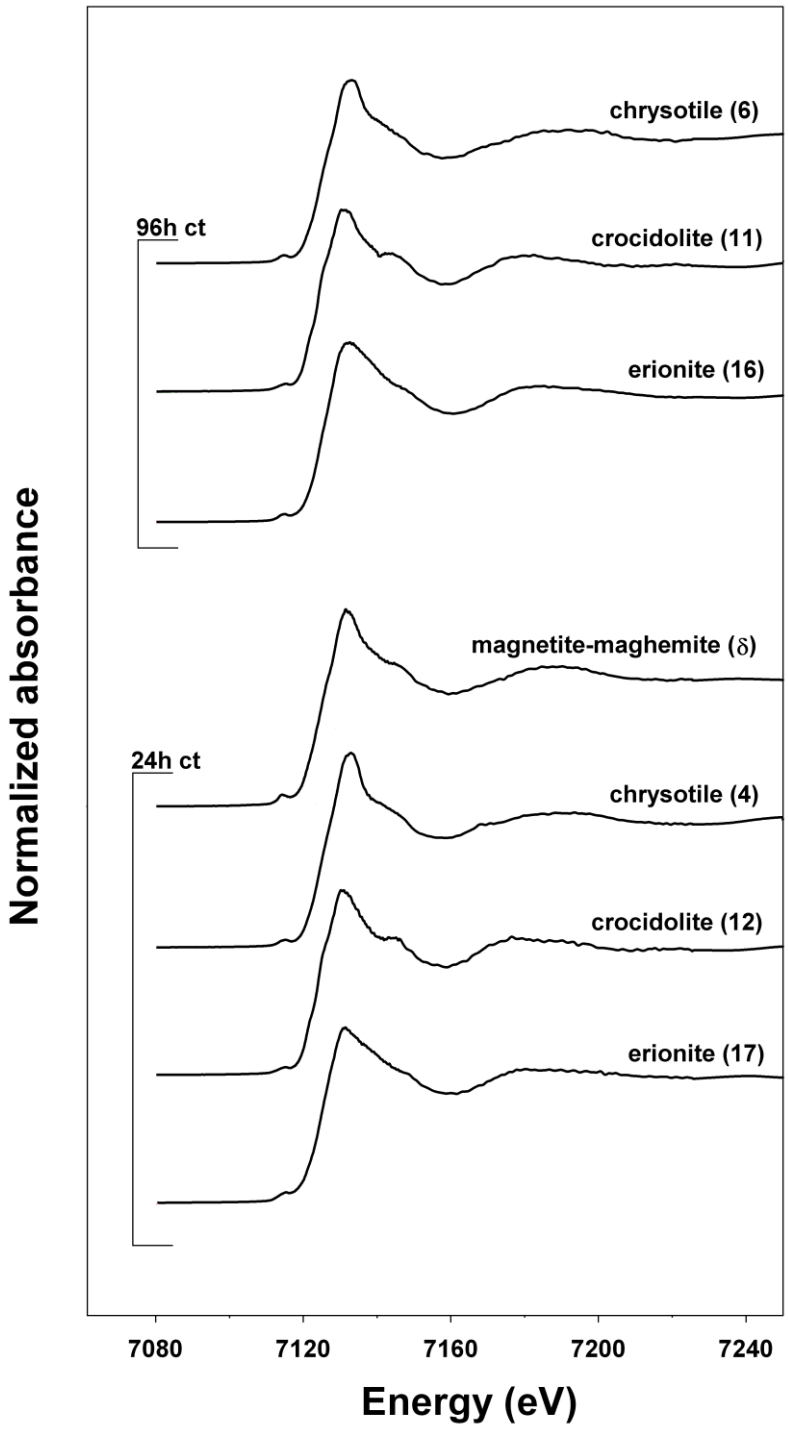

Fig. 3.2.20. Representative Fe K-edge XANES spectra of samples after 24 and 96h ct in Met5A cell culture. Numbers and symbols in brackets indicate the point at which it was collected, as shown in Fig. 3.2.13.

As an example, Fig. 3.2.20 reports a set of representative Fe K-edge μ-XANES spectra of the investigated fibres together with a spectrum collected on a magnetite-maghemite particle. Data were collected on samples that have been in contact with Met5A cell culture; spectra of samples treated with Beas2B are not reported as they are very similar. The results of the pre-edge analysis are listed in Table 3.2.20.

Table 3.2.20
XANES pre-edge parameters of chrysotile (top) crocidolite (medium) and erionite (bottom). Reported data are the average result of the deconvolution of pre-edges of all collected spectra within the sample.

crocidolite UICC	Component position (eV)	Component area	Total area	Centroid position (eV)
BeaS2B 24h *ct*	7112.33	0.008	0.08(1)	7114.29(8)
	7113.68	0.030		
	7115.10	0.041		
BeaS2B 96h *ct*	7112.35	0.009	0.08(1)	7114.24(9)
	7113.73	0.031		
	7115.14	0.036		
MeT5A 24h *ct*	7112.35	0.011	0.081(2)	7114.22(8)
	7113.76	0.030		
	7115.08	0.040		
MeT5A 96h *ct*	7112.41	0.011	0.07(2)	7114.20(6)
	7113.79	0.027		
	7115.13	0.032		
chrysotile UICC				
BeaS2B 24h *ct*	7112.59	0.016	0.11(2)	7114.26(6)
	7114.02	0.051		
	7115.23	0.040		
BeaS2B 96h *ct*	7112.42	0.012	0.09(1)	7114.24(8)
	7113.93	0.046		
	7115.24	0.036		
MeT5A 24h *ct*	7112.54	0.006	0.101(4)	7114.47(7)
	7113.88	0.045		
	7115.26	0.050		
MeT5A 96h *ct*	7112.68	0.015	0.11(1)	7114.30(7)
	7114.07	0.050		
	7115.23	0.040		
erionite				
BeaS2B 96h *ct*	7112.78	0.025	0.12(2)	7114.3(1)
	7114.13	0.049		
	7115.45	0.043		
MeT5A 24h *ct* - 1	7112.50	0.014	0.10(2)	7114.13(9)
	7113.65	0.041		
	7114.99	0.049		
MeT5A 24h *ct* - 2	7112.81	0.003	0.09(1)	7114.54(6)
	7113.78	0.034		
	7115.11	0.054		
MeT5A 96h *ct*	7112.49	0.008	0.09(2)	7114.33(9)
	7113.84	0.037		
	7115.12	0.042		

3.2.5 XRPD experiments at ID13 – ESRF

The conducted experiment allowed to obtain high-resolution powder-like XRD patterns. In total, several hundred of frames for each sample were collected, and after the operations of merging and averaging, about 30 analyzable spectra were produced for each sample, like that reported in the following figures.

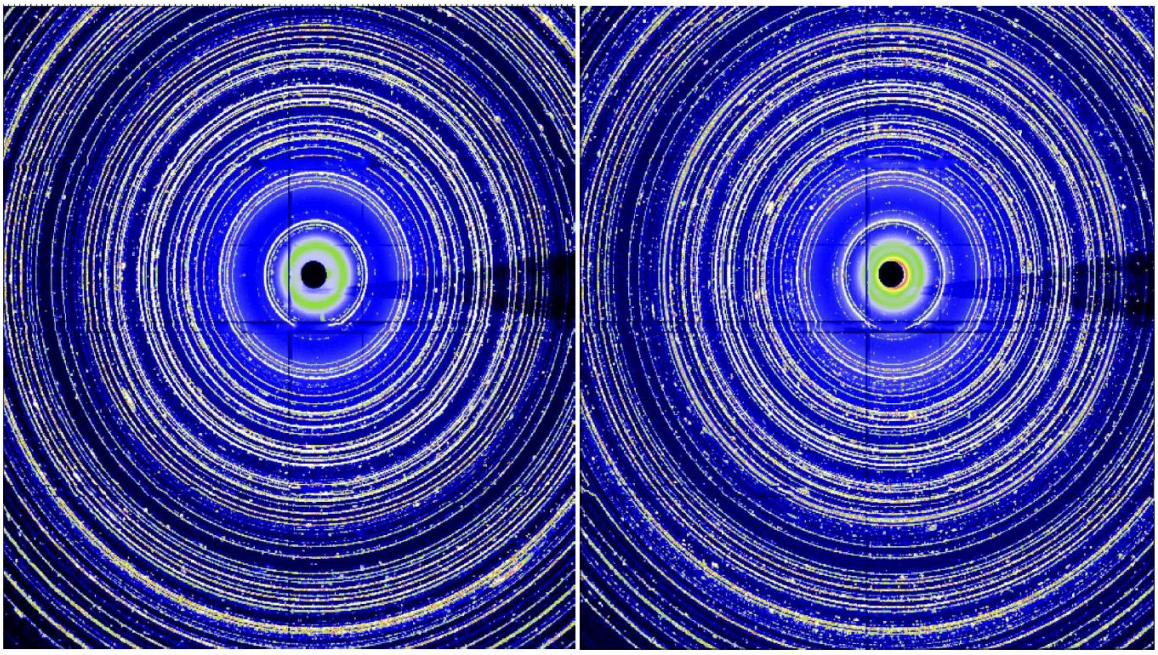

Fig. 3.2.21. XRD pattern of untreated crocidolite (left) and crocidolite fibres extracted from rat tissues (residence time of 80 weeks).

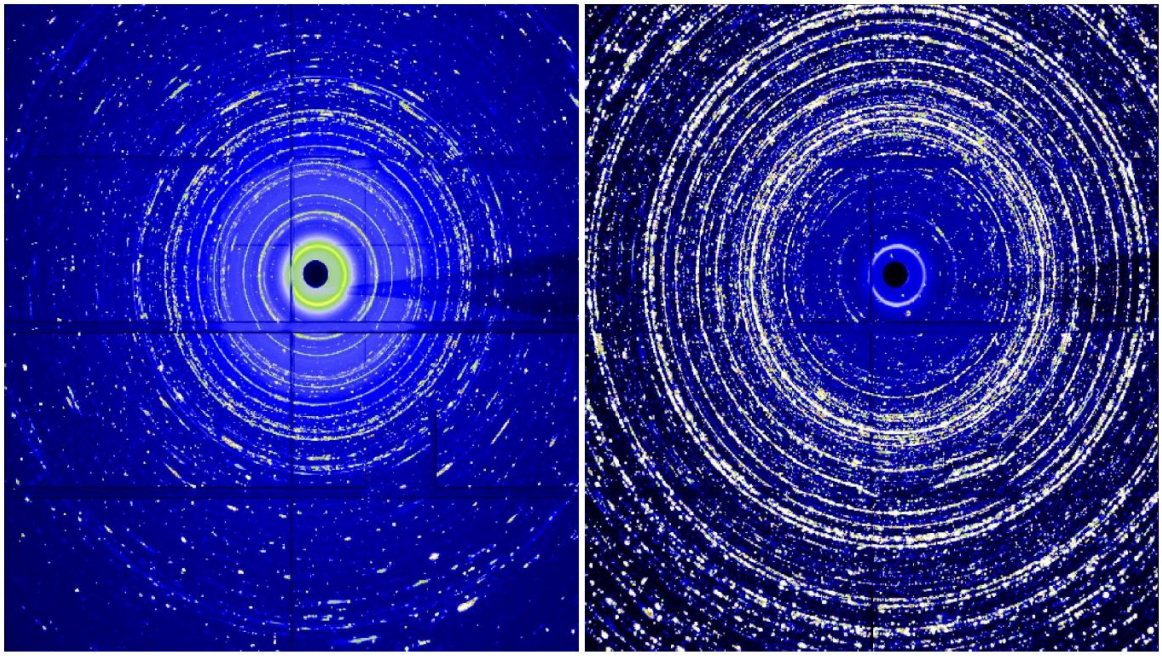

Fig. 3.2.22. XRD pattern of untreated chrysotile UICC (left) and chrysotile fibres extracted from rat tissues (residence time of 80 weeks).

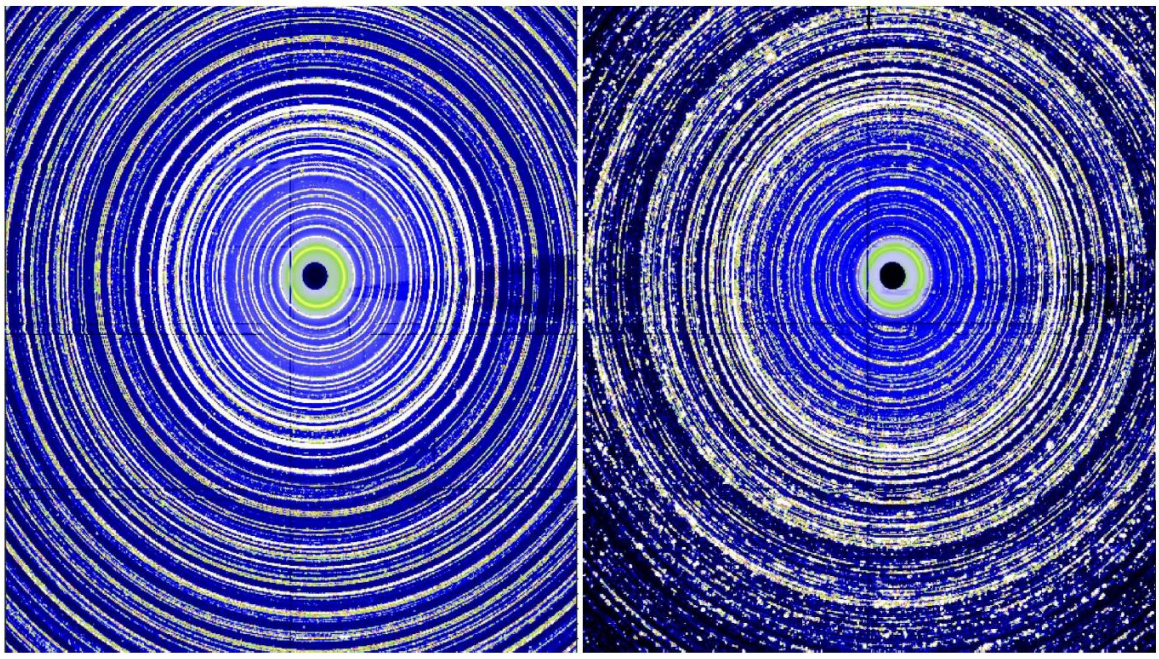

Fig. 3.2.23. XRD pattern of untreated erionite (left) and erionite fibres extracted from rat tissues (residence time of 104 weeks).

4 – DISCUSSION

4.1 Surface reactivity of mineral fibres

The surface reactivity of a mineral fibre is influenced by several parameters, the most important being the surface area and the fibre size. In fact, besides the intrinsic chemical stability of each mineral fibre type, a larger surface area determines an higher reactivity and consequently an higher dissolution rate. Observing the diagram in Fig. 4.1.1, it's clear that there is a significant difference between chrysotile and amphiboles, and the inverse relationship between size of the fibres and their surface area is confirmed.

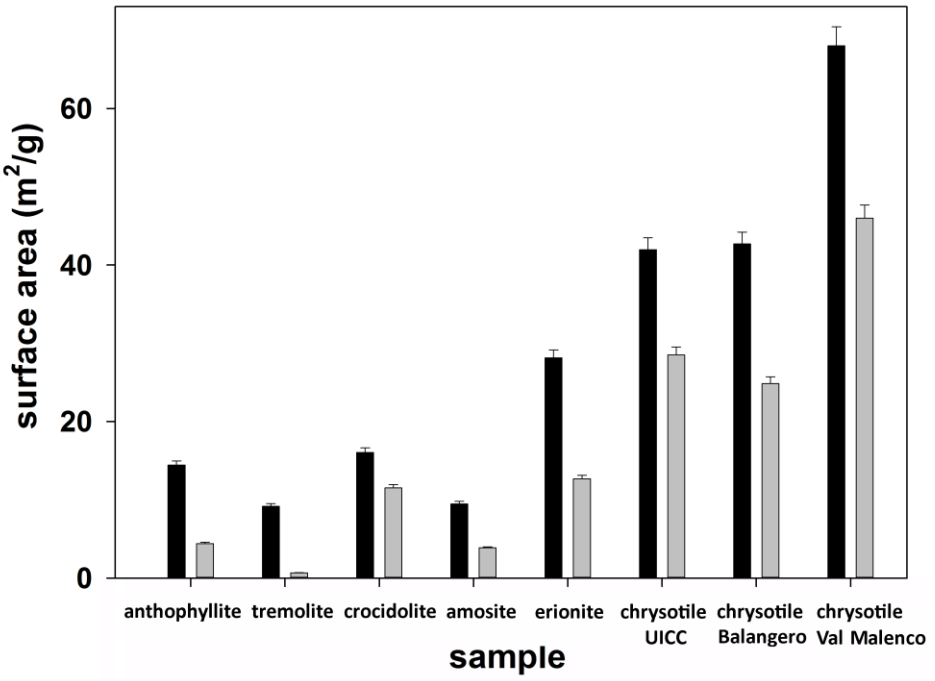

Fig. 4.1.1. Specific surface area of the two size classes obtained from the gravitational separations. Legend: dark columns, short fibres; clear columns, long fibres (data are reported in Table 3.1.10, paragraph 3.6).

The specific surface area of chrysotile is about 3.3 times that of amphiboles for short fibre samples, and about 4.5 times for long fibre samples whereas erionite has a surface area halfway between chrysotile and amphiboles. So, in this regard, chrysotile seems to be the more reactive specie and will dissolve more readily in acidic environment.

Another important factor that plays a key role in the surface reactivity of a mineral fibre is the ζ potential. As reported in paragraph 2.3.5, its value can determine the stability of suspensions and aggregation of particles dispersed in the liquid. Measurements carried out in double distilled water confirm literature data, according to which chrysotiles show positive values (Light and Wei, 1977; Van Oss *et al.* 1999) of ζ potential, while crocidolite (and amphiboles in general) show negative values (Light and Wei, 1977). Surprisingly, negative values of the ζ potential for chrysotile from Val Malenco (both for long and short fibres) were found. This anomaly is not due to an experimental bias as other chrysotiles from the literature display negative ζ potential (Van Oss *et al.* 1999).

Models to explain the differences between surface potential of chrysotile and amphiboles in aqueous medium at neutral pH have been proposed (Bonneau *et al.* 1986; Allen and Smith, 1975; Martinez and Zucker, 1960; Riddick, 1968; Trivedi, 1970; Prasad and Pooley, 1973) but they are not convincing and then a substantial revision is required.

In chrysotile, surface exposure occurs because of the breaking of hydrogen bridges linking two successive tetrahedral–octahedral (TO) units in the interlayer volume, causing the exposure of two surfaces: an unsaturated negative one formed by oxygen atoms (dangling, dark gray in Fig. 4.1.2a) and a negative one saturated by protons (light gray in Fig. 4.1.2a). The protons are insufficient to counterbalance the negative charge so both negatively charged surfaces call for positive charges so that the diffused corona consists of positively charged ions attracted by the negative residue potential. These ions can be protons, hydrated cations, H_3O^+, Mg^{2+} (Martinez *et al.* 1960; Riddick, 1968; Trivedi, 1970) or Na^+, K^+ and Ca^{2+} as compensator cations in chrysotile structure (Hannila and Hallman, 1979; De Waele *et al.* 1983; Surkyn *et al.* 1983) or as cations dissolved in lung fluids. This model and the values of the ζ potential at pH 7 are in line with those reported for kaolinite, whose negatively charged basal faces throughout the whole pH range require compensation by positive cations, whereas edges result to be a combination of the potential on the silica and alumina surfaces (Williams and Williams, 1978; Van Olphen, 1976). In amphiboles, exposure occurs along the planes of the [110] faces. The presence of extra-tetrahedral cations such as Ca^{2+}, Fe^{2+},Fe^{3+}, Mg^{2+} and protons determine a positive charge of the Stern layer, and a resulting attraction of negatively charged molecules to form the diffused corona. Consequently, the ζ potential will have negative values (Fig. 4.1.2b). A similar picture is found in zeolites such as erionite (Polatoglu and Özkan, 2005).

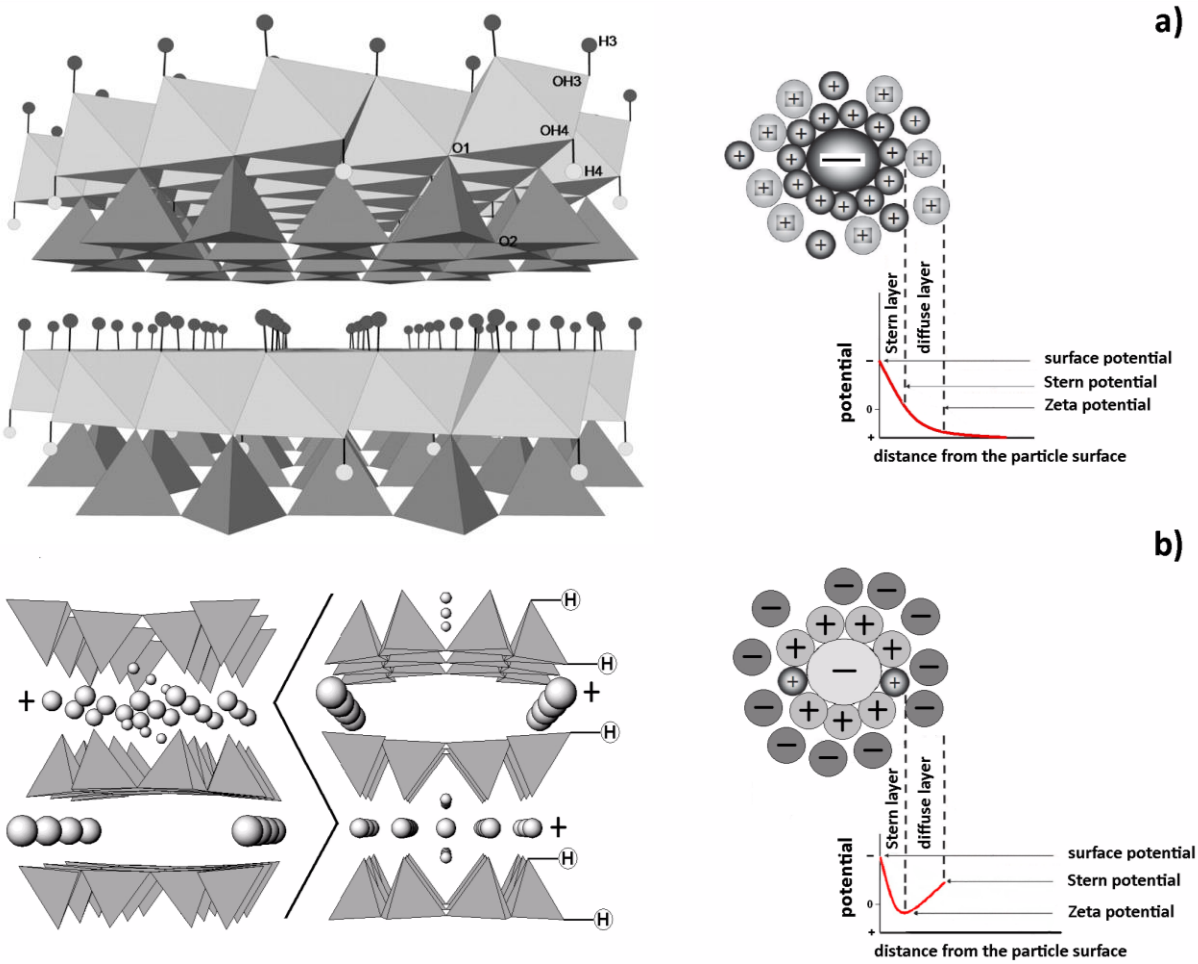

Fig. 4.1.2. Structural models which explain the sign of the ζ potentials of chrysotiles (a) and amphiboles (b). Chrysotile structure along a direction normal to [001]. Structural model of chrysotile taken from Prencipe *et al.* (2009).

The chrysotile from Val Malenco represents a special case. Its negative values of ζ potential in distilled water (table 3.1.12) cannot be due to chemical composition (since it is very similar to that of chrysotile UICC, see table 3.1.7) or to structural parameters, as they are similar to those of chrysotile UICC and Balangero (Table 3.2.11). Possibly, quartz and forsterite impurities present in this sample (and not in the other chrysotiles) can influence the potential, as they have both strongly negative ζ potential (Kaya and Yukselen, 2005; Pokrovsky and Schott, 2000). Another contributing cause could be related to the size of the fibrils; in fact, BET data (Table 3.1.10) shows that this sample posses twice the surface area of the other chrysotiles, despite the major length of its fibres (table 3.1.9); the only reasonable explanation is that fibrils are much thinner compared to those of other chrysotiles. The higher surface area could prompt a faster partial dissolution and release of cations which gather around the surface and increase the positive charge of the Stern layer, calling for a more negatively charged ζ potential.

Variations of the pH and subsequent partial dissolution of the fibres induce variations of the ζ potential which tends to become more negative at high pH values. For chrysotile, in the low pH range, the dissolution reaction of the magnesium hydroxide sheet which leaves a hydrated silica relict (Bernstein *et al.* 2013; Suquet, 1989), brings an excess magnesium concentration at the surface of the fibre and an overall positive ζ potential (Light and Wei, 1977; Pundsack, 1955; Yao *et al.* 2010). According to Feng *et al.* 2013, magnesium ions are simply left on serpentine surface and are responsible for its positive surface charge. In the high pH range, chrysotile is stable and hydroxyls at the surface of the fibre determine an overall negative ζ potential of the particle. Another possibility is that the reversal from positive to negative sign of the ζ potential is due to the electrolytes introduced in solution which replace the protons at the Stern layer and call for negative ζ potential. The ζ potentials of both crocidolite and erionite become more negative in the high pH range. Electrolytes (Na^+) introduced in solution to create alkaline conditions, replace surface protons at the crystal edges and, together with Ca^{2+}, Fe^{2+}, Fe^{3+}, Mg^{2+}, enhance the positive charge of the Stern layer, which in turn call for an even more negative ζ potential.

Despite the differences observed in contact with distilled water, when in contact with organic solutions (Gamble's and SLF solution), all the mineral fibres tend to gain negative and similar values of the ζ potential, as visible in Fig. 4.1.3 (data in Table 3.1.11). It should be remarked that the difference of the ζ potential in distilled water of chrysotile (positive) on one side and amphiboles and erionite (negative) on the other side has been hypothetically assumed as distinctive character to discriminate the potential cytotoxicity (Wagner *et al.* 1974; Kamp, 2009; Kanarek, 2011; Qi *et al.* 2013) of these fibres (low or null in chrysotile and high in amphiboles and erionite).

This result demonstrates instead that the ζ potential is not a discriminating factor when it is measured in contact with organic solutions (namely in the lungs). In this condition, ζ potential turns from positive to negative for chrysotile whereas it becomes less negative for both crocidolite and erionite.

The high concentration of Na^+ present in the organic solutions triggers ion exchange for the surface protons of the chrysotile exposed surfaces so that the Stern layer becomes positive and requires surrounding negative charges. For crocidolite and erionite, the high concentration of Na^+ possibly triggers ion exchange not only for the surface protons but also for the edge extratetrahedral cations with large oxidation number such as Ca^{2+} and Mg^{2+}. The ion exchange decreases the positive charge of the Stern layer which requires a less negative ζ potential.

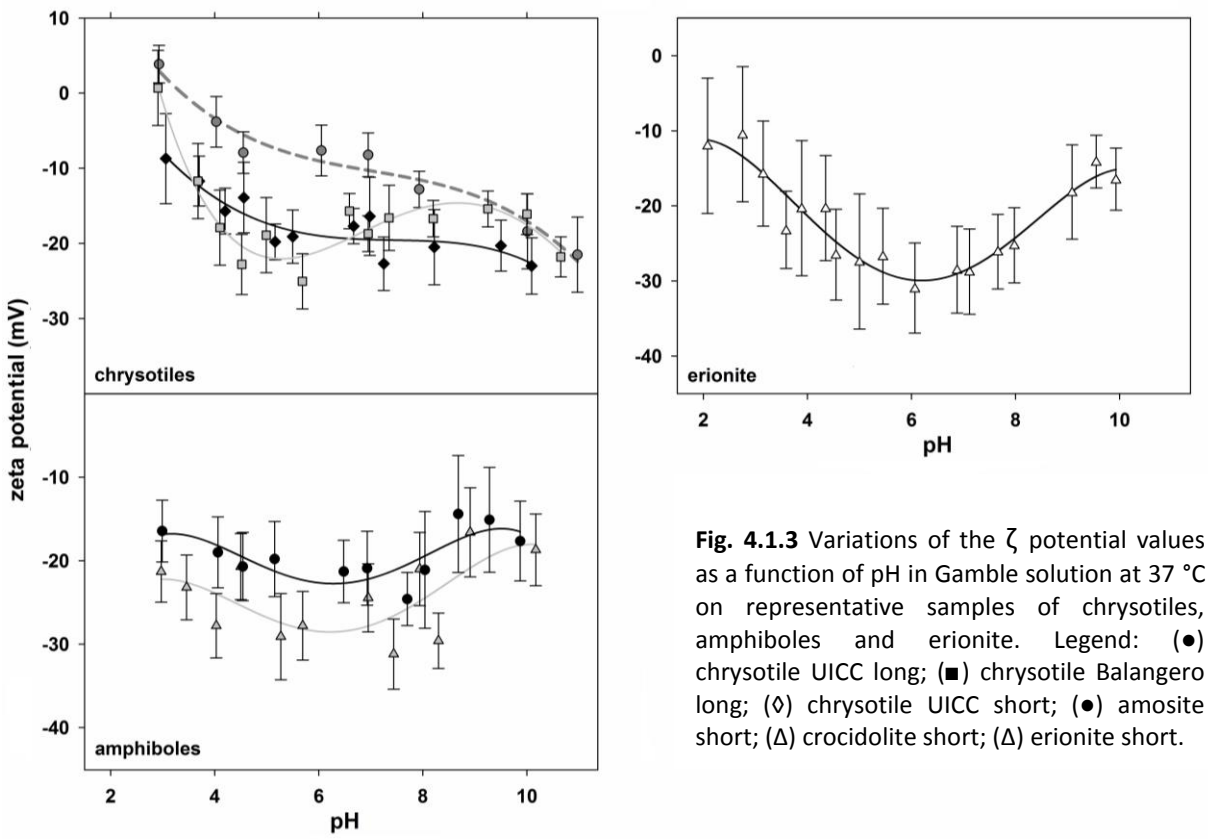

Fig. 4.1.3 Variations of the ζ potential values as a function of pH in Gamble solution at 37 °C on representative samples of chrysotiles, amphiboles and erionite. Legend: (●) chrysotile UICC long; (■) chrysotile Balangero long; (◊) chrysotile UICC short; (●) amosite short; (Δ) crocidolite short; (Δ) erionite short.

The reduction of the absolute values of ζ potentials has already been observed for chrysotile and crocidolite in the presence of the surfactant dipalmitoyl phosphatidylcholine (DPPC) by Light and Wey (1977). The ζ potential of the fibres at pH 4.5 and 7.0 (that of phagolysosomes and of extra-cellular environment) is invariably negative, with values approximately in the range −10 to −26 mV. The lack of differences among the various fibre species is probably the reason why Van Oss *et al.* (1999) reported that the value and sign of ζ potential is irrelevant to the degree of their pathogenicity. Our results instead demonstrates that the ζ potential of mineral fibres may influence or may be influenced by several bio-chemical and physical parameters:

(1) Hemolytic potential: Light and Wey (1977) observed that when DPPC was added to the fibre suspension, hemolytic activity decreased for all UICC fibre standards (by 87% for amosite and crocidolite and 25% for chrysotiles) and that in general, a decrease of the absolute value of the ζ potential decreases the hemolytic activity. The decrease of the ζ potential of the fibres is an effect of the defensive response acted by the macrophage cells to minimize hemolytic damage.
A reduction of the magnitude of the ζ potential of the fibres should correspond to a decrease of the hemolytic activity. According to Gabor and Anca (1975) the mechanism for hemolysis induced by the fibres relies on the formation of lipid-bilayer clusters, normally extending homogeneously through the entire lipid bilayer (Fig. 4.1.4). Clustering occurs because of the coulombic repulsion of negatively charged sialic acid groups with negatively charged fibres. Although ion permeability through lipid bilayers is very low, ions can readily penetrate those regions of the erythrocyte membrane, where the clusters of glycoproteins are formed, causing hemolytic activity.

In support of this model, it was demonstrated that ζ potential of insoluble nanoparticles has been correlated with hemolytic potential (Cho *et al.* 2012). In this scenario, when nanoparticles enter the acidic lysosome milieu, enzymatic digestion of the corona by lysosomal enzymes (Wallace *et al.* 1992) occurs and may cause the reversal of negative ζ potential. Thus, the positively charged nanoparticles may interact with the negatively charged internal face of the lysosomal membrane (lysosomal destabilization) and trigger and inflammation cascade in the lung (acute lung inflammogenicity; Hornung *et al.* 2008). As far as chrysotile and Mg-amphiboles are concerned, following the behavior of MgO-nanoparticles (Cho *et al.* 2012) no inflammation is expected by the release of non-toxic Mg^{2+}.

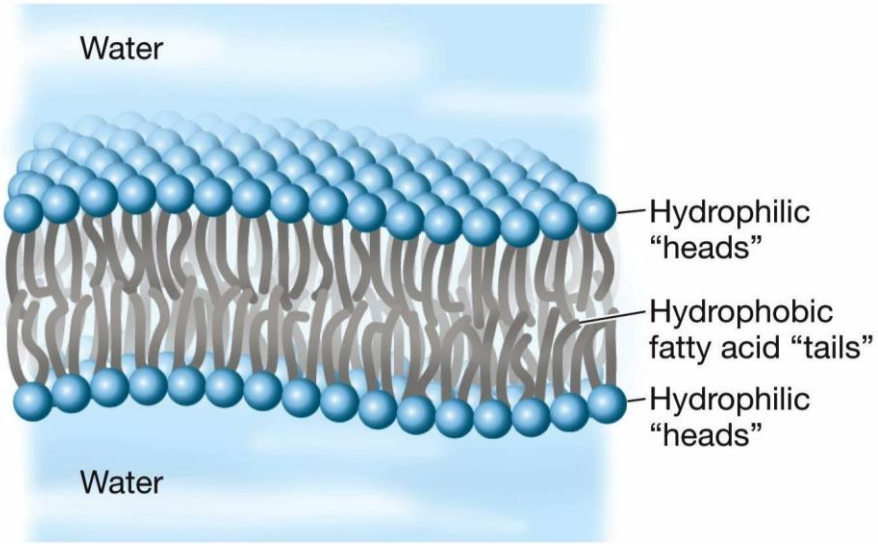

Fig. 4.1.4. Representation of phospholipid bilayer; the hydrophilic polar heads can be grouped because of their repulsion with negatively charged fibers (image from Sadava *et al.* 2007).

(2) ROS production: Iron associated with asbestos promotes the formation of the highly reactive $HO^{\bullet}$ from the oxidation of ferrous iron (Fe^{2+}) to ferric iron (Fe^{3+}) by H_2O_2 released by the macrophages during the inflammatory burst (Fenton reaction; Kamp and Weitzman, 1999).

Superoxide and other biological reducing agents can eventually reduce Fe^{3+} iron back to redox active Fe^{2+} iron (family of catalyzed Haber–Weiss reactions). The existence of a negatively charged surface (negative ζ potential), source of electrons, on the fibres prompt the formation of $HO^{\bullet}$ via the reaction with peroxide: $H_2O_2 + e^{-} \rightarrow HO^{\bullet} + OH^{-}$.

The mechanism is identical to that described for freshly cut quartz surfaces in biological medium (Donaldson and Borm, 1998) where silanol groups (Si-OH) and ionized silanol groups (Si-O-) on the surface play a major role in interaction with membranes (Nolan *et al.* 1981; Fubini *et al.* 1995). In lung lining fluid or in tissue fluid, these products of hemolytic cleavage can give rise to $HO^{\bullet}$ and H_2O_2 (Castranova *et al.* 1996; Donaldson and Borm, 1998).

(3) Fibre encapsulation by collagen and iron-rich proteins: In support of the proviso that the decrease of the ζ potential of the fibres is caused by the defensive chemical cellular response during macrophage phagocytosis, literature data report that the negatively charged reactive surface favours the binding of collagen and redox activated Fe-rich proteins, to form the so-called asbestos bodies.
In fact, alveolar macrophage ingestion of asbestos fibres triggers a fibrogenic response from fibroblasts via the release of growth factors (mainly TGF-β), cytokines, TNF-α, interleukin-1β (IL-1β), which collectively promote collagen deposition and asbestos encapsulation by mucopolysaccharides and Fe-rich proteins (ferritin, hemosiderin) that can be redox activated (Liu *et al.* 2013).

(4) Apoptosis: According to the model of mitochondria-endoplasmic reticulum cross talk in asbestos-induced apoptosis (Liu *et al.* 2013), endoplasmic reticulum stress due to the fibre interaction causes activation of an unfolded protein response and Ca^{2+} release which, in turn, lead to activation of mitochondria-regulated apoptosis (Fig. 4.4.3). Because the Ca^{2+} release to the mitochondria is necessary for the induction of intrinsic apoptosis, the whole cellular response cycle may be broken if the negatively charged corona of the mineral fibres attract and fix the Ca^{2+} ions. This model is in agreement with the ζ potential data shown in Table 3.1.13, where it can be noted that, when Ca^{2+} ions are introduced in solution (by the addition of $CaCl_2*2H_2O$) the ζ potential of all mineral fibres changes radically towards positive values, which means that Ca^{2+} ions are fixing to the Stern layer or to the outer corona.

(5) Fibre agglomeration: We have seen that ζ potential of the fibres at pH 4.5 and 7.0 display values in the range −10 to −26 mV, with no remarkable differences among the various fibre species. At such values of ζ potential, processes such as agglomeration are favoured (Fig. 4.1.5). This is a critical point as it is known that culture conditions with most agglomeration induce highest biological responses (Gualtieri *et al.* 2012; Sharma *et al.* 2014).

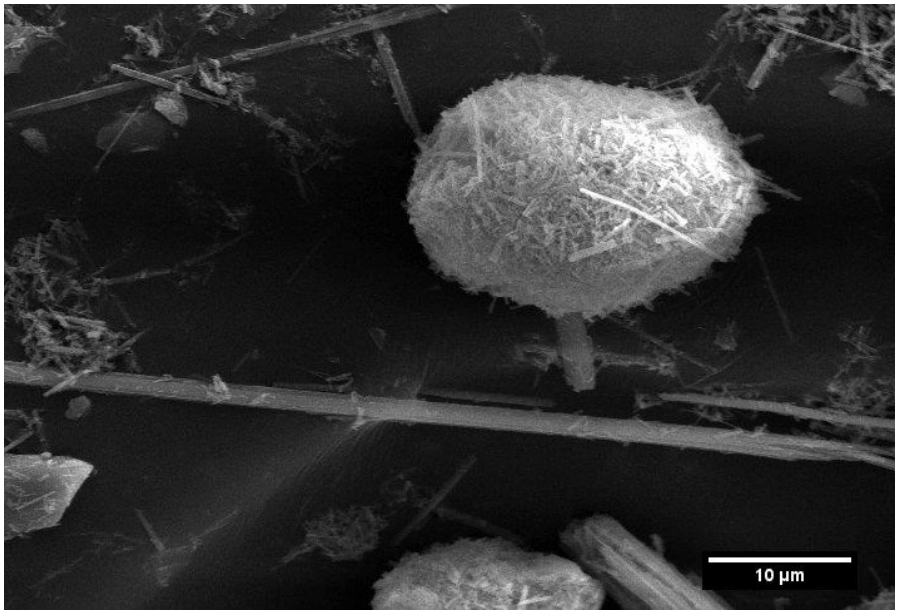

Fig. 4.1.5. SEM image of a ball-like cluster in the crocidolite sample.

(6) Fibre size: Measurements carried out in organic solutions at 37 °C show a slight general trend of long fibres (with smaller surface area) having values of ζ potential with more positive sign and lower values than short fibres (Table 3.1.11). This may be due to higher surface reactivity of short fibres, prompting partial dissolution and release of cations which gather around the surface and increase the positive charge of the Stern layer. The latter calls for a more negatively charged ζ potential. The dilemma regarding the different pathogenicity of short vs. long fibres is still an open issue. According to the hypothesis of Stanton *et al.* (1981), the ability of mineral particles to cause cancer is mostly a function of size rather than physico-chemical properties.
Recent studies (Turci *et al*. 2012) showed that the fibre size has fundamental importance to define the toxicity of a fibre and that short chrysotile fibres (nanofibres) do not exhibit the same cytotoxicity of the long fibres. Our results reveal that short fibres with higher absolute values of ζ potential are more stable in solution and less aggregated that long fibres. The latter have a tendency to aggregation and, in conjunction with frustrated phagocytosis by macrophages, should trigger more potent inflammatory response than short fibres.

(7) Temperature: It was found that temperature affects the value of the ζ potential both in distilled water and in Gamble's solution (Figs. 3.1.20; 3.1.21 and 3.1.22). Assuming the same fibre size, it turns out that the ζ potential becomes more negative (assumes higher absolute values) at 25 °C. This variation is significant for amphiboles and erionite whereas it is within the experimental error for chrysotile UICC. Although the literature describing the influence of temperature on the ζ potential is scanty, it was generally observed that ζ potential becomes more negative with temperature increase (Venditti *et al.* 2006). The opposite phenomenon is observed here. The influence of temperature on the ζ potential is a result of changes in silanol equilibrium, adsorption equilibria and diffused double-layer thickness (Revil *et al.* 1999). Notwithstanding, exceptions are reported in the literature (Ramachandran and Somasundaran, 1986) indicating that temperature dependence of the ζ potential, if any, is structure-related and influenced by other chemical factors, such as pH.

4.2 Iron in mineral fibres

4.2.1 Occurrence

From the collected XANES, EXAFS and Fe^{57} Mössbauer data, the presence of both Fe^{2+} and Fe^{3+} oxidation states, disordered over different structural sites, has been detected. This is clearly observable in Fig. 4.2.1 (that is a modified version of the variogram from Wilke *et al.* 2005), where the XANES pre-edge parameters of our samples are plotted against that of standard reference compounds.

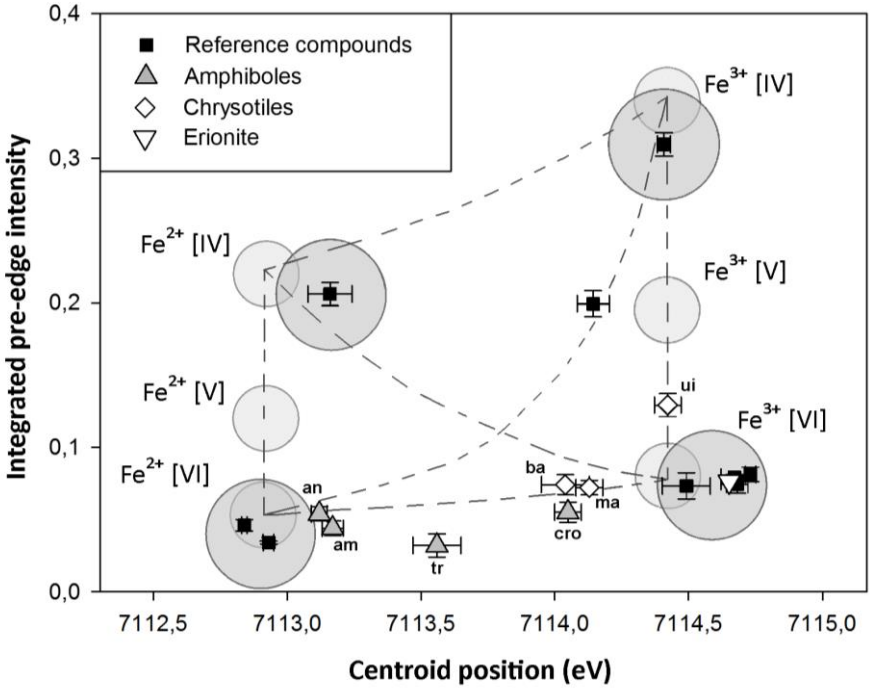

Fig. 4.2.1. Pre-edge parameters of samples and reference compounds plotted in the modified variogram from Wilke *et al.* (2005). Little grey fields designate pre-edge parameters for the Fe co-ordination and oxidation state whereas dashed lines between fields indicate the variation of pre-edge parameters assuming binary mixtures of respective end-members (Wilke *et al.* 2005); larger grey fields designate our pre-edge parameters.

The obtained cationic distribution of Fe ions in our samples are in general agreement with literature data and will be hereby discussed in detail. Important to note that, since literature data (Wilke *et al.* 2001, 2005; Giacobbe *et al.* 2010) possess the iron threshold calibrated at variable energies, they have all been rescaled to be compared to our data (threshold of iron at 7112.00 eV).

Amphiboles

As reported in the introduction (1.1.1) Fe^{2+} ions can be potentially hosted in the octahedral M(1), M(2), M(3) and M(4) positions (Stroink *et al.* 1980; Whitfield and Freeman, 1967) whereas Fe^{3+} can only be hosted in the M(1), M(2) and M(3) positions (Stroink *et al.* 1980; Cameron and Papike, 1979). A sketch of the structure unit of amphibole asbestos is reported in Fig. 4.2.2.

In anthophyllite, the pre-edge peaks centroid position at 7113.13 eV (Table 3.2.9) indicates the presence of Fe^{2+} in agreement with Mössbauer (MS) information from the literature (Stroink *et al*. 1980).

The total pre-edge peaks area of 0.054 points to iron hosted only in octahedral position (Table 3.2.9). The best fit of the EXAFS data was obtained with a first shell composed of three oxygen atoms at 2.07 Å and 2.08 Å, respectively.
Unfortunately, the quality of the data is poor (see Fig. 3.2.8) and it was not possible to accomplish a better fit (see the R-factor and Debye-Waller in Table 3.2.10). As reported in many MS studies on anthophyllite samples (Stroink *et al.* 1980; Hawthorne, 1983; Law 1989), the population of Fe^{2+} in *M*(4) is much larger than the population in *M*(1), *M*(2) and *M*(3); Fe^{3+} ions, if any, are expected to be confined in *M*(2) site although in some cases the occurrence of small amounts of Fe^{3+} in *M*(1) or *M*(3) sites has been reported. Hence, anthophyllite results to be mainly composed of Fe^{2+} with a very low amount of Fe^{3+}, both in octahedral coordination, with Fe^{2+} ions preferably hosted in M(4) site.

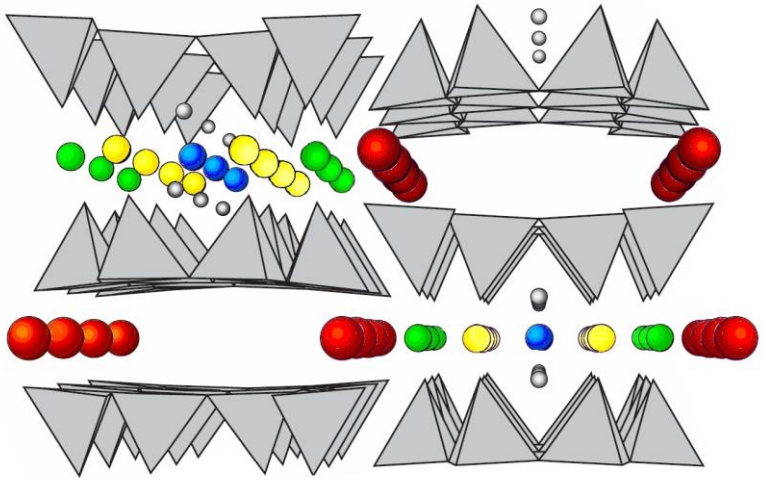

Fig. 4.2.2. Sketch of the structure unit of amphibole asbestos composed of one-dimensional double-chains (a–b crystallographic plane). Yellow=M(1), green=M(2), blue =M(3) and red=M(4).

For amosite, XANES pre-edge centroid position at 7113.17 eV and total pre-edge peaks area of 0.044 indicate predominance of Fe^{2+} hosted only in octahedral position (Table 3.2.10 and Fig. 4.2.1) in agreement with MS data (Table 3.1.15). EXAFS data (Table 3.2.10) confirm a first shell of 6 oxygen atoms at a mean distance of 2.083 Å, slightly shorter but still close to the theoretical value of octahedral Fe^{2+}-O (2.14 Å). MS data of the cummingtonite-grunerite series (Stroink *et al.* 1980; Whitfield and Freeman, 1967; Bancroft *et al.* 1967) were fitted using a model with Fe^{2+} ions preferably in *M*(4) site with respect to *M*(2). According to this model, 35% of the total Fe^{2+} is hosted in *M*(4) site, and remaining Fe^{2+} ions randomly distributed over *M*(1), *M*(2) and *M*(3) sites. Therefore, despite amosite generally contains much more iron with respect to anthophyllite, the models of cation distribution are comparable, with octahedral Fe^{2+} largely prevailing over Fe^{3+}.
Regarding crocidolite, XANES data evidence comparable fractions of Fe^{2+} and Fe^{3+}, with a pre-edge centroid position at 7114.05 eV (Table 3.2.9), halfway between that of the Fe^{2+} and Fe^{3+} standards and in agreement with MS information from literature (Stroink *et al.* 1980; Fantauzzi *et al.* 2010). The total area of the pre-edge peaks 0.054 indicates that iron has an octahedral coordination. EXAFS data confirms a first shell of six oxygen atoms at a mean distance of 2.059 Å (Table 3.2.10). This value is right in between the theoretical value of octahedral Fe^{2+}-O (2.140 Å) and the theoretical value of octahedral Fe^{3+}-O (2.015 Å). Thus, iron in UICC crocidolite has comparable amount of ferrous and ferric iron both in octahedral coordination (Fig. 4.2.1).

In a structural study about the Bolivian crocidolite Whittaker (1949) reported that site *M*(4) is partially vacant with magnesium largely prevailing over iron. MS data from the literature (Whitfield and Freeman, 1967; Stroink *et al.* 1980; Pacella *et al.* 2012; Fantauzzi *et al.* 2010) confirm that Fe^{3+} ions are mainly found in the peripheral *M*(2) positions with a small proportion in *M*(1) and *M*(3) while most of the Fe^{2+} ions occupy *M*(1) and *M*(3), the innermost positions. In concert, the distance of 2.09 Å obtained from EXAFS refinement is consistent with the average interatomic distances of six oxygen atoms (2.088 Å) with respect to Fe ions within *M*(1), *M*(2) and *M*(3) positions calculated from an ideal structural model of crocidolite.

Tremolite displays a pre-edge centroid position at 7113.56 eV (Table 3.2.9) close to that of Fe^{2+} (Fig. 4.2.1) whereas the total pre-edge area of 0.032 is the lowest among the investigated samples and indicates that iron is only in octahedral position. These findings are in agreement with MS data (Table 3.1.15). The best fit of the EXAFS data (Table 3.2.10), collected in fluorescence mode, was obtained with a single shell of six oxygen atoms at 2.093 Å. This is consistent with the coexistence of Fe^{2+} and Fe^{3+}, with Fe^{2+} as dominant species, falling between the theoretical value of octahedral Fe^{2+}-O (2.14 Å) and that of octahedral Fe^{3+}-O (2.015 Å). Literature data on tremolite samples characterized with MS and other techniques reports that approximately 40% of Fe^{2+} is located *M*(2) site, while the remaining is disordered over both *M*(1) and *M*(3) sites (Pacella *et al.* 2008; Ballirano *et al.* 2008; Pacella *et al.* 2010; Pacella *et al.* 2012; Fantauzzi *et al.* 2010). Considering the site multiplicity, an almost disordered distribution of iron over sites *M*(1), *M*(2) and *M*(3) may be predicted, while Fe^{3+} is ordered in *M*(2) site.

Chrysotiles

In chrysotile, both Fe^{2+} and Fe^{3+} ions can replace magnesium in the octahedral sheet (Stroink *et al.* 1980; Hardy and Aust, 1995) furthermore, Fe^{3+} ions may eventually replace Si ions although this position may preferentially host Al^{3+} (Blaauw *et al.* 1979; O'Hanley and Dyar, 1998).

Regarding chrysotile UICC, XANES data evidence major fractions of Fe^{3+} with respect to Fe^{2+}, with a pre-edge peaks centroid position at 7114.42 eV (Table 3.2.9). The total pre-edge peaks area of 0.129 indicates that iron is hosted in both octahedral and tetrahedral environment. This is confirmed by the EXAFS data (Table 3.2.10), showing two different site positions for iron: one having a first shell of four oxygen atoms at 1.860 Å and another one with a first shell of six oxygen atoms at 2.028 Å. The first shell is compatible with Fe^{3+} tetrahedral environment (theoretical distance 1.865 Å) while the second one with an octahedral environment mainly Fe^{3+} with a small presence of Fe^{2+} (theoretical distances 2.015 Å and 2.140 Å, respectively). The presence of tetrahedral iron is widely justified by the previous MS study on this sample (Stroink *et al.* 1980) showed that about 60% of total iron belongs to magnetite. Hence, assigning all tetrahedral iron to magnetite/maghemite and taking into account its contribution for octahedral Fe^{2+} and Fe^{3+}, UICC chrysotile sample displays ferric iron prevailing over ferrous iron (in agreement with Bowes and Farrow, 1997) both in octahedral coordination (Fig. 4.2.1).

In the Balangero chrysotile, XANES data suggest comparable fractions of Fe^{2+} and Fe^{3+}, with a pre-edge peaks centroid position at 7114.04 eV (Table 3.2.9). The total pre-edge peaks area of 0.074 points to iron mainly in octahedral environment, with possible minor presence of tetrahedral iron. EXAFS refinements show two site positions: a first shell of four oxygen atoms at distance of 1.770 Å (attributed to tetrahedral ferric iron from magnetite) and another with six oxygen atoms at 2.054 Å (Table 3.2.10), consistent with

an octahedral environment halfway between Fe^{2+} and Fe^{3+} (theoretical distances 2.140 Å and 2.015 Å, respectively). Based on MS results (Table 3.1.15), about 30% of the total iron is attributed to magnetite and 70% to chrysotile.
Magnetite, given to the observed non-stoichiometric Fe^{3+}/Fe_{tot} ratio, shows a 10% oxidation to maghemite. In chrysotile Fe^{2+} is higher than Fe^{3+} (40% and 30% of Fe_{tot}, respectively). Although MS cannot discriminate iron present in chrysotile from iron present in other silicate (e.g. balangeroite), a relevant contribution from silicate impurities should be ruled out because: i) despite Val Malenco and Balangero chrysotiles are of different origin (with different silicate phase impurities) spectra are very similar; ii) silicate phase impurities have low iron content. In conclusion, from the convergence of XANES, EXAFS and MS data, it is possible to conclude that iron in chrysotile sample from Balangero is half ferrous and half ferric, both hosted in octahedrally-coordinated sites (Fig. 4.2.1).
Concerning the Val Malenco sample, XANES pre-edge centroid position at 7114.13 eV and total pre-edge peaks area of 0.072 indicate comparable fractions of Fe^{2+} and Fe^{3+} almost exclusively in 6-fold coordination (Table 3.2.9 and Fig. 4.2.1). EXAFS results are in agreement with XANES data and very similar to that of Balangero chrysotile with a first shell of four oxygen atoms at a distance of 1.810 Å and another with six oxygen atoms at 2.033 Å (Table 3.2.10) amongst the octahedral theoretical Fe^{2+}-O distance at 2.140 Å and the theoretical Fe^{3+}-O distance at 2.015 Å. Based on MS data (Table 3.1.15), 27% of the total iron belongs to magnetite and 73% to chrysotile.
Magnetite is partially oxidized to maghemite (in the order of 6%), in agreement with the low area of XANES pre-edge peaks, indicating low presence of tetrahedral iron (confirmed by EXAFS results). Hence, Val Malenco chrysotile displays comparable amount of Fe^{2+} and Fe^{3+} in octahedral position, very similar to that observed for Balangero chrysotile.

Erionite

In erionite, Fe^{3+} ions may virtually replace Al^{3+} ions in the framework or can be found in the extraframework cavities as octahedral free $Fe(H_20)_6{}^{3+}$ molecules whereas high-spin Fe^{2+} can be octahedrally coordinated in extraframework sites (Roque-Malherbe *et al.* 1990). It was also reported iron in the form of Fe^{3+}-bearing oxide-like nanoparticles, on the external surface of the silica walls of a fibrous erionite from Rome, Oregon, USA (Ballirano *et al.* 2009; 2015). In our erionite sample, XANES data confirm the presence of only Fe^{3+}, having a pre-edge peaks centroid position at 7114.65 eV (Table 3.2.9) and in agreement with MS results (Table 3.1.15). The pre-edge peaks area of 0.076 reveals that iron is hosted only in octahedrally-coordinated positions, confirmed also by the EXAFS results, with a first shell of six oxygen atoms at a mean distance of 2.011 Å (Table 3.2.10). The absence of magnetic sextets in MS data (typical of iron oxide), allows to assess that oxide-like nanoparticles, if present, must have a dimension under the resolution limit of the measurement, namely <18 nm (Ballirano *et al.* 2009; Fierro *et al.* 2011).
Moreover is important to note that, concerning XPS analyses, the deconvolution of the Fe $2p_{3/2}$ peak was possible, although the iron content of the sample (from EMPA) was largely insufficient. This is probably due to the fact that iron is only found on the surface of the fibres. To support this hypothesis, TEM analysis were performed on this sample (using a TEM JEM 2010, 200 Kv, supplied at CIGS, University of Modena and Reggio Emilia) and the observations evidenced spherical particles (<10 nm) on the surface of the fibres (Fig. 4.2.3a); locally, clusters of these particles were detected. EDS analysis reveals that such clusters are enriched in iron with respect to the bulk (Fig. 4.2.3b).

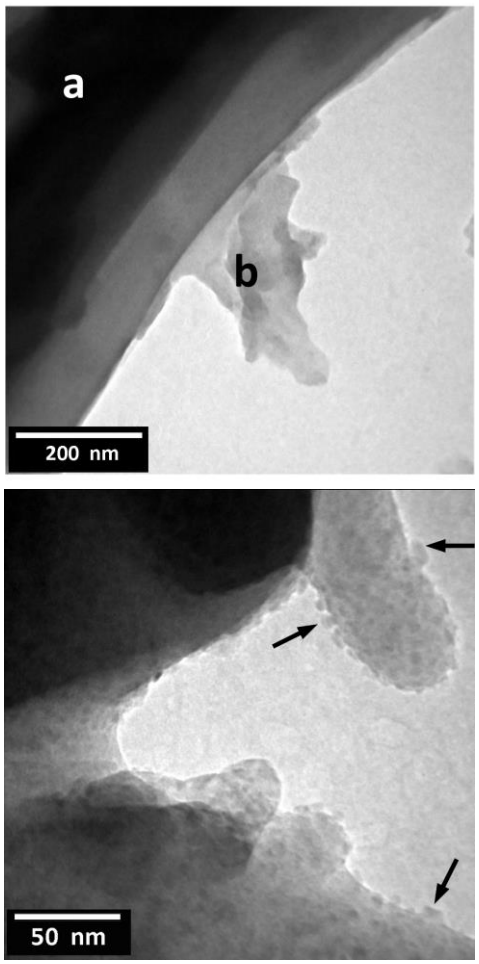

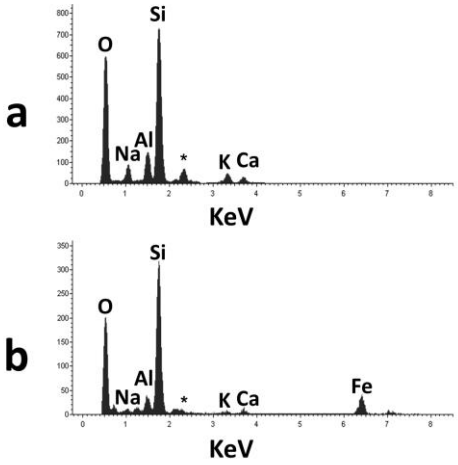

Fig. 4.2.3. High-resolution TEM images of erionite sample: (a) fibre with spherical nanoparticles on the surface (indicated by arrows); (b) clustering of particles (indicated with the letter b) with EDS spectra; *contaminant from the grid.

These results are preliminary and requires further experimental evidence to definitely rule out the possibility of iron present as 6-fold coordinated extraframework cation in the zeolite cages. However, in the investigated erionite, iron seems to be in octahedral coordination inside oxide-like nanoparticles present at the surface of the fibres. Notably, this conclusion is in perfect agreement with that of Ballirano *et al.* (2009 and 2015) despite the different origin of the samples investigated.

4.2.2 The role of iron concerning the toxicity of mineral fibres

Iron in mineral fibres may be responsible for carcinogenic activity namely via ROS/RNS production during the frustrated phagocytosis-induced inflammatory burst (Kamp and Weitzman, 1999). Reactive $HO^{\bullet}$ are responsible for secondary geno-toxicity via damage to proteins and DNA, cell injury/mutation, nucleotide coenzyme destruction, membrane damage, apoptosis, lipid peroxidation (Bucher *et al.* 1983), and fibre encapsulation by collagen and iron-rich proteins (Liu *et al.* 2013). It is the synergy of (i) fibrous-asbestiform crystal habit which triggers off frustrated phagocytosis and production of H_2O_2 and (ii) active iron present at the surface of the fibres, to be the key factor of potential fibre toxicity as it promotes the formation of reactive $HO^{\bullet}$ species by the surface Fenton reaction chain. In this frame, the findings reported in Turci *et al.* (2011) on synthetic chrysotile are of paramount importance: a fibre that does not contain iron is non-reactive in terms of ROS generation and cellular damage.

However, even a very small amount of iron induces radical reactivity, cyto- and geno-toxicity. Iron-containing particles such as hematite (Craighead and Gibbs, 2008) and magnetite are not active.

Hematite has a lamellar crystal habit and magnetite is sub-spherical. Their crystal habit promotes complete internalization (Champion and Mitragotri, 2006) without ROS production. For crocidolite, the ability to be mobilized from the fibre surface (surface activity), rather than the amount of iron in the crystal lattice, are important for the generation of ROS (Fenoglio *et al.* 2001). In contrast to crocidolite, chrysotile is not rich in iron and the surface is less effective at generating hydroxyl radicals (Gulumian and Van Wyk, 1991).

The collected results in this thesis show that in all investigated mineral fibres, iron is found in octahedral cavities. Fe^{3+} is in a peripheral octahedral cavity *M*(2) in amphiboles and inside the octahedral sheet in chrysotiles. In erionite it is present as octahedrally coordinated Fe^{3+} likely in surface oxide nanoparticles. Fe^{2+} is hosted in the internal octahedral cavities *M*(1) and *M*(3) in amphiboles and inside the octahedral sheet in chrysotiles. It should be remarked that Fe^{2+} is located in the innermost structure positions inside the crystal lattice less affected by oxidation. To cause production of $HO^{\bullet}$ species, such iron must be available at the surface of the mineral fibre in contact with the organic medium. At the fibre surface, even Fe^{2+} ions are stable in the acidic pH environment of the lysosomes vacuoles (Wang *et al.* 2010).

Because production of $HO^{\bullet}$ species requires iron to be available at the surface of the mineral fibre in contact with H_2O_2 released in the organic medium, during the persistent inflammatory activity, a dependency upon the dissolution rate of the fibre is also expected (Craighead and Gibbs, 2008) as progressive dissolution of the fibre structure made bulk iron available at the surface. Although the experiments about the dissolution kinetics of chrysotiles and amphiboles are still in progress, some semi-quantitative conjectures to link the dissolution time of the fibres to the amount of iron converted from bulk iron to surface iron can be made. If a mean 0.1 µm diameter fibre size for convenience is assumed (as available literature data refer to this mean diameter size) together with a zero order reaction (compatible with the model described in Guldberg *et al.* 1998) for the bulk dissolution of the fibre, the estimated total dissolution time of the fibre in organic medium at pH = 4 (in days) are: amosite = ca. 2500 d, chrysotile = ca. 239 d, crocidolite = ca. 5000 d (Table 2 in Gualtieri *et al.,* 2012), and tremolite = ca. 18250 d (Rozalen *et al.,* 2013), in the span of time of the dissolution of chrysotile (239 d), the following amount of iron (Fe^{2+} + Fe^{3+} wt%, calculated from the chemical formulas) is released: amosite = 3.0 wt%, chrysotile = 1.1-2.3 wt%, crocidolite = 1.3 wt%, and tremolite = 0.02 wt%. If we assume anthophyllite to have the same dissolution rate of crocidolite, the amount of total iron released in 239 d is 0.37 wt%. Hence, a proposed ranking of ability of asbestos fibres to generate *available surface iron-related* (pristine bulk iron made available at the surface of the fibre during the dissolution process) hydroxyl radicals may be: amosite > crocidolite ≈ chrysotile > anthophyllite > tremolite.

The ranking intentionally does not include erionite which requires an individual explanation. It is well known that although exposure to erionite is less widespread, this zeolite species is more potent than chrysotile asbestos in causing mesothelioma (Coffin *et al.* 1992; Carbone *et al.*, 2007). Erionite is fibrous-asbestiform, it possesses a very low dissolution rate in acid media (Eborn and Aust, 1995), and also the total iron content is low (Fe^{3+} only = 0.55 wt%) thus, *available surface iron-related* hydroxyl radicals should be in principle negligible.

On the other hand, if we assume that Fe^{3+}-rich oxide nanoparticles are all concentrated at the fibre surface, despite total content of iron is low, it is all available at the fibre surface and may be dissolved at pH = 4, forming active Fenton $Fe(OH)^{2+}$ groups in acid solution, as sketched in Fig. 4.2.4a (Cornell and Schwertmann, 1996).
It can be speculated that the remain of such dissolution process is a monolayer of $Fe(OH)^{2+}$ groups retained at the zeolite surface as this molecular group fits the 6-membered ring present in the erionite framework with a tetrahedral T2 site composing the 6-membered window rich in Al^{3+} (Cametti *et al.*, 2013) as drafted in Fig. 4.2.4b.

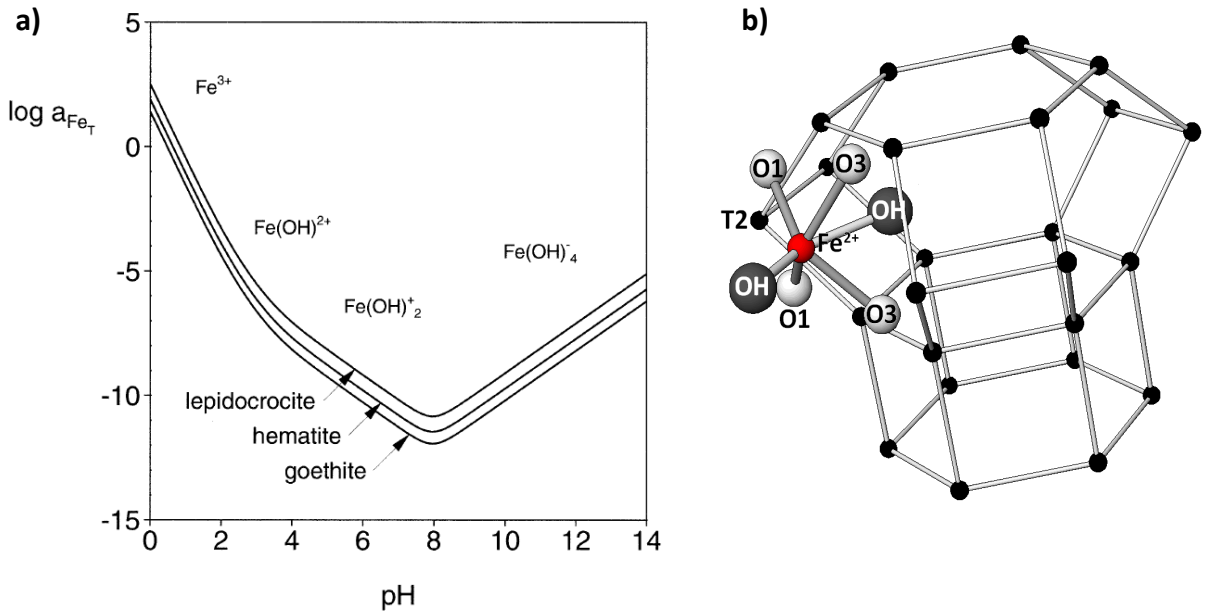

Fig. 4.2.4. a) Solubilities of goethite, hematite and lepidocrocide as a function of pH (from Cornell and Schwertmann, 1996); b) Scheme of how the $Fe(OH)^{2+}$ groups could remain retained at the 6-membered ring present in the erionite framework and rich in Al^{3+}.

The data collected at MCX beamline (ELETTRA) using anomalous scattering XRPD will be crucial to validate the proposed model, but they are still in progress and require the support of TEM data.
The selectivity for the 6-membered ring of erionite for iron is in concert with the empirical prediction reported in Fubini and Mollo (1995) who postulated that only a few surface iron species on mineral samples are in the right redox and coordination state to be active in the hydroxyl radical production. The predicted density of such surface iron sites should be relevant as all iron is originally present as fibre coating of Fe^{3+}-rich oxide nanoparticles. This model is in agreement with the findings reported in Fach *et al.* (2003) on synthetic Fe-exchanged erionite. Moreover, the model plausibly applies to most of the natural erionite samples, such as erionite-K from Rome, Oregon, U.S.A. (Ballirano *et al.*, 2009) and explains the affinity for iron of this zeolite species.

4.3 Changes of mineral fibres in contact with human cell cultures

As reported in paragraph 2.2.4, representative samples of crocidolite UICC, chrysotile UICC, chrysotile Val Malenco and erionite have been treated with culture diploid human non tumorigenic bronchial epithelial (Beas2B) and pleural transformed mesothelial (MeT5A) cells. The differences in the behaviour of the fibres in contact with both pleural and bronchial cell cultures with up to 96 h *ct* will eventually support a general model explaining the toxicity of these relevant mineral fibres and shed light on the global issue of chrysotile. The results obtained for each fibre species will be discussed in detail.

Chrysotile UICC

The distribution of iron in the XRF maps which belongs to the fibres allow to indirectly observe if overall variations of their crystal habit occur in contact with the cells. Within the intrinsic resolution limits of the data, chrysotile fibres seem not to change their overall crystal habit with residence time in the organic cultures (see for example Figs. 2.4.11, 3.2.13 and 3.2.14) despite peak broadening and disappearance of major reflections observed in µ-XRD spectra of the samples treated for 96h *ct* in both cell cultures (Fig. 3.2.15 and 3.2.18) clearly indicate amorphization of the crystalline structure. Amorphization seems to occur via a *pseudo-morphosis* process where fibres change their molecular arrangement without macro/microscopic modification. *Pseudo-morphosis* has already been reported for chrysotile treated at temperature higher than 700 °C (Giacobbe *et al*. 2010) with the difference that at high temperature, recrystallization drives the transformation from chrysotile to forsterite at a molecular scale (see an example in Fig. 4.3.1).

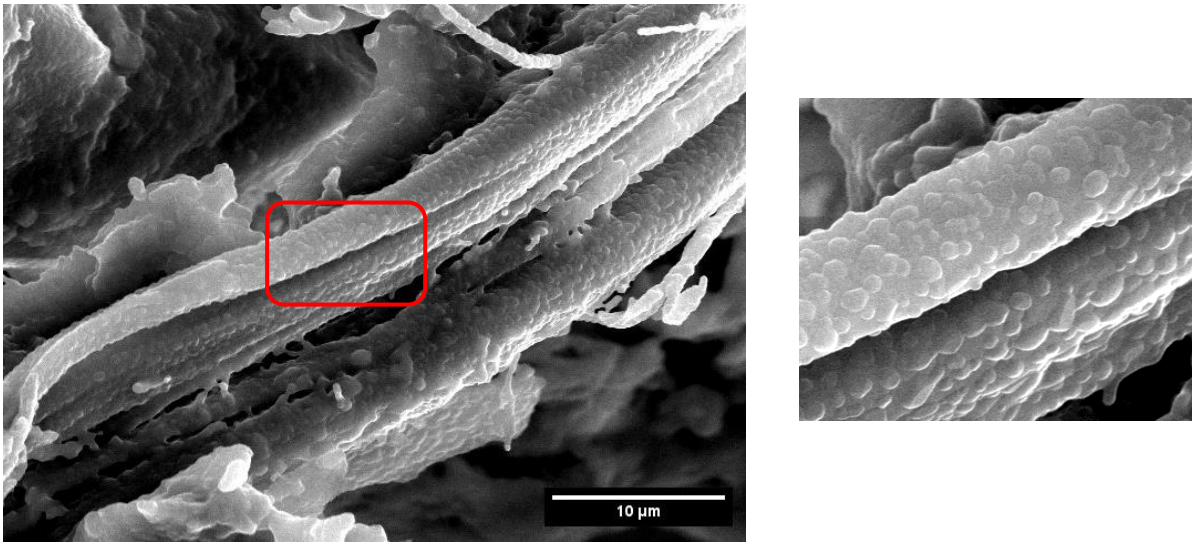

Fig. 4.3.1. SEM image of a pseudo-morphic chrysotile fibre, recrystallized following heat treatment; on the right, a magnification of the highlighted area showing clearly the recrystallisation, is reported.

Here, (*pseudo-morphic*) amorphization of the fibres is the mechanism observed at atomic scale. A TEM study recently confirmed these observations with amorphization of the fibres driven by mobilization of Mg (Vigliaturo, 2015). This mechanism of amorphization consists of differential dissolution of the Mg-centered octahedral layer: Hargreaves and Taylor (1946) reported that if chrysotile is leached with diluted acid, the magnesia layer can be removed and the structure of original chrysotile is amorphous in type.

Seshan (1983) reported that through acid attack, chrysotile surface became silica-like and Mg is lost from the fibres during amorphization. Wypych *et al*. (2005) also reported that the acid-leached product of chrysotile consisted of layered hydrated disordered silica with a distorted structure, resembling the silicate layer existing in the original mineral. Similar observations are also reported in Bernstein *et al*. (2013), Fig. 4.3.2.

Fig. 4.3.2. Chrysotile Fiber Disintegration: The magnesium is dissolved at neutral pH and the silica matrix is broken up at acid pH (From Bernstein *et al*. 2013).

XRF maps also show that the process of amorphization does not occur via a simple contracting dissolution process, with release of ions in the organic suspension, as apparently the distribution of iron within and around the fibres does not change from 24 to 96h treatment. It is then conceivable to postulate that the mechanism of *pseudo-morphic* amorphization is the first step of dissolution of chrysotile, taking place in the first days/weeks in contact with organic medium. Later, dissolution *sensu stricto* (physical-chemical dissolution of the fibres) should occur with a much slower kinetic rate as the nature of the reactant (residual Mg-poor and silica rich fibre) is much less cooperative to dissolve in acid environment. Although the reaction rate of this second step is much slower (the estimated total dissolution time of chrysotile fibres with a diameter of 0.1 µm is 239 d; Pollastri *et al*. 2015, paper 2, pag. 169), evidence of dissolution *sensu stricto* is given by long term and *in vivo* studies that witness of a limited biodurability of chrysotile fibres.

If the product of *pseudo-morphic* amorphization is a highly reactive silica rich fibre with a surface analogous in nature to that of quartz or cristobalite, the toxic potential of the fibre may be even enhanced as, besides the activity of surface iron species, silanol groups (Si-OH) and ionized silanol groups (Si-O-) on the surface play a major role in interaction with membranes (Fubini *et al*., 1995). In lung lining fluid or in tissue fluid, these products of hemolytic cleavage can give rise to HO• and H_2O_2 (Donaldson *et al*., 1998).

The method of preparation of the samples was carried out to enrich the fibre content with respect to the organic matter to perform statistically meaningful electron microscopy (reported elsewhere) investigations and XRD experiments. Unfortunately, such method has a drawback: it may provoke dissolution of iron-rich organic aggregates such as asbestos bodies. But, in any case, our experiments with *ct* times as long as 96 h are in line with the literature data showing that asbestos bodies are rarely observed around fibres in contact with cell media for short times. This also apply to the fibres species crocidolite and erionite.

The positions of the XANES pre-edge peak centroids of the samples treated with both cell cultures from 24 to 96h *ct* revealed that most of iron is present as Fe^{3+} hosted in octahedral position, and that its chemical environment does not undergo major modifications with respect to untreated samples (Fig. 4.3.3).

Considering the already discussed key role of iron in determining the toxicity of mineral fibres, its persistence in the structure, and especially at the surface of the reacting fibres, may lead to production of highly reactive toxic $HO^{\bullet}$ species during the first step of the dissolution reaction observed here.
Regarding the values of the Lx profile parameter (Table 3.2.18), when in contact with bronchial Beas2B culture, peaks broadening due to *pseudo-morphic* amorphization is more intense compared to mesothelial MeT5A. This may indicate that Beas2B cells are more aggressive than mesothelial MeT5A cells. Such differences may be related to the different physical interaction of the cells with the fibres as bronchial cells display a ciliated globular shape with a mean cell diameter of 10 µm whereas mesothelial cells are predominantly flattened with a mean diameter of the cell disk of about 25 µm (Mutsaers, 2004).

Crocidolite UICC

Crocidolite fibres are apparently stable in the organic cultures (Fig. 3.2.13 and 3.2.14). Accordingly, peak broadening from the µ-XRD spectra of the samples treated for 96h *ct* in both cell cultures (Fig. 3.2.16, 3.2.19 and Table 3.2.18) is minor, indicating that amorphization, if any, is at a very preliminary stage. Peak intensities show some variations that are explained later in terms of structure modification. The very slow dissolution rate of crocidolite with respect to chrysotile is well documented in the literature (Hesterberg and Hart, 2000; Bernstein *et al*., 2013). In concert with our results, a recent TEM study confirmed our observations as UICC crocidolite in contact with bronchial and mesothelial cell cultures that shows slightly amorphized boundaries (Vigliaturo, 2015).
Although Pacella *et al*. (2014; 2015) reported a highly ordered crystal lattice for both crocidolite and tremolite in dissolution experiments using phosphate buffered solution at pH = 7.4 after 168 h, their high resolution TEM observations also showed the early formation of an amorphous layer which readily enriched in iron and prompted the formation of iron-rich nanoparticles. Such result is compatible with the findings of the present work, even if the detection of a thin iron-rich amorphous layer or nanoparticles is way beyond the resolution of the experiments.
XRD data point to a limited, if any, structure amorphization; on the other side, they witness of intrastructure modifications with cation migration and reorganization. In fact, although the analysis of the data collected at ID13 (ESRF) will be crucial to validate the proposed model, the results of the cation distribution of crocidolite after 96 h *ct* in both cell cultures (Table 3.2.19), evidence that Na atoms originally in the large interchain site labelled Am as well as Mg in the octahedral site M(1) migrate out of the structure. Fe^{2+} in the inner octahedral site also migrates from M(3) site. Pacella *et al*. (2014) also observed that the early dissolution of crocidolite promotes bulk Fe^{2+} sites to occur on the fibre surface. Preferential leaching of Mg and Na was also observed for crocidolite and tremolite during dissolution (Pacella *et al*., 2014; 2015). Shen *et al*. (2000) also reported initial ion exchange (mostly $Fe^{2+} \leftrightarrow Na^{+}$) for crocidolite after 2 h exposure to an iron chloride solution. For crocidolite fibres in contact with mice tissues, Gualtieri *et al*. (2013) observed intra-structure diffusion, with iron migrating from site M2 to site M1 although it is not possible to assess whether intra-structural iron oxidation occurs for crocidolite in contact with organic tissues. The cation mobilization seems to regard Na and possibly Ca too, in agreement with the picture drawn by Pascolo *et al*. (2013) who postulate cation mobilization as the first step of interaction of asbestos fibres with tissues.

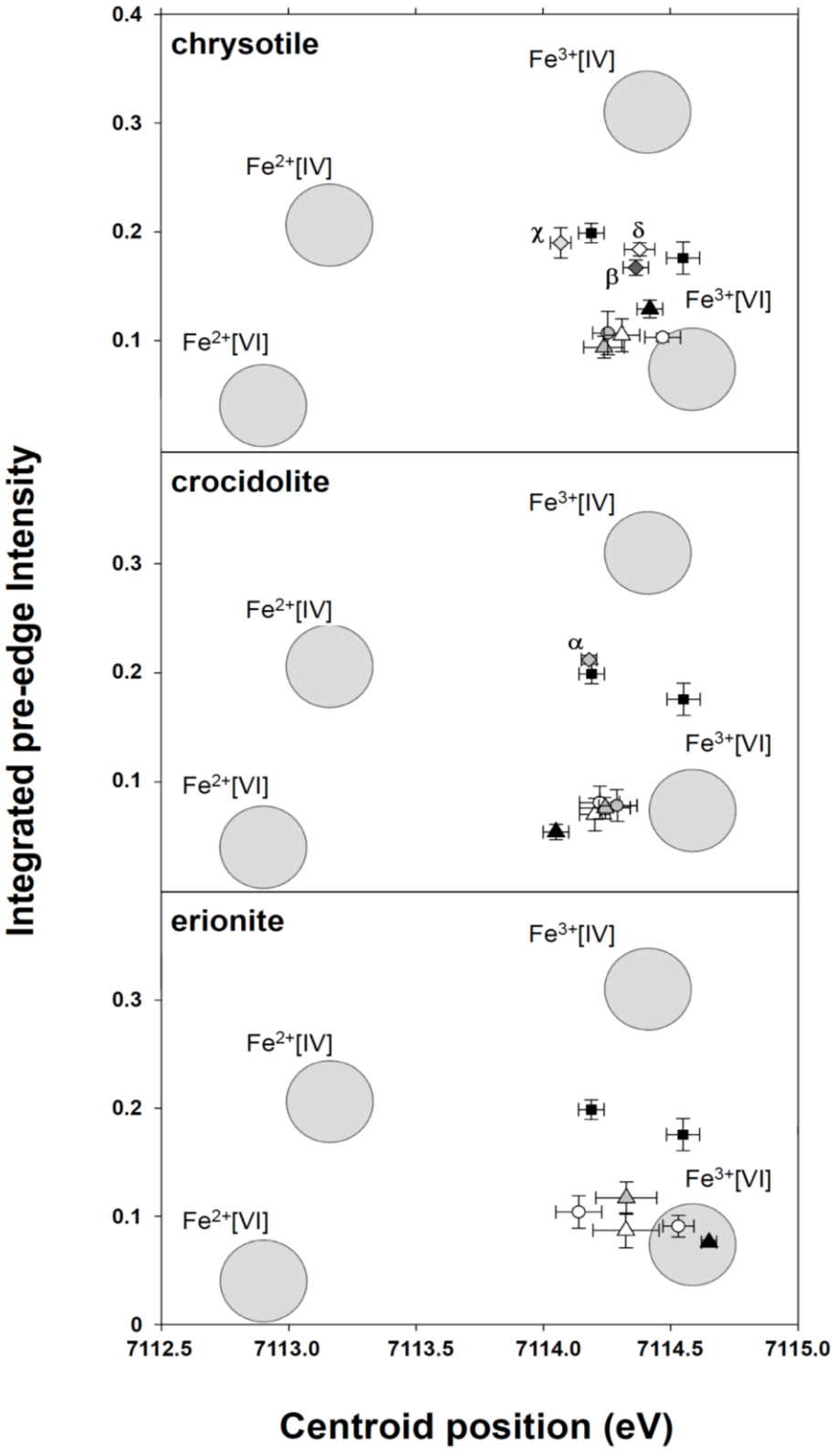

Fig. 4.3.3. Pre-edge parameters of samples plotted in the same variogram of Fig. 4.2.1. Grey fields designate pre-edge parameters for the Fe co-ordination and oxidation state. Legend: (■) Pre edge-parameters of standard samples of magnetite and maghemite; (▲) Parameters of the untreated samples.
Grey symbols: Samples treated with BeaS2B (circles 24h *ct*, triangles 96h *ct).*
White symbols: Samples treated with MeT5A (circles 24h *ct*, triangles 96h *ct)*.
Diamonds: magnetite-maghemite particles with greek letters indicating the point at which it was made the collection, as shown in Fig. 3.2.13 and 3.2.14.

From XANES pre-edge peaks parameters (Fig. 4.3.3) iron results slightly oxidized compared to the untreated sample, in agreement with the results obtained by Pacella *et al.* (2014) and Pollastri *et al*. (2015; paper 2, pag. 169). Iron oxidation of crocidolite, especially at the fibre surface is one of the key factors explaining the great cytotoxic potential of this mineral fibre. In fact, during the Fenton-type reactions, Fe^{2+} is oxidized by H_2O_2 with a chain reaction $H_2O_2 + HO^{\bullet} \rightarrow HO_2^{\bullet}/O_2^{\bullet} + H_2O$; $Fe^{3+} + HO_2^{\bullet}/O_2^{\bullet} \rightarrow Fe^{2+} + O_2 + H^+$ (family of catalysed Haber-Weiss reactions). The generated $HO^{\bullet}$ is thought to be the predominant damaging species *in vivo* because they are generated by elements such as iron often capable of binding to DNA itself allowing $HO^{\bullet}$ production to occur in the immediate vicinity of the DNA (Pryor, 1988).
The iron-rich sub-spherical particles observed in the maps consist of maghemite-magnetite particles (see for example Fig. 3.2.14, spot α) originally present as impurities in the raw fibres. None of the typical ferrihydrite broad bands (Drits *et al*., 1993) have been detected in the powder patterns.

Erionite

The presence of intense diffraction peaks (Fig. 3.2.17) and the slight variation observed in the Lx profile parameter at 96 h *ct* with respect to the 24 h *ct* data, (Table 3.2.18) confirm that this mineralogical specie hardly dissolves in acidic media (Eborn and Aust, 1995; Van Oss *et al*. 1999). The quality of the data does not allow to rule out the presence of a minor fraction of amorphous material which could be produced by an early step of amorphization (Vigliaturo, 2015).
After 96h *ct*, ion exchange and migration of Na atoms is observed (Table 3.2.19).
Mobility of Na cations has already recently reported for Na-erionite exchanged with Fe (Ballirano *et al*., 2015) and witness of a high mobility of this cation in contact with aggressive solutions. Also for erionite, XRD data collected at ID13 (ESRF) will be crucial to obtain a clear structure model of erionite in contact with organic tissues.
Concerning the XANES data, Fe^{3+} hosted in octahedral position is the prevailing species even for erionite, with its chemical environment that does not undergo major modifications with respect to untreated samples (Fig. 4.3.3). As iron-rich nanoparticle, it may quickly dissolve in contact with the cells, developing an acidic pH, to form low nuclearity active Fenton $Fe(OH)^{2+}$ groups which in turn oxidize via Fenton-type reactions prompting massive production of $HO^{\bullet}$; if these active Fenton groups persist at the zeolite surface during its low dissolution, this would explain the high potential cyto-toxicity of this mineral fibre.
In concert with literature data, a comparison of the dissolution mode of the three fibre species clearly suggests that chrysotile dissolves much faster that crocidolite and erionite. The first step of chrysotile dissolution occurs via a *pseudo-morphic* amorphization and will be later followed by dissolution *sensu stricto* (physical-chemical dissolution of the fibres). Both crocidolite and erionite seem to react adapting their chemistry to the surrounding environment. They both release Na in suspension and crocidolite show a rearrangement of the Fe atoms in the octahedral cavities likely prompted by oxidation. The formation of a silica-rich fibre skeleton after *pseudo-amorphization* of chrysotile, characterized by silanol groups (Si-OH) and ionized silanol groups (Si-O-), may prompt production of HO• in synergy with surface iron species. If this proviso is correct, chrysotile may be much more reactive and cytotoxic *in vitro* in the (very) short term whereas the activity of crocidolite and erionite would be much more sluggish but persistent in the long term. In this frame, it is not surprising that chrysotile has been considered to be as potent as crocidolite in

activating leukocytes in the short term (van Oss *et al*., 1999). On the same line, MTT assay of cells' viability conducted up to 72 h in contact with mesothelial cells showed that chrysotile was more cytotoxic than crocidolite, with the highest percentage of apoptotic cells (4%) observed after 72 h of treatment with 10 µg/cm^2 of chrysotile (Levresse *et al*., 1997). The same authors also found that after crocidolite treatment p53 induction was lower than in chrysotile-treated cells and motivated the cytotoxic behaviour to the fibres' ability to induce DNA damage via generation of reactive oxygen species.
These results are described in the submitted paper Pollastri *et al.* 2016.

4.4 Towards a model explaining the toxicity of mineral fibres

Considering the huge amount of collected data and the obtained results, what can be said about mineral fibres? Surely, that the toxicity of a mineral fibre is determined by a multitude of factors, all strongly correlated with each other. In order to simplify, an outline of the defense mechanisms adopted by the body (and of the particular circumstances in which they are not effective) against mineral fibers deposited in the lungs, is reported below:

1. The first defence mechanism of the body is the filtration of the breathed air in the nasopharyngeal region (upper airways passages - nose, nasal cavity and throat, Fig. 4.4.1). In general, this filter is effective only for particles having an aerodynamic diameter >10 µm (the aerodynamic diameter is the diameter of a spherical particle that has the same settling velocity as another particle regardless of its shape, size or density), while smaller particles are deposited in the tracheobronchial and alveolar regions (Boubel *et al.*, 2013). These last are defined as regulated fibres (paragraph 1.1). This mechanism would be perfect, but mineral fibres are unusual from the morphological point of view, having small diameters (usually < 0.5 µm) and a wide range of lengths, from few microns up to decimetres (Gualtieri, 2012). Because of this, extremely long fibres penetrate and deposit beyond the ciliated airways (Donaldson, 2009).

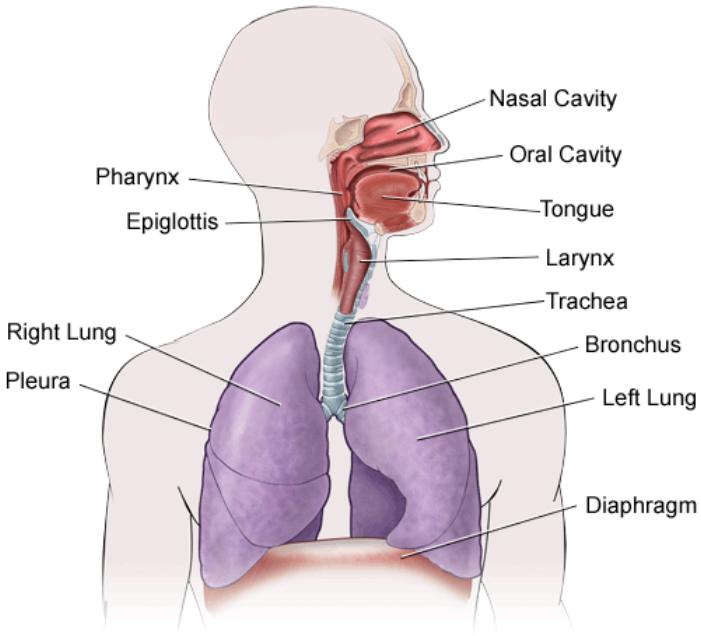

Fig. 4.4.1. Anatomy of the respiratory system

2. In the event that the fibres reach the lungs, the second defence mechanism of the body is the engulfment, acted by alveolar macrophages, of fibres shorter than their mean diameter (<10 µm) followed by an attempt to dissolve the embedded fibre within phagolysosomes (which develop an acidic chemical environment (pH = 4–4.5). This process take place in parallel to the mobilization of the particle-containing macrophages towards airways, where they are transported out from the lungs via mucociliary clearance.

However, this mechanism does not work or is not effective in the following cases:

- The fibres longer than 10-15 µm cannot be engulfed by macrophages (Stanton *et al.,* 1981; Searl *et al.,* 1999; Donaldson *et al.,* 2010) so frustrated phagocytosis accompanied by inflammatory burst occurs with release of highly reactive cyto- and geno-toxic substances occurring extracellularly (Fig. 4.4.2).
- Although physical engulfment is successful, the mechanism permits to dissolve only chrysotile but not crocidolite and erionite fibres. So, even though complete engulfment of short fibres occurs, such fibres cannot be dissolved, eventually promoting inflammatory activity and release of highly reactive cyto- and geno-toxic substances.
- The toxic substances can kill the macrophage cells before they can clear the engulfed particles, causing the immediate release of internal chemicals (Dodson and Hammar, 2011).
- Regardless of the nature of inhaled fibre, in overload conditions, the ability of macrophages to clear fibres from the alveoli is considerably reduced (Dodson and Hammar, 2011; Damjanov, 2012).

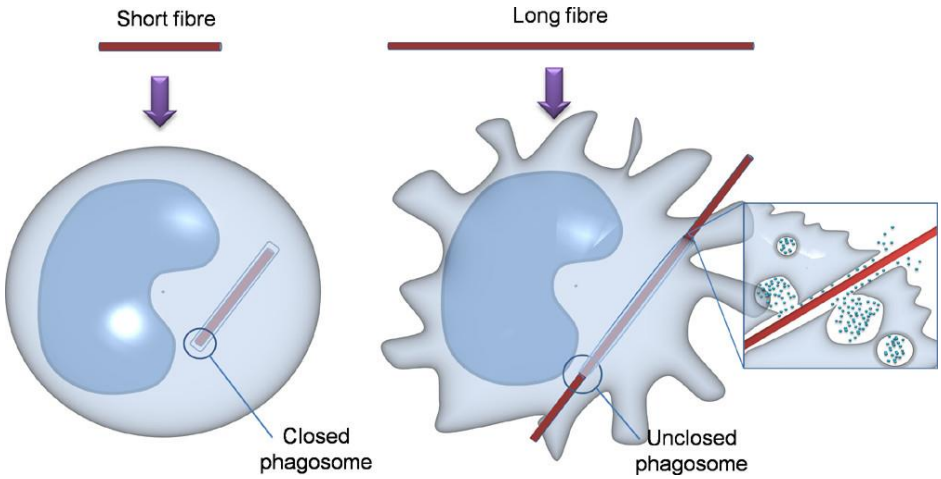

Fig. 4.4.2. Representation of short fibre complete phagocytosis and long fibre –mediated frustrated phagocytosis. Short fibres can be fully engulfed by macrophages whereas long fibres are too long to be fully taken up leading to an unclosed membrane and leakage of cell content. (From Schinwald and Donaldson, 2012).

3. At this point, the only available defence is the formation of asbestos bodies (ABs), aimed at isolating the toxic reactive fibre. But, in the situation in which the fibre cannot be cleared and before it can be fully isolated by the formation of an AB, its persistence inside the alveoli may be a constant source of inflammation, because:
   - The release of factors that promote a potent pro-inflammatory cytokine response from adjacent mesothelial cells, due to frustrated phagocytosis (Fig. 4.4.2; Schinwald and Donaldson, 2012).
   - The synergy of (i) fibrous-asbestiform crystal habit which triggers off frustrated phagocytosis and production of H2O2 and (ii) active iron present at the surface of the fibres promotes the formation of highly reactive ROS/RNS species via Fenton like chain reaction (Fig.4.4.3) (Kamp and Weitzman, 1999).

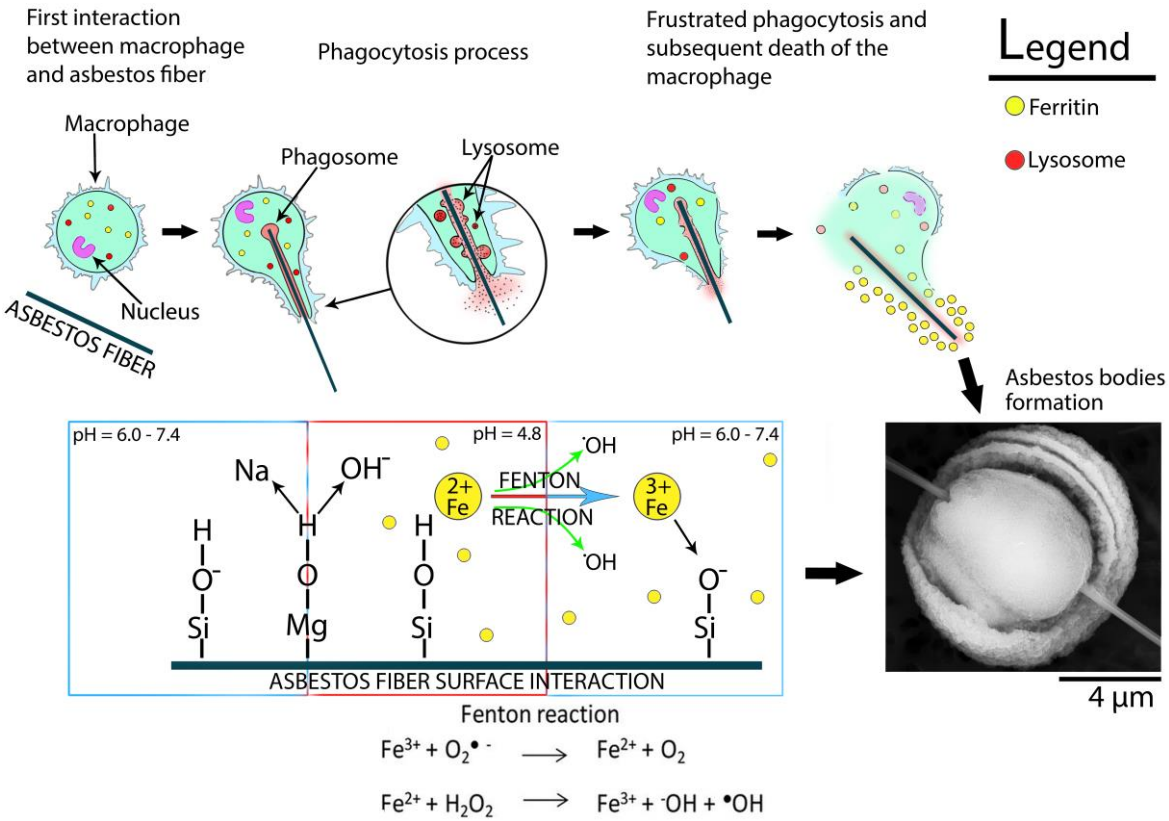

Fig. 4.4.3. Representation of frustrated phagocytosis and of the Fenton like chain reactions that occur at the surface of the fibres (Bursi Gandolfi, 2015 private comm.).

- If the product of *pseudomorphic* amorphization of chrysotile is an highly reactive silica-rich fibre with a surface analogous in nature to that of quartz or cristobalite, the toxic potential of the fibre may be even enhanced as, besides the activity of surface iron species, silanol groups (Si-OH) and ionized silanol groups (Si-O-) on the surface play a major role in interaction with membranes (Fubini *et al*., 1995). In lung lining fluid or in tissue fluid, these products of hemolytic cleavage can give rise to HO• and H_2O_2 (Donaldson *et al*., 1998).
- Fibre agglomeration, known to induce the highest biological responses (Gualtieri *et al.* 2012; Sharma *et al.* 2014), is favoured by the low and negative values of the ζ potential (in the range -10 to -26 mV).
- The sequestration of Ca^{2+} ions by the negatively charged mineral surface could undermine the apoptotic response, crucial to counteract the transforming potential of the carcinogenic fibres (Fig. 4.4.4).

Moreover, it should be considered that the coating process with ABs formation requires nutrients (namely Fe, P and other elements) to form the hemosiderin and porphyrins rich core of ABs. Nevertheless, considering the chemical stability of the fibres (especially crocidolite and erionite) in contact with the tissues, the release of active nutrients such as Fe is poor and cannot promote massive nucleation and growth of ABs. Hence, the source of Fe (but also P and other elements) to form the hemosiderin and porphyrins rich core of ABs must be organic, likely provided by cytoplasmic ferritin from phagocytes or from ferritin circulating in plasma.

Unfortunately, nutrients are physiologically limited in the organism and are likely not sufficient to provide coating of all asbestos fibres, especially in overload conditions (Bursi *et al.* 2015).

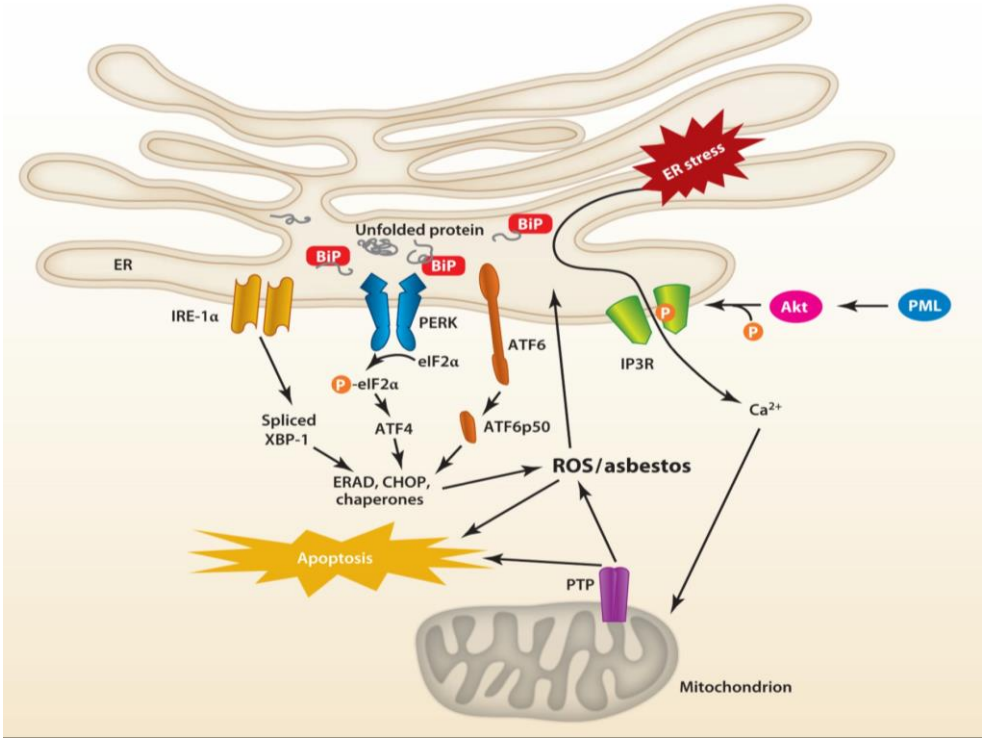

Fig. 4.4.4. Hypothetical model of mitochondria–endoplasmic reticulum (ER) cross talk in asbestos induced apoptosis. ER stress due to asbestos causes Ca^{2+} release and activation of an unfolded protein response (UPR), especially inositol-requiring kinase 1α (IRE-1α), which lead to activation of mitochondria-regulated apoptosis. But Ca^{2+} ions can be trapped by the negatively charged mineral surface and the entire mechanism could be compromised (image taken from Liu *et al.* 2013).

A special case concerns the erionite sample: its fibres possess an average size smaller than those of the macrophage (3.2 µm; Bursi *et al.* 2015) and therefore they can be completely engulfed, but not dissolved, given the great chemical stability of erionite in acidic environment. So, on the basis of the aforementioned mechanisms, the activation of the second defense mechanism of the body, namely the isolation of the fibers through the formation of ABs, should be observed.
However, in rats inoculated with erionite fibers, in no case ABs were observed (Bursi *et al.* 2015) and this is apparently in contrast with the literature data. In fact, it is known that erionite fibres can form bodies morphologically identical to typical ABs (Dumortier *et al.* 2001). Moreover, ABs were observed in BALF of villagers of Tuzköy (Turkey) exposed to erionite, but is important to note that erionite fibres from Tuzköy are much longer (65.7% of the fibres had a diameter greater than 4 µm) than the erionite fibres considered here.
Hence, ABs do not form probably because the size of the fibres is much shorter than 10 µm and phagocytosis actually occurs, and since ABs only nucleate on long fibres that cannot be engulfed and subject to complete phagocytosis, this second mechanism of defence is not necessarily invoked as phagocytosis is apparently successful. Unfortunately, we have seen that erionite is stable in acidic environment and then its fibres cannot be dissolved.

Also chrysotile from Val Malenco turns out to be different with respect to other chrysotiles: In fact, there are no literature data about relevant cases of exposure and subsequent diseases in the areas of occurrence of this mineral fibre. This could be related to the greater length of its fibres resulting in a low release of respirable fibres and/or in a release of fibres with a size that can be intercepted in the upper airways of the respiratory system. Another contributing cause could be related to the surface area of this sample, that is twice the surface area of the other chrysotiles, and could prompt a faster partial dissolution rate.

At the end of this paragraph, we can state that the mechanisms that lead to the onset of cancer (mainly lung cancer and pleural / peritoneal mesothelioma) are still unclear. But this lack of knowledge is not exclusive of the mineral fibres-related cancers, since although the connection between inflammation and cancer is generally accepted (Grivennikov *et al.* 2010; Grivennikov and Karin 2010; Gonda *et al.* 2009), several questions remain; for example, can inflammation cause neoplasia in the absence of an exogenous carcinogenic agent? (Mantovani *et al.* 2008). The exact mechanisms by which a wound-healing process turns into cancer are actual topics of intense research (Reuter *et al.* 2010 and references therein); for these reasons, the only thing that can be said is that in the case the inflammation lasts for a longer period of time compared to acute inflammation (namely chronic inflammation), the host can be predisposed to various chronic diseases, including cancer (Lin and Karin, 2007).

From all these considerations, a list of chemical-physical characteristics that a mineral must possess to be considered potentially toxic, can be defined. It is important to emphasize the fact that it seems to be the simultaneous presence of several factors in determining the toxicity potential of mineral fibers. An excellent example is iron: We have seen how the presence of active iron present at the surface of the fibres is a key factor of toxicity as it promotes the formation of reactive HO• species by the surface Fenton reaction chain (Fig. 4.4.3).

Nevertheless, iron-containing particles such as hematite (Craighead and Gibbs, 2008) and magnetite seems to be not active! The explanation could lie in their crystal habit (lamellar for hematite and sub-spherical for magnetite) which promotes full engulfment by macrophage (Mitragotri and Champion, 2006) without ROS production.

So, in order to develop a general model describing the toxicity of mineral fibres, all the physical-chemical characteristics relevant to the toxicity could be incorporated into a sort of general empirical formula and quantified, in order to gain a final value which is a function of the degree of toxicity potential of that mineral (an example is reported in Table 4.4.1). This general model of classification (actually in progress) would be very useful to predict a priori the toxicity potential of unknown mineral fibre, in order to prevent new cases of mass exposure as that of Biancavilla (Italy) for fluoro-edenite (Comba *et al.* 2003) and Tuzcöy (Turkey) for erionite (Dumortier *et al.* 2001).

Table 4.4.1
Parameters considered in the model of toxicity.

Macro-parameter	Label	Parameter	Related toxicity paramet.
Fibre size and morphometric	1a	Aspect ratio/length	Frustrated phagocytosis and/or inflammatory burst
	1b	Inhalation aerodynamic diameter	Airways deposition depth
	1c	Asbestiform crystal habit	Airways deposition depth
	1d	Density of the fibre	Airways deposition depth
	1e	Hygroscopic vs. hydrophobic character	Airways deposition depth
Content of iron and toxic elements	2a	Normalized Fe content	Production of free radicals
	2b	Surface vs. bulk Fe	Production of free radicals
	2c	Fe^{2+} vs. Fe^{3+}	Production of free radicals
	2d	Toxic elements other than Fe	Various toxic bio-chemical reactions, ROS production
Biodurability/ dissolution	4a	Biodurability (fiber dissolution rate)	Frustrated phagocytosis, chronic inflammation
	4b	Biodurability (rate of iron release)	Production of free radicals
	4c	Production of silica relicts during dissolution	Production of free radicals
	4d	Rate of release of active toxic elements	Various toxic bio-chemical reactions, ROS production
Surface charge	5a	ζ Potential (surface chemical interaction)	ROS production, toxic bio-chemical reactions, interference with ER cross-talk.
	5b	ζ Potential (aggregation of fibres)	Frustrated phagocytosis, chronic inflammation

5 – CONCLUSIONS

The aim of this thesis was the characterization of the main mineral fibres of social and economic-industrial importance starting with a full mineralogical-structural and microstructural investigations, in order to explain the nature of the biological interaction mechanisms of chrysotile, amphiboles and erionite and compare them so to draw a convincing rank of toxicity of mineral fibres.
The characterization of samples was performed using a combination of several analytical techniques, both from conventional and non-conventional sources. The collected data allowed to determine the impurities present within the samples and to calculate their crystal chemical structure. In addition, special attention was given to the surface reactivity of the fibers, measuring the surface area and the ζ potential in various chemical-physical conditions. The structural environment of iron has been extensively studied as well, through X-ray Absorption and Fe^{57} Mössbauer spectroscopy.
The achieved results allowed to determine that:

- The specific surface area of chrysotile is about 3.3 times that of amphibole for short fibre samples, and about 4.5 times for long fibre samples whereas erionite has a surface area halfway between chrysotile and amphiboles.

- In double distilled water, chrysotiles show positive values of the ζ potential (with the exception of chrysotile from Val Malenco), whereas amphiboles and erionite show negative values. In contact with organic solutions, all fibres display negative and similar values of ζ potential, clearly showing that this parameter cannot be considered a discriminating factor when it is measured in conditions that reproduce the cell environment. This could impair the apoptotic response, crucial to counteract the transforming potential of the carcinogenic fibres, through sequestration of Ca^{2+} ions by the negatively charged mineral surface.

- All investigated fibres possess iron in octahedral cavities, with Fe^{2+} ions located in the innermost structure positions inside the crystal lattice less affected by oxidation. Taking into account the much shorter dissolution time of chrysotile with respect to amphiboles (although the latter are much more rich in iron) the release of iron could be comparable. This finding may indicate that the overall toxicity potential of chrysotile is not lower than that of amphiboles, since production of hydroxyl radicals requires iron to be available at the surface of the mineral fibre in contact with H_2O_2 released in the organic medium, during the persistent inflammatory activity.

- Erionite turns out to be a special case since iron seems to be present as octahedrally coordinated Fe^{3+} likely inside a surface coating of oxide nanoparticles available at the surface.

- Considering the dissolution rates and the iron content, a proposed ranking of ability of asbestos fibres to generate *available surface iron-related* (pristine bulk iron made available at the surface of the fibre during the dissolution process) hydroxyl radicals may be: amosite > crocidolite ≈ chrysotile > anthophyllite > tremolite. The ranking intentionally does not include erionite, since its toxicity model and the exact location of iron should be validated.

- The contact of chrysotile fibres with human cell cultures leads to amorphization, interpreted as the first dissolution step, later followed by dissolution *sensu stricto*. Crocidolite shows minor early signs of amorphization whereas erionite seems to be the more stable fibre species in contact with the cells. The formation of a silica-rich fibre skeleton after *pseudo-amorphization* of chrysotile may prompt the production of $HO^{\bullet}$ in synergy with surface iron species; this could indicate that chrysotile may be much more reactive and cytotoxic *in vitro* in the (very) short term whereas the activity of crocidolite and erionite would be much more sluggish but persistent in the long term.

Considering the collected data, all the mechanisms that activate when a mineral fibre comes in contact with the human body have been schematically summarized.
In order to develop a general model describing the toxicity of mineral fibres, the combination of physical and chemical characteristics should be considered in determining the potential toxicity of a fiber (such as size, presence of iron, biodurability). These characteristics could be incorporated into a sort of general empirical formula, and quantified in order to gain a final value which is a function of the toxicity potential of that mineral. This general model would be very useful to predict a priori the toxicity potential of unknown mineral fibre, in order to prevent new cases of mass exposure.

6 – WORK IN PROGRESS AND FUTURE PERSPECTIVES

In order to understand the mechanisms determining the toxicity of mineral fibres and get a comprehensive model, some aspects still need to be clarified. Regarding erionite, it will be of fundamental importance to confirm the presence of iron at the surface of the fibres. In this regard, the analysis of XRPD data collected at ELETTRA in proximity of the absorption K-edge of iron (about 7 keV) and at 10 keV will be crucial; in addition, the data must be confirmed by further and detailed TEM analysis.

Another fundamental piece of the puzzle will be represented by the results of the dissolution experiments (currently in progress) of fibres in contact with SLF solutions at acidic pH, which can give a figure (for the first time systematically) about the dissolution rates of amphiboles, chrysotile and erionite, in conjunction with SEM and XRPD analysis of the treated material at different times, in order to evaluate which elements are released in relation to the contact time and to confirm definitively the amorphization of chrysotile as a first step of its dissolution.

These data must be then compared with the XRD data collected at ID13 on fibres extracted from rat tissues, in order to understand the reliability of the dissolution experiments and to identify (and of course justify) any possible differences that exist between *in vivo* and *in vitro* experiments. In fact, prudence must be taken in extrapolating results based on instillation in experimental animals to human inhalation because, similarly to inhalation induced studies (Bernstein *et al.* 2013), the fibre burdens due to injection process in the intrapleural/intraperitoneal space of the rats may be excessive or unreliable if compared to both nasal inhalation in the rats and human inhalation as no fibre sorting through the upper respiratory tracts occurs. Moreover, there may be a fibre aggregation effect during instillation to form sort of fibre bundles that would be very unlikely to reach the intrapleural/intraperitoneal space, where normal inhalation takes place.

Regarding the chrysotile issue, it will be useful to fully characterize chrysotile fibres within human lungs, in order to verify the crystallinity of the fibres in real exposure conditions and to correlate the results to those obtained from dissolution experiments and from fibres extracted from rat tissues.

Once completed the collection and interpretation of all data, it will be necessary to try to summarize the characteristics relevant to the toxicity of a mineral fibre, in order to define a general toxicity model. The obtained model should be tested on unknown mineral fibres from the toxicological point of view. Potential candidates for this test could be zeolitic minerals such as mordenite and ferrierite (which are rather common in many different rock types) since their crystal habit can be fibrous and they can be classified as regulated; in addition, iron can be present at their surface in the form of impurity or in the crystal lattice.

7 - REFERENCES

Alberti, A., Martucci, A., Galli, E., & Vezzalini, G. (1997). A reexamination of the crystal structure of erionite. *Zeolites*, *19*(5), 349-352.

Allen, M. P., & Smith, R. W. (1975). Dissolution of asbestos minerals in acid and buffered salt solutions. 3rd Conf. *Intern. Phys. Chem. Minéral. Asbestos. Québec: Univ. Laval, Sect*, 4-16.

Andreozzi, G. B., Ballirano, P., Gianfagna, A., Mazziotti-Tagliani, S., & Pacella, A. (2009). Structural and spectroscopic characterization of a suite of fibrous amphiboles with high environmental and health relevance from Biancavilla (Sicily, Italy). *Am. Min., 94(10)*, 1333-1340.

ATSDR (Agency for Toxic Substances and Disease Registry) (2001). Chemical-specific health consultation: tremolite asbestos and other related types of asbestos. Atlanta, GA: U. S. Department of Health and Human Services.

Bailey, S. W. (1988) Hydrous phyllosilicates (exclusive of micas), *Rev. Mineral. 19*, pp 725.

Ballirano, P., Andreozzi, G. B., & Belardi, G. (2008). Crystal chemical and structural characterization of fibrous tremolite from Susa Valley, Italy, with comments on potential harmful effects on human health. *Am. Min.*, *93*(8-9), 1349-1355.

Ballirano, P., Pacella, A., Cremisini, C., Nardi, E., Fantauzzi, M., Atzei, D., ... & Cametti, G. (2015). Fe (II) segregation at a specific crystallographic site of fibrous erionite: A first step toward the understanding of the mechanisms inducing its carcinogenicity. *Microporous and Mesoporous Materials*, *211*, 49-63.

Ballirano, P., Andreozzi, G. B., Dogan, M., & Dogan, A. U. (2009). Crystal structure and iron topochemistry of erionite-K from Rome, Oregon, USA. *Am. Min., 94(8-9)*, 1262-1270.

Bancroft, G. M., Maddock, A. G., Burns, R. G., & Strens, R. G. J. (1966). Cation distribution in anthophyllite from Mössbauer and infra-red spectroscopy. *Nature, 212*, 913–915.

Bancroft, G. M., Burns, R. G., & Maddock, A. G. (1967). Determination of cation distribution in cummingtonite-grunerite series by Mössbauer spectra. *Am. Min.*, *52*(7-8), 1009.

Bard, D., Yarwood, J., & Tylee, B. (1997). Asbestos fibre identification by Raman microspectroscopy. *J. Raman Spect.*, *28*(10), 803-809.

Bariş, B., Demir, A. U., Shehu, V., Karakoca, Y., Kisacik, G., & Bariş, Y. I. (1995). *Env.* fibrous zeolite (erionite) exposure and malignant tumors other than mesothelioma. *J. of Env. pathology, Toxicol. Oncol.: official organ of the International Society for Env. Toxicol. Cancer, 15(2-4)*, 183-189.

Basham, M., Filik, J., Wharmby, M. T., Chang, P. C., El Kassaby, B., Gerring, M., Aishima, J., Levik, K., Pulford, B. C. A., Sikharulidze, I., Sneddon, D., Webber, M., Dhesi, S. S., Maccherozzi, F., Svensson, O., Brockhauser, S., Náray, G. & Ashton, A. W. (2015*).* Data Analysis WorkbeNch (DAWN). *J. Sync. Rad., 22(3)*, 853-858.

Baumann, F., Ambrosi, J. P., & Carbone, M. (2013). Asbestos is not just asbestos: an unrecognized health hazard. *Lancet Onc.*, *14*(7), 576-578.

Becklake, M. R., Bagatin, E., & Neder, J. A. (2007). Asbestos-related diseases of the lungs and pleura: uses, trends and management over the last century [State of the Art Series. Occupational lung disease in high-and low-income countries, Edited by M. Chan-Yeung. Number 3 in the series]. *Int. J. Tub. Lung Dis., 11(4)*, 356-369.

Benarie, M. (1986). Asbestiform fibers—Nonoccupational health risks: prepared by a Committee of the National *Res.* Council, National Academy Press, Washington DC, 1984, 334 pp.

Bernstein, D. M. (2014). The health risk of chrysotile asbestos. *Current opinion in pulmonary medicine, 20(4)*, 366-370.

Bernstein, D. M., Donaldson, K., Decker, U., Gaering, S., Kunzendorf, P., Chevalier, J., & Holm, S. E. (2008). A biopersistence study following exposure to chrysotile asbestos alone or in combination with fine particles. *Inhalation Toxicol.*, *20*(11), 1009-1028.

Bernstein, D. M., Dunnigan, J., Hesterberg, T., Brown, R., Velasco, J. A. L., Barrera, R., Hoskins J., & Gibbs, A. (2013). Health risk of chrysotile revisited. *Critical Rev. Toxicol.*, *43*(2), 154-183.

Bish, D. L., & Post, J. E. (1993). Quantitative mineralogical analysis using the Rietveld full-pattern fitting method. *Am. Min.*, *78*(9-10), 932-940.

Blaauw, C., Stroink, G., Leiper, W., & Zentilli, M. (1979) Mössbauer analysis of some canadian chrysotiles*, Can. Min., 17*, 713–717.

Bloise, A., Catalano, M., Barrese, E., Gualtieri, A. F., Gandolfi, N. B., Capella, S., & Belluso, E. (2015). TG/DSC study of the thermal behaviour of hazardous mineral fibres*. J. Thermal Anal. Cal.*, 1-15.

Bonneau, L., Suquet, H., Malard, C., & Pezerat, H. (1986). Studies on surface properties of asbestos: I. Active sites on surface of chrysotile and amphiboles. *Env. Res., 41*(1), 251-267.

Boubel, R. W., Vallero, D., Fox, D. L., Turner, B., & Stern, A. C. (2013). *Fundamentals of air pollution*. Elsevier.

Bowes, D. R., & Farrow, C. M. (1997). Major and trace element compositions of the UICC standard asbestos samples. *Am. J. Ind. Med.*, *32*(6), 592-594.

Broaddus, V. C. (2001). Apoptosis and asbestos-induced disease: Is there a connection?. *Journal of Laboratory and Clinical Medicine*, *137*(5), 314-315.

Brown, D. M., Kinloch, I. A., Bangert, U., Windle, A. H., Walter, D. M., Walker, G. S., Scotchford, C. A., Donaldson, K., & Stone, V. (2007). An in vitro study of the potential of carbon nanotubes and nanofibres

Brunauer, S., Emmett, P. H., & Teller, E. (1938). Adsorption of gases in multimolecular layers. *J. Am. Chem. Soc., 60(2)*, 309-319.

Bucher, J. R., Tien, M., & Aust, S. D. (1983). The requirement for ferric in the initiation of lipid peroxidation by chelated ferrous iron. *Biochem. Biophys. Res. Comm.*, *111*(3), 777-784.

Cameron, M., & Papike, J. J. (1979). Amphibole crystal chemistry: A review. *Fort. Min.*, *57*, 28-67.

Cametti, G., Pacella, A., Mura, F., Rossi, M., & Ballirano, P. (2013). New morphological, chemical, and structural data of woolly erionite-Na from Durkee, Oregon, USA. *Am. Min.*, *98*(11-12), 2155-2163.

Carbone, M., Emri, S., Dogan, A. U., Steele, I., Tuncer, M., Pass, H. I., & Baris, Y. I. (2007). A mesothelioma epidemic in Cappadocia: scientific developments and unexpected social outcomes. *Nature Rev. Cancer*, *7*(2), 147-154.

Carbone, M., Yang, H., Pass, H. I., Krausz, T., Testa, J. R., & Gaudino, G. (2013). BAP1 and cancer. *Nature Rev. Cancer*, 13(3), 153-159.

Castranova, V., VanDyke, K., Wu, L., Dalal, N. S., & Vallyathan, V. (1996). Suppression of silica-induced toxicity with organosilane surface coating. *Silica and Silica-induced Lung Disease, CRC Press, Inc., Boca Raton, FL*, 283-291.

Ceglia, A., Nuyts, G., Cagno, S., Meulebroeck, W., Baert, K., Cosyns, P., Nys, K., Thienpont, H., Janssens K., & Terryn, H. (2014). A XANES study of chromophores: the case of black glass. *Anal. Met.*, 6(8), 2662-2671.

Champion, J. A., & Mitragotri, S. (2006). Role of target geometry in phagocytosis. *Proceedings of the National Academy of Sciences of the United States of America*, *103*(13), 4930-4934.

Cho, W. S., Duffin, R., Thielbeer, F., Bradley, M., Megson, I. L., MacNee, W., Craig Poland, A., Lang Tran, C., & Donaldson, K. (2012). Zeta potential and solubility to toxic ions as mechanisms of lung inflammation caused by metal/metal-oxide nanoparticles. *Toxicol. Sciences, 126*(2), 469–477

Coffin, D. L., Cook, P. M., & Creason, J. P. (1992). Relative mesothelioma induction in rats by mineral fibers: comparison with residual pulmonary mineral fiber number and epidemiology. *Inhalation Toxicol., 4*(3), 273-300.

Comba, P., Gianfagna, A., & Paoletti, L. (2003). Pleural mesothelioma cases in Biancavilla are related to a new fluoro-edenite fibrous amphibole. *Arch. Env. Health*: *An Int. J.*, 58(4), 229-232.

Coombs, D.S., Alberti, A., Armbruster, T., Artioli, G., Colella, C., Galli, E., Grice, J.D., Liebau, F., Mandarino, J.A., Minato, H., Nickel, E.H., Passaglia, E., Peacor, D.R., Quartieri, S., Rinaldi R., Ross, M., Sheppard, R.A., Tillmanns, E., & Vezzalini, G. (1997). Recommended nomenclature for zeolite minerals: Report of the subcommittee on zeolites of the *Int.* Mineralogical Association, Commission on New Minerals and Mineral Names. *Can. Min.*, *35*, 1571-1606.

Cornell, R. M., & Schwertmann, U. (1996). The iron oxide. *VCH, New York*, pp. 573.

Craighead, J. E., Abraham, J. L., Churg, A., Green, F. H., Kleinerman, J., Pratt, P., Seemayer, T.A,, Vallyathan V,, & Weill, H. (1982). The pathology of asbestos-associated diseases of the lungs and pleural cavities: diagnostic criteria and proposed grading schema. Report of the Pneumoconiosis Committee of the College of American Pathologists and the National Institute for Occupational Safety and Health. *Arc. Pat. Lab. Med.*, 106(11), 544.

Craighead, J. E., & Gibbs, A.R. (2008). Asbestos and its Diseases, Oxford University Press, pp. 403.

Cressey, B. A., Cressey, G., & Cernik, R. J. (1994). Structural variations in chrysotile asbestos fibers revealed by synchrotron X-ray diffraction and high-resolution transmission electron microscopy. *Can. Min.*, *32*, 257-257.

Croce, A., Musa, M., Allegrina, M., Rinaudo, C., Baris, Y. I., Dogan, A. U., Powers, A., Rivera, Z., Bertino, P., Yang, H., Gaudino, G. & Carbone, M. (2013). Micro-Raman spectroscopy identifies crocidolite and erionite fibers in tissue sections. *J. Raman Spect.*, *44*(10), 1440-1445.

Damjanov, I., (2012) Atlas of Histopathology, Jaypee Brothers Medical Publishers (P) LTD, pp. 393.

De Grave, E., & Van Alboom, A. (1991). Evaluation of ferrous and ferric Mössbauer fractions. *Phys. Chem. Min.*, *18*(5), 337-342.

De Waele, J. K., Verhaert, I., Vansant, E. F., & Adams, F. C. (1983). Laser microprobe mass analysis (LAMMA) and adsorption study of aliphatic alkylammonium ions and alkylamines on asbestos fibre surfaces. *Surf. Inter. Anal.*, *5*(5), 186-192.

Devouard, B., & Baronnet, A. (1995). Axial diffraction of curved lattices: geometrical and numerical modeling. Application to chrysotile. *Eu. J. Min.*, 835-846.

Dikensoy, O. (2008). Mesothelioma due to environmental exposure to erionite in Turkey. *Curr. Op. Pulm. Med.*, *14*(4), 322-325.

Dinnebier, R. E., & Billinge, S. J. (2008). Powder diffraction: theory and practice. Royal society of chemistry.

Dodson, R. F., Atkinson, M. A., & Levin, J. L. (2003). Asbestos fiber length as related to potential pathogenicity: a critical review. *American journal of industrial medicine*, *44*(3), 291-297.

Dodson, R. F., & Hammar, S. P. (Eds.). (2011). *Asbestos: risk assessment, epidemiology, and health effects*. CRC press.

Dogan, A. U., & Dogan, M. (2008). Re-evaluation and re-classification of erionite series minerals. *Env. Geochem. Health*, *30*(4), 355-366.

Doll, R. (1993). Mortality from lung cancer in asbestos workers 1955. *British J. Ind. Med.*, *50*(6), 485.

Donaldson, K. (2009). The inhalation toxicology of *p*-aramid fibrils. *Critical Rev. toxicol.*, *39*(6), 487-500.

Donaldson, K., & Borm, P. J. (1998). The quartz hazard: a variable entity. *Ann. Occ. Hygiene*, *42*(5), 287-294.

Donaldson, K., Murphy, F. A., Duffin, R., & Poland, C. A. (2010). Asbestos, carbon nanotubes and the pleural mesothelium: a review of the hypothesis regarding the role of long fibre retention in the parietal pleura, inflammation and mesothelioma. *Part. fibre Toxicol.*, *7*(1), 1-17.

Droop, G. T. R. (1987). A general equation for estimating Fe^{3+} concentrations in ferromagnesian silicates and oxides from microprobe analyses, using stoichiometric criteria. *Min. Mag.*, *51*(361), 431-435.

Dumortier, P., Coplü, L., Broucke, I., Emri, S., Selcuk, T., De Maertelaer, V., De Vuist, P., & Baris, I. (2001). Erionite bodies and fibres in bronchoalveolar lavage fluid (BALF) of residents from Tuzköy, Cappadocia, Turkey. *Occ. Env. Med.*, *58*(4), 261-266.

Dyar, M.D., Mackwell, S.M., McGuire, A.V., Cross, L.R., & Robertson, J.D., (1993). Crystal chemistry of Fe^{3+} and H^{+} in mantle kaersutite: Implications for mantle metasomatism. *Am. Min.*, *78*, 968-979.

Emri, S., Demir, A., Dogan, M., Akay, H., Bozkurt, B., Carbone, M., & Baris, I. (2002). Lung diseases due to *Env.* exposures to erionite and asbestos in Turkey. *Toxicol. Lett., 127*(1), 251-257.

Fach, E., Waldman, W. J., Williams, M., Long, J., Meister, R. K., & Dutta, P. K. (2002). Analysis of the biological and chemical reactivity of zeolite-based aluminosilicate fibers and particulates. *Env. Health Perspect.*,*110*(11), 1087.–1096.

Falini, G., Foresti, E., Gazzano, M., Gualtieri, A. F., Leoni, M., Lesci, I. G., & Roveri, N. (2004). Tubular-Shaped Stoichiometric Chrysotile Nanocrystals. *Chem. Eu. J.*, *10*(12), 3043-3049.

Fantauzzi, M., Pacella, A., Atzei, D., Gianfagna, A., Andreozzi, G. B., & Rossi, A. (2010). Combined use of X-ray photoelectron and Mössbauer spectroscopic techniques in the analytical characterization of iron oxidation state in amphibole asbestos. *Anal. Bioanal. Chem.*, *396*(8), 2889-2898.

Farmer, V. C. (1974). *Infrared spectra of minerals*. Mineralogical society.

Fenoglio, I., Prandi, L., Tomatis, M., & Fubini, B. (2001). Free radical generation in the toxicity of inhaled mineral particles: the role of iron speciation at the surface of asbestos and silica. *Redox Rep.*, *6*(4), 235-241.

Ferraris, G., & Ivaldi, G. (2002). Structural features of micas. *Rev. Min. Geochem.*, *46*(1), 117-153.

Fierro, G., Moretti, G., Ferraris, G., & Andreozzi, G. B. (2011). A Mössbauer and structural investigation of Fe-ZSM-5 catalysts: Influence of Fe oxide nanoparticles size on the catalytic behaviour for the NO-SCR by C_3H_8. *App. Cat. B: Env.*, *102*(1), 215-223.

Finger, L. W. (1969). The crystal structure and cation distribution of a grunerite. *Mineralogical Society of America Special Paper*, *2*, 95-100.

Fubini, B., Bolis, V., Cavenago, A., & Volante, M. (1995). Physicochemical properties of crystalline silica dusts and their possible implication in various biological responses. *Scandinavian J. Work, Env. & Health*, 9-14.

Gabor, S., & Anca, Z. (1975). Effect of asbestos on lipid peroxidation in the red cells. *British J. Ind. Med.*, *32*(1), 39-41.

Gandolfi, N. B., Gualtieri, A. F., Pollastri, S., Tibaldi, E., & Belpoggi, F. (2016). Assessment of asbestos body formation by high resolution FEG–SEM after exposure of Sprague–Dawley rats to chrysotile, crocidolite, or erionite. *J. Haz. Mat.* , 306, 95-104.

Gard, J. A., & Tait, J. M. (1973). Refinement of the crystal structure of erionite. In *Proc. 3rd Int. Conf. Mol. Sieves* (pp. 94-99).

Gard, J. A., & Tait, J. M. (1972). The crystal structure of the zeolite offretite, $K_{1.1}Ca_{1.1}Mg_{0.7}[Si_{12.8}Al_{5.2}O_{36}]*15.2H_2O$. *Acta Cryst. Section B: Struct. Cryst. Crystal Chem.*, *28*(3), 825-834.

Giacobbe (2012) Doctorate Thesis in Earth Sciences, Doctoral School of Multiscale Modelling, Computational Simulation and Characterization in Material Science, . University of Modena and Reggio Emilia, Italy.

Giacobbe, C., Gualtieri, A. F., Quartieri, S., Rinaudo, C., Allegrina, M., & Andreozzi, G. B. (2010). Spectroscopic study of the product of thermal transformation of chrysotile-asbestos containing materials (ACM). *Eu. J. Min.* , *22*(4), 535-546.

Gianfagna, A., Andreozzi, G. B., Ballirano, P., Mazziotti-Tagliani, S., & Bruni, B. M. (2007). Structural and chemical contrasts between prismatic and fibrous fluoro-edenite from Biancavilla, Sicily, Italy. *The Can. Min.*, 45(2), 249-262.

Gigli L. (2014) Doctorate Thesis in Earth Sciences, Doctoral School of Earth System Sciences Environment, Resources and Cultural Heritage, Department of Chemical and Geological Sciences, University of Modena and Reggio Emilia, Italy.

Gonda, T. A., Tu, S., & Wang, T. C. (2009). Chronic inflammation, the tumor microenvironment and carcinogenesis. *Cell Cycle*, *8*(13), 2005-2013.

Gottardi, G., & Galli, E. (1985). Natural Zeolites. Springer Berlin Heidelberg. pp 409.

Greenwood, N. N., & Gibb, T. C. (1971). Mössbauer spectroscopy. London: Chapman and Hall.

Grivennikov, S. I., Greten, F. R., & Karin, M. (2010). Immunity, inflammation, and cancer. *Cell*, *140*(6), 883-899.

Grivennikov, S. I., & Karin, M. (2010). Inflammation and oncogenesis: a vicious connection. *Current opinion in genetics & development*, *20*(1), 65-71.

Gualtieri, A. F., Artioli, G., Passaglia, E., Bigi, S., Viani, A., & Hanson, J. C. (1998). Crystal structure-crystal chemistry relationships in the zeolites erionite and offretite. *Am. Min.*, *83*(5-6), 590-606.

Gualtieri, A. F. (2000). Accuracy of XRPD QPA using the combined Rietveld–RIR method. *J. App. Cryst.*, *33*(2), 267-278.

Gualtieri, A. F. (2012). Mineral fibre-based building materials and their health hazards. In F. Pacheco-Torgal, S. Jalali, and A. Fucic, Eds., Toxicity of Building Materials, pp. 166–195. Woodhead, Cambridge.

Gualtieri, A. F., Giacobbe, C., Rinaudo, C., Croce, A., Allegrina, M., Gaudino, G., Yang, H., & Carbone, M. (2013). Preliminary results of the spectroscopic and structural characterization of mesothelioma inducing crocidolite fibers injected in mice. *Per. Min.*, *82*(2).

Gualtieri, A. F., Viani, A., Sgarbi, G., & Lusvardi, G. (2012). In vitro biodurability of the product of thermal transformation of cement–asbestos. *J. Haz. Mat.* , *205*, 63-71.

Gualtieri, M., Skuland, T., Iversen, T. G., Låg, M., Schwarze, P., Bilaničová, D., Pojana, C., & Refsnes, M. (2012). Importance of agglomeration state and exposure conditions for uptake and pro-inflammatory responses to amorphous silica nanoparticles in bronchial epithelial cells. *Nanotoxicol.*, *6*(7), 700-712.

Guldberg, M., Christensen, V. R., Perander, M., Zoitos, B., Koenig, A. R., & Sebastian, K. (1998). Measurement of in-vitro fibre dissolution rate at acidic pH. *Ann. Occ. Hygiene*, *42*(4), 233-243.

Gulumian, M., & van Wyk, J. A. (1991). Oxygen Consumption, Lipid Peroxidation and Mineral Fibres. In *Mechanisms in Fibre Carcinogenesis* (pp. 439-446). Springer US.

Hannila, H. H., & Hallman, E. D. (1979). The adsorption of gold sols on asbestos surface charge sites. *Powder Tec.*, *23*(2), 149-157.

Hardy, J. A., & Aust, A. E. (1995). Iron in asbestos chemistry and carcinogenicity. *Chem. Rev.*, *95*(1), 97-118.

Hawthorne, F. C. (1978). The crystal chemistry of the amphiboles. VIII. The crystal structure and site chemistry of fluoro-riebeckite. *Can. Min.*, *16*, 187-194.

Hawthorne, F. C. (1981). Crystal chemistry of the amphiboles. *Rev. Min. Geochem.*, *9*(1), 1-102.

Hawthorne, F. C. (1983). The crystal chemistry of the amphiboles, *Can. Min., 21*, 173–480.

Hawthorne, F. C., & Della Ventura, G. (2007). Short-range order in amphiboles. *Rev. Min. Geochem.*, *67*(1), 173-222.

Hillerdal, G. (1999). Mesothelioma: cases associated with non-occupational and low dose exposures. *Occ. Environ. Med.*, *56*(8), 505-513.

Hollan, J. P. & Smith, D. D. (2001). Asbestos, Clinical Environmental Health and Exposures, 2nd Edition, Lippincott Williams and Wilkins, Philadelphia, pp. 1214-1227.

Hornung, V., Bauernfeind, F., Halle, A., Samstad, E. O., Kono, H., Rock, K. L.,Fitzgerald, K.A., & Latz, E. (2008). Silica crystals and aluminum salts activate the NALP3 inflammasome through phagosomal destabilization. *Nature Imm.*, *9*(8), 847-856.

Hunter, R. J., (1981). Zeta Potential in Colloid Science. Principles and Applications. New York: Academic Press, p. 386.

Jagodzinski, V. H., & Bagchi, S. N. (1954). Die gerollte Struktur des Chrysotils. *Neues Jahrbuch für Mineralogie: Monatshefte*, 97.

Kamp, D. W. (2009). Asbestos-induced lung diseases: an update. *Trans. Res.*, *153*(4), 143-152.

Kamp, D. W., & Weitzman, S. A. (1999). The molecular basis of asbestos induced lung injury. *Thorax*, *54*(7), 638-652.

Kanarek, M. S. (2011). Mesothelioma from chrysotile asbestos: update. *Annals Ep., 21*(9), 688-697.

Kawahara, A., & Curien, H. (1969). La structure cristalline de l'érionite. *Bull. Soc. Française Min. Crist.*, *92*, 250-256.

Kaya, A., & Yukselen, Y. (2005). Zeta potential of clay minerals and quartz contaminated by heavy metals. *Can. Geotec. J.*, *42*(5), 1280-1289.

Lagarec, K., & Rancourt, D. G. (1998). Mössbauer spectral analysis software for windows 1.0. Department of Physics, University of Ottawa, Canada.

Larson, A. C., & Von Dreele, R. B. (1988). Generalized structure analysis system. University of California.

Larson, T. C., Antao, V. C., & Bove, F. J. (2010). Vermiculite worker mortality: estimated effects of occupational exposure to Libby amphibole. *J. Occ. Env. Med.*, *52*(5), 555-560.

Law, A. D. (1989). Studies of the orthoamphiboles. IV. Mössbauer spectra of anthophyllites and gedrites. *Min. Mag.*, *53*, 181-91.

Lemen, R. A., Dement, J. M., & Wagoner, J. K. (1980). Epidemiology of asbestos-related diseases. *Env. Health Perspect., 34*, 1.

Leoni, M., Gualtieri, A. F., & Roveri, N. (2004). Simultaneous refinement of structure and microstructure of layered materials. *Journal of applied crystallography*, *37*(1), 166-173.

Li, M., Gunter, M. E., & Fukagawa, N. K. (2012). Differential activation of the inflammasome in THP-1 cells exposed to chrysotile asbestos and Libby "six-mix" amphiboles and subsequent activation of BEAS-2B cells. *Cytokine*, *60*(3), 718-730.

Light, W. G., & Wei, E. T. (1977). Surface charge and hemolytic activity of asbestos. *Env. Res.*, *13*(1), 135-145.

Lin, W. W., & Karin, M. (2007). A cytokine-mediated link between innate immunity, inflammation, and cancer. *J. of Clinical Investigation*,*117*(5), 1175-1183.

Liu, G., Cheresh, P., & Kamp, D. W. (2013). Molecular basis of asbestos-induced lung disease. *Ann. Rev. Pathol.*, *8*, 161.

Liu, W., Ernst, J. D., & Courtney Broaddus, V. (2000). Phagocytosis of crocidolite asbestos induces oxidative stress, DNA damage, and apoptosis in mesothelial cells. *Am. J. Res. Cell Mol. Biol.*,*23*(3), 371-378.

Long, G. J., Cranshaw, T. E., & Longworth, G. (1983). The ideal Mössbauer effect absorber thickness. *Mössbauer Effect Reference and Data J., 6*(2), 42-49.

Maltoni, C., & Minardi, F. (1989). Recent results of carcinogenicity bioassays of fibres and other particulate materials. Non-occupational exposure to mineral fibers. *IARC scientific publications, (90),* 46-53.

Mantovani, A., Allavena, P., Sica, A., & Balkwill, F. (2008). Cancer-related inflammation. *Nature*, *454*(7203), 436-444.

Martinez, E., & Zucker, G. L. (1960). Asbestos ore body minerals studied by zeta potential measurements. *J. Phys. Chem.*, *64*(7), 924-926.

Mirabelli, D., Calisti, R., Barone-Adesi, F., Fornero, E., Merletti, F., & Magnani, C. (2008). Excess of mesotheliomas after exposure to chrysotile in Balangero, Italy. *Occ. Env. Med.*, *65*(12), 815-819.

Mobilio, S., Boscherini, F., & Meneghini, C. (Eds.). (2014). *Synchrotron Radiation: Basics, Methods and Applications*. Springer.

Mosselmans, J. F. W., Quinn, P. D., Dent, A. J., Cavill, S. A., Moreno, S. D., Peach, A., Leicester, P.J., Keylock, S.J., Gregory, S.R., Atkinson, K.D., & Rosell, J. R. (2009). I18-the microfocus spectroscopy beamline at the Diamond Light Source. *J. Sync. Rad. , 16*(6), 818-824.

Mossman, B. T., & Churg, A. (1998). Mechanisms in the pathogenesis of asbestosis and silicosis. *Am. J. Res. Crit. Care Med.*, *157*(5), 1666-1680.

Mossman, B. T., Bignon, J., Corn, M., Seaton, A., & Gee, J. B. (1990). Asbestos: scientific developments and implications for public policy. *Science, 247*(4940), 294-301.

Mossman, B. T., Kamp, D. W., & Weitzman, S. A. (1996). Mechanisms of carcinogenesis and clinical features of asbestos-associated cancers. *Can. Invest., 14*(5), 466-480.

Mottana, A. (2004). X-ray absorption spectroscopy in mineralogy: Theory and experiment in the XANES region. in Spectroscopic Methods in Mineralogy ,A. Beran ,E. Libowi pp 465, 552.

Murad, E., & Cashion, J. (2011). *Mössbauer spectroscopy of environmental materials and their industrial utilization*. Springer Science & Business Media.

Newville, M. (2001). IFEFFIT: interactive XAFS analysis and FEFF fitting. *J. Sync. Rad., 8*(2), 322-324.

Newville, M. (2014). Fundamentals of XAFS. *Rev. in Min. Geochem. , 78*(1), 33-74.

NIOSH (National Institute of Occupational Safety and Health) (2011). Current Intelligence Bulletin 62. Asbestos fibers and other elongate mineral particles: State of the science and roadmap for research. Department of Health and Human Services, Centers for Disease Control and Prevention, DHHS (NIOSH) Publication Number 2011-159.

Nolan, R. P., Langer, A. M., Harington, J. S., Oster, G., & Selikoff, I. J. (1981). Quartz hemolysis as related to its surface functionalities. *Env. Res.*, *26*(2), 503-520.

Nygren, J., Suhonen, S., Norppa, H., & Linnainmaa, K. (2004). DNA damage in bronchial epithelial and mesothelial cells with and without associated crocidolite asbestos fibers. *Env. Mol. Mutag.*, *44*(5), 477-482.

O'Hanley, D. S., & Dyar, M. D. (1998). The composition of chrysotile and its relationship with lizardite. *Can. Min.*, *36*, 727-740.

Pacella, A., Andreozzi, G. B., Ballirano, P., & Gianfagna, A. (2008). Crystal chemical and structural characterization of fibrous tremolite from Ala di Stura (Lanzo Valley, Italy). *Per. Min.*, *77*(2), 51-62.

Pacella, A., Andreozzi, G. B., & Fournier, J. (2010). Detailed crystal chemistry and iron topochemistry of asbestos occurring in its natural setting: A first step to understanding its chemical reactivity. *Chem. Geol.*, *277*(3), 197-206.

Pacella, A., Andreozzi, G. B., Fournier, J., Stievano, L., Giantomassi, F., Lucarini, G., Rippo., M.R., & Pugnaloni, A. (2012). Iron topochemistry and surface reactivity of amphibole asbestos: relations with in vitro toxicity. *Anal. Bioanal. Chem.*, *402*(2), 871-881.

Pache, J. C., Janssen, Y. M., Walsh, E. S., Quinlan, T. R., Zanella, C. L., Low, R. B., Taatjes, D. J.& Mossman, B. T. (1998). Increased epidermal growth factor-receptor protein in a human mesothelial cell line in response to long asbestos fibers. *Am. J. Pathol.*, *152*(2), 333.

Pascolo, L., Gianoncelli, A., Schneider, G., Salomé, M., Schneider, M., Calligaro, C., Kiskinova, M., Melato, M., & Rizzardi, C. (2013). The interaction of asbestos and iron in lung tissue revealed by synchrotron-based scanning X-ray microscopy. *Sci. Rep.*, *3*.

Passaglia, E., Artioli, G., & Gualtieri, A. (1998). Crystal chemistry of the zeolites erionite and offretite. *Am. Min.*, *83*(5-6), 577-589.

Pfau, J. C., Sentissi, J. J., Weller, G., & Putnam, E. A. (2005). Assessment of autoimmune responses associated with asbestos exposure in Libby, Montana, USA. *Env. Health Perspect.*, 25-30.

Pokrovsky, O. S., & Schott, J. (2000). Forsterite surface composition in aqueous solutions: a combined potentiometric, electrokinetic, and spectroscopic approach. *Geochim. Cosmochim. Acta*, *64*(19), 3299-3312.

Polatoğlu, İ. (2005). Chemical behaviour of clinoptilolite rich natural zeolite in aqueous medium (Doctoral dissertation, İzmir Institute of Technology).

Pollastri, S., Gualtieri, A. F., Gualtieri, M. L., Hanuskova, M., Cavallo, A., & Gaudino, G. (2014). The zeta potential of mineral fibres. *J. Haz. Mat. , 276*, 469-479.

Pollastri, S., D'Acapito, F., Trapananti, A., Colantoni, I., Andreozzi, G. B., & Gualtieri, A. F. (2015). The chemical environment of iron in mineral fibres. A combined X-ray absorption and Mössbauer spectroscopic study. *J. Haz. Mat.* , *298*, 282-293.

Prasad, N. A., & Pooley, F. D. (1973). Characteristics of amphibole asbestos dust surfaces in aqueous media with reference to quartz. *J. App. Chem. Biotec.*, *23*(9), 675-687.

Prencipe, M., Noel, Y., Bruno, M., & Dovesi, R. (2009). The vibrational spectrum of lizardite-1T [$Mg_3Si_2O_5(OH)_4$] at the Γ point: A contribution from an ab initio periodic B3LYP calculation. *Am. Min.*, *94*(7), 986-994.

Pugnaloni, A., Lucarini, G., Giantomassi, F., Lombardo, L., Capella, S., Belluso, E Zizzi, A., Panico, A. M., Biagini, G. & Cardile, V. (2007). In vitro study of biofunctional indicators after exposure to asbestos-like fluoro-edenite fibres. *Cell Mol. Biol. (Noisy-le-grand)*, *53*(Suppl), OL965-980.

Pundsack, F. L. (1955). The Properties of Asbestos. I. The Colloidal and Surface Chemistry of Chrysotile. *J. Phys. Chem.*, *59*(9), 892-895.

Sadava, D., Heller, H. C., Orians, G. H., Purves, W. K., & Hillis, D. M. (2007). Life: The science of biology (ed.). USA: The Courier Companies.

Qi, F., Okimoto, G., Jube, S., Napolitano, A., Pass, H. I., Laczko, R., Demay, R.M., Khan, G., Tiirikainen, M., Rinaudo, C., Croce, A., Yang, H., Gaudino, G., Carbone, M. (2013). Continuous exposure to chrysotile asbestos can cause transformation of human mesothelial cells via HMGB1 and TNF-α signaling. *Am. J. Pat., 183*(5), 1654-1666.

Ramachandran, R., & Somasundaran, P. (1986). Effect of temperature on the interfacial properties of silicates. *Colloids and Surfaces*, *21*, 355-369.

Rancourt, D. G., & Ping, J. Y. (1991). Voigt-based methods for arbitrary-shape static hyperfine parameter distributions in Mössbauer spectroscopy. *Nuc. Inst. Met. in Physics Res. Section B: Beam Interactions with Materials and Atoms*, *58*(1), 85-97.

Rasband, W. S. (2008). ImageJ. *http://rsbweb. nih. gov/ij/*.

Ravel, Á., & Newville, M. (2005). ATHENA, ARTEMIS, HEPHAESTUS: data analysis for X-ray absorption spectroscopy using IFEFFIT. *J. Sync. Rad., 12*(4), 537-541.

Revil, A., Pezard, P. A., & Glover, P. W. J. (1999). Streaming potential in porous media: 1. Theory of the zeta potential. *J. Geophys. Res.: Solid Earth, 104*(B9), 20021-20031.

Riddick T.M. (1968) Control of Colloid Stability through Zeta Potential, Zeta-Mater Inc., New York, pp. 320–331.

Rietveld, H. M. (1967). Line profiles of neutron powder-diffraction peaks for structure refinement. *Acta Crystallographica*, *22*(1), 151-152.

Rietveld, H. M. (1969). A profile refinement method for nuclear and magnetic structures. *J. App. Cryst., 2*(2), 65-71.

Roggli, V. L., & Brody, A. R. (1984). Changes in numbers and dimensions of chrysotile asbestos fibers in lungs of rats following short-term exposure. *Exp. Lung Res.*, *7*(2), 133-147.

Roggli, V. L., & Brody, A. R. (1990). The role of electron microscopy in experimental models of pneumoconiosis. *Lung Biol. Health Dis.*, *48*, 315-343.

Roggli, V. L., Vollmer, R. T., Butnor, K. J. & Sporn, T. A. (2002). Tremolite and mesothelioma. *Ann. Occ. Hyg.*, *46*(5), 447-453.

Roque-Malherbe, R., Diaz-Aguila, C., Reguera-Ruiz, E., Fundora-Lliteras, J., López-Colado, L., & Hernández-Vélez, M. (1990). The state of iron in natural zeolites: A Mössbauer study. *Zeolites*, *10*(7), 685-689.

Roushdy-Hammady, I., Siegel, J., Emri, S., Testa, J. R., & Carbone, M. (2001). Genetic-susceptibility factor and malignant mesothelioma in the Cappadocian region of Turkey. *The Lancet*, *357*(9254), 444-445.

Rozalen, M., Ramos, M. E., Huertas, F. J., Fiore, S., & Gervilla, F. (2013). Dissolution kinetics and biodurability of tremolite particles in mimicked lung fluids: Effect of citrate and oxalate. *J. Asian Earth Sci.*, *77*, 318-326.

Sayers, D. E., Stern, E. A., & Lytle, F. W. (1971). New technique for investigating noncrystalline structures: Fourier analysis of the extended X-ray-absorption fine structure. *Phys. Rev. Lett., 27*(18), 1204.

Schinwald, A., & Donaldson, K. (2012). Use of back-scatter electron signals to visualise cell/nanowires interactions in vitro and in vivo; frustrated phagocytosis of long fibres in macrophages and compartmentalisation in mesothelial cells in vivo. *Part. Fibre Toxicol.*, *9*(1), 1.

Schlenker, J. L., Pluth, J. J., & Smith, J. V. (1977). Dehydrated natural erionite with stacking faults of the offretite type. *Acta Cryst. Section B: Str. Cryst. Chem.*, *33*(10), 3265-3268.

Searl, A., Buchanan, D., Cullen, R. T., Jones, A. D., Miller, B. G., & Soutar, C. A. (1999). Biopersistence and durability of nine mineral fibre types in rat lungs over 12 months. *Ann. Occ. Hygiene*, *43*(3), 143-153.

Sharma, G., Kodali, V., Gaffrey, M., Wang, W., Minard, K. R., Karin, N. J., Teeguarden, J. G., & Thrall, B. D. (2014). Iron oxide nanoparticle agglomeration influences dose rates and modulates oxidative stress-mediated dose–response profiles in vitro. *Nanotoxicol.*, *8*(6), 663-675.

Sheldrick, G. M. (2015). Crystal structure refinement with SHELXL. *Acta Cryst. Section C: Structural Chemistry*, *71*(1), 3-8.

Silvestri, S., Magnani, C., Calisti, R., & Bruno, C. (2001). The experience of the Balangero chrysotile asbestos mine in Italy: Health effects among workers mining and milling asbestos and the health experience of persons living nearby. *Can. Min.*, 177-186.

Skinner, H.C.W., Ross, M., & Frondel, C. (1988) Asbestos and other fibrous materials, Mineralogy, Crystal Chemistry, and Health Effects, Oxford University Press, New York.

Smith, J. V., & Bennett, J. M. (1981). Enumeration of 4-connected 3-dimensional nets and classification of framework silicates; the infinite set of ABC-6 nets; the Archimedean and sigma-related nets. *Am. Min.*, *66*(7-8), 777-788.

Smoluchowski, M. Von (1903). Contribution à la théorie de l'endosmose électrique etde quelques phénomènes corrélatifs, *Bull. Int. Acad. Sci. Cracovie. Classe Sci. Math. Nat. 3A*(43A) 182–199.

Sparnaay, M. J. (1972). The electrical double layer (Vol. 4). Pergamon.

Stănescu-Dumitru, R. (2008). FTIR asbestos presence identification in the occupational environment. *Spectroscopy*, *4*, 6.

Stanton, M. F., Layard, M., Tegeris, A., Miller, E., May, M., Morgan, E., & Smith, A. (1981). Relation of particle dimension to carcinogenicity in amphibole asbestoses and other fibrous minerals. *J. Nat. Cancer Inst.*, *67*(5), 965-975.

Staples, L. W., & Gard, J. A. (1959). The Fibrous Zeolite Erionite: Its Occurrence, Unit cell, and Structure. Mineralogical Society.

Stern O. (1924). The theory of the electrolytic double-layer, Z. Elektrochem. 30, 508–516.

Stroink, G., Blaauw, C., White, C. G., & Leiper, W. (1980). Mössbauer characteristics of UICC standard reference asbestos samples. *Can. Min.*, *18*(3), 285-290.

Suquet, H. (1989). Effects of dry grinding and leaching on the crystal structure of chrysotile. *Clays and clay Min.*, *37*(5), 439-445.

Surkyn, P., Waele, J. D., & Adams, F. (1983). Laser Microprobe Mass Analysis for Source Identification of Air Particulate Mattert. *Int. J. Env. Anal. Chem.*, *13*(4), 257-274.

Toby, B. H. (2001). EXPGUI, a graphical user interface for GSAS. *J. App. Cryst.*, *34*(2), 210-213.

Trivedi, M.S. (1970) Thesis, Mackay School of Mines, University of Nevada, Reno.

Turci, F., Colonna, M., Tomatis, M., Mantegna, S., Cravotto, G., Gulino, G., Aldieri, E., Ghigo, D., & Fubini, B. (2012). Surface reactivity and cell responses to chrysotile asbestos nanofibers. *Chem. Res. Toxicol.*, *25*(4), 884-894.

Van Olphen, in: G.D. Parfitt, K.S.W. Sing (Eds.) (1976) Characterization of Powder Surfaces, Academic Press, New York, pp. 428–455.

Van Oss, C. J., Naim, J. O., Costanzo, P. M., Giese, R. F., Wu, W., & Sorling, A. F. (1999). Impact of different asbestos species and other mineral particles on pulmonary pathogenesis. *Clays and Clay Min.*, *47*(6), 697-707.

Veblen, D.R. (1981). Amphiboles and Other Hydrous Pyriboles. *Rev. Min. 9*A. pp. 372.

Venditti, R., Xuan, X., & Li, D. (2006). Experimental characterization of the temperature dependence of zeta potential and its effect on electroosmotic flow velocity in microchannels. *Microfluidics and Nanofluidics*, *2*(6), 493-499.

Viani, A., Peréz-Estébanez, M., Pollastri, S., & Gualtieri, A. F. (2016). In situ synchrotron powder diffraction study of the setting reaction kinetics of magnesium-potassium phosphate cements. *Cement and Concrete Research*,*79*, 344-352.

Vigliaturo, R. (2015) Doctorate Thesis in Earth Sciences, Doctoral School of Sciences and Innovative Technologies. The University of Torino, Italy.

Virta, R. L. (2002). Zeolites, in: US Geological Survey Minerals Yearbook, pp. 84-1.

Virta, R. L. (2003). Asbestos: Geology, Mineralogy, Mining, and Uses. Open-File Report 02-149. US Department of the Interior. *US Geological Survey.*

Vlaic, G., & Olivi, L. (2004). EXAFS Spectroscopy: a Brief Introduction. *Croatica Chem. Acta*, *77*(3), 427-433.

Wagner, J. C., Berry, G., Skidmore, J. W., & Timbrell, V. (1974). The effects of the inhalation of asbestos in rats. *British J. of cancer*, *29*(3), 252.

Walitzi, E., Walter, F., & Ettinger, K. (1989). Refinement of the crystal-structure of anthophyllite from Ochsenkogel - Gleinalpe, Austria. *Zeit. Fur Krist.*, *188*(3-4), 237-244

Wallace, W. E., Keane, M. J., Mike, P. S., Hill, C. A., Vallyathan, V., & Regad, E. D. (1992). Contrasting respirable quartz and kaolin retention of lecithin surfactant and expression of membranolytic activity following phospholipase A2 digestion. *J. Toxicol. Env. Health, Part A Current Issues*, *37*(3), 391-409.

Wang, W., Zhou, M., Mao, Q., Yue, J., & Wang, X. (2010). Novel NaY zeolite-supported nanoscale zero-valent iron as an efficient heterogeneous Fenton catalyst. *Cat. Comm.*, *11*(11), 937-941.

Whitfield, H. J., & Freeman, A. G. (1967). Mössbauer study of amphiboles. *J. Inorg. Nuc. Chem.*, *29*(4), 903-914.

Whittaker, E. J. W. (1956). The structure of chrysotile. II. Clino-chrysotile. *Acta Cryst.*, *9*(11), 855-862.

Wicks, F. J., & O'Hanley, D. S. (1988). Serpentine minerals; structures and petrology. *Rev. Min. Geochem.*, *19*(1), 91-167.

Wilke, M., Farges, F., Petit, P. E., Brown, G. E., & Martin, F. (2001). Oxidation state and coordination of Fe in minerals: An Fe K-XANES spectroscopic study. *Am. Min.*, *86*(5-6), 714-730.

Wilke, M., Partzsch, G. M., Bernhardt, R., & Lattard, D. (2005). Determination of the iron oxidation state in basaltic glasses using XANES at the K-edge. *Chem. Geology*, *220*(1), 143-161.

Wilke, M., Farges, F., Partzsch, G. M., Schmidt, C., & Behrens, H. (2007). Speciation of Fe in silicate glasses and melts by in-situ XANES spectroscopy. *Am. Min.*, *92*(1), 44-56.

Williams, D. J. A., & Williams, K. P. (1978). Electrophoresis and zeta potential of kaolinite. *J. Colloid Interf. Sci.*, *65*(1), 79-87.

Willmott, P. R., Meister, D., Leake, S. J., Lange, M., Bergamaschi, A., Böge, M., ... & Chen, Q. (2013). The materials science beamline upgrade at the Swiss Light Source. *J. Sync. Rad.*, *20*(5), 667-682.

Wu, D., Tan, W., Zhang, Q., Zhang, X., & Song, H. (2014). Effects of ozone exposure mediated by BEAS-2B cells on T cells activation: a possible link between environment and asthma. *Asian Pacific J. Allergy Imm.*, *32*(1), 25-34.

Yada, K. (1971). Study of microstructure of chrysotile asbestos by high-resolution electron microscopy. *Acta Cryst. Section A: Crystal Physics, Diffraction, Theoretical and General Crystallography*, *27*(6), 659-664.

Yano, E., Wang, Z. M., Wang, X. R., Wang, M. Z., & Lan, Y. J. (2001). Cancer mortality among workers exposed to amphibole-free chrysotile asbestos. *Am. J. Epidem.*, *154*(6), 538-543.

Yao, S., DellaVentura, G., & Petibois, C. (2010). *Anal.* characterization of cell–asbestos fiber interactions in lung pathogenesis. *Anal. Bioanal. Chem.*, *397*(6), 2079-2089.

Yarborough, C. M. (2007). The risk of mesothelioma from exposure to chrysotile asbestos. *Curr. Op. Pul. Med.*, *13*(4), 334-338.

Young, R. A. (1993). The Rietveld Method, IUCr. *Monographs on Crystallography, Oxford University Press, Oxford*.

Young, R. A., & Wiles, D. B. (1982). Profile shape functions in Rietveld refinements. *J. App. Cryst.*, *15*(4), 430-438.

Web sites:

www.ammrf.org.au
www.atsdr.cdc.gov
www.cefns.nau.edu
www.diamond.ac.uk
www.iop.org
www.iza-online.org
www.particle.dk
www.rsc.org

Paper 1

The zeta potential of mineral fibres

Pollastri, S., Gualtieri, A. F., Gualtieri, M. L., Hanuskova, M., Cavallo, A., & Gaudino, G.

Journal of Hazardous Materials 276 (2014) 469–479

Contents lists available at ScienceDirect

Journal of Hazardous Materials

journal homepage: www.elsevier.com/locate/jhazmat

The zeta potential of mineral fibres

Simone Pollastri[a], Alessandro F. Gualtieri[a,*], Magdalena Lassinantti Gualtieri[b], Miriam Hanuskova[b], Alessandro Cavallo[c], Giovanni Gaudino[d]

[a] Dipartimento di Scienze Chimiche e Geologiche, Università di Modena e Reggio Emilia, Via S. Eufemia 19, I-41121 Modena, Italy
[b] Dipartimento Ingegneria "Enzo Ferrari", Università degli studi di Modena e Reggio Emilia, I-41100 Modena, Italy
[c] Dipartimento di Scienze dell'ambiente e del territorio e di Scienze della terra, Università di Milano-Bicocca, I-20126 Milano, Italy
[d] University of Hawai'I Cancer Center, Honolulu, HI 96813, USA

HIGHLIGHTS

- For the first time, zeta potential of mineral fibres was systematically investigated.
- A revised model explaining the zeta potential of chrysotile, amphiboles and erionite was postulated.
- In contact with organic solutions, all fibres tend to assume negative values of zeta potential.
- The decrease of the zeta potential of the fibres is a defensive chemical macrophage response.
- The negative zeta potential at the fibre surface prompts the formation of carcinogenic free radicals.

ARTICLE INFO

Article history:
Received 4 March 2014
Received in revised form 29 April 2014
Accepted 21 May 2014
Available online 29 May 2014

Keywords:
Asbestos
Mineral fibres
Zeta potential
BET
Pathogenicity

ABSTRACT

For the first time, the zeta (ξ) potential of pathogenic mineral fibres (chrysotiles, amphiboles and erionite) was systematically investigated to shed light on the relationship between surface reactivity and fibre pathogenicity. A general model explaining the zeta potential of chrysotile, amphiboles and erionite has been postulated. In double distilled water, chrysotiles showed positive values while crocidolite and erionite showed negative values. In contact with organic solutions, all fibres exhibited negative values of zeta potential. The decrease of the surface potential is deemed to be a defensive chemical response of the macrophage cells to minimize hemolytic damage. Negatively charged surfaces favour the binding of collagen and redox activated Fe-rich proteins, to form the so-called asbestos bodies and prompt the formation of $HO^{\bullet}$ via the reaction with peroxide ($H_2O_2 + e^- \rightarrow HO^{\bullet} + HO^-$). An additional mechanism accounting for higher carcinogenicity is possibly related to the Ca^{2+} sequestration by the fibres with surface negative potential, impairing the mitochondrial apoptotic pathway. It was also found that with a negative zeta potential, the attractive forces prevailed over repulsions and favoured processes such as agglomeration responsible of a tumorigenic chronic inflammation.

1. Introduction

Mineral fibres are ubiquitous on Earth. Among them, the most relevant are asbestos fibres (chrysotile and amphiboles) and the zeolite erionite [1]. Chrysotile is a trioctahedral hydrous layer silicate with a curved lattice [2–6]. Amphibole family includes actinolite, tremolite, crocidolite (fibrous variety of riebeckite), amosite (fibrous variety of grunerite) and anthophyllite. Amphiboles are double-chain silicates with oxygen atoms of the chains coordinated to both (Si, Al) and other cation sites [7]. Erionite is a common natural fibrous zeolite [8] whose framework is composed of columns of cancrinite cages [9–13] connected by a double six-membered ring of tetrahedra (hexagonal prism).

Although these mineral fibres may induce lethal lung diseases if inhaled [14–20], there is still considerable debate in the scientific community to whether chrysotile asbestos is a mesothelial carcinogen to humans [20–22]. As a matter of fact, all amphibole asbestos minerals are banned worldwide whereas chrysotile is banned only in the countries adopting the line of the International Agency for Research on Cancer (IARC) of the World Health Organization and the National Toxicology Program, which includes chrysotile in Group 1 "substance carcinogenic to humans" [23–29]. Surprisingly erionite, a human carcinogen listed by the IARC as a Group 1 Carcinogen, has not been banned to date [30].

* Corresponding author. Tel.: +39 059 2055810; fax: +39 059 2055887.
E-mail address: alessandro.gualtieri@unimore.it (A.F. Gualtieri).

http://dx.doi.org/10.1016/j.jhazmat.2014.05.060
0304-3894/

Table 1
Nature and details of the investigated mineral fibres.

Sample	Ideal chemical formula	Provenance	Notes
Chrysotile	$Mg_3(OH)_4Si_2O_5$	Quebec (Canada)[a]	UICC standard Chrysotile "B" Canadian NB #4173-111-1
Chrysotile	$Mg_3(OH)_4Si_2O_5$	Val Malenco, Sondrio (Italy)	
Chrysotile	$Mg_3(OH)_4Si_2O_5$	Balangero, Turin (Italy)	
Crocidolite	$Na_2(Fe^{2+},Mg)_3Fe_2^{3+}Si_8O_{22}(OH)_2$	Koegas Mine, Northern Cape (South Africa)	UICC standard Crocidolite South African NB #4173-111-3
Amosite	$(Fe^{2+},Mg)_7Si_8O_{22}(OH)_2$	Penge mine, Northern Province (South Africa)	
Tremolite	$Ca_2Mg_5Si_8O_{22}(OH)_2$	Val d'Ala, Turin (Italy)	
Anthophyllite	$(Mg, Fe^{2+})_7Si_8O_{22}(OH)_2$	Paakkila mine, Paakkila (Finland)	UICC standard Anthophylite Finnish NB #4173-111-5
Erionite	$(Ca,K_2,Na_2)_2(Al_4Si_{14}O_{36})\cdot 15H_2O$	Jersey, NE (USA)	

[a] Mixture of fibre from the firms Bells, Carey, Cassair, Flintkote, Johns-Manville, Lake, Normandie and National, proportioned roughly to represent Canadian production of asbestos products at that time.

A number of physiochemical properties such as fibre size, surface charge and activity, ability to generate reactive oxygen species, biodurability (for definition, a biodurable fibre is poorly cleared by lung macrophages, do not readily dissolve in the fluids lining the lungs, and can therefore persist in the lungs for decades), and iron content are deemed to be play a role in inducing asbestos correlated lung diseases, specifically mesothelioma [2,20,31–44]. As the physical and structural properties of fibres are primary determinants of biological effects [45,46], it is surprising that zeta potential (ξ) has not been thoroughly investigated to date.

Stern [47] developed a model called "electrical double layer" or Gouy–Chapman–Stern model. According to it, the double layer is composed of two coronas: the first one, called Stern layer (with a Stern potential), is fixed to a very short distance from the surface of the solid (the particle itself with a surface potential); the second one is widespread, penetrating to a certain extent in the liquid phase. Within this diffused layer, there is a theoretical boundary where ions and particles form a stable entity. The potential that exists at this boundary is known as zeta potential. A high absolute (negative or positive) value of zeta potential gives greater stability to the colloidal systems, because electrostatic repulsions which prevent the aggregation of dispersed particles are originated. When the absolute value of the potential is low, coagulation and flocculation are favoured. Generally, the line of separation between stable and unstable suspensions is taken from −30 mV to +30 mV. The zeta potential can be determined from electrosmotic velocity [48]:

$$\xi = -\frac{v_{eo}\eta}{E\varepsilon_0\varepsilon}$$

where v_{eo} is the electrosmotic velocity, η is the viscosity of the medium, E is the applied electric field strength, ε_0 is the permittivity of vacuum, ε is the dielectric constant of the medium, assuming that ε and η have the same values in the double layer as in the bulk solution.

In distilled water, zeta potential of amphiboles is negative while chrysotile shows positive values [46,49–51]. Zeta potential of asbestos fibres have been calculated using the mobility electrophoresis [46,48]. The reported values for the standard UICC (Union for International Cancer Control) asbestos at pH 7.4 are +40.5 and +52.5 mV for chrysotile, −50.5 mV for crocidolite, −58.5 mV for amosite, and −54.0 mV for anthophyllite. It is interesting to note that the addition of an organic component to mimic the extracellular surface of lung tissue determines a significant reduction in the absolute value of zeta potential as a function of pH. In other studies about the surface chemistry of amosite asbestos, a value of about −50 mV at pH 7.5 was reported [49] whereas a value of −22 mV was reported for chrysotile at pH 7 in distilled water [50]. In Ref. [52], at pH 7 in distilled water, chrysotile zeta potential was found to be +39 mV, whereas the amphiboles crocidolite, amosite and anthophyllite zeta potential were −50, −51 and −44 mV, respectively.

To elucidate the relationship between surface reactivity and potential toxicity of mineral fibres, the zeta potential of eight selected species, relevant for industrial applications and health issues, was systematically investigated in this work for the first time.

2. Experimental procedure

The investigated mineral fibres are reported in Table 1. Considering that (i) regulated fibres are by definition those with a length >5 μm, diameter <3 μm, and with an aspect ratio (length to diameter) of >3; (ii) differences in toxic potential may exist between short and long fibres, two distinct dimensional classes for each sample were obtained by gravitational separation experiments. All samples were preliminary disaggregated in distilled water, using a common mechanical shredder. Successively, the suspension was further mildly ground in agate mortar. The product of the preliminary coarse disaggregation was diluted in distilled water and the resulting suspension was subjected to ultrasonic treatment for 15 min. Wet gravitational separations were conducted using an Appiani cylinder [53], by introducing the homogeneous suspension into the cylinder, vigorously stirring it for 5 min and letting the suspended fibres to settle at the bottom of the cylinder. According to the Stokes' law [54], the settling velocity depends upon the density, size, and shape of the suspended particles so that coarse particles settle faster that fine particles. Following a number of experimental tests, the settling time was set to 3 h. At the end of each experimental run, both the sediment and the suspension were collected, placed in separate beakers, and dried at 100 °C for 2 h.

The two products of the gravitational wet separation experiments were characterized by scanning electron microscopy (SEM) to determine the average class particle size. The combined SEM/EDS study was conducted using a Philips XL-40/604 instrument equipped with an energy dispersive X-rays fluorescence spectrometer (EDS). For the observations, a tiny amount of sample was loaded on an aluminium stub and coated with a 10 nm thick gold layer. The statistical analysis aimed at determining the average fibre size of each sample was conducted using the ImageJ software (version 1.42q, Wayne Rasband National Institute of Health, USA).

Quantitative chemical compositions of all sample fibres were determined by Electron Microprobe analysis (EPMA) using a JEOL 8200 Super Probe instrument with W hairpin type filament, minimum accelerating voltage of 30 kV. The content of the structure volatiles (basically water) was independently determined by thermogravimetric (TG) analysis using a Netzsch STA 449C Jupiter in the temperature range 20–1000 °C and a heating rate of 10 °C min^{-1}.

The BET specific surface area was determined using a Gemini V instrument (Micromeritics) and nitrogen as probe gas. About 500 mg of sample was mounted in the sample holder and conditioned at 50 °C prior to measurement. The precise weight of the sample was consequently determined using an analytical balance.

The zeta potential of the fibres belonging to the two size classes was determined both in distilled water and in organic Gamble's

Table 2
The composition of the Gamble's solution. Liquid compositions starting from 250 ml of double-distilled water. 40% (15 ml) of formaldehyde was added to prevent growth of algae.

Reagent	Quantity used (mg)
$NaHCO_3$	0.7
NaCl	1.6
$CaCl_2{\cdot}2H_2O$	64.0
Na_2HPO_4	37.0
Na_2SO_4	20.0
$MgCl_2{\cdot}6H_2O$	53.0
$C_2H_5NO_2$ (glycine)	29.5
Na_3 citrate$\cdot 2H_2O$	38.3
Na_3 tartrate$\cdot 2H_2O$	45.0
Na pyruvate	43.0
Na lactate (60%, w/w)	72.5

modified solution [55], the latter reproducing the body environment. The reagents used and their quantities are shown in Table 2. With respect to the original formula, 250 ml of double-distilled water solution were used and no HCl was added. The pH of the obtained solution was monitored using a Criston Series 2000 instrument. A few drops of NaOH were also added to obtain a neutral pH. A starting solution having pH 7 was chosen to reproduce the extra-cellular environment. Subsequently, a part of the solution was adjusted to pH 4.5 using diluted HCl, to replicate the chemical environment of the macrophage cells. Hence, for all the fibres, measurements were conducted at pH 4.5 and 7. For selected samples, measurements in the pH range 3–10 were conducted. The pH modifications in these cases were done using dilute HCl and NH_4OH solutions.

Zeta potential measurements were carried out using a Zetasizer Nano Series instrument (Malvern). Sample fibres were added to the solute in a weight percentage of 0.1%. In addition to variations of the pH values, measurements were also conducted at different temperatures (25 °C and 37 °C, the latter being the physiological temperature of human body). An instrumental standard error is associated to each measurement of the zeta potential. Such error is also reported (in parenthesis) in all the tables. Despite of it, triplicate measurements were conducted for many samples to check for the reproducibility of the result.

3. Results and discussion

Chemical formula, specific surface area and length of the investigated mineral fibres are reported in Table 3. Spot electron microprobe WDS analyses were performed on accurately selected fibres and should be highly reliable.

For each mineral species, Fig. 1 reports the average length of the two classes of long and short fibres. Gravitational separations gave

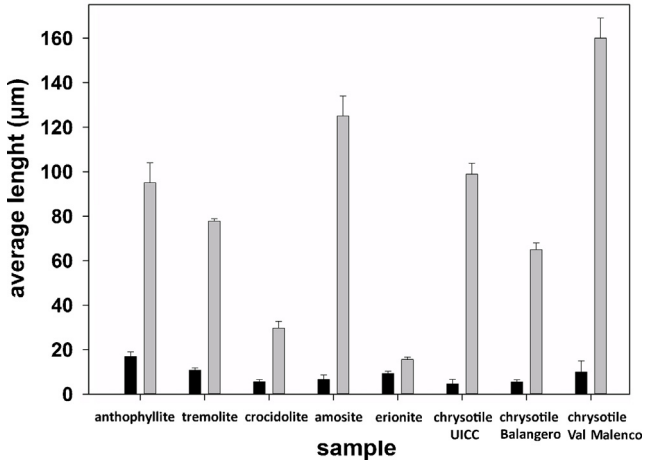

Fig. 1. Fibres' length of the two size classes obtained from the gravitational separations. Legend: dark columns, short fibres; gray columns, long fibres.

positive results, allowing the achievement of a short fibre class with length generally <20 μm and a long fibre class with length generally >15 μm.

Specific surface area measurements confirm the expected inverse relationship between size and surface area of mineral fibres. The specific surface area of chrysotile is about 3.3 times that of amphibole for short fibre samples, and about 4.5 times for long

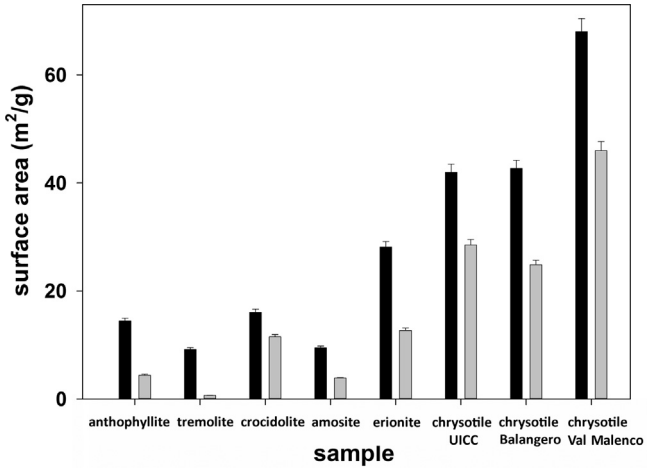

Fig. 2. Specific surface area of the two size classes obtained from the gravitational separations. Legend: dark columns, short fibres; clear columns, long fibres.

Table 3
Chemical formula determined using electron microprobe and thermogravimetric (TG) analysis. TG allowed the determination of the water content. Table reports also the surface area (BET analysis) and average length (SEM analysis) of investigated fibres.

Sample	Calculated chemical formula*	Short fibres sample		Long fibres sample	
		Surface area (m^2/g)	Fibre length (μm)	Surface area (m^2/g)	Fibre length (μm)
Chrysotile UICC	$(Mg_{5.93}Fe^{2+}_{0.11}Al_{0.02}Fe^{3+}_{0.01})_{6.07}Si_{4.03}O_{10}(OH)_{7.66}$	42 (1)	5 (2)	29 (1)	99 (5)
Chr Balangero	$(Mg_{5.81}Fe^{2+}_{0.21}Al_{0.27}Fe^{3+}_{0.03}Cr_{0.01})_{6.33}Si_{3.97}O_{10}(OH)_{7.11}$	43 (2)	6 (1)	24.8 (9)	65 (3)
Chr Val Malenco	$(Mg_{5.85}Fe^{2+}_{0.11}Al_{0.02}Ni_{0.01})_{5.99}Si_{4.01}O_{10}(OH)_{7.86}$	68 (9)[a]	10 (5)	45 (2)	160 (9)
Amosite	$(Ca_{0.02}Na_{0.01})(Fe^{2+}_{5.36}Mg_{1.48}Fe^{3+}_{0.11}Mn_{0.06})_{7.01}(Si_{7.93}Al_{0.01})_{7.94}O_{21.94}(OH)_{2.06}$	9.5 (3)	7 (2)	3.9 (1)	125 (9)
Anthophyllite	$Ca_{0.04}(Mg_{5.81}Fe^{2+}_{0.92}Fe^{3+}_{0.21}Mn_{0.04})_{6.98}(Si_{7.83}Al_{0.02})_{7.85}O_{21.63}(OH)_{2.37}$	14.4 (5)	17 (2)	4.4 (2)	95 (9)
Crocidolite	$(Na_{1.96}Ca_{0.03}K_{0.01})_2(Fe^{2+}_{2.34}Fe^{3+}_{2.05}Mg_{0.52})_{4.91}(Si_{7.84}Al_{0.02})_{7.86}O_{21.36}(OH)_{2.64}$	16.1 (6)	6 (1)	11.5 (4)	30 (3)
Tremolite	$(Ca_{1.91}Na_{0.06}K_{0.01})_{1.98}(Mg_{4.71}Fe^{2+}_{0.22}Fe^{3+}_{0.08}Mn_{0.02})_{5.03}(Si_{8.01}Al_{0.02})_{8.03}O_{22.14}(OH)_{1.86}$	9.2 (3)	11 (1)	0.66 (2)	78 (1)
Erionite	$(Na_{5.31}K_{2.18}Ca_{0.15}Mg_{0.11}Fe^{3+}_{0.29})_{8.04}(Si_{27.84}Al_{7.85})_{35.69}O_{72}{\cdot}20.3H_2O$	28 (1)	9 (1)	12.7 (5)	16 (1)

The parenthesis reports the standard error on the measurements.
* The Fe^{3+} concentration was independently calculated using the Droop method using stoichiometric criteria.
[a] Calculated from geometrical measurements.

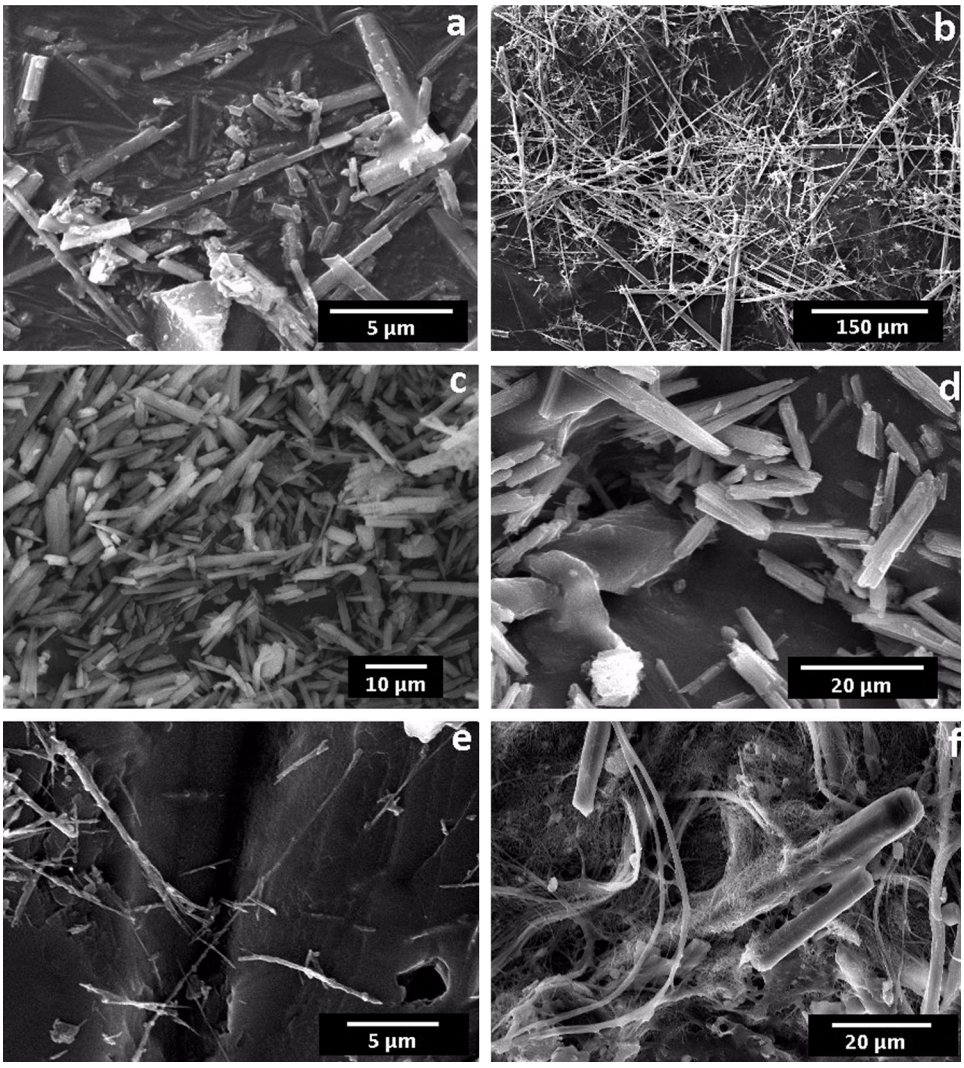

Fig. 3. SEM gallery of mineral fibres with selected examples of the two size classes: (a and b) amosite short vs. long; (c and d) erionite short vs. long; (e and f) Balangero chrysotile short vs. long.

fibre samples while erionite has a surface area halfway between chrysotile and amphiboles (about half of chrysotile surface area and about twice that of amphibole: see Fig. 2). A larger surface area determines a higher reactivity of the mineral fibres in solution. Besides the intrinsic chemical stability of each mineral fibre type, chrysotile fibres will dissolve more readily in acidic environment, like the one found in lung tissue, because of their large surface area. Among the chrysotile species, the less biodurable fibre is likely chrysotile from Val Malenco (see Table 3). Among the amphibole fibres, tremolite and amosite are the most biodurable. Because of the dissolution process, a higher concentration of cations (Mg^{2+} in the case of chrysotile) will be released and a zeta potential establishes around the outside of the Stern's layer.

Fig. 3 reports a representative gallery of high-resolution SEM images of long and short fibres evidencing a clear difference in terms of fibre length between the two size classes.

Table 4
Zeta potentials of the mineral fibres in suspensions in double distilled water (concentration 0.1 wt%): (a) 37 °C; (b) 25 °C.

(a)

pH (±0.2)		3.0	4.0	5.0	6.0	6.5	7.0	7.5	8.0	8.5	9.0	10.0	10.5
Chrysotile UICC	Long	–	+26 (2)[a]	+19 (2)	+10 (3)	–	+12 (2)	–	+8 (3)	–	+4 (2)	−7 (4)	–
Crocidolite	Short	−16 (3)	−31 (5)	−34 (5)	−38 (6)	−34 (4)	−36 (5)	−37 (4)	−39 (7)	−37 (4)	−37 (5)	−39 (5)	−42 (5)
Erionite	Short	−21 (4)	−25 (5)	−26 (5)	−31 (5)	–	−33 (6)	–	−35 (7)	–	−35 (8)	−37 (5)	–

(b)

pH (±0.2)		3.0	4.0	4.5	5.0	6.0	6.5	7.0	8.0	9.0	10.0	10.5
Chrysotile UICC	Long	–	+29 (3)	–	+28 (3)	+17 (3)	–	+10 (3)	+7 (4)	+8 (5)	−10 (4)	–
Crocidolite	Short	−16 (4)	−26 (4)	−32 (4)	−36 (4)	–	−38 (5)	−40 (5)	−43 (7)	−43 (6)	−45 (6)	−48 (6)
Erionite	Short	−26 (6)	−34 (6)	–	−38 (7)	−40 (7)	–	−40 (7)	−42 (7)	−41 (6)	−47 (7)	−48 (6)

[a] All zeta potentials are expressed in mV.

Table 5
Zeta potentials of the investigated mineral fibres in contact with the Gamble's solution (concentration 0.1 wt%) at 25 °C.

pH (±0.2)	4.0	4.5	5.0
Chrysotile UICC			
L[a]	−8 (4)[b]	–	–
S[a]	–	–	–
Crocidolite			
L	–	–	–
S	–	−26 (5)	–
Anthophyllite			
L	–	−15 (5)	–
S	–	−20 (4)	–
Erionite			
L	–	–	–
S	–	−33 (5)	−36 (9)

[a] L = long; S = short.
[b] All zeta potentials are expressed in mV.

All collected zeta potentials (with standard error in the parenthesis) are listed in Tables 4–6; measures were primarily addressed to the collection of the zeta potentials of all mineral fibres in contact with the organic solution at pH 4.5 and 7 but several additional measures were performed to better understand the variation of zeta potential as a function of physical and chemical parameters.

Measurements carried out in double distilled water (Table 4) confirm literature data, according to which chrysotiles show positive values of the zeta potential, while crocidolite show negative values. The calculated values match those reported in [56] albeit the value of our Quebec chrysotile is less positive (+12 mV vs. +35.2 and +46.3 mV). Surprisingly, negative values of the zeta potential for chrysotiles from Globe and Salt River (Arizona) and Shabani (Zimbabwe) have also been reported in [56].

Bonneau et al. [51,57–61] explained the differences in surface potential of chrysotile and amphibole in aqueous medium at neutral pH but the proposed model is not convincing and required a substantial revision. We advanced that in chrysotile, surface exposure occurs because of the breaking of hydrogen bridges linking two successive tetrahedral–octahedral (TO) units in the interlayer volume. Two surfaces are exposed: an unsaturated one formed by oxygen atom (dangling) and a negative one saturated by protons. The negatively charged surface is surrounded by protons but they are not sufficient to counterbalance the charge, for which the diffused corona (that determines the value of the zeta potential) consists of positively charged ions attracted by the negative residue potential. These ions can be protons, hydrated cations, H_3O^+, Mg^{2+} [58–60] or Na^+, K^+ and Ca^{2+} as compensator cations in chrysotile structure (Fig. 4a) [62–64]. This model and the value of the zeta potential at pH 7 are in line with those reported for kaolinite, whose negatively charged basal faces throughout the whole pH range require compensation by positive cations, whereas edges result to be a combination of the potential on the silica and alumina surfaces [65,66].

In amphiboles, exposure occurs along the planes of the (1 1 0) faces. The presence of extra-tetrahedral cations such as Ca^{2+}, Fe^{2+}, Fe^{3+}, Mg^{2+} and protons determine a positive charge of the Stern layer, and a resulting attraction of negatively charged molecules to form the diffused corona. Consequently, the zeta potential will have negative values (Fig. 4b). A similar picture is found in zeolites such as erionite [67]. As previously mentioned, pH variations and subsequent partial dissolution of the fibres (whose rate is faster for chrysotile with respect to erionite and amphiboles [68,69]) induce a variation of the zeta potential which tends to become more negative at high pH values. For chrysotile, in the low pH range, the dissolution reaction of the magnesium hydroxide sheet, which leaves a hydrated silica relict [69,70], brings about an excess magnesium concentration at the surface of the fibre and an overall positive zeta potential [46,71,72]. According to Feng et al. [73], magnesium ions are simply left on serpentine surface and are responsible for its positive surface charge. In the high pH range, chrysotile is stable and hydroxyls at the surface of the fibre determine an overall negative zeta potential of the particle. Another possibility is that the reversal from positive to negative sign of the zeta potential is due to the electrolytes introduced in solution which replace the protons at the Stern layer and call for negative zeta potential.

The zeta potentials of both crocidolite and erionite become more negative in the high pH range. Electrolytes (Na^+) introduced in solution to create alkaline conditions, replace surface protons at the crystal edges and, together with Ca^{2+}, Fe^{2+}, Fe^{3+}, Mg^{2+}, enhance the positive charge of the Stern layer, which in turn call for an even more negative zeta potential.

Fig. 5 reports the variation of the zeta potential in double distilled water at 25 °C, 37 °C and in Gamble's solution at 37 °C for UICC chrysotile, UICC crocidolite and erionite. In contact with the organic solution, all fibres show negative values of zeta potential (see Tables 4–6).

Fig. 6 reports the variation of the zeta potential in Gamble's solution at 37 °C for chrysotiles, amphiboles and erionite. Despite the differences observed for the samples in contact with distilled water, when in contact with the organic solution, all the mineral fibres tend to gain negative and similar values of the zeta potential. The difference of the zeta potential in distilled water of chrysotile (positive) on one side and amphiboles and erionite (negative) on the other side has been hypothetically assumed as distinctive character to discriminate the potential cytotoxicity [19–22] of these fibres (low or null in chrysotile and high in amphiboles and erionite). Our work demonstrates instead that the zeta potential is not a discriminating factor when it is measured in contact with the Gamble's solution, a condition mimicking fibres immersed in the interstitial, i.e. extracellular environment. All the zeta potentials are reduced (i.e., they assume lower absolute values) in the Gamble's solution with respect to the distilled water.

In the Gamble's solution, zeta potential turns from positive to negative for chrysotile whereas it becomes less negative for both crocidolite and erionite. The high concentration of Na^+ present in the Gamble's solution triggers ion exchange for the surface protons of the chrysotile exposed surfaces so that the Stern layer becomes positive and requires surrounding negative charges. For crocidolite and erionite, the high concentration of Na^+ possibly triggers ion exchange not only for the surface protons but also for the edge extratetrahedral cations with large oxidation number such as Ca^{2+}, Mg^{2+}. The ion exchange decreases the positive charge of the Stern layer which requires a less negative zeta potential. The reduction of the absolute values of zeta potentials has already been observed in the literature for chrysotile and crocidolite in the presence of the surfactant dipalmitoyl phosphatidylcholine (DPPC) [46].

The zeta potential of the fibres displayed at pH 4.5 and 7.0 is invariably negative, with values approximately in the range −10 to −26 mV. As already reported, there are no remarkable differences among the various fibre families (chrysotiles, amphiboles and erionite). The lack of differences among the various fibre species is probably the reason why Van Oss et al. [56] reported that the value and sign of zeta potential is irrelevant to the degree of their pathogenicity. This work instead demonstrates that the zeta potential of mineral fibre may influence or may be influenced by several bio-chemical and physical parameters:

(1) *Hemolytic potential*. Light and Wey [46] observed that when DPPC was added to the fibre suspension, hemolytic activity decreased for all UICC fibre standards (by 87% for amosite and crocidolite and 25% for chrysotiles) and that in general, a decrease

Table 6
Zeta potentials of the mineral fibres in suspensions in Gamble's solution (concentration 0.1 wt%) at 37 °C.

pH (±0.2)	2.5	3.0	3.5	4.0	4.5	5.0	5.5	6.0	6.5	7.0	7.5	8.0	8.5	9.0	9.5	10.0	10.5	11.0
Chrysotile UICC																		
L[a]	–	+4 (2)[b]	–	−4 (3)	−8 (3)	–	–	−8 (3)	–	−8 (3)	–	−13 (2)	–	–	–	−18 (5)	–	−21 (5)
S[a]	–	−9 (6)	−12 (3)	−16 (3)	−14 (5)	−20 (2)	−19 (4)	–	−18 (2)	−16 (5)	−22 (4)	−20 (5)	–	–	−20 (3)	−20 (4)	–	–
Chrysotile Balangero																		
L	–	+1 (5)	−12 (5)	−18 (5)	−23 (4)	−19 (5)	−25 (4)	–	−16 (2)	−19 (2)	−17 (4)	−17 (2)	–	−15 (2)	–	−16 (3)	−22 (3)	–
S	–	–	–	–	−27 (3)	–	−13 (9)	–	–	−27 (3)	–	–	–	–	–	–	–	–
Chrysotile Val Malenco																		
L	–	–	–	–	−26 (4)	–	−21 (6)	–	–	−27 (7)	–	–	–	–	–	–	–	–
S	–	–	–	–	−27 (2)	–	−27 (3)	–	–	−23 (2)	–	–	–	–	–	–	–	–
Crocidolite																		
L	–	–	−20 (4)	–	−23 (5)	–	–	−22 (4)	–	−20 (6)	–	–	–	–	–	–	–	–
S	–	−21 (4)	−23 (4)	−28 (4)	−21 (4)	−29 (5)	−28 (4)	–	–	−24 (4)	−31 (4)	−21 (4)	−30 (3)	−17 (5)		−19 (4)	–	–
Amosite																		
L	–	–	–	–	−13 (3)	–	−23 (8)	–	–	−24 (5)	–	–	–	–	–	–	–	–
S	–	−16 (4)	–	−19 (4)	−21 (4)	−20 (5)	–	–	−21 (4)	−21 (4)	−25 (3)	−21 (7)	−14 (7)	−15 (6)	–	−18 (5)	–	–
Tremolite																		
L	–	–	–	–	−15 (5)	–	−17 (4)	–	–	−17 (5)	–	–	–	–	–	–	–	–
S	–	–	–	–	−17 (4)	–	−19 (5)	–	–	−20 (5)	–	–	–	–	–	–	–	–
Anthophyllite																		
L	–	–	–	−6 (8)	−5 (3)	–	–	–	–	−15 (3)	–	–	–	–	–	–	–	–
S	–	–	–	–	−15 (6)	–	–	–	–	−17 (4)	–	–	–	–	–	–	–	–
Erionite																		
L	–	–	–	–	−25 (4)	–	–	−23 (5)	–	−20 (6)	–	–	–	–	–	–	–	–
S	−11 (5)	−16 (6)	−23 (5)	−20 (5)	−26 (6)	−27 (5)	−27 (6)	−31 (6)	−28 (6)	−29 (6)	−26 (5)	−25 (5)	–	−18 (6)	−14 (4)	−16 (4)	–	–

[a] L = long; S = short.
[b] All zeta potentials are expressed in mV.

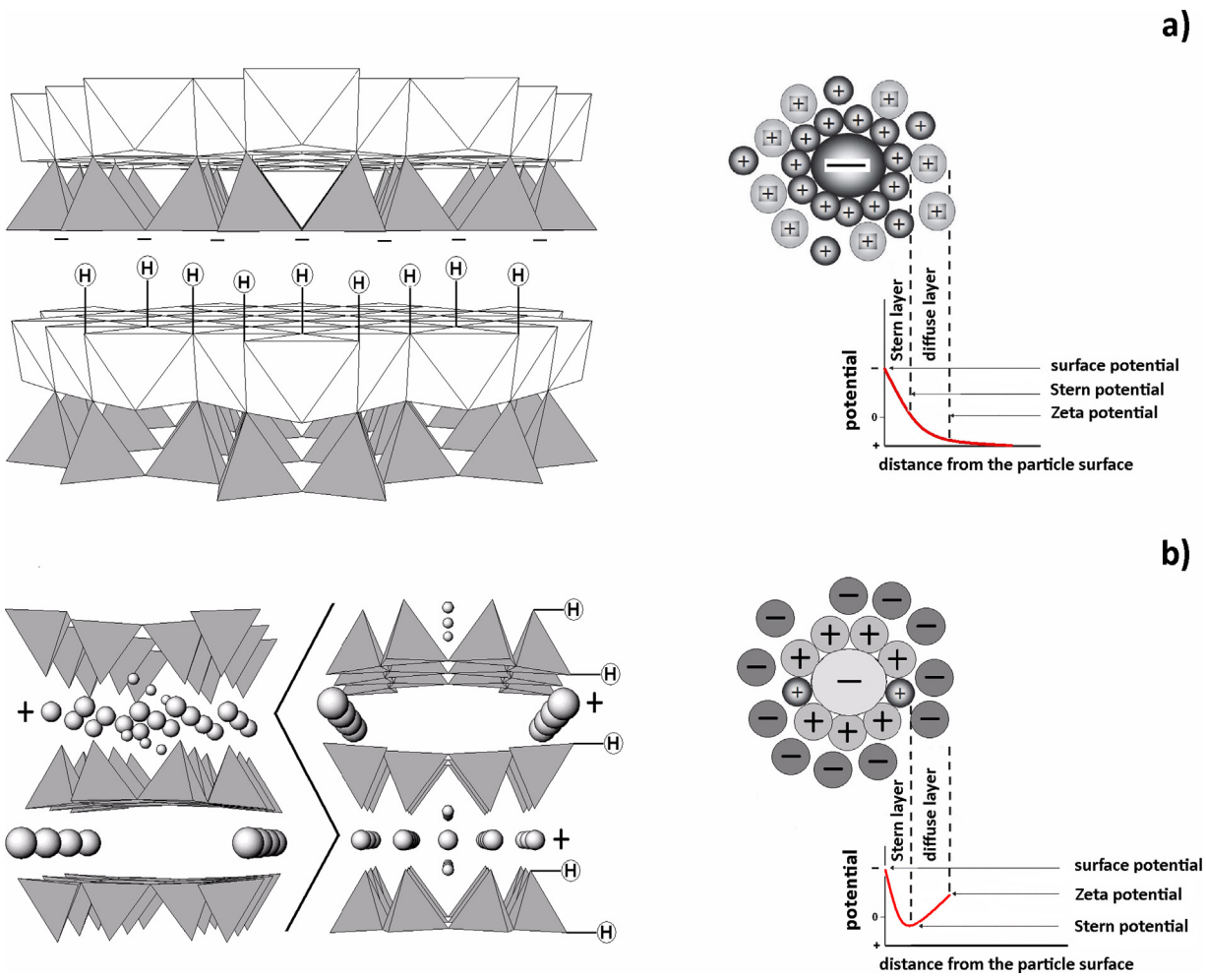

Fig. 4. Structural models which explain the sign of the zeta potentials of chrysotiles (a) and amphiboles (b).

of the absolute value of the zeta potential decreases the hemolytic activity. The decrease of the zeta potential of the fibres is an effect of the defensive response acted by the macrophage cells to minimize hemolytic damage. A reduction of the magnitude of the zeta potential of the fibres should correspond to a decrease of the hemolytic activity. According to [46,74], the mechanism for hemolysis induced by the fibres relies on the formation of lipid-bilayer clusters, normally extending homogeneously through the entire lipid bilayer. Clustering occurs because of the coulombic repulsion of negatively charged sialic acid groups with negatively charged fibres. Although ion permeability through lipid bilayers is very low, ions can readily penetrate those regions of the erythrocyte membrane, where the clusters of glycoproteins are formed, causing hemolytic activity. In support of this model, it was demonstrated that zeta potential of insoluble nanoparticles has been correlated with hemolytic potential [75]. In this scenario, when nanoparticles enter the acidic lysosome milieu, enzymatic digestion of the corona by lysosomal enzymes [76] occurs and may cause the reversal of negative zeta potential. Thus, the positively charged nanoparticles may interact with the negatively charged internal face of the lysosomal membrane (lysosomal destabilization) and trigger and inflammation cascade in the lung (acute lung inflammogenicity) [77]. As far as chrysotile and Mg-amphiboles are concerned, following the behaviour of MgO-nanoparticles [75] no inflammation is expected by the release of non-toxic Mg^{2+}.

(2) *ROS production*. It is well documented that iron associated with asbestos promotes the formation of the highly reactive HO• from the oxidation of ferrous iron (Fe^{2+}) to ferric iron (Fe^{3+}) by H_2O_2 released by the macrophages during the inflammatory burst (Fenton reaction) [78]. Superoxide and other biological reducing agents can eventually reduce Fe^{3+} iron back to redox active Fe^{2+} iron (family of catalyzed Haber–Weiss reactions). The existence of a negatively charged surface (negative zeta potential), source of electrons, on the fibres prompt the formation of HO• via the reaction with peroxide: $H_2O_2 + e^- \rightarrow HO^\bullet + OH^-$. The mechanism is identical to that described for freshly cut quartz surfaces in biological medium [79] where silanol groups (Si—OH) and ionized silanol groups (Si—O—) on the surface play a major role in interaction with membranes [80,81]. In lung lining fluid or in tissue fluid, these products of hemolytic cleavage can give rise to HO• and H_2O_2 [79,82].

(3) *Fibre encapsulation by collagen and iron-rich proteins*. In support of the proviso that the decrease of the zeta potential of the fibres is caused by the defensive chemical cellular response during macrophage phagocytosis, literature data report that the negatively charged reactive surface favours the binding of collagen and redox activated Fe-rich proteins, to form the so-called asbestos bodies. In fact, alveolar macrophage ingestion of asbestos fibres triggers a fibrogenic response from fibroblasts via the release of growth factors (mainly TGF-β), cytokines, TNF-α, interleukin-1β (IL-1β), which collectively promote collagen deposition and asbestos encapsulation by mucopolysaccharides and Fe-rich proteins (ferritin, hemosiderin) that can be redox activated [83].

(4) *Apoptosis*. According to the model of mitochondria-endoplasmic reticulum cross talk in asbestos-induced apoptosis [83], endoplasmic reticulum stress due to the fibre interaction

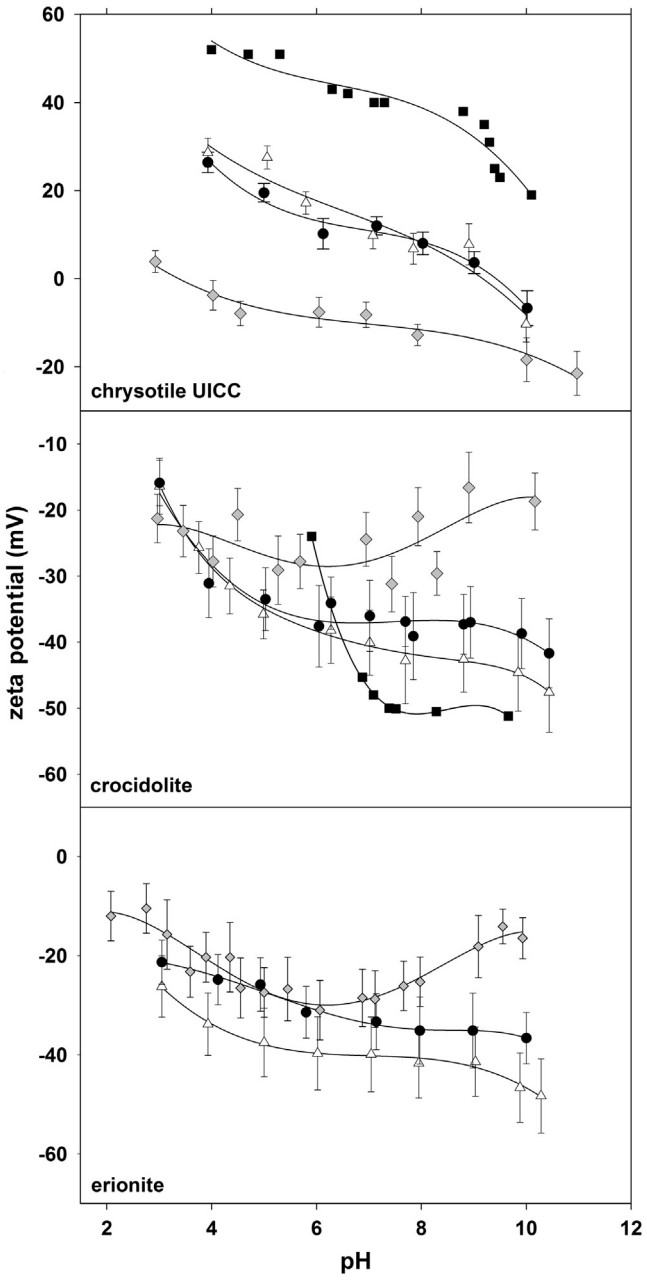

Fig. 5. Variations of the zeta potential values as a function of pH in different chemical–physical conditions on representative samples (chrysotile UICC, crocidolite and erionite). Legend: (■) Light and Wei [47] (25 °C distilled water); (●) 37 °C double distilled water; (△) 25 °C double distilled water; (♦) 37 °C Gamble solution.

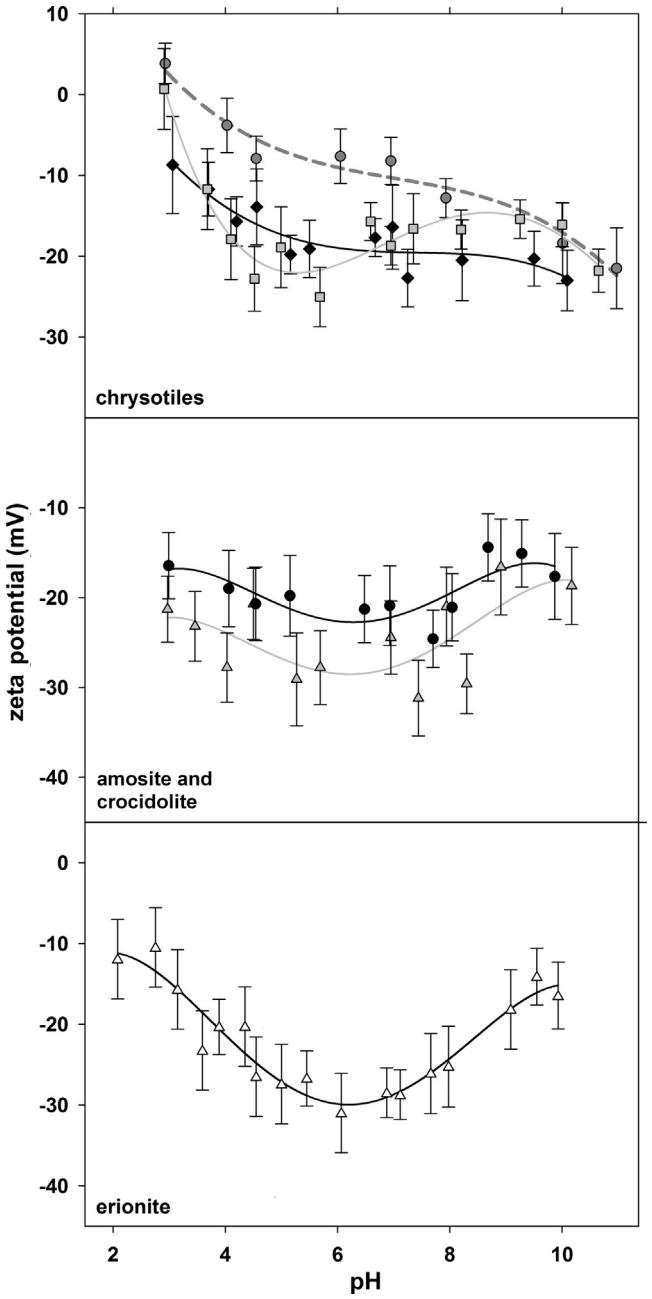

Fig. 6. Variations of the zeta potential values as a function of pH in Gamble solution at 37 °C on representative samples of chrysotiles, amphiboles and erionite. Legend: (●) chrysotile UICC long; (■) chrysotile Balangero long; (♦) chrysotile UICC short; (●) amosite short; (▲) crocidolite short; (△) erionite short.

causes activation of an unfolded protein response and Ca^{2+} release which, in turn, lead to activation of mitochondria-regulated apoptosis. Because the Ca^{2+} release to the mitochondria is necessary for the induction of intrinsic apoptosis, the whole cellular response cycle may be broken if the negatively charged corona of the mineral fibres attract and fix the Ca^{2+} ions. Besides the interference with the apoptotic process, fixation of divalent calcium atoms in the Stern layer or in the outer corona can alter the value and sign of the zeta potential of the fibres.

(5) *Fibre agglomeration*. We have seen that zeta potential of the fibres at pH 4.5 and 7.0 display values in the range −10 to −26 mV, with no remarkable differences among the various fibre species. At such values of zeta potential, processes such as agglomeration are favoured. This is a critical point as it is known that culture conditions with most agglomeration induce highest biological responses [84,85].

(6) *Fibre size*. Measurements carried out in Gamble's solution at 37 °C show a slight general trend of long fibres (with smaller surface area) having values of zeta potential with more positive sign and lower values than short fibres (see Fig. 7 and Table 4). This may be due to higher surface reactivity of the short fibres, prompting partial dissolution and release of cations which gather around the surface and increase the positive charge of the Stern layer. The latter calls for a more negatively charged zeta potential. The dilemma regarding the different pathogenicity of short vs. long fibres is still an open issue. According to the Stanton hypothesis [86], ability of mineral particles to cause cancer is mostly a function of size rather than physico-chemical properties. Recent studies [87] showed that

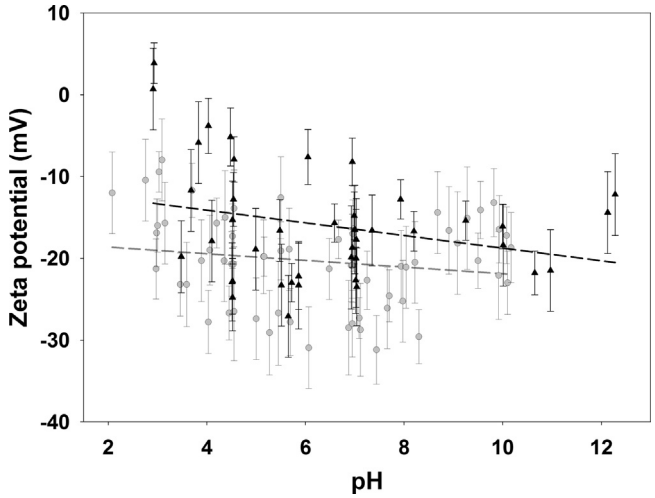

Fig. 7. Zeta potential values of short fibres vs. long fibres in Gamble solution at 37 °C of all investigated sample. Legend: (▲) long fibres; (●) short fibres.

the fibre size has fundamental importance to define the toxicity of a fibre and that short chrysotile fibres (nanofibres) do not exhibit the same cytotoxicity of the long fibres. Our results reveal that short fibres with higher absolute values of zeta potential are more stable in solution and less aggregated that long fibres. The latter, as we have seen above, have a tendency to aggregation and should trigger more potent inflammatory response than short fibres.

(7) *Temperature*. It was found that temperature affects the value of the zeta potential both in distilled water and in Gamble's solution (Fig. 5). In general, assuming the same fibre size, it turns out that the zeta potential becomes more negative (assumes higher absolute values) at 25 °C. This variation is significant for amphiboles and erionite whereas it is within the experimental error for the UICC chrysotile. Although the literature describing the influence of temperature on the zeta potential is scanty, it was generally observed that zeta potential becomes more negative with temperature increase ([88] and references therein). The opposite phenomenon is observed here. The influence of temperature on the zeta potential is a result of changes in silanol equilibrium, adsorption equilibria, and diffused double-layer thickness [89]. Notwithstanding, exceptions are reported in the literature (e.g., zeta potential became more positive at acidic pH with temperature increase for Na-kaolinite, [90]) indicating that temperature dependence of the zeta potential, if any, is structure-related and influenced by other chemical factors, such as pH.

4. Conclusions

The zeta potential of selected mineral fibres (chrysotiles, amphiboles and erionite) of industrial and social importance was investigated to understand the relationship between surface reactivity and fibre pathogenicity. In double distilled water, chrysotiles show positive values of the zeta potential, while crocidolite and erionite show negative values. In contact with the Gamble's solution, all fibres display negative zeta potential, clearly showing that this parameter cannot be considered a discriminating factor when it is measured in contact with an organic solution reproducing cell environment. In modelling the effects of surface potential of mineral fibres, many physical–chemical parameters such as *hemolytic potential*, *ROS production*, *fibre encapsulation, fibre size* and *temperature* should be considered. Among these, *apoptosis* is a major factor with the endoplasmic reticulum stress that activates an unfolded protein response and Ca^{2+} release leading to activation of mitochondria-regulated apoptosis. Because Ca^{2+} ions are required for the induction of intrinsic apoptosis by mitochondria, the Ca^{2+} ion sequestration by the negatively charged mineral surface, may impair the apoptotic response, crucial to counteract the transforming potential of the carcinogenic fibres. *Fibre agglomeration*, known to induce the highest biological responses, is favoured by negative values of the zeta potential.

Acknowledgments

This research was conducted within the granted Italian National PROGETTO DI UNA UNITÀ DI RICERCA (PRIN) 2010–2011 – prot. 2010MKHT9B_004 "Interazione fra minerali e biosfera: conseguenze per l'ambiente e la salute umana". Part of this work is taken from the bachelor thesis of E. Neviani. Prof. N. Perchiazzi is kindly acknowledged for the calculation of the chemical formula of the mineral fibres and Dr. A. Bloise for the determination of the chemical volatile components using thermogravimetry.

References

[1] F. Baumann, J.P. Ambrosi, M. Carbone, Asbestos is not just asbestos: an unrecognised health hazard, Lancet Oncol. 14 (7) (2013) 576–578.
[2] E.J.W. Whittaker, The structure of chrysotile. II. Clino-chrysotile, Acta Crystallogr. 9 (11) (1956) 855–862.
[3] S.W. Bailey (Ed.), Hydrous Phyllosilicates, Mineralogical Society of America, 1988, p. 725.
[4] B. DeVouard, A. Baronnet, Axial diffraction of curved lattices; geometrical and numerical modeling; application to chrysotile, Eur. J. Mineral. 7 (4) (1995) 835–846.
[5] F.J. Wicks, E.J.W. Whittaker, A reappraisal of the structures of the serpentine minerals, Can. Mineral. 13 (3) (1975) 227–243.
[6] F.J. Wicks, D.S. O'Hanley, Serpentine minerals; structures and petrology, Rev. Mineral. Geochem. 19 (1) (1988) 91–167.
[7] D.R. Veblen, Reviews in Mineralogy, vol. 9A: Amphiboles and Other Hydrous Pyriboles – Mineralogy, Mineralogical Society of America, BookCrafters Inc., Chelsea, MI, USA, 1981, pp. 372.
[8] R.L. Virta, Zeolites, in: US Geological Survey Minerals Yearbook-2002, 2002, pp. 84-1.
[9] L.W. Staples, J.A. Gard, The fibrous zeolite erionite: its occurrence, unit cell, and structure, Mineral. Mag. 32 (1959) 261–281.
[10] J.A. Gard, J.M. Tait, The crystal structure of the zeolite offretite, $K_{1.1}Ca_{1.1}Mg_{0.7}[Si_{12.8}Al_{5.2}O_{36}]\cdot 15.2H_2O$, Acta Crystallogr. B 28 (3) (1972) 825–834.
[11] J.V. Smith, J.M. Bennett, Enumeration of 4-connected 3-dimensional nets and classification of framework silicates; the infinite set of ABC-6 nets; the Archimedean and sigma-related nets, Am. Mineral. 66 (7–8) (1981) 777–788.
[12] A. Gualtieri, G. Artioli, E. Passaglia, S. Bigi, A. Viani, J.C. Hanson, Crystal structure-crystal chemistry relationships in the zeolites erionite and offretite, Am. Mineral. 83 (5) (1998) 590–606.
[13] P. Ballirano, G.B. Andreozzi, M. Dogan, A.U. Dogan, Crystal structure and iron topochemistry of erionite-K from Rome, Oregon, USA, Am. Mineral. 94 (8–9) (2009) 1262–1270.
[14] J.E. Craighead, J.L. Abraham, A. Churg, F.H. Green, J. Kleinerman, P.C. Pratt, T.A. Seemayer, V. Vallyathan, H. Weill, The pathology of asbestos-associated diseases of the lungs and pleural cavities: diagnostic criteria and proposed grading schema. Report of the Pneumoconiosis Committee of the College of American Pathologists and the National Institute for Occupational Safety and Health, Arch. Pathol. Lab. Med. 106 (11) (1982) 544.
[15] R.D. Doll, Mortality from lung cancer in asbestos workers, Br. J. Ind. Med. 12 (1955) 81.
[16] R.A. Lemen, J.M. Dement, J.K. Wagoner, Epidemiology of asbestos-related diseases, Environ. Health Perspect. 34 (1980) 1.
[17] B.T. Mossman, D.W. Kamp, S.A. Weitzman, Mechanisms of carcinogenesis and clinical features of asbestos-associated cancers, Cancer Invest. 14 (5) (1996) 466–480.
[18] M.R. Becklake, E. Bagatin, J.A. Neder, Asbestos-related diseases of the lungs and pleura: uses, trends and management over the last century, in: M. Chan-Yeung (Ed.), State of the Art Series. Occupational Lung Disease in High- and Low-Income Countries, Number 3 in the series. Int. J. Tuberculosis Lung Dis. 11 (4) (2007) 356–369.
[19] D.W. Kamp, Asbestos-induced lung diseases: an update, Transl. Res. 153 (4) (2009) 143–152.
[20] F. Qi, G. Okimoto, S. Jube, A. Napolitano, H.I. Pass, R. Laczko, R.M. Demay, G. Khan, M. Tiirikainen, C. Rinaudo, A. Croce, H. Yang, G. Gaudino, M. Carbone, Continuous exposure to chrysotile asbestos can cause transformation of human mesothelial cells via HMGB1 and TNF-α signaling, Am. J. Pathol. 183 (5) (2013) 1654–1666.
[21] J.C. Wagner, G. Berry, J.W. Skidmore, V. Timbrell, The effects of the inhalation of asbestos in rats, Br. J. Cancer 29 (3) (1974) 252–269.

[22] M.S. Kanarek, Mesothelioma from chrysotile asbestos: update, Ann. Epidemiol. 21 (9) (2011) 688–697.
[23] G.P. Maresca, J.H. Puffer, M. Germine, Asbestos in lake and reservoir waters of Staten Island, New York: source, concentration, mineralogy, and size distribution, Environ. Geol. Water Sci. 6 (4) (1984) 201–210.
[24] B.T. Mossman, A. Churg, Mechanisms in the pathogenesis of asbestosis and silicosis, Am. J. Respir. Crit. Care Med. 157 (5) (1998) 1666–1680.
[25] J.P. Hollan, D.D. Smith, Asbestos. Clinical Environmental Health and Toxic Exposures, Lippincott Williams & Wilkins, Philadelphia, 2001, pp. 1214–1227.
[26] E. Yano, Z.M. Wang, X.R. Wang, M.Z. Wang, Y.J. Lan, Cancer mortality among workers exposed to amphibole-free chrysotile asbestos, Am. J. Epidemiol. 154 (6) (2001) 538–543.
[27] V.L. Roggli, R.T. Vollmer, K.J. Butnor, T.A. Sporn, Tremolite and mesothelioma, Ann. Occup. Hyg. 46 (5) (2002) 447–453.
[28] J.C. Pfau, J.J. Sentissi, G. Weller, E.A. Putnam, Assessment of autoimmune responses associated with asbestos exposure in Libby, Montana, USA, Environ. Health Perspect. 113 (1) (2005) 25.
[29] C.M. Yarborough, The risk of mesothelioma from exposure to chrysotile asbestos, Curr. Opin. Pulmonary Med. 13 (4) (2007) 334–338.
[30] O. Dikensoy, Mesothelioma due to environmental exposure to erionite in Turkey, Curr. Opin. Pulmonary Med. 14 (4) (2008) 322–325.
[31] B.T. Mossman, J. Bignon, M. Corn, A. Seaton, J.B. Gee, Asbestos: scientific developments and implications for public policy, Science 247 (4940) (1990) 294–301.
[32] A.B. Kane, P. Boffetta, R. Saracci, J.D. Wilbourn, Mechanisms of fibre carcinogenesis, IARC Sci. Publ. 140 (1996) 11–34.
[33] C. Oze, Biodurability of chrysotile and tremolite asbestos in simulated lung and gastric fluids, Am. Mineral. 95 (5–6) (2010) 825–831.
[34] S.H. Park, A.E. Aust, Participation of iron and nitric oxide in the mutagenicity of asbestos in *hgprt*$^{-}$, *gpt*$^{+}$ Chinese hamster V79 cells, Cancer Res. 58 (6) (1998) 1144–1148.
[35] R. Okayasu, L. Wu, T.K. Hei, Biological effects of naturally occurring and man-made fibres: in vitro cytotoxicity and mutagenesis in mammalian cells, Br. J. Cancer 79 (9–10) (1999) 1319–1324.
[36] M.C. Jaurand, Mechanisms of fiber-induced genotoxicity, Environ. Health Perspect. 105 (Suppl. 5) (1997) 1073–1084.
[37] M.J. Keane, J.W. Stephens, B.Z. Zhong, W.E. Miller, T.M. Ong, W.E. Wallace, A study of the effect of chrysotile fiber surface composition on genotoxicity in vitro, J. Toxicol. Environ. Health A 57 (8) (1999) 529–541.
[38] S.K. Eborn, A.E. Aust, Effect of iron acquisition on induction of DNA single-strand breaks by erionite, a carcinogenic mineral fiber, Arch. Biochem. Biophys. 316 (1) (1995) 507–514.
[39] B. Fubini, L. Mollo, Role of iron in the reactivity of mineral fibers, Toxicol. Lett. 82 (1995) 951–960.
[40] L.G. Korkina, A.D. Durnev, T.B. Suslova, Z.P. Cheremisina, N.O. Daugel-Dauge, I.B. Afanas'ev, Oxygen radical-mediated mutagenic effect of asbestos on human lymphocytes: suppression by oxygen radical scavengers, Mutat. Res. 265 (2) (1992) 245–253.
[41] T.K. Hei, Z.Y. He, K. Suzuki, Effects of antioxidants on fiber mutagenesis, Carcinogenesis 16 (7) (1995) 1573–1578.
[42] A. Xu, L.J. Wu, R.M. Santella, T.K. Hei, Role of oxyradicals in mutagenicity and DNA damage induced by crocidolite asbestos in mammalian cells, Cancer Res. 59 (23) (1999) 5922–5926.
[43] K. Unfried, C. Schürkes, J. Abel, Distinct spectrum of mutations induced by crocidolite asbestos clue for 8-hydroxydeoxyguanosine-dependent mutagenesis in vivo, Cancer Res. 62 (1) (2002) 99–104.
[44] K. Donaldson, F.A. Murphy, R. Duffin, C.A. Poland, Asbestos, carbon nanotubes and the pleural mesothelium: a review of the hypothesis regarding the role of long fibre retention in the parietal pleura, inflammation and mesothelioma, Part. Fibre Toxicol. 7 (5) (2010) 1–17.
[45] A. Morgan, J.C. Evans, A. Holmes, Deposition and clearance of inhaled fibrous minerals in the rat. Studies using radioactive tracer techniques, Inhaled Part. 4 (1975) 259–274.
[46] W.G. Light, E.T. Wei, Surface charge and hemolytic activity of asbestos, Environ. Res. 13 (1) (1977) 135–145.
[47] O. Stern, The theory of the electrolytic double-layer, Z. Elektrochem. 30 (1924) 508–516.
[48] M. von Smoluchowski, Contribution à la théorie de l'endosmose électrique et de quelques phénomènes corrélatifs, Bull. Int. Acad. Sci. Cracovie. Classe Sci. Math. Nat. 3A (43A) (1903) 182–199.
[49] J. Ralston, J.A. Kitchener, The surface chemistry of amosite asbestos, an amphibole silicate, J. Colloid Interface Sci. 50 (2) (1975) 242–249.
[50] K. Seshan, How are the physical and chemical properties of chrysotile asbestos altered by a 10-year residence in water and up to 5 days in simulated stomach acid? Environ. Health Perspect. 53 (1983) 143–148.
[51] L. Bonneau, H. Suquet, C. Malard, H. Pezerat, Studies on surface properties of asbestos: I. Active sites on surface of chrysotile and amphiboles, Environ. Res. 41 (1) (1986) 251–267.
[52] J. Khorami, D. Nadeau, Physicochemical characterization of asbestos and attapulgite mineral fibers before and after treatment with phosphorus oxychloride, Thermochim. Acta 108 (1986) 279–287.
[53] C. Jolicoeur, P. Roberge, J.L. Fortier, Separation of short fibers from bulk chrysotile asbestos fiber materials: analysis and physico-chemical characterization, Can. J. Chem. 59 (7) (1981) 1140–1148.
[54] H. Lamb, Hydrodynamics, sixth edition, Cambridge Univ. Press, Cambridge, 1993, pp. 738.
[55] M. Guldberg, V.R. Christensen, M. Perander, B. Zoitos, A.R. Koenig, K. Sebastian, Measurement of *in-vitro* fibre dissolution rate at acidic pH, Ann. Occup. Hyg. 42 (4) (1998) 233–243.
[56] C.J. Van Oss, J.O. Naim, P.M. Costanzo, R.F. Giese, W. Wu, A.F. Sorling, Impact of different asbestos species and other mineral particles on pulmonary pathogenesis, Clays Clay Miner. 47 (6) (1999) 697–707.
[57] M.P. Allen, R.W. Smith, Dissolution of asbestos minerals in acid and buffered salt solutions, in: 3rd Conf. Int. Phys. Chem. Minéral. Asbestos, Univ. Laval, Sect., Québec, 1975, pp. 4–16.
[58] E. Martinez, G.L. Zucker, Asbestos ore body minerals studied by zeta potential measurements, J. Phys. Chem. 64 (7) (1960) 924–926.
[59] T.M. Riddick, Control of Colloid Stability through Zeta Potential, Zeta-Mater Inc., New York, 1968, pp. 320–331.
[60] M. Trivedi, M.S. Thesis, Mackay School of Mines, University of Nevada, Reno, 1970.
[61] N.A. Prasad, F.D. Pooley, Characteristics of amphibole asbestos dust surfaces in aqueous media with reference to quartz, J. Appl. Chem. Biotechnol. 23 (9) (1973) 675–687.
[62] H.H. Hannila, E.D. Hallman, The adsorption of gold sols on asbestos surface charge sites, Powder Technol. 23 (2) (1979) 149–157.
[63] J.K. De Waele, I. Verhaert, E.E. Vansant, E.C. Adams, LAMMA analysis and adsorption study of aliphatic alkylammonium ions and alkylamines on asbestos fiber surfaces, Surf. Interface Anal. 5 (5) (1983) 186–192.
[64] P. Surkyn, J.D. Waele, F. Adams, Laser microprobe mass analysis for source identification of air particulate matter, Int. J. Environ. Anal. Chem. 13 (4) (1983) 257–274.
[65] D.J.A. Williams, K.P. Williams, Electrophoresis and zeta potential of kaolinite, J. Colloid Interface Sci. 65 (1) (1978) 79–87.
[66] H. Van Olphen, in: G.D. Parfitt, K.S.W. Sing (Eds.), Characterisation of Powder Surfaces, Academic Press, New York, 1976, pp. 428–455.
[67] İ. Polatoğlu, S.F. Özkan, Chemical Behaviour of Clinoptilolite Rich Natural Zeolite in Aqueous Medium (Diss.), İzmir Institute of Technology, İzmir, 2005.
[68] M.J. Osmond-McLeod, C.A. Poland, F. Murphy, L. Waddington, H. Morris, S.C. Hawkins, S. Clark, R. Aitken, M.J. McCall, K. Donaldson, Durability and inflammogenic impact of carbon nanotubes compared with asbestos fibres, Part. Fibre Toxicol. 8 (15) (2011).
[69] D. Bernstein, J. Dunnigan, T. Hesterberg, R. Brown, J.A.L. Velasco, R. Barrera, J. Hoskins, A. Gibbs, Health risk of chrysotile revisited, Crit. Rev. Toxicol. 43 (2) (2013) 154–183.
[70] H. Suquet, Effects of dry grinding and leaching on the crystal structure of chrysotile, Clays Clay Miner. 37 (5) (1989) 439–445.
[71] F.L. Pundsack, The properties of asbestos. I. The colloidal and surface chemistry of chrysotile, J. Phys. Chem. 59 (9) (1955) 892–895.
[72] S. Yao, G. DellaVentura, C. Petibois, Analytical characterization of cell–asbestos fiber interactions in lung pathogenesis, Anal. Bioanal. Chem. 397 (6) (2010) 2079–2089.
[73] B. Feng, Y.P. Lu, Q.M. Feng, P. Ding, N. Luo, Mechanisms of surface charge development of serpentine mineral, Trans. Nonferrous Met. Soc. China 23 (4) (2013) 1123–1128.
[74] S. Gabor, Z. Anca, Effect of asbestos on lipid peroxidation in the red cells, Br. J. Ind. Med. 32 (1) (1975) 39–41.
[75] W.S. Cho, R. Duffin, F. Thielbeer, M. Bradley, I.L. Megson, W. MacNee, G.A. Poland, C.L. Tran, K. Donaldson, Zeta potential and solubility to toxic ions as mechanisms of lung inflammation caused by metal/metal oxide nanoparticles, Toxicol. Sci. 126 (2) (2012) 469–477.
[76] W.E. Wallace, M.J. Keane, P.S. Mike, C.A. Hill, V. Vallyathan, E.D. Regad, Contrasting respirable quartz and kaolin retention of lecithin surfactant and expression of membranolytic activity following phospholipase A2 digestion, J. Toxicol. Environ. Health A 37 (3) (1992) 391–409.
[77] V. Hornung, F. Bauernfeind, A. Halle, E.O. Samstad, H. Kono, K.L. Rock, K.A. Fitzgerald, E. Latz, Silica crystals and aluminum salts activate the NALP3 inflammasome through phagosomal destabilization, Nat. Immunol. 9 (8) (2008) 847–856.
[78] D.W. Kamp, S.A. Weitzman, The molecular basis of asbestos induced lung injury, Thorax 54 (7) (1999) 638–652.
[79] K.E.N. Donaldson, P.J. Borm, The quartz hazard: a variable entity, Ann. Occup. Hyg. 42 (5) (1998) 287–294.
[80] R.P. Nolan, A.M. Langer, J.S. Harington, G. Oster, I.J. Selikoff, Quartz hemolysis as related to its surface functionalities, Environ. Res. 26 (2) (1981) 503–520.
[81] B. Fubini, V. Bolis, A. Cavenago, M. Volante, Physicochemical properties of crystalline silica dusts and their possible implication in various biological responses, Scand. J. Work Environ. Health\ 21 (suppl. 2) (1995) 9–14.
[82] V. Castranova, K. VanDyke, L. Wu, N.S. Dalal, V. Vallyathan, Suppression of silica-induced toxicity with organosilane surface coating, in: Silica and Silica-induced Lung Disease, CRC Press, Inc., Boca Raton, FL, 1996, pp. 283–291.
[83] G. Liu, P. Cheresh, D.W. Kamp, Molecular basis of asbestos-induced lung disease, Annu. Rev. Pathol. 8 (2013) 161–187.
[84] G. Sharma, V. Kodali, M. Gaffrey, W. Wang, K.R. Minard, N.J. Karin, J.G. Teeguarden, B.D. Thrall, Iron oxide nanoparticle agglomeration influences dose rates and modulates oxidative stress-mediated dose-response profiles in vitro, Nanotoxicology 8 (6) (2014) 663–675.
[85] M. Gualtieri, T. Skuland, T.G. Iversen, M. Låg, P. Schwarze, D. Bilaničová, G. Pojana, M. Refsnes, Importance of agglomeration state and exposure conditions

for uptake and pro-inflammatory responses to amorphous silica nanoparticles in bronchial epithelial cells, Nanotoxicology 6 (7) (2012) 700–712.
[86] M.F. Stanton, M. Layard, A. Tegeris, E. Miller, M. May, E. Morgan, A. Smith, Relation of particle dimension to carcinogenicity in amphibole asbestoses and other fibrous minerals, J. Natl. Cancer Inst. 67 (5) (1981) 965–975.
[87] F. Turci, M. Colonna, M. Tomatis, S. Mantegna, G. Cravotto, G. Gulino, E. Aldieri, D. Ghiro, B. Fubini, Surface reactivity and cell responses to chrysotile asbestos nanofibers, Chem. Res. Toxicol. 25 (4) (2012) 884–894.
[88] R. Venditti, X. Xuan, D. Li, Experimental characterization of the temperature dependence of zeta potential and its effect on electroosmotic flow velocity in microchannels, Microfluid. Nanofluid. 2 (6) (2006) 493–499.
[89] A. Revil, P.A. Pezard, P.W.J. Glover, Streaming potential in porous media: 1. Theory of the zeta potential, J. Geophys. Res.: Solid Earth (1978–2012) 104 (B9) (1999) 20021–20031.
[90] R. Ramachandran, P. Somasundaran, Effect of temperature on the interfacial properties of silicates, Colloids Surf. 21 (1986) 355–369.

Paper 2

The chemical environment of iron in mineral fibres. A combined X-ray absorption and Mössbauer spectroscopic study.

Pollastri, S., D'Acapito, F., Trapananti, A., Colantoni, I., Andreozzi, G. B., & Gualtieri, A. F.

Journal of Hazardous Materials 298 (2015) 282–293

Contents lists available at ScienceDirect

Journal of Hazardous Materials

journal homepage: www.elsevier.com/locate/jhazmat

The chemical environment of iron in mineral fibres. A combined X-ray absorption and Mössbauer spectroscopic study

Simone Pollastri[a,*], Francesco D'Acapito[b], Angela Trapananti[b], Ivan Colantoni[c], Giovanni B. Andreozzi[d], Alessandro F. Gualtieri[a]

[a] Department of Chemical and Geological Sciences, University of Modena and Reggio Emilia, Via S. Eufemia 19, I-41121 Modena, Italy
[b] CNR-IOM-OGG c/o ESRF, GILDA CRG, 71 Rue des Martyrs, F-38000 Grenoble, France
[c] Department of Physics, University of Rome "Tor Vergata", Via della ricerca scientifica 1, I-00133 Roma, Italy
[d] Department of Earth Sciences, Sapienza University of Rome, Piazzale Aldo Moro 5, I-00185 Roma, Italy

HIGHLIGHTS

- For the first time, mineral fibres were investigated using EXAFS spectroscopy.
- In all investigated mineral fibres, iron is found in octahedral sites.
- Erionite contains octahedrally coordinated Fe^{3+} as surface oxide nanoparticles.
- The amount of hydroxyl radicals released by fibres depends on their dissolution rate.

ARTICLE INFO

Article history:
Received 12 January 2015
Received in revised form 14 April 2015
Accepted 8 May 2015
Available online 12 May 2015

Keywords:
Asbestos
Mineral fibres
Iron
Chemical environment
Toxicity

ABSTRACT

Although asbestos represents today one of the most harmful contaminant on Earth, in 72% of the countries worldwide only amphiboles are banned while controlled use of chrysotile is allowed. Uncertainty on the potential toxicity of chrysotile is due to the fact that the mechanisms by which mineral fibres induces cyto- and geno-toxic damage are still unclear. We have recently started a long term project aimed at the systematic investigation of the crystal-chemistry, bio-interaction and toxicity of the mineral fibres. This work presents a systematic structural investigation of iron in asbestos and erionite (considered the most relevant mineral fibres of social and/or economic-industrial importance) using synchrotron X-ray absorption and Mössbauer spectroscopy. In all investigated mineral fibres, iron in the bulk structure is found in octahedral sites and can be made available at the surface via fibre dissolution. We postulate that the amount of hydroxyl radicals released by the fibers depends, among other factors, upon their dissolution rate; in relation to this, a ranking of ability of asbestos fibres to generate hydroxyl radicals, resulting from available surface iron, is advanced: amosite > crocidolite ≈ chrysotile > anthophyllite > tremolite. Erionite, with a fairly high toxicity potential, contains only octahedrally coordinated Fe^{3+}. Although it needs further experimental evidence, such available surface iron may be present as oxide nanoparticles coating and can be a direct cause of generation of hydroxyl radicals when such coating dissolves.

1. Introduction

In the realm of mineral fibres, the asbestos family (chrysotile and amphiboles) and the zeolite erionite are certainly the most feared ones [1,2]. Chrysotile is a hydrous layer silicate with a cylindrical lattice [3,4,5]. The family of fibrous amphiboles [6] includes actinolite, tremolite, crocidolite, amosite and anthophyllite. Fibrous erionite is a widespread zeolite of both sedimentary and hydrothermal origin [7,8].

Although it was proven that all these mineral fibres, if inhaled, may induce lethal lung diseases [9,10,11,12,13,14], there is still considerable controversy in the scientific community to whether chrysotile asbestos is actually a potent carcinogen to humans [15,16]. At the moment, all amphibole asbestos minerals are banned worldwide whereas chrysotile is banned only in the countries where the line of the international agency for research on cancer (IARC) of the World Health Organization and the national toxicology program is fostered [17,18,19,20,21,22]. Erionite, a

* Corresponding author. Tel.: +39 059 2055806; fax: +39 059 2055887.
E-mail address: simone.pollastri@unimore.it (S. Pollastri).

http://dx.doi.org/10.1016/j.jhazmat.2015.05.010
0304-3894/

human carcinogen listed by the IARC as a Group 1 Carcinogen, surprisingly has not been banned to date [23].

Fibre size, surface activity, ability to generate reactive oxygen species, biopersistence [24], iron content and iron-bodies formation are all factors deemed to play a role in inducing asbestos correlated lung diseases [2,24,25,26,27,28,29,30,31,32,33,34,35]. Specifically, iron associated with asbestos promotes the formation of highly reactive $HO^{\bullet}$ species via a Fenton like chain reaction. The initiation of the chain reaction is the reduction of ferric iron (Fe^{3+}) by H_2O_2 released by the macrophages during the inflammatory burst [14,36]: $Fe^{3+} + H_2O_2 \rightarrow Fe^{2+} + HO_2^{\bullet}/O_2^{\bullet} + H^+$. Fe^{2+} is then oxidized by another H_2O_2 molecule and the chain propagates through reactions: $H_2O_2 + HO^{\bullet} \rightarrow HO_2^{\bullet}/O2^{\bullet} + H_2O$; $Fe^{3+} + HO_2^{\bullet}/O2^{\bullet} \rightarrow Fe^{2+} + O_2 + H^+$ (family of catalysed Haber-Weiss reactions). $HO^{\bullet}$ is thought to be the predominant damaging species in vivo because elements which generate them such as iron are often capable of binding to DNA itself allowing $HO^{\bullet}$ production to occur in the immediate vicinity of the DNA [37]. Both the presence and the speciation (oxidation state and coordination environment) of iron were shown to be important factors of asbestos toxicity [38–51]. For this reason, iron-bearing mineral fibres have been investigated in the past using various experimental techniques: for example, Canadian chrysotiles, including the UICC standard, with Mössbauer spectroscopy (MS) [52,53]; tremolite asbestos from the Susa Valley (Italy) with combined MS and X-ray diffraction (XRD) [54]; erionite from Rome (Oregon, USA) with combined MS and XRD [55]; UICC crocidolite and Italian tremolite asbestos with combined MS and X-ray photoelectron spectroscopy (XPS) [41]; synthetic asbestos nanofibres with MS [38]; asbestos fibres in human lung tissues of naval shipyard workers with synchrotron X-ray fluorescence (XRF) mapping and micro-XANES [33].

Despite the large amount of spot data, a systematic study of the chemical environment of iron in the most important mineral fibres is still missing to date. The present work fulfils this

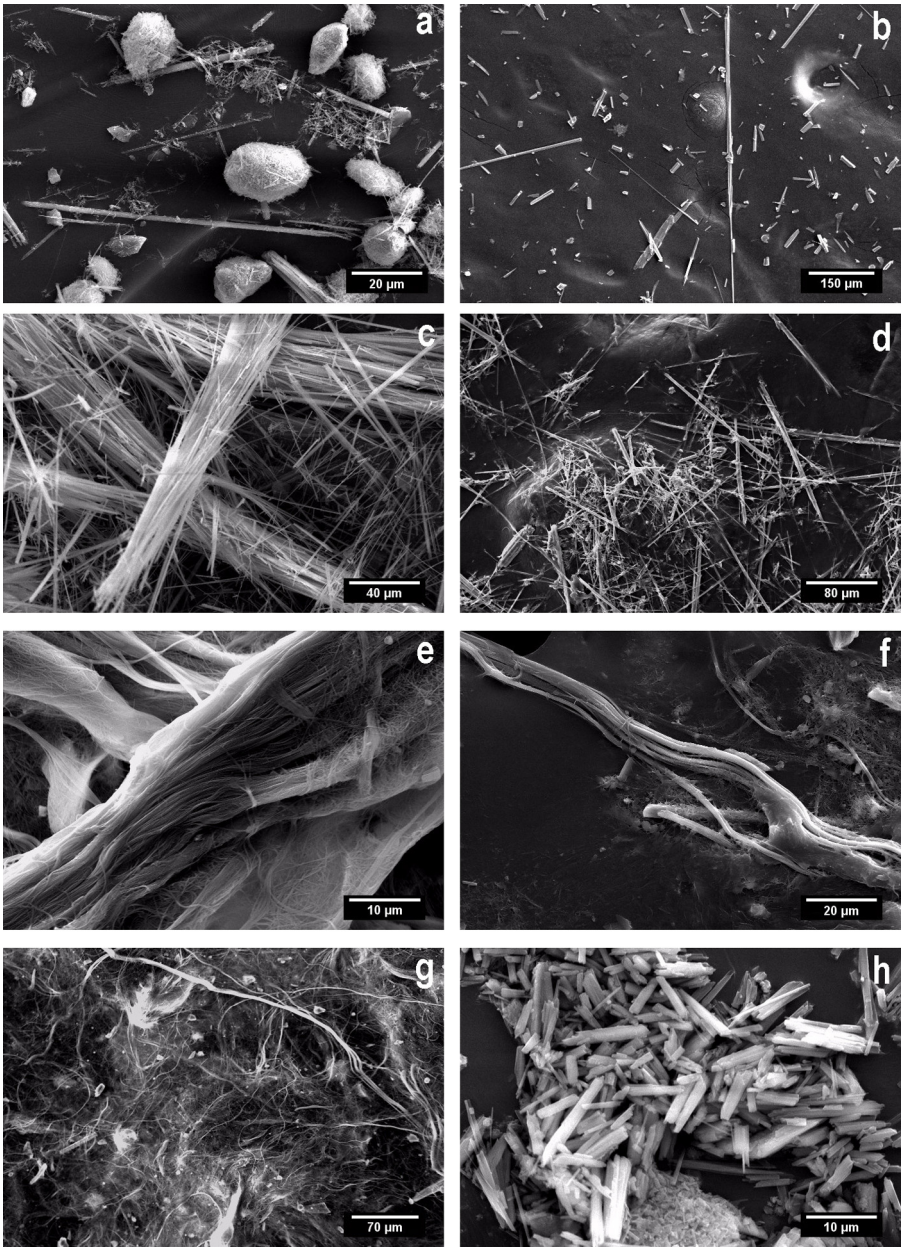

Fig. 1. High-resolution SEM images of investigated samples: (a) crocidolite; (b) tremolite; (c) anthophyllite; (d) amosite; (e) chrysotile Val Malenco; (f) chrysotile Balangero; (g) chrysotile UICC; (h) erionite.

gap and reports a systematic structural investigation of the most relevant iron-bearing mineral fibres using two powerful and complementary techniques to determine the chemical environment of iron in almost any kind of material. Specifically, synchrotron X-ray absorption (XAS) spectroscopy permits to determine coordination number and oxidation state of iron thanks to the analysis of the XANES pre-edge parameters (total area and centroid position) whereas EXAFS refinements allow to estimate Fe—O distances and a structure model for the iron chemical environment. Mössbauer spectroscopy (MS) allows to quantitatively determine the percentages of Fe^{2+} and Fe^{3+}, their coordination number and to distinguish them depending on whether the iron belongs to magnetic phases (e.g. impurities as magnetite and hematite) or silicate phases. The investigated fibres were formerly fully characterized in [56].

2. Experimental

2.1. Materials and preliminary characterization

The samples investigated in this study are:

(1) UICC standard amosite amphibole asbestos $[(Ca_{0.02}Na_{0.01})(Fe^{2+}_{5.36}Mg_{1.48}Fe^{3+}_{0.11}Mn_{0.06})_{7.01}(Si_{7.93}Al_{0.01})_{7.94}O_{21.94}(OH)_{2.06}]$ with minor impurities of calcite, hematite, and quartz;

(2) UICC standard antophyllite amphibole asbestos $[Ca_{0.04}(Mg_{5.81}Fe^{2+}_{0.92}Fe^{3+}_{0.21}Mn_{0.04})_{6.98}(Si_{7.83}Al_{0.02})_{7.85}O_{21.63}(OH)_{2.37}]$ with impurities of biotite, clinochlore/vermiculite and talc;

(3) UICC standard crocidolite amphibole asbestos $[(Na_{1.96}Ca_{0.03}K_{0.01})_2(Fe^{2+}_{2.34}Fe^{3+}_{2.05}Mg_{0.52})_{4.91}(Si_{7.84}Al_{0.02})_{7.86}O_{21.36}(OH)_{2.64}]$, with minor impurities of hematite, magnetite, and quartz;

(4) tremolite amphibole asbestos from Val d'Ala (Italy) $[(Ca_{1.91}Na_{0.06}K_{0.01})_{1.98}(Mg_{4.71}Fe^{2+}_{0.22}Fe^{3+}_{0.08}Mn_{0.02})_{5.03}(Si_{8.01}Al_{0.02})_{8.03}O_{22.14}(OH)_{1.86}]$ with minor impurities of antigorite, clinochlore, hematite and talc;

(5) UICC standard chrysotile asbestos $[Mg_{5.93}Fe^{2+}_{0.11}Al_{0.02}Fe^{3+}_{0.01})_{6.07}Si_{4.03}O_{10}(OH)_{7.66}]$ with impurities of brucite, calcite, clinochlore, dolomite, magnetite, microcline, pyroaurite and talc;

(6) chrysotile asbestos from Balangero (Italy) $[(Mg_{5.81}Fe^{2+}_{0.21}Al_{0.27}Fe^{3+}_{0.03}Cr_{0.01})_{6.33}Si_{3.97}O_{10}(OH)_{7.11}]$, with impurities of antigorite, balangeroite, calcite, clinochlore, diopside, dolomite, magnetite, microcline, plagioclase, and talc;

(7) chrysotile asbestos from Val Malenco (Italy) $[(Mg_{5.85}Fe^{2+}_{0.11}Al_{0.02}Ni_{0.01})_{5.99}Si_{4.01}O_{10}(OH)_{7.86}]$ with impurities of calcite, forsterite, magnetite, quartz and very minor impurities of lizardite/antigorite and clinochlore;

(8) erionite (fibrous) from Jersey, Nevada (USA) $[(Na_{5.31}K_{2.18}Ca_{0.15}Mg_{0.11}Fe^{3+}_{0.29})_{8.04}(Si_{27.84}Al_{7.85})_{35.69}O_{72}\cdot 28.13H_2O]$ with impurities of clinoptilolite.

Powdered samples were investigated with scanning electron microscopy (SEM). The specimens were mounted on Al stubs and coated with gold (10 nm thick film). Micrographs were collected using an ESEM Quanta-200 instrument.

2.2. Methods

The details of the experimental methods are reported in Supplementary material 1.

2.2.1. XAS

Fe K-edge XAS spectra were collected at the GILDA-BM08 CRG beamline (ESRF, Grenoble, France; [57]). For all the experiments, energy calibration was achieved using iron foil as reference with the position of the first inflection point taken at 7112.0 eV. The following reference compounds were used: almandine (Fe^{2+} [VIII]),

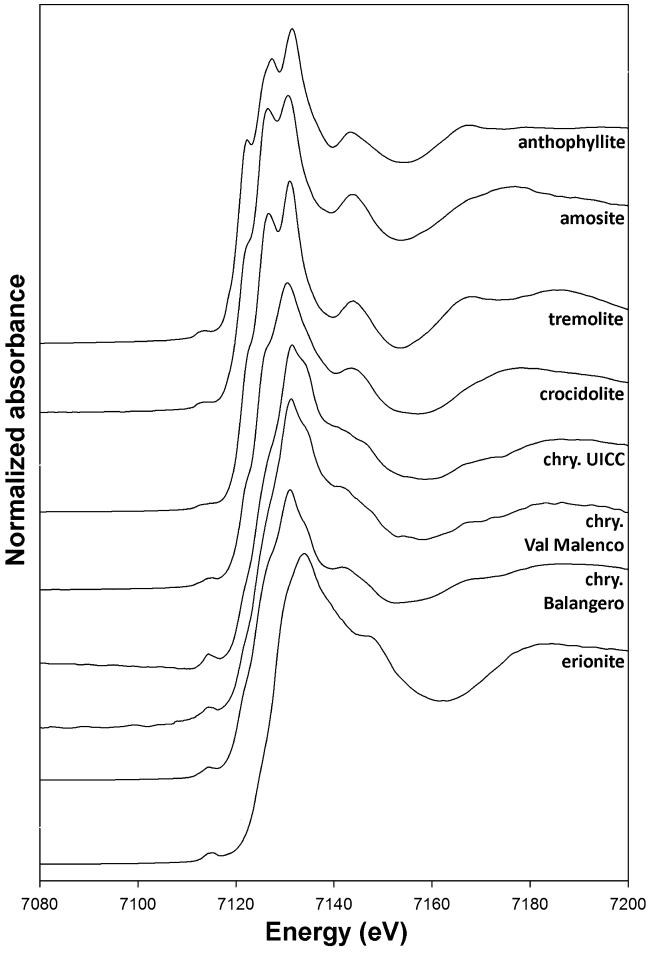

Fig. 2. Fe K-edge XANES spectra of investigated samples.

Table 1
XANES pre-edge parameters of reference compounds (a) and investigated samples (b). All reported data are the average result obtained from a minimum of three analysis.

(a)

Sample	Iron oxidation state	Coordination	Total area	r^2	Centroid position (eV)
Olivine	+2	VI	0.046 (4)	0.9993	7112.84 (1)
Siderite	+2	VI	0.034 (1)	0.9990	7112.93 (2)
Almandine	+2	VIII	0.039 (8)	0.9996	7113.01 (3)
Hercynite	+2	IV	0.206 (8)	0.9996	7113.16 (7)
Hematite	+3	VI	0.073 (9)	0.9995	7114.49 (7)
Goethite	+3	VI	0.074 (6)	0.9991	7114.68 (4)
Magnetite	+2	VI	0.199 (9)	0.9997	7114.19 (5)
	+3	IV-VI			
Silicalite	+3	IV	0.310 (8)	0.9984	7114.41 (2)
Biotite		VI	0.061 (2)	0.9996	7114.37 (3)
$FePO_4$_1	+3		0.079 (2)	0.9994	7114.67 (5)
$FePO_4$ - 2	+3		0.081 (5)	0.9995	7114.73 (2)

(b)

Sample	Total area	r^2	Centroid position (eV)
Anthophyllite	0.054 (5)	0.9997	7113.13 (3)
Amosite	0.044 (5)	0.9997	7113.17 (4)
Tremolite	0.032 (8)	0.9996	7113.56 (7)
Crocidolite	0.054 (7)	0.9993	7114.05 (5)
Chrysotile Balangero	0.074 (7)	0.9991	7114.04 (9)
Chrysotile Val Malenco	0.072 (5)	0.9990	7114.13 (5)
Chrysotile UICC	0.129 (8)	0.9997	7114.42 (5)
Erionite	0.076 (2)	0.9994	7114.65 (3)

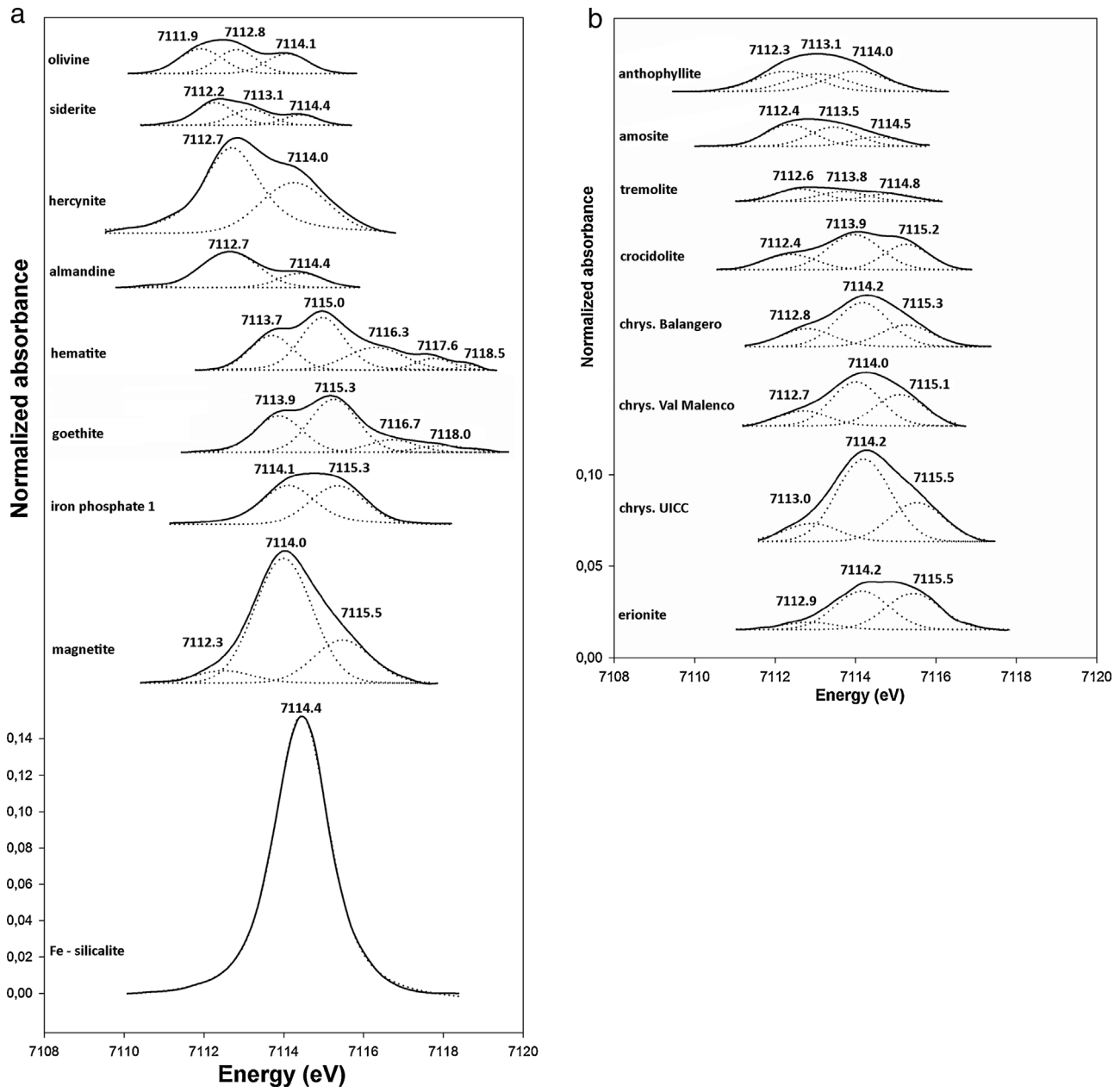

Fig. 3. Fit of the pre-edge peaks of the reference compounds (a) and investigated samples (b). All reported fits are the average result obtained from a minimum of three data analysis; Fe–silicalite fit is not clearly visible as the fit line is almost totally overlapped to the experimental points.

hercynite (Fe^{2+} [IV]), siderite (Fe^{2+} [VI]), olivine (Fe^{2+} [VI]), biotite (Fe^{2+} [VI]), hematite (Fe^{3+}[VI]), goethite (Fe^{3+}[VI]), magnetite (Fe^{2+} [VI]) and Fe^{3+} [IV–VI]), iron phosphate (Fe^{3+} [IV]) (2 samples) and silicalite (Fe^{3+} [IV]). The X-ray absorption near edge structure (XANES) spectra of samples and reference compounds were normalized with respect to the high-energy side of the curve using Athena [58] and then subtracted from the pre-edge background using the program Origin 6.0. The analysis of the pre-edge region was then performed by least-square fitting of pseudo-Voigt functions to the pre-edge spectral envelope, using the program PeakFit 4.12. EXAFS spectra were analyzed using IFEFFIT-1.2.9 package [58,59].

2.2.2. Mössbauer

For the Mössbauer experiments, given the different Fe content of the various samples, a variable amount of 10–100 mg was used so that Fe total content of the absorber was between 1 and 5 wt.%, within the limits for the thin absorber thickness described in [60]. ^{57}Fe-Mössbauer spectra were collected at room temperature (RT), using a conventional spectrometer operating in constant acceleration mode with a ^{57}Co source of nominal strength of 25 mCi in rhodium matrix, and recorded with a multi-channel analyzer using 512 channels. The spectra were fit using the Recoil 1.04 fitting program [61]. Data analysis involved a curve-fitting procedure made assuming a Lorentzian peak shape. The statistical best fit was obtained by using the reduced χ^2 method. Fitting of Quadrupole Splitting Distribution was also tested (following an approach previously used [62–63]) but did not improve the fit obtained with Lorentzian curves.

3. Results

Fig. 1 reports a gallery of high-resolution SEM images of the investigated fibres (details about SEM analysis are given in [56]).

All amphibole asbestos species exhibit a marked needle-like crystal habit (Fig. 1a–d) with a heterogeneous size distribution. As already remarked in [56] some fibres tend to agglomerate into ball-like clusters (see for example crocidolite in Fig. 1a). Chrysotile species show instead a marked flexible fibrous-asbestiform crystal habit with bundles of long and short fibres (Fig. 1e–g). Erionite crystals (Fig. 1h) are short and stubby with an even size distribution.

Concerning the XAS data, several Fe–bearing minerals [64–76] were used as a reference. The Fe K-edge XANES spectra of the investigated samples are reported in Fig. 2. Fig. 3 reports the fit of the pre-edge peaks of the reference compounds (a) and investigated samples (b) whereas Fig. 4 the results of the fit of the EXAFS spectra. EXAFS refinements of reference compounds were performed using the structure models reported in [77–82]. Table 1(a, b) and Table 2(a, b) report the relevant data obtained from the XANES and EXAFS analysis; details about the analysis and detailed Table 1 and 2 are reported in the Supplementary material 2 "Details of the Results". During the analysis, some constraints have been used due to both the complexity of the oxygen atoms geometry in the first shell and the relevant structure disorder [83].

Room-temperature ^{57}Fe-Mössbauer spectra of amosite, erionite, chrysotile Balangero, chrysotile Val Malenco and erionite Jersey are shown in Fig. 5. Refined hyperfine parameters are reported in Table 3 together with literature data available for the investigated samples (symbols and correction factors according to [84–86]). Details about the Mössbauer analysis are also reported in the Supplementary material 2 "Details of the Results".

Table 2
(a) Reference compounds; (b) samples. Crystallographic data and structural parameters as obtained from the *R*-space fit by using the theoretical references.

a)

Shells	Ref. comp.	Ref.	N	R(Å)
hematite	Fe_2O_3	[77]		
Fe—O_1			3	1.938
Fe—O_2			3	2.105
goethite	FeO(OH)	[78]		
Fe—O_1			1	1.890
Fe—O_2			2	1.928
Fe—O_3			1	2.014
Fe—O_4			2	2.087
almandine	$Fe_3Al_2(SiO_4)_3$	[79]		
Fe—O_1			4	2.146
Fe—O_2			4	2.285
hercynite	$FeAl_2O_4$	[80]		
Fe—O_1			4	1.949
siderite	$FeCO_3$	[81]		
Fe—O_1			6	2.113
biotite	–	[82]		
Fe—O_1			2	1.994
Fe—O_2			2	2.070
Fe—O_3			2	2.137

b)

Shells	%	Ref.[a]	N	R(Å)
anthophyllite				
Fe—O_1			3	2.07 (3)
Fe—O_2			3	2.08 (3)
amosite				
Fe—O_1			6	2.083 (4)
tremolite				
Fe—O_1			6	2.093 (4)
crocidolite				
Fe—O_1			6	2.059 (8)
chry. Balangero				
Site1 - Fe—O_1	0.2[b]		4	1.770 (5)
Site2 - Fe—O_1	0.8[b]		6	2.054 (4)
chry. Val Malenco				
Site1 - Fe—O_1	0.2[b]		4	1.81 (3)
Site2 - Fe—O_1	0.8[b]		6	2.033 (3)
chry. UICC				
Site1 - Fe—O_1	0.3[b]		4	1.86 (2)
Site2 - Fe—O_1	0.7[b]		6	2.028 (6)
erionite				
Fe—O_1			6	2.011 (8)

[a] References are not reported because structural models have been modified from the original (number of oxygens, number of coordination spheres).
[b] Kept fixed in the refinement to the values from the Mössbauer analysis.

4. Discussion

4.1. Iron chemical environment in minerals fibres

The XANES pre-edge peak centroids and the Mössbauer spectra of the investigated samples revealed the presence of both Fe^{2+} and Fe^{3+} oxidation states and that the two iron species are disordered over different structural sites (Fig. 6 and Table 1). Fig. 6 is a modified version of the variogram from [72]. Because literature data [71,72,87] have the iron threshold calibrated at variable energies, they have all been rescaled to be compared to our data (threshold of iron at 7112.00 eV). The obtained cationic distribution of Fe ions in our samples are in general agreement with literature data [88–95] and will be hereby discussed in detail.

4.1.1. Amphiboles

In amphiboles, with a general formula $AB_2C_5T_8O_{22}W_2$ [96] Fe^{2+} ions can be potentially hosted in the octahedral positions C, namely *M*(1), *M*(2), *M*(3), and (B), namely *M*(4) [53,91,92], whereas Fe^{3+} can only be hosted in the C positions [53,93,97]. These sites are sandwiched between two double silicate chains [40] being *M*(3) the innermost inside the structure. *M*(1) is close to *M*(3) whereas *M*(2) and *M*(4) are peripheral, shifted towards the edge of the double silicate chain.

In UICC anthophyllite, the pre-edge peaks centroid position at 7113.13(3) eV (Table 1) indicates the presence of Fe^{2+} in agreement with MS information from the literature (Table 3). The total pre-edge peaks area of 0.054(5) points to iron hosted only in octahedral position (Table 1). The best fit of the EXAFS data was obtained with a first shell composed of three oxygen atoms at 2.07 Å and 2.08 Å, respectively. Unfortunately, the quality of the data is poor (see Fig. 4a) and it was not possible to accomplish a better fit (see the R-factor and Debye–Waller in Table 2). As reported in many MS studies on anthophyllite samples [53,100,101], the population of Fe^{2+} in *M*(4) is much larger than the population in *M*(1), *M*(2) and *M*(3); Fe^{3+} ions, if any, are expected to be confined in *M*(2) site although in some cases the occurrence of small amounts of Fe^{3+} in *M*(1) or *M*(3) sites has been reported. Hence, UICC anthophyllite results to be mainly composed of Fe^{2+} with a very low amount of Fe^{3+}, both in octahedral coordination, with Fe^{2+} ions preferably hosted in *M*(4) site.

For UICC amosite, XANES pre-edge centroid position at 7113.17(4) eV and total pre-edge peaks area of 0.044(5) indicate predominance of Fe^{2+} hosted only in octahedral position (Table 1 and Fig. 6) in agreement with MS data (Table 3). EXAFS data (Table 2) confirm a first shell of six oxygen atoms at a mean distance of 2.083 Å, slightly shorter but still close to the theoretical value of octahedral Fe^{2+}—O (2.14 Å). MS data of the cummingtonite-grunerite series [53,92,98,99] were fitted using a model with Fe^{2+} ions preferably in *M*(4) site with respect to *M*(2). According to this model, 35% of the total Fe^{2+} is hosted in *M*(4) site, and remaining Fe^{2+} ions randomly distributed over *M*(1), *M*(2) and *M*(3) sites. Therefore, despite UICC amosite generally contains much more iron with respect to UICC anthophyllite, the models of cation distribution are comparable, with octahedral Fe^{2+} largely prevailing over Fe^{3+}.

Tremolite from Val d'Ala displays a pre-edge centroid position at 7113.56(7) eV (Table 1) close to that of Fe^{2+} (Fig. 6) whereas

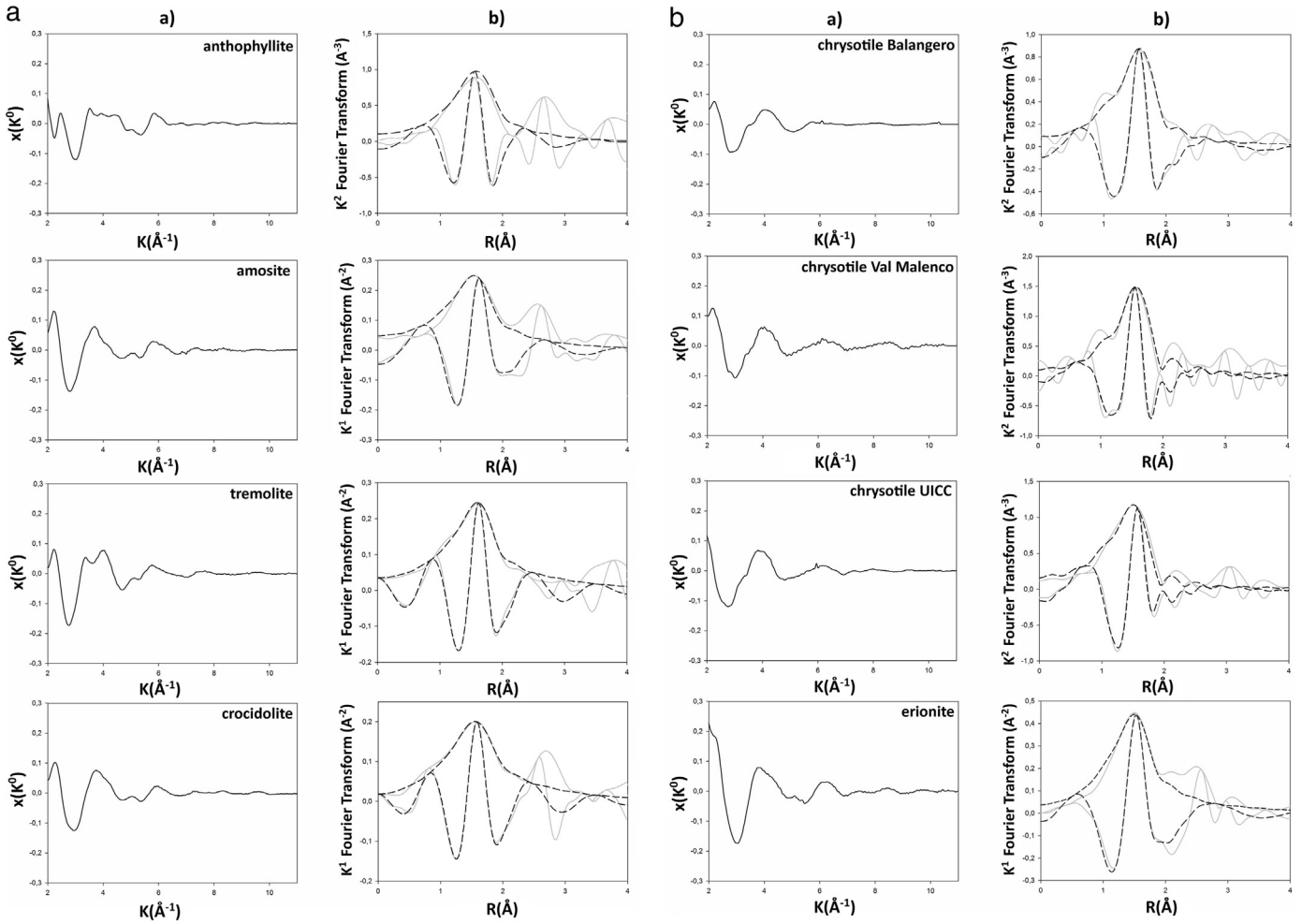

Fig. 4. Results of the fit of the EXAFS spectra: (a) $\chi(k0)$ experimental data; (b) $k1,2$ Fourier transformed experimental (gray solid line) and fitted (black medium dash) data of investigated samples, both supplied with the real part.

the total pre-edge area of 0.032(8) is the lowest among the investigated samples and indicates that iron is only in octahedral position. These findings are in agreement with MS data (Table 3). The best fit of the EXAFS data (Table 2), collected in fluorescence mode, was obtained with a single shell of six oxygen atoms at 2.093 Å. This is consistent with the coexistence of Fe^{2+} and Fe^{3+}, with Fe^{2+} as dominant species, falling between the theoretical value of octahedral Fe^{2+}-O (2.14 Å) and that of octahedral Fe^{3+}-O (2.015 Å). Literature data on tremolite samples characterized with MS and other techniques reports that approximately 40% of Fe^{2+} is located $M(2)$ site, while the remaining is disordered over both $M(1)$ and $M(3)$ sites [41,43,44,54,88]. Considering the site multiplicity, an almost disordered distribution of iron over sites $M(1)$, $M(2)$ and $M(3)$ may be predicted, while Fe^{3+} is ordered in $M(2)$ site.

As far as UICC crocidolite is concerned, XANES data evidence comparable fractions of Fe^{2+} and Fe^{3+}, with a pre-edge centroid position at 7114.05(5) eV (Table 1), halfway between that of the Fe^{2+} and Fe^{3+} standards and in agreement with MS information (Table 3). The total area of the pre-edge peaks 0.054(7) indicates that iron has an octahedral coordination. EXAFS data confirms a first shell of six oxygen atoms at a mean distance of 2.059 Å (Table 2). This value is right in between the theoretical value of octahedral Fe^{2+}-O (2.140 Å) and the theoretical value of octahedral Fe^{3+}-O (2.015 Å). Thus, iron in UICC crocidolite has comparable amount of ferrous and ferric iron both in octahedral coordination (Fig. 6). This finding is in concert with the literature data [40,41]. A structural study about the Bolivian crocidolite [93] reported that site $M(4)$ is partially vacant with magnesium largely prevailing over iron. MS data from the literature [41,44,53,92,94] confirm that Fe^{3+} ions are mainly found in the peripheral $M(2)$ positions with a small proportion in $M(1)$ and $M(3)$ while most of the Fe^{2+} ions occupy $M(1)$ and $M(3)$, the innermost positions. In concert, the distance of 2.09 Å obtained from EXAFS refinement is consistent with the average interatomic distances of six oxygen atoms (2.088 Å) with respect to Fe ions within $M(1)$, $M(2)$ and $M(3)$ positions calculated from an ideal structural model of crocidolite.

4.1.2. Chrysotiles

Chrysotile, with an ideal formula $Mg_3Si_2O_5OH_4$, is composed of an Mg-centred octahedral sheet and a Si-centred tetrahedral sheet. Both Fe^{2+} and Fe^{3+} ions can replace magnesium [40,53]. Fe^{3+} ions may eventually replace Si ions although this position may preferentially host Al^{3+} [52,102].

As far as UICC chrysotile is concerned, XANES data evidence major fractions of Fe^{3+} with respect to Fe^{2+}, with a pre-edge peaks centroid position at 7114.42(5) eV (Table 1). The total pre-edge peaks area of 0.129(8) indicates that iron is hosted in both octahedral and tetrahedral environment. This is confirmed by the EXAFS data (Table 2), showing two different site positions for iron: one having a first shell of four oxygen atoms at 1.860 Å and another one with a first shell of six oxygen atoms at 2.028 Å. The first shell is compatible with Fe^{3+} tetrahedral environment

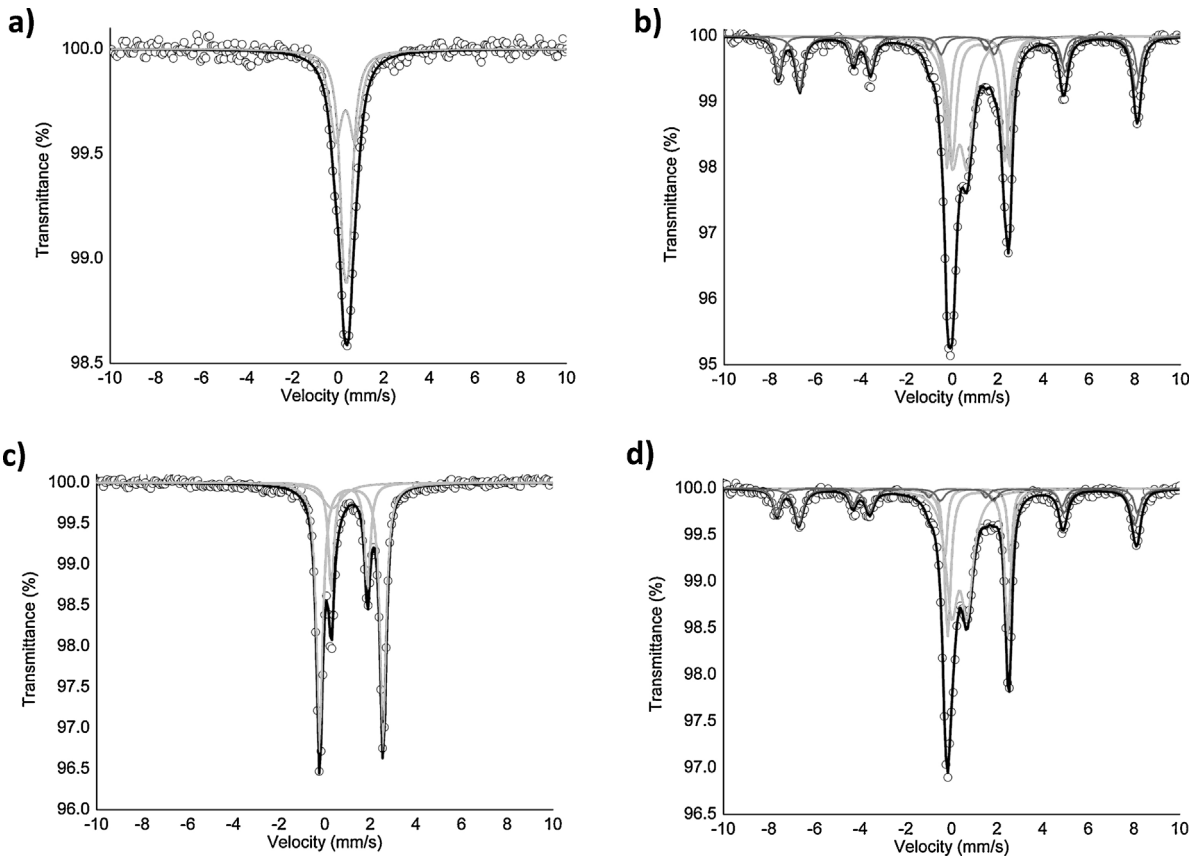

Fig. 5. Representative RT ^{57}Fe Mössbauer spectra of the investigated samples: (a) erionite; (b) chrysotile Balangero; (c) amosite; (d) chrysotile Val Malenco. Open circles = experimental spectrum; black thick line = calculated spectrum; light gray thin line = Fe^{2+} and Fe^{3+} paramagnetic subspectra; dark grey thin line = $Fe^{2.5+}$ and Fe^{3+} magnetic subspectra.

(theoretical distance 1.865 Å) while the second one with an octahedral environment mainly Fe^{3+} with a small presence of Fe^{2+} (theoretical distances 2.015 Å and 2.140 Å, respectively). The presence of tetrahedral iron is widely justified by the previous MS study on this sample [53] showed that about 60% of total iron belongs to magnetite. Hence, assigning all tetrahedral iron to magnetite/maghemite and taking into account its contribution for octahedral Fe^{2+} and Fe^{3+}, UICC chrysotile sample displays ferric iron prevailing over ferrous iron (in agreement with [103]) both in octahedral coordination (Fig. 6).

In the Balangero sample, XANES data suggest almost comparable fractions of Fe^{2+} and Fe^{3+}, with a pre-edge peaks centroid position at 7114.04(9) eV (Table 1). The total pre-edge peaks area of 0.074(7) points to iron mainly in octahedral environment, with possible minor presence of tetrahedral iron. EXAFS refinements show two site positions: a first shell of four oxygen atoms at distance of 1.770 Å (attributed to tetrahedral ferric iron from magnetite) and another with six oxygen atoms at 2.054 Å (Table 2), consistent with an octahedral environment halfway between Fe^{2+} and Fe^{3+} (theoretical distances 2.140 Å and 2.015 Å, respectively). Based on MS results (Table 3), about 30% of the total iron is attributed to magnetite and 70% to chrysotile. Magnetite, given to the observed non-stoichiometric Fe^{3+}/Fe_{tot} ratio, shows a 10% oxidation to maghemite. In chrysotile Fe^{2+} is higher than Fe^{3+} (40% and 30% of Fe_{tot}, respectively). Although MS cannot discriminate iron present in chrysotile from iron present in other silicate (e.g. balangeroite), a relevant contribution from silicate impurities should be ruled out because: (i) despite Val Malenco and Balangero chrysotiles are of different origin (with different silicate phase impurities) spectra are very similar; (ii) silicate phase impurities have low iron content. In conclusion, from the convergence of XANES, EXAFS and MS data, it is possible to conclude that iron in chrysotile sample from Balangero is half ferrous and half ferric, both hosted in octahedrally-coordinated sites (Fig. 6).

Concerning the Val Malenco sample, XANES pre-edge centroid position at 7114.13(5) eV and total pre-edge peaks area of 0.072(5) indicate comparable fractions of Fe^{2+} and Fe^{3+} almost exclusively in 6-fold coordination (Table 1 and Fig. 6). EXAFS results are in agreement with XANES data and very similar to that of Balangero

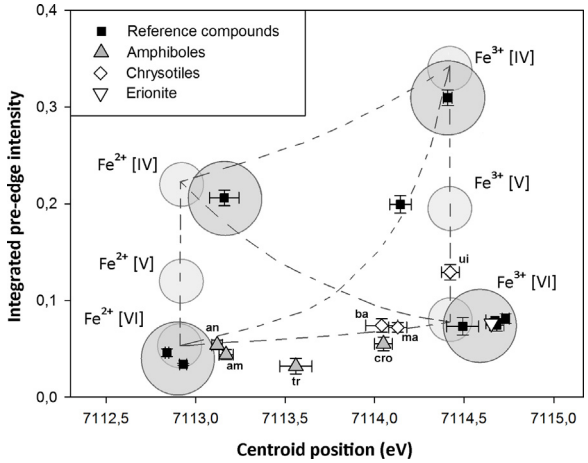

Fig. 6. Pre-edge parameters of samples and reference compounds plotted in the modified variogram from [72]. Little grey fields designate pre-edge parameters for the Fe co-ordination and oxidation state whereas dashed lines between fields indicate the variation of pre-edge parameters assuming binary mixtures of respective end-members [72]; larger grey fields designate our pre-edge parameter.

Table 3
Room temperature ^{57}Fe Mössbauer hyperfine parameters for the investigated fibrous samples compared to extant data from literature.

Sample	X^2	Fe^{2+}				Fe^{3+}					Fe^{3+}_{raw}	Fe^{3+}_{corr}
		δ (δ_0) (mm/s)	ΔE_Q (Δ_0) (mm/s)	Γ (σ_Δ) (mm/s)	Area (%)	δ (δ_0) (mm/s)	ΔE_Q (Δ_0) (mm/s)	Γ (σ_Δ) (mm/s)	(H) Tesla	Area (%)	(% Fe_{tot})	(% Fe_{tot})
Amosite	1.12	1.16	2.79	0.32	64	0.30	0.00	0.82		9	9	8
UICC standard		1.08	1.57	0.32	26							
Amosite		1.14	2.80	0.38	53	0.37	1.06	0.68		9	9	7
UICC standard[b]		1.07	1.58	0.52	38							
Anthophyllite		1.11	2.64	0.48	38						0	
UICC standard[b]		1.10	1.82	0.32	62							
Crocidolite	3.16	1.07	2.92	0.03		0.37	1.00	1.86			57	52
UICC standard[a]		1.07	2.64	0.38		0.37	0.43	0.18				
Crocidolite		1.12	2.90	0.34	38	0.38	0.42	0.31		42	42	37
UICC standard[b]		1.13	2.42	0.34	20							
Tremolite	0.79	1.19	2.92	0.17	48	0.25	2.16	0.62		7	15	12
Ala di Stura[a]		1.19	1.89	0.20	37	0.25	1.02	0.32		8		
Chrysotile	0.97	1.14	2.73	0.30	17	0.33	0.66	0.64		30	51	43
Balangero		1.16	2.32	0.44	23	*0.26*			*49*	*12*		
						0.68			*46*	*18*		
Chrysotile	0.88	1.13	2.88	0.24	10	0.35	0.69	0.62		37	56	47
Val Malenco		1.15	2.63	0.33	26	*0.26*			*49*	*10*		
						0.67			*46*	*17*		
Chrysotile		1.12	2.65			*0.34*	0.75				70	57
UICC standard[b]						*0.20*	0.34					
Erionite	0.49					0.35	0.24	0.44		55	100	100
Jersey, Nevada						0.32	0.85	0.64		45		
Erionite	0.89					0.34	0.34	0.50		80	100	100
Rome, Oregon[c]						0.38	1.17	0.40		20		

Notes: center shift (δ) measured with respect to α-iron. Lorentzian site analysis: uncertainties were estimated at about ± 0.02 mm/s for both δ, quadrupole splitting (ΔEQ) and line width (Γ), ±0.5 Tesla for magnetic field (H), and no less than ±3 % for absorption area (expressed as % of Fe_{tot}). In italics: parameters assigned to Fe^{3+} and $Fe^{2.5+}$ of accessory magnetite in chrysotile. Fe^{3+} raw: area of absorption peaks assigned to Fe^{3+}; Fe^{3+}_{corr}: obtained from raw value by applying the correction factor of Dyar et al. [86] for amphiboles and chrysotiles, and that of De Grave and Van Alboom [84] for magnetite; this parameter is referred to the total amount of Fe^{3+} in the sample (including possible impurities). Symbols according to Rancourt and Ping [85].

[a] Original data from [41]: in this case the QSD parameters center shift (δ0), center of Gaussian components (Δ0) and Gaussian width (σΔ) are reported.
[b] Original data from [53].
[c] Original data from [55].

chrysotile with a first shell of four oxygen atoms at a distance of 1.810 Å and another with six oxygen atoms at 2.033 Å (Table 2) amongst the octahedral theoretical Fe^{2+}-O distance at 2.140 Å and the theoretical Fe^{3+}-O distance at 2.015 Å. Based on MS data (Table 3), 27% of the total iron belongs to magnetite and 73% to chrysotile. Magnetite is partially oxidized to maghemite (in the order of 6%), and this is in agreement with the low area of XANES pre-edge peaks, indicating the low presence of tetrahedral iron (confirmed by EXAFS results). Hence, Val Malenco chrysotile displays comparable amount of Fe^{2+} and Fe^{3+} in octahedral position, very similar to that observed for Balangero chrysotile.

Because in chrysotiles, magnetic contributions (mainly due to accessory magnetite) have been excluded, the following new formulas should be considered:

Chrysotile UICC $Mg_{5.93}\,Fe^{2+}_{0.04}\,Al_{0.02}\,Fe^{3+}_{0.08})_{6.07}\,Si_{4.03}\,O_{10}\,(OH)_{7.66}$.

Chrysotile Balangero $(Mg_{5.81}\,Fe^{2+}_{0.15}\,Al_{0.27}\,Fe^{3+}_{0.09}\,Cr_{0.01})_{6.33}Si_{3.97}O_{10}\,(OH)_{7.11}$.

Chrysotile Val Malenco $(Mg_{5.85}\,Fe^{2+}_{0.06}\,Al_{0.02}\,Fe^{3+}_{0.05}\,Ni_{0.01})_{5.99}\,Si_{4.01}\,O_{10}\,(OH)_{7.86}$.

4.1.3. Erionite

In the zeolite erionite, with a general chemical formula $K_2(Na,Ca_{0.5})_8[Al_{10}Si_{26}O_{72}]\cdot 30H_2O$ [8,55] Fe^{3+} ions may virtually replace Al^{3+} ions in the framework or can be found in the extraframework cavities as octahedral free $Fe(H_20)_6{}^{3+}$ molecules whereas high-spin Fe^{2+} can be octahedrally coordinated in extraframework sites [95]. It was also reported iron in the form of Fe^{3+}-bearing oxide-like nanoparticles, on the external surface of the silica walls of a fibrous erionite from Rome, Oregon, USA [55].

In our sample from Jersey, Nevada, XANES data confirm the presence of only Fe^{3+}, having a pre-edge peaks centroid position at 7114.65(3) eV (Table 1) close to the area of Fe^{3+}-rich standards and in agreement with MS results (Table 3). The total pre-edge peaks area of 0.076(2) reveals that iron is hosted only in octahedrally-coordinated positions. This figure is confirmed by the EXAFS results showing a first shell of six oxygen atoms at a mean distance of 2.011 Å (Table 2), very close to the theoretical distance Fe^{3+}-O (2.015 Å) in the octahedron. Based on MS data, the absence of magnetic sextets typical of iron oxide, allows us to assess that oxide-like nanoparticles, if present, must have a dimension under the resolution limit of the measurement at RT, namely <18 nm (according to [55,89] and references therein). To support this hypothesis, TEM analysis were also performed on this sample and the observations evidenced spherical particles (<10 nm) on the surface of the fibres (Fig. 7a); locally, clusters of these particles were detected. EDS analysis reveals that such clusters are enriched in iron with respect to the bulk (Fig. 7b). Iron in the investigated erionite is in octahedral coordination inside oxide-like nanoparticles present at the surface of the fibres. These results are preliminary and requires further experimental evidence to definitely rule out the possibility of iron present as 6-fold coordinated extraframework cation in the zeolite cages. Notably, this conclusion is in perfect agreement with that of Ballirano [55] despite the different origin of the sam-

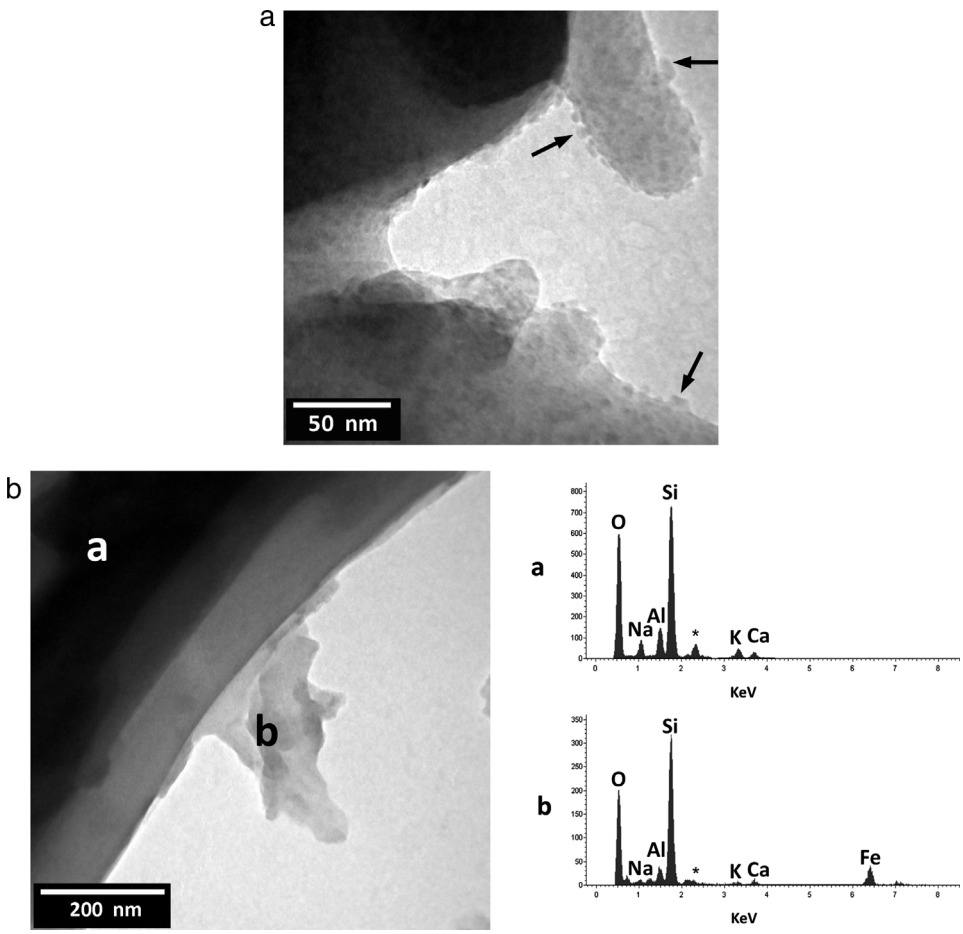

Fig. 7. High-resolution TEM images of erionite sample: (a) fibre with spherical nanoparticles on the surface (indicated by arrows); (b) clustering of particles (indicated with the letter b) with EDS spectra; *contaminant from the grid.

ples investigated. Because it was found that Fe^{+3} does not belong to the zeolite structure, the chemical formula should be written as $(Na_{5.35}K_{2.19}Ca_{0.15}Mg_{0.11}Ti_{0.05})_{7.85}(Si_{28.01}Al_{7.90})_{35.91}O_{72}{\cdot}28.13H_2O$.

4.2. Iron crystal chemistry and fibre toxicity

Iron in mineral fibres may be responsible for carcinogenic activity namely via ROS/RNS production during the phagocytosis-induced inflammatory burst [104]. Reactive HO• are responsible for secondary genotoxicity via damage to proteins and DNA, cell injury/mutation, nucleotide coenzyme destruction, membrane damage, apoptosis, lipid peroxidation [105], and fibre encapsulation by collagen and iron-rich proteins [106]. It is the synergy of (i) fibrous-asbestiform crystal habit which triggers off partial phagocytosis/frustrated internalization and production of H_2O_2 and (ii) active iron present at the surface of the fibres, to be the key factor of potential fibre toxicity as it promotes the formation of reactive HO•species by the surface Fenton reaction chain. In this frame, the findings of Turci [38] on synthetic chrysotile are of paramount importance: a fibre that does not contain iron is non-reactive in terms of ROS generation and cellular damage. However, even a very small amount of iron induces radical reactivity, cyto- and geno-toxicity. Iron-containing particles such as hematite [107] and magnetite are not active. Hematite has a lamellar crystal habit and magnetite is sub-spherical. Their crystal habit promotes complete internalization [108] without ROS production. For crocidolite, the ability to be mobilized from the fibre surface (surface activity), rather than the amount of iron in the crystal lattice, are important for the generation of ROS [109]. In contrast to crocidolite, chrysotile is not rich in iron and the surface is less effective at generating hydroxyl radicals [110].

Our results show that in all investigated mineral fibres, iron is found in octahedral cavities. Fe^{3+} is in a peripheral octahedral cavity ($M(2)$) in amphiboles and inside the octahedral sheet in chrysotiles. In erionite it is present as octahedrally coordinated Fe^{3+} likely in surface oxide nanoparticles. Fe^{2+} is hosted in the internal octahedral cavities $M(1)$ and $M(3)$ in amphiboles and inside the octahedral sheet in chrysotiles. It should be remarked that Fe^{2+} is located in the innermost structure positions inside the crystal lattice less affected by oxidation. To cause production of HO• species, such iron must be available at the surface of the mineral fibre in contact with the organic medium. At the fibre surface, even Fe^{2+} ions are stable at acid pH of the macrophage environment [111].

Because production of HO• species requires iron to be available at the surface of the mineral fibre in contact with H_2O_2 released in the organic medium, during the persistent inflammatory activity, a dependency upon the dissolution rate of the fibre is also expected [107]. In fact, progressive dissolution of the fibre structure makes bulk iron available at the surface. Although a specific study is planned within this long term project, we can make some semi-quantitative conjectures to link the dissolution time of the fibres to the amount of iron converted from bulk iron to surface iron. If we assume a mean 0.1 μm diameter fibre size for convenience (as available literature data refer to this mean diameter size) and a zero order reaction (compatible with the model described in [112]) for the bulk dissolution of the fibre, the estimated total dissolution time of the fibre in organic medium at pH 4 are: amosite = ca. 2500 d, chrysotile = ca. 239 d, crocidolite = ca. 5000 d

(Table 2 in [113]), and tremolite = ca. 18,250 d [114], in the span of time of the dissolution of chrysotile (239 d), the following amount of iron (Fe^{2+} + Fe^{3+} wt.%, calculated from the chemical formulas) is released: amosite = 3.0 wt.%, chrysotile = 1.1–2.3 wt.%, crocidolite = 1.3 wt.%, and tremolite = 0.02 wt.%. If we assume anthophyllite to have the same dissolution rate of crocidolite, the amount of total iron released in 239 d is 0.37 wt.%. Hence, a proposed ranking of ability of asbestos fibres to generate available surface iron-related (pristine bulk iron made available at the surface of the fibre during the dissolution process) hydroxyl radicals may be: amosite > crocidolite ≈ chrysotile > anthophyllite > tremolite.

The ranking intentionally does not include erionite which requires an individual explanation. It is well known that although exposure to erionite is less widespread, this zeolite species is more potent than chrysotile asbestos in causing mesothelioma [115,116]. Erionite is fibrous-asbestiform and its frustrated phagocytosis readily prompts H_2O_2 production. Notwithstanding, its dissolution rate is very low in acid media [25], total iron content is low (Fe^{3+} only = 0.55 wt.%), and available surface iron-related hydroxyl radicals should be in principle negligible. On the other hand, if we assume that Fe^{3+}-rich oxide nanoparticles are all concentrated at the fibre surface, despite total content of iron is low, it is all available via dissolution at pH 4, forming low nuclearity active Fenton $Fe(OH)^{2+}$ group in acid solution [117]. We can speculate that the remain of such dissolution process is a monolayer of $Fe(OH)^{2+}$ groups retained at the zeolite surface as this molecular group fits the 6-membered ring present in the erionite framework with a tetrahedral T2 site composing the 6-membered window rich in Al^{3+} [118]. Structural studies using synchrotron anomalous scattering powder diffraction experiments are in progress to validate the proposed model. The selectivity for the 6-membered ring of erionite for iron is in concert with the empirical prediction of Fubini and Mollo [26] who postulated that only a few surface iron species on mineral samples are in the right redox and coordination state to be active in the hydroxyl radical production. The predicted density of such surface iron sites should be relevant as all iron is originally present as fibre coating of Fe^{3+}-rich oxide nanoparticles. This model is in agreement with the findings of Fach [119] on synthetic Fe-exchanged erionite. Moreover, the model plausibly applies to most of the natural erionite samples (see for example erionite-K from Rome, Oregon, U.S.A. [55]) and explains the affinity for iron of this zeolite species.

5. Conclusions

In this spectroscopy work, the chemical environment of iron has been investigated for selected mineral fibres of industrial and social importance. In all investigated mineral fibres, iron is found in octahedral cavities. Fe^{2+} is located in the innermost structure positions inside the crystal lattice less affected by oxidation. In amphiboles, Fe^{3+} is in a peripheral octahedral cavity $M(2)$ whereas Fe^{2+} is in an internal octahedral cavity $M(1)$ and $M(3)$. Both Fe^{3+} and Fe^{2+} fill octahedral cavities in chrysotiles.

The potential to release hydroxyl radicals as source of toxicity of mineral fibres also depends upon their dissolution time and surface iron availability, with chrysotile showing much shorter dissolution time than amphiboles and hence comparable release of iron. This finding may indicate that the overall toxicity potential of chrysotile is not lower than that of amphiboles as far as the surface availability of iron is concerned. The case of erionite is more complicated. Iron is present as octahedrally coordinated Fe^{3+} likely inside a surface coating of oxide nanoparticles, available at the surface, which dissolve in acid environment, releasing Fenton active $Fe(OH)^{2+}$ groups of low nuclearity.

Acknowledgments

The XAS data were collected at the BM08 GILDA-CRG beamline at the European Synchrotron Radiation Facility (ESRF) in Grenoble (France) under the beam time allocated for the experiment 08-01-954 (March 2014). Two anonymous referees are kindly acknowledged for their careful revision of the manuscript.

Appendix A. Supplementary data

Supplementary data associated with this article can be found, in the online version, at http://dx.doi.org/10.1016/j.jhazmat.2015.05.010

References

[1] F. Baumann, J.P. Ambrosi, M. Carbone, Asbestos is not just asbestos: an unrecognised health hazard, Lancet Oncol. 14 (2013) 576–578.
[2] B.T. Mossman, J. Bignon, M. Corn, A. Seaton, J.B. Gee, Asbestos: scientific developments and implications for public policy, Science 247 (1990) 294–301.
[3] E.J.W. Whittaker, The structure of chrysotile. II. Clino-chrysotile, Acta Cryst. 9 (1956) 855–862.
[4] S.W. Bailey, Hydrous phyllosilicates (exclusive of micas), Rev. Mineral. 19 (1988) 725.
[5] B. DeVouard, A. Baronnet, Axial diffraction of curved lattices; geometrical and numerical modeling; application to chrysotile, Eur. J. Mineral. 7 (1995) 835–846.
[6] D.R. Veblen, Amphiboles and other hydrous pyriboles – mineralogy, Rev. Mineral. 9A (1981) 372.
[7] J.A. Gard, J.M. Tait, The crystal structure of the zeolite offretite, $K_{1.1}Ca_{1.1}Mg_{0.7}[Si_{12.8}Al_{5.2}O_{36}]\cdot 15.2H_2O$, Acta Cryst. 28 (1972) 825–834.
[8] A.F. Gualtieri, G. Artioli, E. Passaglia, S. Bigi, A. Viani, J.C. Hanson, Crystal structure-crystal chemistry relationships in the zeolites erionite and offretite, Am. Mineral. 83 (1998) 590–606.
[9] R. Doll, Mortality from lung cancer in asbestos workers, Brit. J. Ind. Med. 12 (1955) 81–86.
[10] R.A. Lemen, J.M. Dement, J.K. Wagoner, Epidemiology of asbestos-related diseases, Environ. Health Perspect. 34 (1980) 1–11.
[11] J.E. Craighead, J.L. Abraham, A. Churg, F.H. Green, J. Kleinerman, P.C. Pratt, T.A. Seemayer, V. Vallyathan, H. Weill, The pathology of asbestos-associated diseases of the lungs and pleural cavities: diagnostic criteria and proposed grading schema. Report of the pneumoconiosis committee of the college of american pathologists and the national institute for occupational safety and health, Arch. Pathol. Lab. Med. 106 (1982) 544–596.
[12] B.T. Mossman, D.W. Kamp, S.A. Weitzman, Mechanisms of carcinogenesis and clinical features of asbestos-associated cancers, Cancer Invest. 14 (1996) 466–480.
[13] M.R. Becklake, E. Bagatin, J.A. Neder, Asbestos-related diseases of the lungs and pleura: uses, trends and management over the last century [state of the art series. Occupational lung disease in high-and low-income countries, edited by M. Chan-Yeung. Number 3 in the series], The Int. J. Tuberculosis Lung Dis. 11 (2007) 356–369.
[14] D.W. Kamp, Asbestos-induced lung diseases: an update, Translational Res. 153 (2009) 143–152.
[15] M.S. Kanarek, Mesothelioma from chrysotile asbestos: update, Ann. Epidemiol. 21 (2011) 688–697.
[16] F. Qi, G. Okimoto, S. Jube, A. Napolitano, H.I. Pass, R. Laczko, R.M. Demay, G. Khan, M. Tiirikainen, C. Rinaudo, A. Croce, H. Yang, G. Gaudino, M. Carbone, Continuous exposure to chrysotile asbestos can cause transformation of human mesothelial cells via HMGB1 and TNF-α signaling, Am. J. Pathol. 183 (2013) 1654–1666.
[17] B.T. Mossman, A. Churg, Mechanisms in the pathogenesis of asbestosis and silicosis, Am. J. Respir. Crit. Care Med. 157 (1998) 1666–1680.
[18] J.P. Hollan, D.D. Smith, Asbestos, Clinical Environmental Health and Exposures, 2nd Edition, Lippincott Williams and Wilkins, Philadelphia, 2001, pp. 1214–1227.
[19] E. Yano, Z.M. Wang, X.R. Wang, M.Z. Wang, Y.J. Lan, Cancer mortality among workers exposed to amphibole-free chrysotile asbestos, Am. J. Epidemiol. 154 (2001) 538–543.
[20] V.L. Roggli, R.T. Vollmer, K.J. Butnor, T.A. Sporn, Tremolite and mesothelioma, Ann. Occup. Hyg. 46 (2002) 447–453.
[21] J.C. Pfau, J.J. Sentissi, G. Weller, E.A. Putnam, Assessment of autoimmune responses associated with asbestos exposure in Libby, Montana, USA, Environ. Health Perspect. 113 (2005) 25–30.
[22] C.M. Yarborough, The risk of mesothelioma from exposure to chrysotile asbestos, Curr. Opin. Pulm. Med. 13 (2007) 334–338.
[23] O. Dikensoy, Mesothelioma due to environmental exposure to erionite in Turkey, Curr. Opin. Pulm. Med. 14 (2008) 322–325.
[24] K. Donaldson, F.A. Murphy, R. Duffin, C.A. Poland, Asbestos, carbon nanotubes and the pleural mesothelium: a review of the hypothesis

regarding the role of long fibre retention in the parietal pleura, inflammation and mesothelioma, Part. Fibre Toxicol. 7 (2010) 1–17.
[25] S.K. Eborn, A.E. Aust, Effect of iron acquisition on induction of DNA single-strand breaks by erionite, a carcinogenic mineral fiber, Arch. Biochem. Biophys. 316 (1995) 507–514.
[26] B. Fubini, L. Mollo, Role of iron in the reactivity of mineral fibers, Toxicol. Lett. 82 (1995) 951–960.
[27] T.K. Hei, Z.Y. He, K. Suzuki, Effects of antioxidants on fiber mutagenesis, Carcinogenesis 16 (1995) 1573–1578.
[28] M.C. Jaurand, Mechanisms of fiber-induced genotoxicity, Environ. Health Perspect. 105 (1997) 1073–1084.
[29] M.J. Keane, J.W. Stephens, B.Z. Zhong, W.E. Miller, T.M. Ong, W.E. Wallace, A study of the effect of chrysotile fiber surface composition on genotoxicity in vitro, J. Toxicol. Environ. Health Part A 57 (1999) 529–541.
[30] R. Okayasu, L. Wu, T.K. Hei, Biological effects of naturally occurring and man-made fibres: in vitro cytotoxicity and mutagenesis in mammalian cells, Br. J. Cancer 79 (1999) 1319–1324.
[31] A. Xu, L.J. Wu, R.M. Santella, T.K. Hei, Role of oxyradicals in mutagenicity and DNA damage induced by crocidolite asbestos in mammalian cells, Cancer Res. 59 (1999) 5922–5926.
[32] A.J. Ghio, A. Churg, V.L. Roggli, Ferruginous bodies: implications in the mechanism of fiber and particle toxicity, Toxicol. Pathol. 32 (2004) 643–649.
[33] L. Pascolo, A. Gianoncelli, G. Schneider, M. Salomé, M. Schneider, C. Calligaro, M. Kiskinova, M. Melato, C. Rizzardi, The interaction of asbestos and iron in lung tissue revealed by synchrotron-based scanning X-ray microscopy, Nat. Sci. Rep. 3 (2013) 1123.
[34] B. Fubini, C.O. Arean, Chemical aspects of the toxicity of inhaled mineral dusts, Chem. Soc. Rev. 28 (1999) 373–381.
[35] A. Shukla, M. Gulumian, T.K. Hei, D. Kamp, Q. Rahman, B.T. Mossman, Multiple roles of oxidants in the pathogenesis of asbestos-induced diseases, Free Radical Biol. Med. 34 (2003) 1117–1129.
[36] M. Hartmann, S. Kullmann, H. Keller, Wastewater treatment with heterogeneous Fenton-type catalysts based on porous materials, J. Mat. Chem. 20 (2010) 9002–9017.
[37] W.A. Pryor, Why is the hydroxyl radical the only radical that commonly adds to DNA? Hypothesis: it has a rare combination of high electrophilicity, high thermochemical reactivity, and a mode of production that can occur near DNA, Free Radical Biol. Med. 4 (1988) 219–223.
[38] F. Turci, M. Tomatis, I.G. Lesci, N. Roveri, B. Fubini, The iron-related molecular toxicity mechanism of synthetic asbestos nanofibres: a model study for high-aspect-ratio nanoparticles, Chem. A Eur. J. 17 (2011) 350–358.
[39] C. Bergamini, R. Fato, G. Biagini, A. Pugnaloni, F. Giantomassi, E. Foresti, G.I. Lesci, N. Roveri, G. Lenaz, Mitochondrial changes induced by natural and synthetic asbestos fibers: studies on isolated mitochondria, Cell. Mol. Biol. 52 (2007) 905–913.
[40] J.A. Hardy, A.E. Aust, Iron in asbestos chemistry and carcinogenicity, Chem. Rev. 95 (1995) 97–118.
[41] M. Fantauzzi, A. Pacella, D. Atzei, A. Gianfagna, G.B. Andreozzi, A. Rossi, Combined use of X-ray photoelectron and Mössbauer spectroscopic techniques in the analytical characterization of iron oxidation state in amphibole asbestos, Anal. Bioanal. Chem. 396 (2010) 2889–2898.
[42] M. Fantauzzi, A. Pacella, J. Fournier, A. Gianfagna, G.B. Andreozzi, A. Rossi, Surface chemistry and surface reactivity of fibrous amphiboles that are not regulated as asbestos, Anal. Bioanal. Chem. 404 (2012) 821–833.
[43] A. Pacella, G.B. Andreozzi, J. Fournier, Detailed crystal chemistry and iron topochemistry of asbestos occurring in its natural setting: a first step to understanding its chemical reactivity, Chem. Geol. 277 (2010) 197–206.
[44] A. Pacella, G.B. Andreozzi, J. Fournier, L. Stievano, F. Giantomassi, G. Lucarini, M.R. Rippo, A. Pugnaloni, Iron topochemistry and surface reactivity of amphibole asbestos: relations with in vitro toxicity, Anal. Bioanal. Chem. 402 (2012) 871–881.
[45] A. Pacella, M. Fantauzzi, F. Turci, C. Cremisini, M.R. Montereali, E. Nardi, D. Atzei, A. Rossi, G.B. Andreozzi, Dissolution reaction and surface iron speciation of UICC crocidolite in buffered solution at pH 7.4: a combined ICP-OES, XPS and TEM investigation, Geochim. Cosmochim. Acta 127 (2014) 221–232.
[46] S.A. Strobel, P.B. Dervan, Site-specific cleavage of a yeast chromosome by oligonucleotide-directed triple-helix formation, Science 249 (1990) 73–75.
[47] A.J. Werner, M.F. Hochella, G.D. Guthrie, J.A. Hardy, A.E. Aust, J.D. Rimstidt, Asbestiform riebeckite (crocidolite) dissolution in the presence of Fe chelators; implications for mineral-induced disease, Am. Mineral. 80 (1995) 1093–1103.
[48] L.G. Lund, A.E. Aust, Iron mobilization from crocidolite asbestos greatly enhances crocidolite-dependent formation of DNA single-strand breaks in øX174 RFI DNA, Carcinogenesis 13 (1992) 637–642.
[49] C.C. Chao, L.G. Lund, K.R. Zinn, A.E. Aust, Iron mobilization from crocidolite asbestos by human lung carcinoma cells, Arch. Biochem. Biophys. 314 (1994) 384–391.
[50] G. Martra, M. Tomatis, I. Fenoglio, S. Coluccia, B. Fubini, Ascorbic acid modifies the surface of asbestos: possible implications in the molecular mechanisms of toxicity, Chem. Res. Toxicol. 16 (2003) 328–335.
[51] G. Minotti, S.D. Aust, The requirement for iron (III) in the initiation of lipid peroxidation by iron (II) and hydrogen peroxide, J. Biol. Chem. 262 (1987) 1098–1104.
[52] C. Blaauw, G. Stroink, W. Leiper, M. Zentilli, Mössbauer analysis of some canadian chrysotiles, Can. Mineral. 17 (1979) 713–717.
[53] G. Stroink, C. Blaauw, C.G. White, W. Leiper, Mössbauer characteristics of UICC standard reference asbestos samples, Can. Mineral. 18 (1980) 285–290.
[54] P. Ballirano, G.B. Andreozzi, G. Belardi, Crystal chemical and structural characterization of fibrous tremolite from Susa Valley Italy, with comments on potential harmful effects on human health, Am. Mineral. 93 (2008) 1349–1355.
[55] P. Ballirano, G.B. Andreozzi, M. Dogan, A.U. Dogan, Crystal structure and iron topochemistry of erionite-K from Rome, Oregon, USA, Am. Mineral. 94 (2009) 1262–1270.
[56] S. Pollastri, A.F. Gualtieri, M.L. Gualtieri, M. Hanuskova, A. Cavallo, G. Gaudino, The Zeta potential of mineral fibres, J. Hazard. Mater. 276 (2014) 469–479.
[57] F. d'Acapito, A. Trapananti, S. Torrengo, S. Mobilio, X-Ray absorption spectroscopy: the Italian beamline GILDA at the ESRF, NOTIZIARIO Neutroni e Luce di Sincrotrone 19 (2014) 14–23.
[58] B. Ravel, M. Newville, ATHENA, ARTEMIS, HEPHAESTUS. data analysis for X-ray absorption spectroscopy using IFEFFIT, J. Synchrotron Rad. 12 (2005) 537–541.
[59] M. Newville, IFEFFIT: interactive XAFS analysis and FEFF fitting, J. Synchrotron Rad. 8 (2001) 322–324.
[60] G.J. Long, T.E. Cranshaw, G. Longworth, The ideal Mössbauer effect absorber thickness, Mössbauer Eff. Ref. Data J. 6 (1983) 42–49.
[61] K. Lagarec, D.G. Rancourt, RECOIL. Mössbauer spectral analysis software for Windows, version 1.0, Department of Physics, University of Ottawa, Canada (1998).
[62] A. Gianfagna, G.B. Andreozzi, P. Ballirano, S. Mazziotti-Tagliani, B.M. Bruni, Structural and chemical contrasts between prismatic and fibrous fluoro-edenite from Biancavilla, Sicily, Italy, Can. Mineral. 45 (2007) 249–262.
[63] G.B. Andreozzi, P. Ballirano, A. Gianfagna, S. Mazziotti-Tagliani, A. Pacella, Structural and spectroscopic characterization of a suite of fibrous amphiboles with high environmental and health relevance from Biancavilla (Sicily, Italy), Am. Mineral. 94 (2009) 1333–1340.
[64] G. Calas, J. Petiau, Coordination of iron in oxide glasses through high-resolution K-edge spectra: information from the pre-edge, Solid State Commun. 48 (1983) 625–629.
[65] G.A. Waychunas, M.J. Apted, G.E. Brown Jr., X-ray K-edge absorption spectra of Fe minerals and model compounds: near-edge structure, Phys. Chem. Miner. 10 (1983) 1–9.
[66] J.S. Delaney, S. Bajt, M. Newville, S.R. Sutton, M.D. Dyar, Measurement of Fe oxidation state and coordination in geological glasses by synchrotron micro-XANES spectroscopy, Am. Geophys. 77 (1996) 835–836.
[67] Z. Wu, M. Bonnin-Mosbah, J.P. Duraud, N. Metrich, J.S. Delaney, XANES studies of Fe bearing glasses, J. Synchrotron Rad. 6 (1999) 344–346.
[68] L. Galoisy, G. Calas, M.A. Arrio, High-resolution XANES spectra of iron in minerals and glasses: structural information from the pre-edge region, Chem. Geol. 174 (2001) 307–319.
[69] G. Giuli, G. Pratesi, C. Cipriani, E. Paris, Iron local structure in tektites and impact glasses by extended X-ray absorption fine structure and high-resolution X-ray absorption near-edge structure spectroscopy, Geochim. Cosmochim. Acta 66 (2002) 4347–4353.
[70] S. Quartieri, M.P. Riccardi, B. Messiga, F. Boscherini, The ancient glass production of the medieval val gargassa glasshouse: Fe and Mn XANES study, J. Non-Cryst. Solids 351 (2005) 3013–3022.
[71] M. Wilke, F. Farges, P.E. Petit, G.E. Brown, F. Martin, Oxidation state and coordination of Fe in minerals: An Fe K-XANES spectroscopic study, Am. Mineral. 86 (2001) 714–730.
[72] M. Wilke, G.M. Partzsch, R. Bernhardt, D. Lattard, Determination of the iron oxidation state in basaltic glasses using XANES at the K-edge, Chem. Geol. 220 (2005) 143–161.
[73] M. Wilke, F. Farges, G.M. Partzsch, C. Schmidt, H. Behrens, Speciation of Fe in silicate glasses and melts by in-situ XANES spectroscopy, Am. Mineral. 92 (2007) 44–56.
[74] A.J. Berry, H.S.C. O'Neill, K.D. Jayasuriya, S.J. Campbell, G.J. Foran, XANES calibrations for the oxidation state of iron in a silicate glass, Am. Mineral. 88 (2003) 967–977.
[75] K. Zaghib, C.M. Julien, Structure and electrochemistry of $FePO_4{}^*2H_2O$ hydrate, J. Power Sources 142 (2005) 279–284.
[76] Y. Song, P.Y. Zavalij, M. Suzuki, M.S. Whittingham, New iron (III) phosphate phases: crystal structure and electrochemical and magnetic properties, Inorganic Chem. 41 (2002) 5778–5786.
[77] A.H. Hill, F. Jiao, P.G. Bruce, A. Harrison, W. Kockelmann, C. Ritter, Neutron diffraction study of mesoporous and bulk hematite, α-Fe2O3, Chem. Mat. 20 (2008) 4891–4899.
[78] V.S. Coker, A.M. Bell, C.I. Pearce, R.A. Pattrick, G. van der Laan, J.R. Lloyd, Time-resolved synchrotron powder X-ray diffraction study of magnetite formation by the Fe (III)-reducing bacterium geobacter sulfurreducens, Am. Mineral. 93 (2008) 540–547.
[79] T. Armbruster, C.A. Geiger, G.A. Lager, Single-crystal X-ray structure study of synthetic pyrope almandine garnets at 100 and 293K, Am. Mineral. 77 (1992) 512–521.
[80] B. Lavina, B. Cesare, A.M. Álvarez-Valero, H. Uchida, R.T. Downs, A. Koneva, P. Dera, Closure temperatures of intracrystalline ordering in anatectic and

metamorphic hercynite, Fe2+ Al2O4, Am. Mineral. 94 (2009) 657–665.
[81] H. Effenberger, K. Mereiter, J. Zemann, Crystal structure refinements of magnesite, calcite, rhodochrosite, siderite, smithonite, and dolomite with discussion of some aspects of the stereochemistry of calcite type carbonates, Zeitschrift fur kristallographie 156 (1981) 233–243.
[82] S.R. Bohlen, D.R. Peacor, E.J. Essene, Crystal chemistry of a metamorphic biotite and its significance in water barometry, Am. Mineral. 65 (1980) 55–62.
[83] S. Bordiga, R. Buzzoni, F. Geobaldo, C. Lamberti, E. Giamello, A. Zecchina, G. Leofanti, G. Petrini, G. Tozzola, G. Vlaic, Structure and reactivity of framework and extraframework iron in Fe-silicalite as investigated by spectroscopic and physicochemical methods, J. Catalysis 158 (1996) 486–501.
[84] E. De Grave, A. Van Alboom, Evaluation of ferrous and ferric Mössbauer fractions, Phys. Chem. Mineral. 18 (1991) 337–342.
[85] D.G. Rancourt, J.Y. Ping, Voigt-based methods for arbitrary-shape static hyperfine parameter distributions in Mössbauer spectroscopy, Nucl. Instrum. Methods Phys. Res. B58 (1991) 85–97.
[86] M.D. Dyar, S.M. Mackwell, A.V. McGuire, L.R. Cross, J.D. Robertson, Crystal chemistry of Fe^{3+} and H^{+} in mantle kaersutite: implications for mantle metasomatism, Am. Mineral. 78 (1993) 968–979.
[87] C. Giacobbe, A.F. Gualtieri, S. Quartieri, C. Rinaudo, M. Allegrina, G.B. Andreozzi, Spectroscopic study of the product of thermal transformation of chrysotile-asbestos containing materials (ACM), Eur. J. Mineral. 22 (2010) 535–546.
[88] A. Pacella, G.B. Andreozzi, P. Ballirano, A. Gianfagna, Crystal chemical and structural characterization of fibrous tremolite from Ala di Stura (Lanzo Valley, Italy), Per. Mineral. 77 (2008) 51–62.
[89] G. Fierro, G. Moretti, G. Ferraris, G.B. Andreozzi, A Mössbauer and structural investigation of Fe-ZSM-5 catalysts: Influence of Fe oxide nanoparticles size on the catalytic behaviour for the NO-SCR by C_3H_8, Appl. Catal. B: Environ. 102 (2011) 215–223.
[90] G. Moretti, G. Fierro, G. Ferraris, G.B. Andreozzi, V. Naticchioni, N_2O decomposition over [Fe]-MFI catalysts: influence of the Fe_xO_y nuclearity and the presence of framework aluminum on the catalytic activity, J. Catalysis 318 (2014) 1–13.
[91] G.M. Bancroft, A.G. Maddock, R.G. Burns, R.G.J. Strens, Cation distribution in anthophyllite from Mössbauer and infra-red spectroscopy, Nature 212 (1966) 913–915.
[92] H.J. Whitfield, A.G. Freeman, Mössbauer study of amphiboles, J. Inorg. Nucl. Chem. 29 (1967) 903–914.
[93] E.J.W. Whittaker, The structure of Bolivian crocidolite, Acta Cryst. 2 (1949) 312–317.
[94] G.M. Bancroft, R.G. Burns, A.J. Stone, Applications of the Mössbauer effect to silicate mineralogy – II. Iron silicates of unknown and complex crystal structures, Geochim. Cosmochim. Acta 32 (1968) 547–559.
[95] R. Roque-Malherbe, C. Diaz-Aguila, E. Reguera-Ruiz, J. Fundora-Lliteras, L. López-Colado, M. Hernández-Vélez, The state of iron in natural zeolites: a Mössbauer study, Zeolites 10 (1990) 685–689.
[96] F.C. Hawthorne, R. Oberti, G.E. Harlow, W.V. Maresch, R.F. Martin, J.C. Schumacehr, M. Welch, Nomenclature of the amphibole supergroup, Am. Mineral. 97 (2012) 2031–2048.
[97] M. Cameron, J.J. Papike, Amphibole crystal chemistry: a review, Fortschritte der Mineralogie 57 (1979) 28–67.
[98] G.M. Bancroft, R.G. Burns, A.G. Maddock, Determination of cation distribution in cummingtonite-grunerite series by Mössbauer spectra, Am. Mineral. 52 (1967) 1009–1026.
[99] D.C. Kamineni, X-ray and Mössbauer characteristiocs of a cummingtonite from Yellowknife, district of Mackenzie, Can. Mineral. 12 (1973) 230–232.
[100] F.C. Hawthorne, The crystal chemistry of the amphiboles, Can. Mineral. 21 (1983) 173–480.
[101] A.D. Law, Studies of the orthoamphiboles. IV. Mössbauer spectra of anthophyllites and gedrites, Mineral. Mag. 53 (1989) 181–191.
[102] D.S. O'Hanley, M.D. Dyar, The composition of chrysotile and its relationship with lizardite, Can. Mineral. 36 (1998) 727–740.
[103] D.R. Bowes, C.M. Farrow, Major and trace element compositions of the UICC standard asbestos samples, Am. J. Ind. Med. 32 (1997) 592–594.
[104] D.W. Kamp, S.A. Weitzman, The molecular basis of asbestos induced lung injury, Thorax 54 (1999) 638–652.
[105] J.R. Bucher, M. Tien, S.D. Aust, The requirement for ferric iron in the initiation of lipid peroxidation by chelated ferrous iron, Biochem. Biophys. Res. Commun. 111 (1983) 777–784.
[106] G. Liu, P. Cheresh, D.W. Kamp, Molecular basis of asbestos-induced lung disease, Ann. Rev. Pathol. 8 (2013) 161–187.
[107] J.E. Craighead, A.R. Gibbs, Asbestos and its Diseases, Oxford University Press, 2008, pp. 403.
[108] J.A. Champion, S. Mitragotri, Role of target geometry in phagocytosis, PNAS 103 (2006) 4930–4934.
[109] I. Fenoglio, L. Prandi, M. Tomatis, B. Fubini, Free radical generation in the toxicity of inhaled mineral particles: the role of iron speciation at the surface of asbestos and silica, Redox Rep. 6 (2001) 235–241.
[110] M. Gulumian, J.A. Van Wyk, Oxygen Consumption, Lipid Peroxidation and Mineral Fibres, Mech. Fibre Carcinog. 223 (1991) 439–446.
[111] W. Wang, M. Zhou, Q. Mao, J. Yue, X. Wang, Novel NaY zeolite-supported nanoscale zero-valent iron as an efficient heterogeneous Fenton catalyst, Catal. Commun. 11 (2010) 937–941.
[112] M. Guldberg, V.R. Christensen, M. Perander, B. Zoitos, A.R. Koenig, K. Sebastian, Measurement of in-vitro fibre dissolution rate at acidic pH, Ann. Occup. Hyg. 42 (1998) 233–243.
[113] A.F. Gualtieri, A. Viani, G. Sgarbi, G. Lusvardi, In vitro biodurability of the product of thermal transformation of cement – asbestos, J. Hazard. Mater. 205 (2012) 63–71.
[114] M. Rozalen, M.E. Ramos, F.J. Huertas, S. Fiore, F. Gervilla, Dissolution kinetics and biodurability of tremolite particles in mimicked lung fluids: Effect of citrate and oxalate, J. Asian Earth Sci. 77 (2013) 318–326.
[115] M. Carbone, S. Emri, A.U. Dogan, I. Steele, M. Tuncer, H.I. Pass, Y.I. Baris, A mesothelioma epidemic in Cappadocia: scientific developments and unexpected social outcomes, Nat. Rev. Cancer 7 (2007) 147–154.
[116] D.L. Coffin, P. Cook, J.P. Creason, Relative mesothelioma induction in rats by mineral fibers: comparison with residual pulmonary mineral fiber number and epidemiology, Inhalation. Toxicol. 4 (1992) 273–300.
[117] R.M. Cornell, U. Schwertmann, The Iron Oxides, VCH, New York, 1996, pp. 573.
[118] G. Cametti, A. Pacella, F. Mura, M. Rossi, P. Ballirano, New morphological chemical, and structural data of woolly erionite-Na from Durkee, Oregon, USA, Am. Mineral. 98 (2013) 2155–2163.
[119] E. Fach, W.J. Waldman, M. Williams, J. Long, R.K. Meister, P.K. Dutta, Analysis of the biological and chemical reactivity of zeolite-based aluminosilicate fibers and particulates, Environ. Health Perspect. 110 (2003) 1087–1096.

Paper 3

Assessment of asbestos body formation by high resolution FEG–SEM after exposure of Sprague–Dawley rats to chrysotile, crocidolite, or erionite

Bursi Gandolfi N., Gualtieri, A. F., Pollastri, S.,
Tibaldi, E., & Belpoggi, F.

Journal of Hazardous Materials 306 (2016) 95–104

Contents lists available at ScienceDirect

Journal of Hazardous Materials

journal homepage: www.elsevier.com/locate/jhazmat

Assessment of asbestos body formation by high resolution FEG–SEM after exposure of Sprague–Dawley rats to chrysotile, crocidolite, or erionite

Nicola Bursi Gandolfi [a], Alessandro F. Gualtieri [a,*], Simone Pollastri [a], Eva Tibaldi [b], Fiorella Belpoggi [b]

[a] Department of Chemical and Geological Sciences, University of Modena and Reggio Emilia, Via Campi 103, I-41125 Modena, Italy
[b] Cancer Research Centre, European Ramazzini Foundation of Oncology and Environmental Sciences, Castello di Bentivoglio, Via Saliceto 3, Bologna, Italy

HIGHLIGHTS

- Asbestos bodies around chrysotile, crocidolite and erionite fibres inoculated in white rats were studied.
- Asbestos bodies are observed after about 40 weeks from chrysotile and crocidolite but do not form from erionite.
- The size of the fibres controls the formation of asbestos bodies.
- The source of iron to form the asbestos bodies is organic because the dissolution of the fibres is very limited.
- A model explaining the formation of asbestos bodies in chrysotile and crocidolite is postulated.

ARTICLE INFO

Article history:
Received 18 August 2015
Received in revised form
23 November 2015
Accepted 24 November 2015
Available online 11 December 2015

Keywords:
Asbestos bodies
Fibres
Rats
FEG–SEM
Iron

ABSTRACT

This work presents a comparative FEG–SEM study of the morphological and chemical characteristics of both asbestos bodies and fibres found in the tissues of Sprague–Dawley rats subjected to intraperitoneal or intrapleural injection of UICC chrysotile, UICC crocidolite and erionite from Jersey, Nevada (USA), with monitoring up to 3 years after exposure.

Due to unequal dosing based on number of fibres per mass for chrysotile with respect to crocidolite and erionite, excessive fibre burden and fibre aggregation during injection that especially for chrysotile would likely not represent what humans would be exposed to, caution must be taken in extrapolating our results based on instillation in experimental animals to human inhalation. Notwithstanding, the results of this study may help to better understand the mechanism of formation of asbestos bodies.

For chrysotile and crocidolite, asbestos bodies are systematically formed on long asbestos fibres. The number of coated fibres is only 3.3% in chrysotile inoculated tissues. In UICC crocidolite, Mg, Si, and Fe are associated with the fibres whereas Fe, P and Ca are associated with the coating. Even for crocidolite, most of the observed fibres are uncoated as coated fibres are about 5.7%. Asbestos bodies do not form on erionite fibres. The crystal habit, crystallinity and chemistry of all fibre species do not change with contact time, with the exception of chrysotile which shows signs of leaching of Mg.

A model for the formation of asbestos bodies from mineral fibres is postulated. Because the three fibre species show limited signs of dissolution in the tissue, they cannot act as source of elements (primarily Fe, P and Ca) promoting nucleation and growth of asbestos bodies. Hence, the limited number of coated fibres should be due to the lack of nutrients or organic nature.

1. Introduction

Asbestos bodies (ABs) in human lungs were first described as peculiar pigmented crystals by Marchand [1], and reported later by many authors with different names [2–5]. Churg and Warnock [6] univocally defined the terms *asbestos body* to indicate bodies

* Corresponding author. Fax: +39 0592055887.
E-mail address: alessandro.gualtieri@unimore.it (A.F. Gualtieri).

http://dx.doi.org/10.1016/j.jhazmat.2015.11.050
0304-3894/

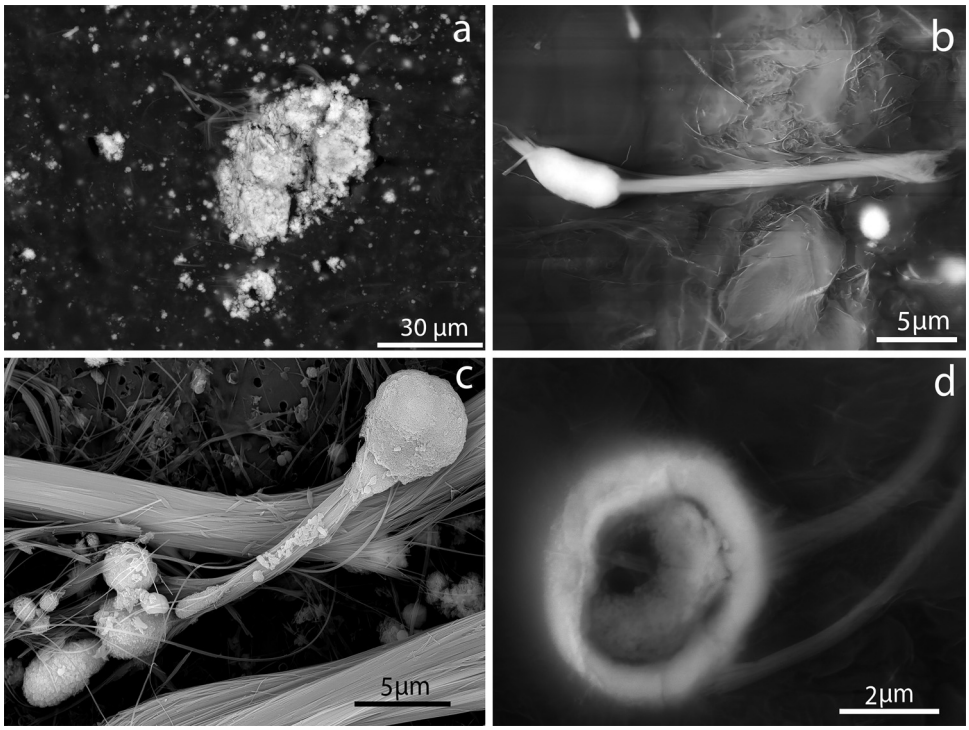

Fig. 1. (a) a large granular structure formed in correspondence of the termination of a chrysotile bundles after 65 weeks of ct; (b) an AB without a well-defined shape formed around chrysotile after 65 weeks of ct; (c) ABs with globular shape at both ends of the chrysotile fibres after 80 weeks ct.; (d) section of a circular AB with a secondary coating layer on a chrysotile fibre after 104 weeks of ct.

containing asbestos fibres, and *ferruginous body* or *pseudoasbestos body* for all non-asbestos-containing structures.

ABs display a variety of shapes like beaded, segmented, dumbbell and others. ABs are generally 20–50 μm long [6–8] with a 2–5 μm diameter [6,7] although exceptions occur (some exceed 200 μm in length [9] or display diameter of only 0.5 μm [5]).

The formation of ABs is a complex mechanism involving a number of factors, such as the nature of the fibre, its morphometry, coating efficiency of the animal host and the instillation process. Haque and Kanz [10] suggested that the time span of formation of ABs in animals is similar in humans. The formation of an AB was first attributed to hemosiderin organic Fe-storage complex [11,12]. Davis [13] suggested that ABs have a biological origin. According to Suzuki and Churg [14,15], formation of ABs deposited in lung parenchyma is due to fibre phagocytosis by alveolar macrophages. According to Koerten et al. [16], ABs may occur in the extracellular environment.

Concerning the influence of the nature of the fibre upon ABs formation, various authors [17–19] noted differences in accumulation of amphibole *vs.* chrysotile fibres within the lungs of different animals, following long-term inhalational exposure. Such differences may be related to the shorter half-life of chrysotile compared to amphiboles [6,19–20]. In general, fibres coated by ABs always coexist with uncoated fibres. The latter are invariably more abundant, with the ratio of uncoated to coated fibres which is much larger in chrysotile than in amphibole asbestos [21]. The infrequency of chrysotile ABs is likely due to its fragmentation into fine and shorter fibrils and to the fact that ABs rarely occur on asbestos fibres shorter than 10 μm [22]. As a matter of fact, ABs tend to form only on fibres longer than 20 μm or more [22–24].

Regarding the influence of the animal host upon ABS formation, *in vivo* studies performed by Vorwald et al. [23] demonstrated that the proliferation of ABs is related to the fibres coating efficiency of the animal species. Rats are poor formers of ABs whereas

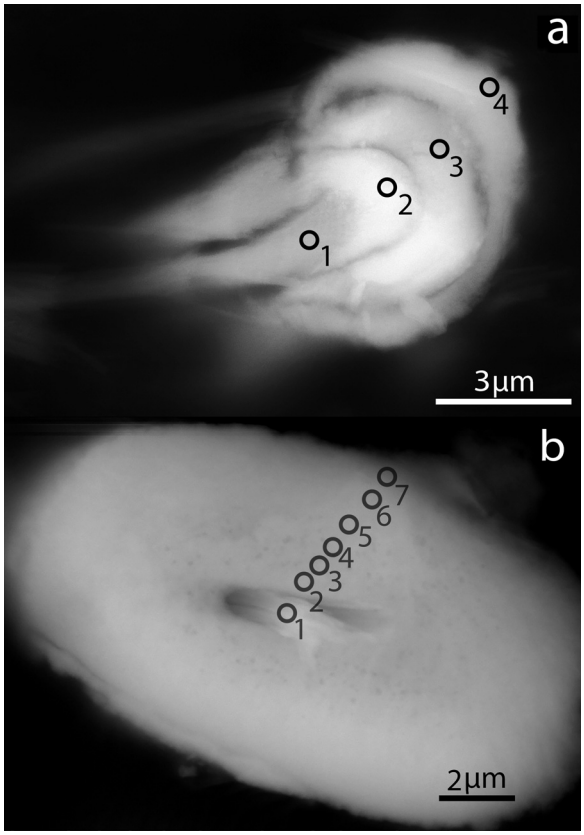

Fig. 2. Black circles = spots of EDS semi-quantitative analyses along the longitudinal section of an AB from chrysotile formed after 80 (a) and 65 (b) weeks of ct in the organ.

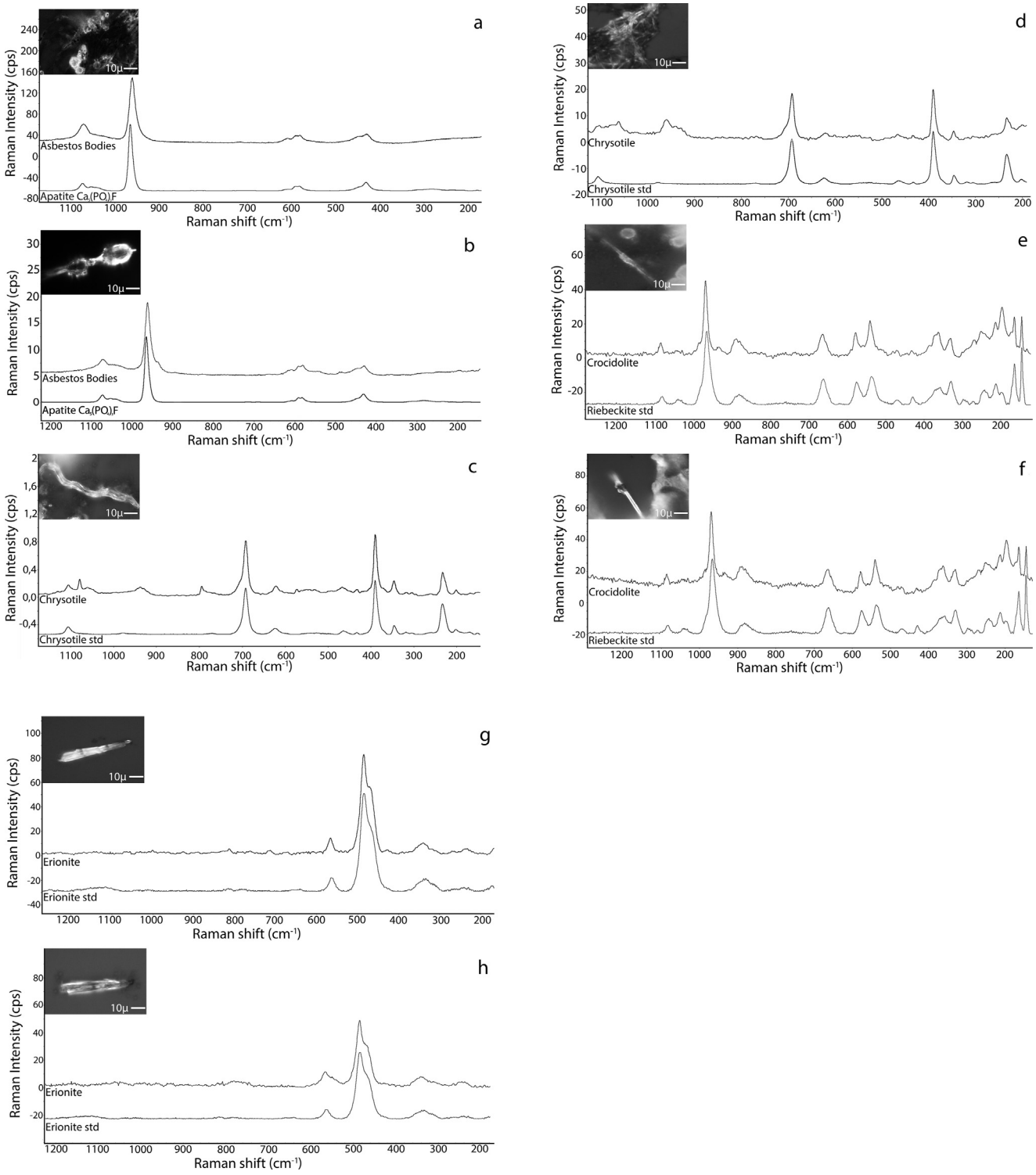

Fig. 3. μ-Raman spectra and reference spectra shown for comparison of (a) an AB formed from chrysotile after 80 weeks of ct; (b) an AB formed from crocidolite after 80 weeks of ct; (c) a chrysotile fibre after 71 weeks of ct; (d) a chrysotile fibre after 80 weeks of ct; (e) a crocidolite fibre after 38 weeks of ct; (f) a crocidolite fibre after 109 weeks of ct; (g) an erionite fibre after 79 weeks of ct; (h) an erionite fibre after 104 weeks of ct.

humans, guinea pigs and hamsters are more efficient creators of ABs [15,25–28].

The choice of the process of fibres' injection (intratracheal or inhalation) has an influence upon the development of ABs [29]. The resultant inflammatory responses were also quite different [30] so caution should be used when extrapolating results based on instillation in animals to the real case of human inhalation exposure [31].

The different factors controlling the formation of ABs also control their chemistry. Harrison et al. [32] showed that the ferritin core is a ferric oxyhydroxide, presumably (FeOOH) or ($FeOOPO_3H_3$) if phosphate is present. The presence of Ca and P has been confirmed by Meyer [33] in ABs, and recent studies using synchrotron soft X-ray imaging have demonstrated that Mg also participates along with Fe to the coating process [34]. Not all ABs possess a Fe-rich

coating. Coating of asbestos fibres with spherules of Ca-phosphate or Ca-oxalate crystals were observed [16].

Despite the huge number of papers directly or indirectly dealing with ABs, their nature, origin and control/influence over the cytotoxicity mechanism of asbestos fibres are still a matter of debate. In particular, it should be clarified if a relationship between the type of AB and the nature of the mineral fibre, in terms of mineralogy, chemistry and geometrical parameters, exists and the reasons why only a limited number of fibres are coated. Another matter of debate regards the source of Fe coating the fibres which is actually unknown and the proviso that coated fibres display a minimal potential for cytotoxicity with the Fe coating bound in such a way that it does not efficiently participate in the generation of reactive oxygen species.

In the attempt to shed some light over the issues listed above, this work reports the results of a combined systematic field emission gun-scanning electron microscopy (FEG–SEM) and micro-Raman study of the morphological and chemical characteristics of both fibres and ABs present in tissues of male and female Sprague–Dawley rats which underwent single intraperitoneal or intrapleural injection of UICC chrysotile, UICC crocidolite and erionite during a long term animal testing for the assessment *in vivo* of fibre carcinogenicity (specifically, induction of mesothelioma). The choice of chrysotile, crocidolite and erionite fibres was prompted by the relevance of these mineral fibres. Chrysotile is a serpentine layer silicate with ideal formula $Mg_3(OH)_4Si_2O_5$; crocidolite is the fibrous variety of riebeckite, an amphibole double-chain silicate with ideal composition $Na_2Fe_3^{2+}Fe_2^{3+}Si_8O_{22}(OH)_2$; erionite is a fibrous zeolite with mean chemical formula $K_2(Na,Ca_{0.5})_8[Al_{10}Si_{26}O_{72}]\cdot 30H_2O$. Chrysotile and crocidolite are the most common asbestos species and have been used since ancient times for nearly 3000 different applications. The distinctive fibrous-asbestiform crystal habit and surface activity, responsible for the outstanding technological properties of asbestos minerals, seem to be also the cause of their potential toxicity. Erionite has a very limited use and is known to induce mesothelioma [35]. Crocidolite is now banned worldwide whereas 72% of the countries worldwide admit the safe use of chrysotile. According to the so-called *amphibole hypothesis*, only amphibole asbestos minerals should be considered carcinogens whereas chrysotile asbestos is assumed to have little potential for producing mesothelioma [36]. The *amphibole hypothesis* is supported by the evidence that chrysotile dissolves reasonably quickly (low biodurability) in the intracellular macrophage environment, during phagocytosis, whereas amphiboles are much more durable (high biodurability) and remain in the lungs for a very long time [37].

2. Experimental

Three mineral fibres of broad economic and social importance were analysed *in situ* in histological tissues of male and female Sprague–Dawley rats by high resolution FEG–SEM microscopy. The three mineral fibres were: (1)UICC standard chrysotile asbestos $[(Mg_{5.93}Fe^{2+}_{0.04}Al_{0.02}Fe^{3+}_{0.08})_{6.07}Si_{4.03}O_{10}(OH)_{7.66}]$ with impurities of brucite, calcite, clinochlore, dolomite, magnetite, microcline, pyroaurite and talc; mean length = 16(1) μm; mean diameter = 0.5(1) μm; (2)UICC standard crocidolite amphibole asbestos $[(Na_{1.96}Ca_{0.03}K_{0.01})_2(Fe^{2+}_{2.34}Fe^{3+}_{2.05}Mg_{0.52})_{4.91}(Si_{7.84}Al_{0.02})_{7.86}O_{21.36}(OH)_{2.64}]$ with minor impurities of hematite, magnetite, and quartz; mean length = 19(1) μm; mean diameter = 0.7(2) μm; (3) fibrous erionite from Jersey, Nevada (USA) $[(Na_{5.31}K_{2.18}Ca_{0.15}Mg_{0.11}Fe^{3+}_{0.29})_{8.04}(Si_{27.84}Al_{7.85})_{35.69}O_{72}\cdot 28.13H_2O]$ with impurities of clinoptilolite; mean length = 4(1) μm; mean diameter = 0.8(1) μm. These fibre species were characterized elsewhere in terms of chemistry, mineralogical composition, fibre size, surface area and activity [38,39].

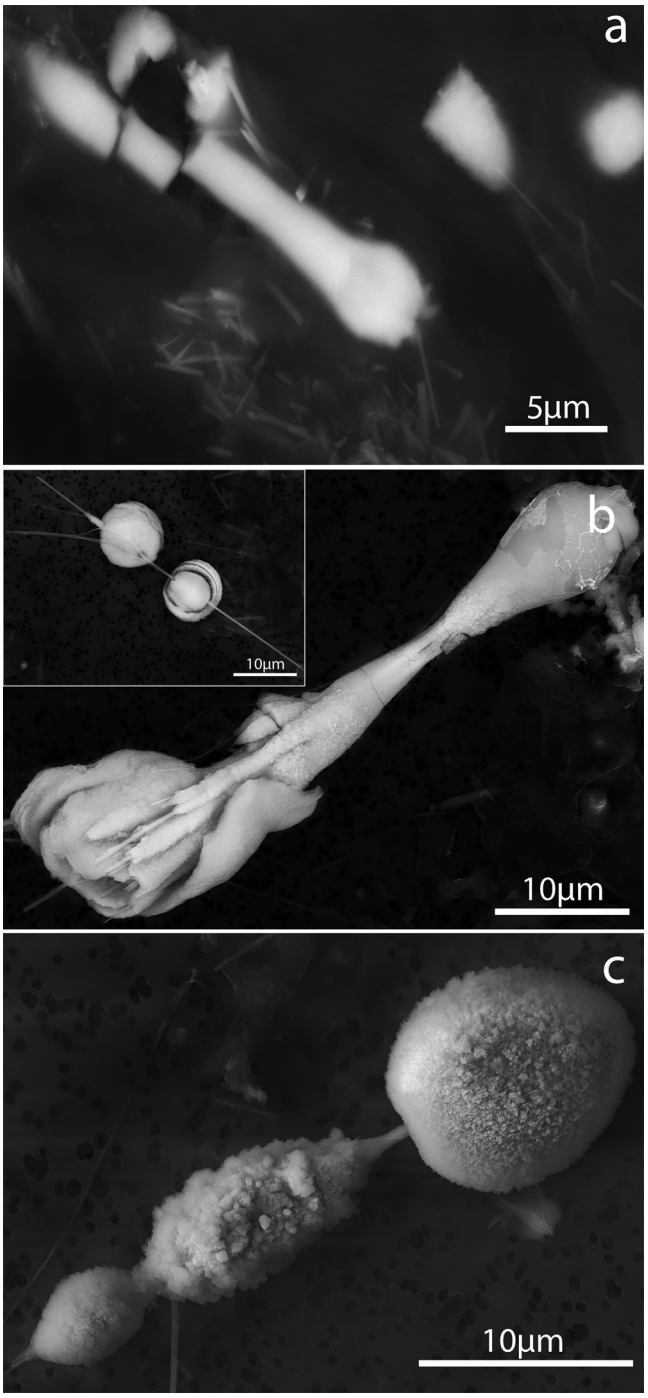

Fig. 4. (a) example of segmentation affecting both crocidolite fibre and its AB coating; (b) an AB on a crocidolite fibre recovered through digestion process after 73 weeks of ct, with a globular clusters at one or both ends of the fibres (inset panel); (c) a peculiar granular AB recovered through digestion process of the inoculated pleural tissue.

The fibres studied here are embedded in unique histological slides of rats investigated during a past long term project for the determination of the carcinogenicity of mineral fibres conducted by the Ramazzini Cancer Research Institute (Bentivoglio, Bologna, Italy). The description of the *in vivo* experiments and the details of the experimental part are reported as Supplementary material 1. For the *in vivo* tests on Sprague–Dawley rats, single 25 mg injection of each mineral fibre in 1 ml of H_2O was delivered [40]. For

the injection in the pleural/peritoneal space of the rats, the calculated number of fibres in 25 mg was 3.2×10^9 ff for chrysotile, 1.0×10^9 ff for crocidolite, and 5.9×10^9 ff for erionite, respectively. The *in vivo* study was conducted 26 years ago [40] and the injected fibres were not counted at that time before the injection process. Hence, the number of injected fibres reported above was not experimentally determined before the injection step but was theoretically calculated from the measured size and diameter distribution, assuming ideal densities. For this reason, it is possible that inaccuracies occur and it is likely that the figures reported in Ref. [41],(see Ref. [42] for the characterization of the UICC chrysotile fibres) are much more accurate as far as the determination of the number of fibres per mass. As a matter of fact, that study, conducted using a cyclone which removed much of the bundles of fibres which exist in the bulk sample, demonstrated that for equal mass, there are 11 times more chrysotile fibres than crocidolite in the air (chrysotile: 3.48–1.5 = 1.96 mg/m^3; 6953 total fibers/cm^3 and 1 mg/m^3 > 3547 fibres/cm^3; crocidolite 6.34 mg/m^3; 2013 total fibres/cm^3 and 1 mg/m^3 > 317 fibres/cm^3) [41].

The detailed observation of the fibres in the organic tissues was performed using a FEI Quanta Nova NanoSEM 450 and a FEI Quanta FEG 450 SEM instruments. Micro-Raman spectra of selected fibres and ABs were also collected employing a DXR Raman spectrometer (Thermo Scientific).

3. Results

3.1. Asbestos bodies

Remarkable variations in size and morphology of ABs formed on chrysotile fibres are detected [43]. Size lengths from 1.5 to 20 μm and diameter ranges from 0.6 to 15 μm. Although the variety of observed shapes is not great for chrysotile fibres, very large structures as long as 50–60 μm are also observed in correspondence to the termination of the chrysotile bundles (Fig. 1a). Fig. 1b shows a globular structure that tends to develop on a fibre without a well-defined shape. Another curious example of AB formed on a chrysotile fibre is shown in Fig. 1c. The coating of the fibre may occur in successive steps (Fig. 1d).

All examined ABs have similar chemical composition with Mg, Si, and low Fe content. In case of secondary deposition, the chemistry of the outer layers does not change (Fig. 2a,b and Table 1a) with respect to the core. EDS spectra show low Fe contents in both fibres and asbestos bodies, in agreement with the low Fe content of chrysotile fibres [38,39]. Si decreases drastically from the core of the chrysotile fibre to the periphery of the AB. EDS qualitative data of chrysotile fibre after 65 weeks of contact/residence time (ct) (Table 1b, relative to a representative coated fibre) is comparable to EDS data collected from a raw chrysotile fibre indicating minor chemical variations of the coated fibre. Other elements like P and Ca are associated with the coating. μ-Raman spectra taken on ABs of both chrysotile (Fig. 3a) and crocidolite (Fig. 3b) display the typical pattern of apatite.

The length and diameter of the Abs in chrysotile show a minor positive trend with ct (see Table 1c). Variation of the chemistry and shape of the ABs with time is not found. Uncoated fibres are detected in all the examined samples with the percentage of coated fibres being 3.3%.

In UICC crocidolite, the size of ABs varies in length from 4 μm to 25 μm, and diameter from 4 μm to 8 μm. ABs are predominantly formed on long asbestos fibres. Eventually, segmentation affects both ABs and the fibres (Fig. 4a). The bodies on crocidolite fibres occur in a variety of forms, tend to vary from cylindrical to elliptical (Fig. 4b), and may produce globular clusters at one or both ends of the fibres (inset panel in Fig. 4b); granular structures were also observed (Fig. 4c).

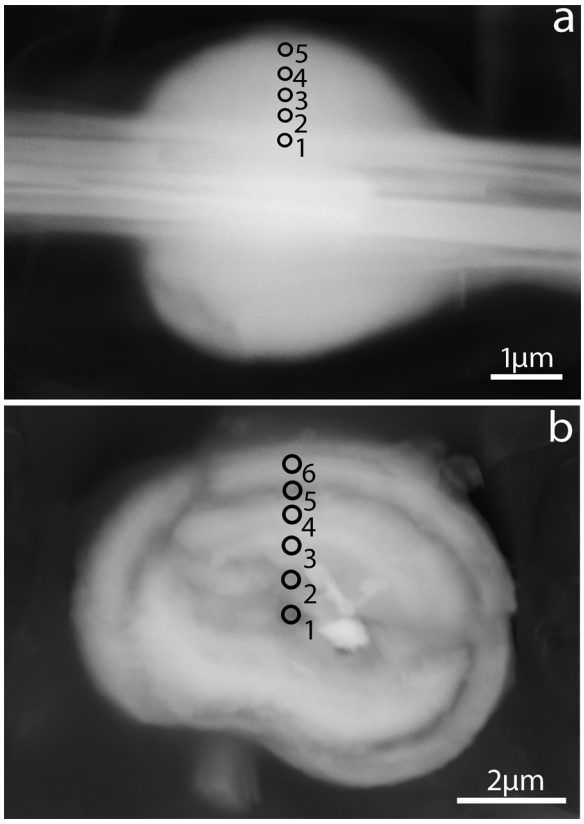

Fig. 5. Black circles = spots of EDS semi-quantitative analyses along the longitudinal section of an AB from crocidolite after 41 (a) and 80 weeks (b) of ct in the tissues.

The diameter of the ABs in crocidolite show a minor negative trend with ct (see Table 2c) whereas the length of the fibres is nearly constant. Significant chemical variations of the ABs of different cts has not been recorded. Even for crocidolite, most of the observed fibres are uncoated. The percentage of coated fibres is 5.7%.

Examples of EDS spot analyses for the crocidolite fibres after 41 and 80 weeks of ct, representative of all the investigated fibres, are reported in Fig. 5a,b and Table 2a,b. Mg, Si, and Fe are associated with the crocidolite fibres whereas Fe, P and Ca are associated with the coating (made of apatite: see Fig. 3b). The Fe and Si content decreases from the core of the fibres to the marginal regions. Secondary elements like K, S, and Ti may be part of the ABs.

Regarding erionite, ABs have not been observed in any samples at any ct.

3.2. Mineral fibres

The mean length of chrysotile fibres ranges from 14.3 to 15.8 μm (Table 3a) with diameters in the range 0.45–0.54 μm. A trend of decrease of both fibre length and diameter with ct in the rat tissues is observed. Surprisingly, the crystal habit does not seem to change with ct. The average size of chrysotile fibres that could produce ABs is 29.6 μm in length and 0.5 μm in diameter. As shown above, the ratio of coated to uncoated fibres is 3.4%. Such ratio does not change with time (Fig. 6).

The EDS spot semi-quantitative analyses of fibres with different ct show an increase of the Si:Mg ratio with respect to the standard chrysotile UICC (UICC: 1.49; 71 weeks: 1.50; 80 weeks: 2.09; 128 weeks: 3.90). *In vivo* leaching process increases the Si:Mg ratio with respect to standard fibres [44]. Although Mg leaching should be accompanied by loss of crystallinity of the fibres, the Raman

Table 1
EDS spot semi-quantitative analyses of: (a) an AB on a chrysotile fibre after 80 weeks of ct in the peritoneum (Fig. 2a); (b) an AB on a chrysotile fibre after 65 weeks of ct in the peritoneum (Fig. 2b);(c) Evolution of the length and diameter of ABs on chrysotile with ct inside the histological tissue.

(a)

EDS spot nr.	Element weight fraction (%)				
	Mg	Si	P	Ca	Fe
1	7.41	4.98	9.09	20.62	0.76
2	1.04	0.98	10.44	30.58	0.08
3	0.66	1.78	11.38	29.91	–
4	1.00	1.32	10.47	22.99	–

(b)

EDS spot nr.	Element weight fraction (%)				
	Mg	Si	P	Ca	Fe
1	3.63	2.32	9.20	18.53	0.36
2	0.53	0.53	10.84	22.31	0.49
3	0.31	0.38	8.72	22.94	0.36
4	0.30	0.53	10.00	23.24	0.21
5	0.27	0.54	9.00	19.99	0.27
6	0.45	0.40	6.85	16.96	0.46
7	0.25	0.53	5.39	15.17	0.78

(c)

Value	Weeks of contact time					
	71		80		128	
	Length (μm)	Diameter (μm)	Length (μm)	Diameter (μm)	Length (μm)	Diameter (μm)
Mean	4.770	2.116	4.637	1.979	5.405	2.317
Standard error	0.199	0.084	0.183	0.069	0.175	0.101
Standard deviation	1.692	0.717	1.550	0.586	1.484	0.856
Median	4.380	2.008	4.024	1.786	5.010	2.182
Number of counted ABs	106		202		103	

Table 2
EDS spot semi-quantitative analyses of: (a) an AB coating a crocidolite fibre after 41 weeks of ct in the peritoneum (Fig. 5a); (b) an AB coating a crocidolite fibre after 80 weeks of ct in the peritoneum (Fig. 5b); (c) evolution of the length and diameter of ABs on crocidolite with ct inside the histological tissue.

(a)

EDS spot nr.	Element weight fraction (%)				
	Mg	Si	P	Ca	Fe
1	0.43	3.86	7.55	19.37	9.26
2	0.80	1.96	10.28	20.14	4.19
3	0.48	1.08	8.32	19.39	2.69
4	0.29	1.00	8.16	19.10	2.36
5	0.30	0.99	5.47	10.68	1.99

(b)

EDS spot nr.	Element weight fraction (%)				
	Mg	Si	P	Ca	Fe
1	0.27	3.76	3.46	8.83	4.11
2	0.07	1.46	8.09	18.93	3.73
3	0.23	1.62	8.13	18.78	3.8
4	-	1.57	8.03	21.00	3.68
5	0.34	1.19	5.26	14.67	3.85
6	0.26	1.51	4.14	9.89	10.58

(c)

Value	Weeks of contact time					
	38		73		109	
	Length (μm)	Diameter (μm)	Length (μm)	Diameter (μm)	Length (μm)	Diameter (μm)
Mean	9.254	4.498	9.473	4.487	8.994	3.449
Standard error	0.434	0.218	0.405	0.165	0.446	0.160
Standard deviation	3.434	1.850	3.434	1.397	3.624	1.297
Median	8.746	4.058	9.135	4.156	7.656	3.110
Number of counted ABs	108		114		136	

spectra (Fig. 3c,d) confirm that crystallinity of most of the fibres is preserved.

The mean length of crocidolite fibres ranges from 13.7 to 18.6 μm (Table 3b) with diameters in the range 0.54–0.71 μm. Concerning the crystal habit, no great variations are observed with

Table 3
(a) Evolution of the length and diameter of the fibres with ct inside the histological tissues: (a) chrysotile; (b) crocidolite; (c) erionite.

(a)

Value	Weeks of contact time					
	71		80		128	
	Length (μm)	Diameter (μm)	Length (μm)	Diameter (μm)	Length (μm)	Diameter (μm)
Mean	15.76	0.54	15.23	0.51	14.30	0.45
Standard error	0.38	0.01	0.31	0.01	0.35	0.01
Standard deviation	8.46	0.19	5.96	0.18	5.84	0.15
Median	14.26	0.51	15.04	0.48	13.25	0.43
Number of counted ABs	494		368		274	

(b)

Value	Weeks of contact time							
	38		73		80		109	
	Length (μm)	Diameter (μm)	Length (μm)	Diameter (μm)	Length (μm)	Diameter (μm)	Length (μm)	Diameter (μm)
Mean	18.59	0.71	15.28	0.64	15.56	0.65	13.68	0.54
Standard error	0.44	0.01	0.34	0.01	0.48	0.02	0.32	0.01
Standard deviation	13.88	0.29	10.90	0.25	17.22	0.78	9.26	0.39
Median	17.38	0.67	14.29	0.60	14.67	0.60	11.01	0.49
Number of counted ABs	1003		996		1249		819	

(c)

Value	Weeks of contact time							
	47		53		95		126	
	Length (μm)	Diameter (μm)	Length (μm)	Diameter (μm)	Length (μm)	Diameter (μm)	Length (μm)	Diameter (μm)
Mean	3.61	0.77	2.98	0.81	2.53	0.75	3.67	0.98
Standard error	0.12	0.03	0.06	0.02	0.10	0.04	0.07	0.03
Standard deviation	2.06	0.45	1.66	0.56	1.29	0.49	1.79	0.69
Median	3.24	0.70	2.63	0.70	2.28	0.66	3.42	0.85
Number of counted ABs	270		664		170		662	

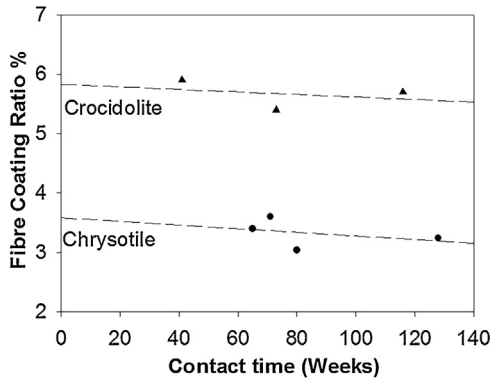

Fig. 6. Ratio of coated to uncoated fibres for both chrysotile and crocidolite.

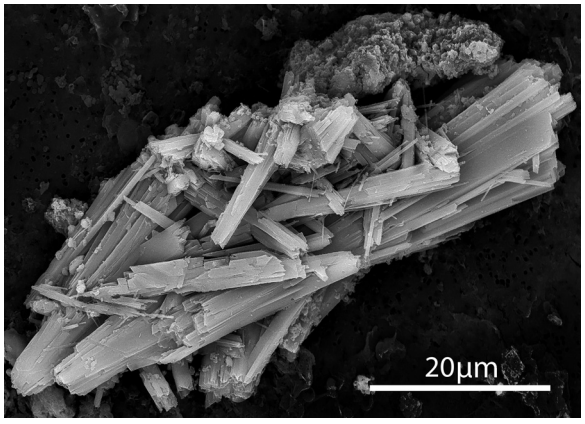

Fig. 7. Representative cluster of erionite fibres in the tissues after 95 weeks.

ct. The average size of crocidolite fibres that could produce ABs is 41.0 μm in length and 0.86 μm in diameter. As shown above, the ratio of coated to uncoated fibres is 6.0 and does not change with time (Fig. 6). The chemistry of the crocidolite fibres undergoes minor variations with ct in the rat tissues. The Raman spectra (Fig. 3e,f) confirm that crystallinity is kept even at greater cts.

Regarding the erionite fibres, they display a typical fibrous habit with stocky short fibres (Fig. 7). The calculated mean fibre length ranges from 2.7 to 3.7 μm (Table 3c) and the diameters are within the range 0.75–0.98 μm. Both fibre length and diameter apparently do not change with ct in the rat tissues. Similarly to crocidolite, the EDS spot semi-quantitative analyses show that the chemistry of the erionite fibres undergoes minor variations with ct in the rat tissues. The Raman spectra (Fig. 3g,h) of the fibres in contact for a short and a long time also confirm that crystallinity is preserved.

4. Discussion

Although prudence must be taken in extrapolating results based on instillation in experimental animals to human inhalation [31], the results of this study may be of help to better understand the mechanism of formation of ABs in chrysotile, crocidolite, and erionite. The authors are aware of major points of concerns that may bias the results of this study: (i) similarly to inhalation induced studies [45], the fibre burdens due to injection process in the intrapleural/intraperitoneal space of the rats may be excessive or unreliable if compared to both nasal inhalation in the rats and human inhalation as no fibre sorting through the upper respiratory tracts occurs; (ii) unequal dosing based on number of fibres per mass for chrysotile with respect to crocidolite and erionite during injection would likely not represent what humans would be actu-

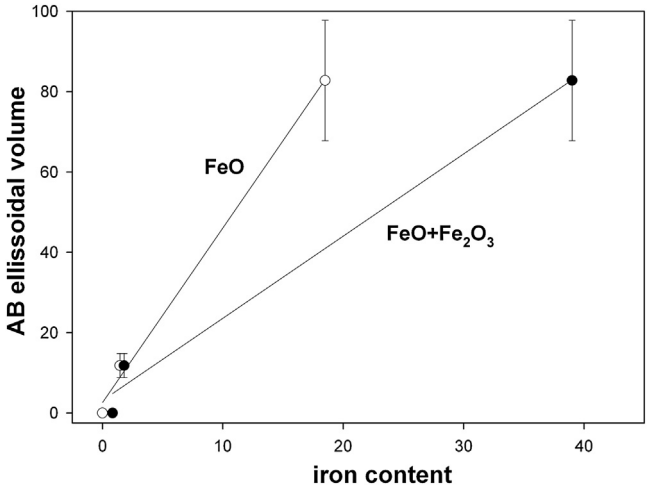

Fig. 8. Plot of the original structural Fe content of the three fibre species as determined from the chemical analysis (both ferrous and total Fe) *vs.* calculated ellissoidal volume of the ABs at the end of the experiments.

ally exposed to; (iii) there may be a fibre aggregation effect during instillation to form sort of fibre bundles that would be very unlikely to reach the intrapleural/intraperitoneal space if normal inhalation takes place.

We have not seem noteworthy differences in the ABs formed in the pleural and peritoneal cavity so the discussion will concern both sites. ABs appear in chrysotile and crocidolite in less than 40 weeks but do not form on erionite fibres. Such short times of formation are in line with literature data [16]. It is generally accepted that the kinetics of formation and time evolution of ABs in rats and humans are comparable although it is out of the aims of this work to understand why humans, hamsters, guinea pigs form ABs efficiently with respect to other animals like cats, rabbits, mice and rats which are poor AB formers [46].

ABs observed around chrysotile and crocidolite fibres are generally smaller (<20 μm and <25 μm for chrysotile and crocidolite, respectively) than those reported in the literature (20–50 μm in length) [6,8]. On the other hand, diameters are comparable [6]. The ratio of coated to uncoated fibres is 3.4% and 6.0% for chrysotile and crocidolite, respectively. ABs nucleate at the surface of fibres longer than 10 μm such as chrysotile (mean length of 15.05 μm) and crocidolite (mean length of 16.15 μm). If fibre length seems to play a key role, apparently diameter does not.

ABs are not found in the tissues inoculated with erionite fibres (mean length of 3.2 μm). This result is apparently in contrast with the literature data. In fact, it is known that erionite fibres can form bodies morphologically identical to typical ABs [47]. ABs were observed in BALF of villagers of Tuzköy (Turkey) exposed to erionite. The erionite fibres from Tuzköy are much longer (65.7% of the fibres had a diameter greater than 4 μm) than the erionite fibres from this study. Hence, ABs do not form on our erionite fibres because the size of the fibres is much shorter than 10 μm and phagocytosis actually occurs.

There is no correlation between iron content of fibres and the number of coated fibres. On the other hand, the original structural content of Fe of the chrysotile, crocidolite and erionite fibres (both ferrous and total Fe) seems to affect the size of the ABs in terms of calculated ellissoidal volume (see the correlation in Fig. 8, despite the poor statistical significance due to the limited number of observations). The slight overestimation of the volume of the chrysotile ABs is due to the fact that ABs of other chemical nature (mainly Ca phosphate) are also included in the total calculated volume. Hence, Fe of the fibres may act as active pool and co-factor for the growth of FeOOH or $FeOOPO_3H_3$ forming the coating but not as key factor for the nucleation of the AB.

It is known that the surface charge of the fibres in terms of ζ potential may also play an important role in the formation of ABs as a negatively charged reactive surface favours the binding of collagen and redox activated Fe-rich proteins [48]. In a previous paper [38], we have measured the ζ potential of these three fibres and found positive values for chrysotile and negative values for crocidolite and erionite. All fibres display negative values in contact with a Gamble solution mimicking the acidic macrophage chemical environment. If we compare those results with the formation mode and number of formed ABs, no relationship is found with the surface charge of the fibres.

ABs only nucleate on long fibres that cannot be engulfed and subject to complete phagocytosis. The first defence mechanism of the organism is the engulfment acted by phagocytes (namely macrophages) which successfully engulf the fibres shorter than their mean diameter and promote their dissolution by intracellular phagocytosis (see for example Liu et al [48]). Phagocytosis occurs inside lysosomes vacuoles which develop an acidic chemical environment (pH = 4–4.5) in the attempt to dissolve the fibres. Although physical engulfment is successful, this mechanism in principle permits to effectively dissolve only chrysotile fibres (not stable in acidic environment) but not crocidolite and erionite (both resistant to acids) [49,50]. This is the reason why even though complete engulfment of short fibres occurs and phagocytosis is apparently successful, such fibres cannot be dissolved.

When the fibres are longer than the mean diameter of the phagocytes (generally assumed >10 μm), frustrated phagocytosis accompanied by inflammatory burst occurs with release of highly reactive cyto- and geno-toxic toxic substances extracellularly. At this point, coating and AB formation occurs, as secondary defence mechanism, aimed at isolating the toxic reactive fibre. The diminished oxidants' generation and reduced toxicity of coated fibres with respect to uncoated fibres has been reported by many authors [8,16] so that AB was called the *tombstone* of the asbestos fibre [51,52]. Unfortunately even the second defence mechanism appears to be poorly effective as we observed that only few fibres are efficiently coated.

Although quantification of the coated fibres *vs.* uncoated fibres may be biased by excessive fibre burden due to instillation, the limited number of observed coated fibres should be due to the lack of nutrients to form the asbestos coating, specifically Fe, P and Ca. Because of the chemical stability of the fibres (especially crocidolite and erionite) in contact with the tissues, release of active nutrients such as Fe is poor and cannot promote massive nucleation and growth of ABs. Hence, the source of Fe (but also P and other elements) to form the hemosiderin and porphyrins rich core of ABs must be organic, likely provided by cytoplasmic ferritin from phagocytes or from ferritin circulating in plasma. This model has been already predicted by Ghio et al. [8] who excluded that iron is from the fibre but from several possible intracellular sources of Fe^{3+} (such as iron associated with adenosine-tryphosphate ATP, DNA and others) that accumulates onto the fibre surface. Of course, nutrients are physiologically limited in the organism and are likely not sufficient to provide coating of all asbestos fibres.

As anticipated, ABs are not observed on erionite fibres because these fibres are very short and complete phagocytosis actually does occur. As explained above, the second mechanism of defence is not necessarily invoked.

In all cases, mesothelioma invariably develops because both primary defensive mechanism (phagocytosis) and secondary defensive mechanism (fibre coating and isolation) for different reasons are poorly effective.

We have seen that a significant number of observed ABs are actually composed of Ca and P (apatite: see Fig. 3a and b). Such

elements must also be provided by the phagocytes and released both intracellularly and extracellularly. We cannot exclude that Ca and P form the primary nuclei of the AB. Governa and Rosanda [53] suggested that the fibres are initially coated with acid mucopolysaccharide and that Ca-apatite may subsequently be deposited. Brody and Hill [54] also observed interstitial precipitates (microcalcifications) from asbestos exposed wild-type rats after 1 month from the 1 h exposure. It is not possible to rule out the presence of other crystalline forms such as Ca-oxalate (CaC_2O_4) which may also form ABs according to Le Bouffant et al. [55]. Koerten et al [16]. found chlorine associated to Ca and P. We also found the same result but the presence of chlorine in our samples is probably due to the digestion process of the organic material which was obtained using NaCl.

5. Conclusions

The results of this work are an attempt to shed some light on the mechanism of formation of ABs in chrysotile, crocidolite, and erionite. It is important to remark that caution must be taken in extrapolating our results, based on instillation in animals, to human inhalation [31], as sources of bias may stem from improbable burdens of unsorted fibres in the intrapleural/intraperitoneal and fibre aggregation during the instillation procedure.

ABs are observed in chrysotile and crocidolite inoculated tissues of wild-type rats in less than 40 weeks but do not coat erionite fibres because their size is very short and phagocytosis is apparently successful. ABs observed around chrysotile and crocidolite fibres are generally smaller than those reported in the literature while diameters are comparable. The ratio of coated to uncoated fibres is 3.4% and 6.0% for chrysotile and crocidolite, respectively, in agreement with the literature data.

ABs do not form on very short fibres but nucleate at the surface of fibres longer than 10 μm. The content of Fe of the fibres apparently does not govern the amount of coated fibres whereas it seems to effect the size of the ABs in terms of calculated ellissoidal volume.

The model we have drawn predicts that ABs nucleate only on long fibres that cannot be engulfed. The first defence mechanism of the organism is the engulfment acted by phagocytes of fibres shorter than their mean diameter and dissolution by intracellular phagocytosis. Although physical engulfment is successful, this mechanism actually permits to effectively dissolve only chrysotile fibres but not crocidolite and erionite. So, even though complete engulfment of short fibres occurs, such fibres cannot be dissolved, eventually promoting inflammatory activity and release of highly reactive cyto- and geno-toxic toxic substances. When the fibres are longer than the mean diameter of the phagocytes, release of highly reactive toxic substances occurs extracellularly. In this event, the second defence mechanism of the organism, coating process with AB formation, is invoked. Regrettably even the second defence mechanism appears to be of reduced potential as only few fibres are efficiently coated. We believe that the small number of coated fibres is due to the limited source of nutrients provided by cytoplasmic ferritin from phagocytes or from ferritin circulating in plasma.

Appendix A. Supplementary data

Supplementary data associated with this article can be found, in the online version, at http://dx.doi.org/10.1016/j.jhazmat.2015.11.050.

References

[1] F. Marchand, Ueber eigenttimliche pigmentkristalle in den lungen, Verhandl. d. deutsche path. Gesellsch. 10 (1906) 223–228.
[2] T. Fahr, Demonstrationen: praparate und microphotogrammes von einen falle von pneumokoniose, Muench. Med. Woch. 61 (1914) 625.
[3] W.E. Cooke, Pulmonary asbestosis, Br. Med. J. 2 (1927) 1024–1025.
[4] M.J. Stewart, A.C. Haddow, Demonstration of the peculiar bodies of pulmonary asbestosis (asbestosis bodies) in material obtained by lung puncture and in the sputum, J. Pathol. Bacteriol. 32 (1929) 172.
[5] V.L. Roggli, Scanning electron microscopic analysis of mineral fibres in human lungs, in: P. Ingram, J.D. Shelburne, V.L. Roggli (Eds.), Microprobe Analysis in Medicine, Hemisphere Pub. Corp., Washington, DC, 1989, pp. 97–110.
[6] A.M. Churg, M.L. Warnock, Asbestos and other ferruginous bodies: their formation and clinical significance, Am. J. Pathol. 102 (3) (1981) 447–456.
[7] V.L. Roggli, Asbestos bodies and non-asbestos ferruginous bodies, in: T.D. Oury, T.A. Sporn, V.L. Roggli (Eds.), Pathology of Asbestos–Associated Diseases, Springer, 2014, p. 2551.
[8] A.J. Ghio, A. Churg, V.L. Roggli, Ferruginous bodies: implications in the mechanism of fibre and particle toxicity, Toxicol. Pathol. 32 (2004) 643–649.
[9] M.L. Farley, S.D. Greenberg, E.H. Shuford Jr., G.A. Hurst, C.G. Spivey, C.S. Christianson, Ferruginous bodies in sputa of former asbestos workers, Acta Cytol. 21 (5) (1977) 693–700.
[10] A.K. Haque, M.F. Kanz, Asbestos bodies in children's lungs: an association with sudden infant death syndrome and bronchopulmonary dysplasia, Arch. Pathol. Lab. Med. 112 (5) (1988) 514–518.
[11] G.M. Richter, Electron microscopy of hemosiderin: presence of ferritin and occurrence of crystalline lattices in hemosiderin deposits, J. Biophys. Biochem. Cytol. 4 (1) (1958) 55–58.
[12] R. Rath, Form und formanderung der asbestosis, Korpechen. Beitr. Silikose-Forsch 81 (1) (1964) 1–10.
[13] J.M.G. Davis, Electron microscope studies of asbestosis in man and animals, Ann. N. Y. Acad. Sci. 132 (1965) 98–111.
[14] Y. Suzuki, J. Churg, Structure and development of the asbestos body, Am. J. Pathol. 55 (1) (1969) 79–107.
[15] Y. Suzuki, J. Churg, Formation of the asbestos body a comparative study with three types of asbestos, Environ. Res. 3 (2) (1970) 107–118.
[16] H.K. Koerten, J. Hazekamp, M. Kroon, W. Th, Daems, asbestos body formation and iron accumulation in mouse peritoneal granulomas after the introduction of crocidolite asbestos fibres, Am J. Pathol. 136 (1) (1990) 141–157.
[17] J.C. Wagner, G. Berry, J.W. Skidmore, V. Timbrell, The effects of the inhalation of asbestos in rats, Br. J. Cancer 29 (1974) 252–269.
[18] K.P. Lee, J.L. Abraham, Lung response to particulates with emphasis on asbestos and other fibrous dusts, Crit. Rev. Toxicol. 14 (1) (1985) 33–86.
[19] D. Bernstein, R. Rogers, P. Smith, The biopersistence of Canadian chrysotile asbestos following inhalation: final results through 1 year after cessation of exposure, Inhalation Toxicol. 17 (1) (2005) 1–14.
[20] A.M. Churg, M.L. Warnock, N. Green, Analysis of the cores of ferruginous (asbestos) bodies from the general population. II. True asbestos bodies and pseudoasbestos bodies, Lab. Invest. 40 (1979) 31–38.
[21] F.D. Pooley, The identification of asbestos dust with an electron microscope analyser, Ann. Occup. Hyg. 18 (3) (1975) 181–186.
[22] A. Morgan, A. Holmes, Concentrations and dimensions of coated and uncoated asbestos fibres in the human lung, Br. J. Ind. Med. 37 (1980) 25–32.
[23] A.J. Vorwald, T.M. Durkan, P.C. Pratt, Experimental studies of asbestosis, Arch. Ind. Hyg. Occup. Med. 3 (1) (1951) 1–43.
[24] B.W. Case, Biological indicators of chrysotile exposure, Ann. Occup. Hyg. 38 (4) (1994) 503–518.
[25] S.K. Botham, P.F. Holt, Development of asbestos bodies on amosite chrysotite and crocidolite fibres in guinea-pig lungs, J. Pathol. 105 (3) (1971) 159–167.
[26] S.K. Botham, P.F. Holt, Asbestos-body formation in the lungs of rats and guinea-pigs after inhalation of anthophyllite, J. Pathol. 107 (4) (1972) 245–252.
[27] S.K. Botham, P.F. Holt, The effects of inhaled crocidolites from Transvaal and North-West Cape mines on the lungs of rats and guinea pigs, Brit. J. Exp. Pathol. 53 (6) (1972) 612–620.
[28] P. Gross, R.T.P. de Treville, Experimental asbestosis. Studies on the progressiveness of the pulmonary fibrosis caused by chrysotile dust, Arch. Environ. Health Int. J. 15 (5) (1967) 638–649.
[29] P.T.C. Harrison, J.C. Heath, Asbestos bodies in rat lung following intratracheal instillation of chrysotile, Lab. Anim. 20 (2) (1986) 132–137.
[30] J.D. Brain, D.E. Knudson, S.P. Sorokin, M.A. Davis, Pulmonary distribution of particles given by intratracheal instillation or by aerosol inhalation, Environ. Res. 11 (1) (1976) 13–33.
[31] V.L. Roggli, A.R. Brody, The role of electron microscopy in experimental models of pneumoconiosis, Lungs Biol. Health Dis. 48 (1990) 315–343.
[32] P.M. Harrison, F.A. Fischbach, T.G. Hoy, Ferric oxyhydroxide core of ferritin, Nature 216 (5121) (1967) 1188–1190.
[33] J. Meyer, Private communication, in: Environmental Research Laboratories, T.N.O., Delft, Holland, 1970.
[34] L. Pascolo, A. Gianoncelli, B. Kaulich, C. Rizzardi, M. Schneider, C. Bottin, M. Polentarutti, M. Kiskinova, A. Longoni, M. Melato, Synchrotron soft X-ray imaging and fluorescence microscopy reveal novel features of asbestos body morphology and composition in human lung tissues, Part. Fibre Toxicol. 8 (2011) 7–17.
[35] M. Carbone, S. Emri, A. Umran Dogan, I. Steele, M. Tuncer, H.I. Pass, Y.I. Baris, A mesothelioma epidemic in Cappadocia: scientific developments and unexpected social outcomes, Nature Rev. 7 (2007) 147–154.
[36] M. Camus, A ban on asbestos must be based on a comparative risk assessment, J. Assoc. Med. Can. 164 (4) (2001) 491–494.

[37] D.M. Bernstein, K. Donaldson, U. Decker, S. Gaering, P. Kunzendorf, J. Chevalier, E. Holm, A biopersistence study following exposure to chrysotile asbestos alone or in combination with fine particles, Inhalation Toxicol. 20 (2008) 1009–1028.
[38] S. Pollastri, A.F. Gualtieri, M. Lassinantti Gualtieri, M. Hanuskova, A. Cavallo, G. Gaudino, The zeta potential of mineral fibres, J. Hazard. Mat. 276 (2014) 469–479.
[39] S. Pollastri, F. D'Acapito, A. Trapananti, I. Colantoni, G.B. Andreozzi, A.F. Gualtieri, The chemical environment of iron in mineral fibres. A combined X-ray absorption and mössbauer spectroscopic study, J. Hazard. Mat. 298 (2015) 282–293.
[40] C. Maltoni, F. Minardi, Recent results of carcinogenicity bioassays of fibres and other particulate materials. Non-occupational exposure to mineral fibres, IARC Sci. Pub. 90 (1989) 46–53.
[41] D.M. Bernstein, R. Rogers, R. Sepulveda, P. Kunzendorf, B. Bellmann, H. Ernst, J.I. Phillips, Evaluation of the deposition, translocation and pathological response of brake dust with and without added chrysotile in comparison to crocidolite asbestos following short-term inhalation: interim results, Toxic. App. Pharm. 276 (2014) 28–46.
[42] D.M. Bernstein, Serpentine and amphibole asbestos, in: H. Salem, S.A. Katz (Eds.), Inhalation Toxicology, 3 ed., CRC Press, 2015, pp. 295–326, Chapter 14.
[43] V.L. Roggli, A.R. Brody, Changes in numbers and dimensions of chrysotile asbestos fibres in lungs of rats following short-term exposure, Exp. Lung Res. 7 (2) (1984) 133–147.
[44] M.C. Jaurand, J. Bignon, P. Sebastien, J. Goni, Leaching of chrysotile asbestos in human lungs: correlation with *in vitro* studies using rabbit alveolar macrophages, Environ. Res. 14 (2) (1977) 245–254.
[45] D. Bernstein, J. Dunnigan, T. Hesterberg, R. Brown, J.A. Legaspi Velasco, R. Barrera, J. Hoskins, A. Gibbs, Health risk of chrysotile revisited, Crit. Rev. Toxicol. 43 (2) (2013) 154–183.
[46] V.L. Roggli, Pathology of human asbestosis: a critical review, in: C.M. Fenoglio-Preiser (Ed.), Advances in Pathology, 2, Year Book Med. Pub., Chicago, 1989, pp. 31–60.
[47] P. Dumortier, L. Çoplü, I. Broucke, S. Emri, T. Selcuk, V. de Maertelaer, P. de Vuyst, I. Baris, Erionite bodies and fibres in bronchoalveolar lavage fluid (BALF) of residents from Tuzkoy, Cappadocia, Turkey, Occup. Environ. Med. 58 (2001) 261–266.
[48] G. Liu, P. Cheresh, D.W. Kamp, Molecular basis of asbestos-induced lung disease, Ann. Rev. Pathol. 8 (2013) 161–187.
[49] C. Oze, K.L. Solt, Biodurability of chrysotile and tremolite asbestos in simulated lung and gastric fluids, Am. Mineral. 95 (2010) 825–831, 5.
[50] A.F. Gualtieri, A. Viani, G. Sgarbi, G. Lusvardi, In vitro biodurability of the product of thermal transformation of cement-asbestos, J. Hazard. Mat. 205–206 (2012) 63–71.
[51] T.L. McLemore, P.M. Stevens, V. Roggli, M.V. Marshall, E.C. Lawrence, S.D. Greenberg, P.M. Stevens, Comparison of phagocytosis of uncoated *versus* coated asbestos fibres by cultured human pulmonary alveolar macrophages, Chest 80 (1) (1981) 39–42.
[52] M. Governa, M. Amati, S. Fontana, I. Visonà, G.C. Botta, F. Mollo, D. Bellis, P. Bo, Role of iron in asbestos-body-induced oxidant radical generation, J. Toxicol. Environ. Health 58 (5) (1999) 279–287.
[53] M. Governa, C. Rosanda, Mechanism of formation of asbestos bodies, Med. Lav. 63 (5) (1972) 179–188.
[54] A.R. Brody, L.H. Hill, Interstitial accumulation of inhaled chrysotile asbestos fibres and consequent formation of microcalcifications, Am. J. Pathol. 109 (1) (1982) 107–114.
[55] L. Le Bouffant, S. Bruyere, J.C. Martin, Quelques observations sur les fibres d'amiante et les formations minerals diverses rencontrees dans les poumons asbestosiques, Rev. Fr. Mal. Respir. 4 (1976) 121–140.

ACKNOWLEDGMENTS

Dott. Francesco D'Acapito, Dott.ssa Angela Trapananti e Dott. Ivan Colantoni per avermi seguito durante il periodo di stage a Gilda.

Dott. Miriam Hanuskova e Dott. Magdalena Lassinantti Gualtieri per il loro prezioso aiuto per le analisi BET e le misure di potenziale Zeta.

Prof. Giovanni B. Andreozzi per le analisi Fe^{57} MÖssbauer e la disponibilità nell'interpretazione dei risultati.

Tutto lo staff del CIGS, in particolare il Dott Massimo Tonelli, la Dott.ssa Maria Cecilia Rossi, il Sig. Giancarlo Urso e il Dott. Mauro Zapparoli per l'assistenza durante le sessioni di lavoro al diffrattometro e al SEM.

Dott. Alberto Viani, Dott. Petra Mácová, Dott. Marta Peréz Estébanez per le analisi FTIR, Raman e per le varie attività svolte in collaborazione.

Dott. Alessandro Cavallo per le analisi EMPA.

Prof. Natale Perchiazzi e il Dott. Marco Lezzerini per le analisi XRPD e per il prezioso contributo ai raffinamenti strutturali.

Dott. Konstantin Ignyatiev per il prezioso aiuto durante gli esperimenti condotti a I18 (DLS) e nell'interpretazione dei dati.

Dott. Manfred Burghammer per l'aiuto durante gli esperimenti condotti a ID13 (ESRF).

Dott. Nicola Bursi Gandolfi per l'aiuto in qualsiasi fase di lavoro, di interpretazione e stesura dei dati, nonché per la compagnia durante le missioni e durante qualsiasi giornata di lavoro.

Tutto lo staff del Centro di Ricerca sul Cancro Cesare Maltoni dell'Istituto Ramazzini, in particolare la Prof.ssa Fiorella Belpoggi e la Dott.ssa Eva Tibaldi per aver procurato e preparato i campioni istologici.

Ovviamente il Prof. Alessandro F. Gualtieri, per tutto, perché sotto la sua guida si ottengono grandi risultati, perché mi ha fatto crescere in maniera esponenziale dal punto di vista scientifico, per l'incredibile intraprendenza e disponibilità a spiegare qualsiasi concetto, in qualsiasi momento.

Ma più di tutti devo ringraziare Lara, per essermi sempre stata accanto in questi anni, per avermi aiutato in qualsiasi frangente, per avermi motivato quando ne avevo bisogno, per aver sopportato le mie infinite lamentele, per avermi regalato i momenti ed i ricordi più belli di tutta la mia vita e per avermi fatto crescere come persona. Se questo lavoro verrà apprezzato, sarà anche per merito tuo.